Using Distributed Energy Resources to Improve Power System Stability and Voltage Unbalance

by

Mengqi Yao

A dissertation submitted in partial fulfillment
of the requirements for the degree of
Doctor of Philosophy
(Electrical and Computer Engineering)
in the University of Michigan
2020

Doctoral Committee:

Associate Professor Johanna Mathieu, Chair
Professor Ian Hiskens
Assistant Professor Dan Molzahn
Associate Professor Siqian Shen

Mengqi Yao
mqyao@umich.edu
ORCID iD: 0000-0001-7013-1979

Dedication

To Wenqing.

Acknowledgments

I moved to Ann Arbor in August 2014, and now I am approaching the end of my PhD study. This six-year journey is intriguing, exhilarating, sometimes stressful, but I will treasure it throughout my whole life. I feel fortunate to have so many mentors and friends to share my joy and guide me through the hard times. I cannot imagine the past years without their help and encouragement.

I would like to sincerely express my deepest gratitude to my PhD advisor, Professor Johanna Mathieu. I am so honored to be her student. She showed me how a professional scientist should perform high-quality research work. I have learned a great deal on technical writing, presentation, and teaching from her. I would like to thank all my committee members, Professor Ian Hiskens, Professor Siqian Shen, and Professor Dan Molzahn, for their invaluable feedback and helpful discussions.

Next, I would like to thank the National Science Foundation (NSF) and the Solar Energy Technologies Office (SETO) of the U.S. Department of Energy (DOE) for providing funding during my doctoral studies.

Finally, I would like to thank my parents for comforting and cheering me up whenever I feel down and tense. Special thanks to my loving husband, Wenqing. Although he did not understand what I was doing, he was always my coding support and emotional trashcan.

Table of Contents

List of Figures

List of Tables

Abbreviations

AVR	Automatic Voltage Regulator
DAE	Differential and Algebraic Equations
DER	Distributed Energy Resources
DR	Demand Response
FACTS	Flexible Alternating Current Transmission Systems
KKT	Karush-Kuhn-Tucker
LIB	Limit Induced Bifurcation
LVUR	Line Voltage Unbalance Rate
ILP	Iterative Linear Programming
INLP	Iterative Nonlinear Programming
IM	Induction Machine
LP	Linear Programming
NLP	Nonlinear Programming
OPF	Optimal Power Flow
PEV	Plug-in Electric Vehicle
PSS	Power system stabilizer
PV	Photovoltaic
PVUR	Phase Voltage Unbalance Rate
SDP	Semidefinite Programming
SDR	Smallest Damping ratio
SNB	Saddle Node Bifurcation
SSV	Smallest Singular Value
SVC	Static VAR Compensator
SVD	Singular Value Decomposition
TCL	Thermostatically controlled load
VSCOPF	Voltage Stability Constrained Optimal Power Flow
VUF	Voltage Unbalance Factor

Abstract

The increasing penetration of renewables has driven power systems to operate closer to their stability boundaries and makes maintaining power quality more difficult. The goals of this dissertation are to develop methods to control distributed energy resources to improve power system stability and voltage unbalance. Specifically, demand response (DR) is used to realize the former goal, and solar photovoltaic (PV) systems are used to achieve the latter.

We present a new DR strategy to change the consumption of flexible loads while keeping the total load constant, improving voltage or small-signal stability without affecting frequency stability. The new loading pattern is only maintained temporarily until the generators can be re-dispatched. Additionally, an energy payback period maintains the total energy consumption of each load at its nominal value. Multiple optimization problems are proposed for determining the optimal loading pattern to improve different voltage or small-signal stability margins. The impact of different system models on the optimal solution is also investigated.

To quantify voltage stability, we choose the smallest singular value (SSV) of the power flow Jacobian matrix and the distance to the closest saddle-node bifurcation (SNB) of the power flow as the stability margins. We develop an iterative linear programming (ILP) algorithm using singular value sensitivities to obtain the loading pattern with the maximum SSV. We also compare our algorithm's performance to that of an iterative nonlinear programming algorithm from the literature. Results show that our ILP algorithm is more computationally scalable. We formulate another problem to maximize the distance to the closest SNB, derive the Karush–Kuhn–Tucker conditions, and solve them using the Newton-Raphson method. We also explore the possibility of using DR to improve small-signal stability. The results indicate that DR actions can improve small-signal characteristics and sometimes achieve better performance than generation actions.

Renewables can also cause power quality problems in distribution systems. To address this issue, we develop a reactive power compensation strategy that uses distributed PV systems to mitigate voltage unbalance. The proposed strategy takes advantage of Steinmetz

design and is implemented via both decentralized and distributed control. We demonstrate the performance of the controllers on the IEEE 13-node feeder and a much larger feeder, considering different connections of loads and PV systems. Simulation results demonstrate the trade-offs between the controllers. It is observed that the distributed controller achieves greater voltage unbalance reduction than the decentralized controller, but requires communication infrastructure. Furthermore, we extend our distributed controller to handle inverter reactive power limits, noisy/erroneous measurements, and delayed inputs. We find that the Steinmetz controller can sometimes have adverse impacts on feeder voltages and unbalance at noncritical nodes. A centralized controller from the literature can explicitly account for these factors, but requires significantly more information from the system and longer computational times. We compare the performance of the Steinmetz controller to that of the centralized controller and propose a new controller that integrates centralized controller results into the Steinmetz controller. Results show that the integrated controller achieves better unbalance improvement compared with that of the centralized controller running infrequently.

In summary, this dissertation presents two demand-side strategies to deal with the issues caused by the renewables and contributes to the growing body of literature that shows that distributed energy resources have the potential to play a key role in improving the operation of the future power system.

Chapter 1

Introduction

A power grid is a network of equipment that produces, transfers, and uses electricity. In other words, a power system can be divided into the following sub-systems: generation, transmission, and distribution system. In the 20th century, the goal of an electric power system was to provide adequate power flows from the power plant to the end user; however, increasing penetrations of distributed energy resources (DERs) now allow end users to transfer power back to the grid, bringing both benefits and challenges to power systems. Common examples of DERs include distributed generation (rooftop photovoltaic (PV) panels, wind turbines), electric vehicles (EV), energy storage, and demand response (DR) applications. Although DERs can mitigate the environmental impacts of power systems and bring economic benefits [4, 14, 109], they also cause some problems. For example, fluctuating renewable energy sources will negatively impact power system stability [41, 131] in transmission systems. Specifically, power-electronics-connected fluctuating renewable generation from wind and solar introduces more variability in operating points, reduces system inertia, and decreases the controllability of active power injections. In addition, these fluctuations in the PV and wind power production have direct consequences to the power quality in distribution systems [43, 78, 127], i.e., voltage fluctuation, voltage unbalance, and harmonic distortion. Despite these challenges, proper DER strategies could also help to overcome these difficulties and improve the stability and reliability of the electric power system.

We consider two kinds of DER in this work: demand response and solar PV systems. The goals of this work are: 1) to develop methods to coordinate flexible loads to improve electric power transmission system stability margins; 2) to develop decentralized strategies to control the reactive power of solar PV systems to mitigate voltage unbalance in distribution systems. The results of this work suggest that demand-side resources can play an active role

in improving several characteristics of the power system.

In the following sections, we present a brief background on power system stability and voltage unbalance. Detailed literature reviews on past efforts using conventional methods or DERs to improve stability and unbalance are also provided. After that, we present the motivations of the research and the main research questions in this dissertation. Finally, we describe the organization and contributions of the rest of the dissertation.

1.1 Power System Stability

In this section, we first provide the definitions of system stability, and then introduce the background on demand response by summarizing the services that DR has already provided in the power system, and by developing the motivation for the first part of the research in this dissertation.

1.1.1 Definition and Literature Review

Electric power system stability refers to the ability to operate normally after a disturbance and is commonly divided into three categories: frequency stability, voltage stability, and rotor angle stability [71].

Frequency stability refers to the ability of a power system to maintain steady frequency (60 Hz in the United States/Canada/Japan, 50 Hz in China/Australia/Europe) after a significant imbalance between generation and load [71]. Common reasons that lead to frequency instability include lack of power generation, cascading outages of transmission lines, and communication malfunction [2]. Previous works [34, 69, 87] have shown the great potential of battery energy storage systems for frequency regulation.

Voltage stability refers to the ability of a power system to maintain acceptable voltages at all buses after disturbances [71]. Maintaining voltage stability is critical because an increasingly stressed power system with fluctuating renewable generation now operates closer to the system's stability limits, to the extent that a small disturbance may lead to voltage collapse. Power flow analysis is necessary for the steady-state voltage stability analysis to obtain the voltage information at all buses. In conventional power flow analysis, we generally assume that the transmission system is balanced so that the network can be represented in the single-phase (positive sequence) form. The power flow problem is a set of nonlinear algebraic equations $F(x, \lambda) = 0$, where x represents system states including voltage magnitudes and

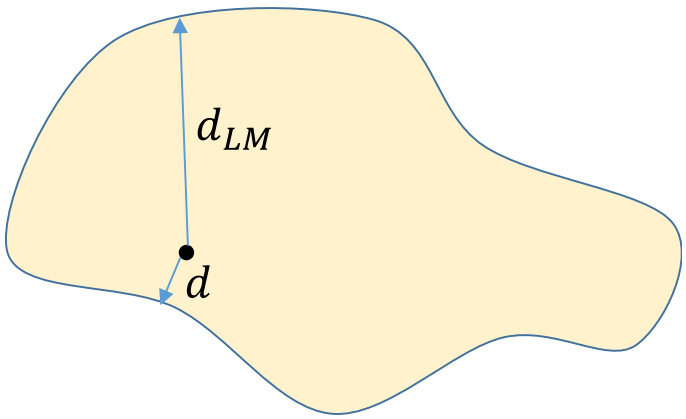

Figure 1.1: A conceptual illustration of the loading margin (d_{LM}) and the distance to the closest SNB (d) in the power flow feasibility region.

angles and λ represents power injections. Numerical techniques, i.e., the Newton-Raphson method [124], are required to solve this set of nonlinear equations.

In order to quantify the voltage stability level of a system, voltage stability margins have been introduced. The steady-state voltage stability margin is used to estimate the distance between the current power system operating point and the unstable operating point. Common stability margins include loading margin, the smallest singular value (SSV) of the power flow Jacobian matrix, and the distance to the closest Saddle-Node-Bifurcation (SNB). Figure 1.1 shows a conceptual illustration of the power flow feasibility region; the point inside the shaded region represents a power flow solution corresponding to a specific power injection pattern λ. The definitions of each margin are:

- **Loading margin** is the distance between the current operating point and the boundary of the feasibility region, assuming that load and generation are increased uniformly (in a multiplicative sense) throughout the system [49], denoted as d_{LM} in Fig. 1.1. The loading margin is commonly calculated using a Continuation Power Flow to compute the distance to instability [3].

- **Smallest singular value** is computed through Singular Value Decomposition (SVD) of the power flow Jacobian matrix $J = \dfrac{\partial F}{\partial x}$. If the SSV equals zero, the operating point is located on the boundary of the power flow feasibility region. Therefore, the magnitude of the SSV gives us a measure of how close the Jacobian is to being singular,

i.e., power flow infeasibility. Feasibility and stability are closely linked [52].

- **Distance to the closest SNB** is the shortest distance between the current operating point and the boundary of the feasibility region [39], denoted as d in Fig. 1.1.

A variety of methods have been proposed to improve these voltage stability margins, including generation dispatch [38, 49, 140], locating/sizing distributed generation [5, 7, 80], and use of advanced power electronic devices [90, 91, 113].

Small-signal stability (one type of rotor angle stability) is the ability of the system to maintain synchronism when subjected to small disturbances. Small-signal and transient characteristics of the transmission network are also strongly influenced by the high penetration of intermittent renewables [112]. The small-signal characteristics of the power system are based on the swing dynamics of the network. In particular, power-system transients are analyzed via the nonlinear swing equations, with small-signal characteristics being extracted from their linearizations around the operating point. The electromechanical modes of the generators are the eigenvalues of the linearized system matrix. The **damping** of the network is one measure of small-signal stability. Two types of damping are commonly considered: the smallest damping ratio and the damping ratios of the critical inter-area modes (electromechnical oscillations in the range of less than 1 Hz [70]). In [31], Kundur and co-authors have addressed a generator re-scheduling problem to increase power transfer while continuing to adhere to a small-signal stability constraint that requires the smallest damping ratio to be larger than a critical value; the problem is solved using a sensitivity-based approach. Several studies have sought to improve the damping ratios of the critical inter-area modes via re-dispatch, whether based on a formal analysis/optimization [31, 85, 86] or from data obtained from wide-area measurement systems [145]. Load reduction in addition to generator re-dispatch to reduce flows on tie-lines has also been considered in [57], with the aim of improving the damping of the critical inter-area mode. The small-signal stability can also be measured by the **distance to the closest Hopf bifurcation**, which is known as the oscillatory stability margin [48, 81]. In [89], the distance is improved by designing the placement of Power System Stabilizers (PSS) and static Var compensators. The **largest real part of the eigenvalues** can alternatively be used to approximate the distance to the small signal stability boundary. Reference [82] includes the largest real part as a stability security constraint in an optimization problem.

1.1.2 Background on Demand Response and Motivation

As defined in [129], Demand Response is "a tariff or program established to motivate changes in electric use by end-use customers in response to changes in the price of electricity over time, or to give incentive payments designed to induce lower electricity use at times of high market prices or when grid reliability is jeopardized". A typical example of Demand Response is when customers temporarily change the temperature set points of their heaters or air conditioners to increase/decrease the power demand of the system. Another example is when customers shift everyday activities (i.e., using dishwashers, washing machines, dryers, etc.) to the off-peak period because the electricity prices are lower. DR participation is growing in wholesale and retail markets [46]. In the United States, about 10.7 GW DR was dispatched in 2017 (58.4% of the enrolled DR capacity) [30]; the number further increased to 12.3 GW in 2018 (59.2% of the enrolled DR capacity) [122]. As predicted in [51], the estimated global market for DR capacity could grow to 200 GW by 2023.

Demand response can bring benefits to the electricity market [6, 19, 20, 129], which can help reduce system costs and improve reliability. DR can also be used to improve power system stability: for example, [23, 116, 147] propose methods to coordinate loads to help balance supply and demand, improving frequency stability. Use of DR may be more cost-effective and environmentally-friendly than alternative approaches to maintain power system stability in the presence of high penetrations of renewables. As we increase the controllability of distributed electric loads to enable their participation in a variety of DR programs and electricity markets [24], we also unleash their potential to provide a variety of stability-related services not typically rewarded in existing programs or markets. We assume that demand response actions are contractual; consumers sign a contract with an aggregator, who will dispatch loads within the limits of the contract. Flexible loads respond to the requested energy change as contracted; otherwise, consumers will pay a penalty. A key research question is whether loads are effective at improving stability margins other than those related to frequency stability, for example, voltage or small-signal stability margins. However, harnessing loads for these purposes requires the development of new algorithms, the design of which influences their effectiveness.

In the past DR program, the flexible load was shifted in time or shed, resulting in decreases and increases in system-wide load. This action involves a temporary loss of comfort and requires decreases/increases in system-wide generation in order to maintain system frequency. In contrast to that, we propose a new DR strategy to shift load consumption in *space*, specifically, reallocating load to different buses while keeping the total loading constant, so

as not to impact system frequency when improving voltage or rotor angle stability. Although in practice primary frequency control will manage small load deviations, we choose to require the total load to remain constant to isolate the impact of load pattern changes from changes in the total loading. We propose to use this strategy if the system is operating close to its feasibility limits (but not so close that emergency actions are immediately necessary) and generators are unable to respond sufficiently-quickly to correct the problem. Fast-acting demand responsive loads coordinated via low-latency communication systems would respond initially until the generators can take over. We will "pay back" the changes to each load in a future period so the total energy consumption of each load is unchanged. We refer to these stability improvement problems as "spatio-temporal DR problems". In this dissertation, we incorporate different stability metrics into the formulation and determine how different metrics impact the control of resources. We also compare the cost and performance of spatio-temporal load shifting to that of generator actions and load shedding. Moreover, we investigate the impact of different system models on the optimal solutions.

1.2 Voltage Unbalance

In this section, we switch our focus to the power quality of distribution systems. We first introduce the definition of voltage unbalance and its influence on the system. Next, a review of the literature on unbalance mitigation is presented. Finally, the motivation for using Steinmetz circuit design is given.

1.2.1 Definitions and Literature Review

In contrast to balanced transmission systems, distribution systems are unbalanced by nature because of the asymmetry of loading across phases and line configurations. Therefore, distribution systems cannot be represented in the single-phase equivalent form; zero and negative sequence components cannot be neglected.

Many distribution networks are experiencing rapid growth in single-phase DERs, such as solar PV generation, and in large single-phase loads, particularly plug-in EVs. Consequently, voltage unbalance is becoming more severe because of fluctuating solar PV generation and irregular electric vehicle charging [13, 108]. Unbalanced voltages can cause overheating, vibration, and reduction in efficiency of three-phase motors and transformers [65, 75, 137]. Using an induction motor as an example, based on [96], a 2.5% voltage unbalance for a 100

hp motor at full-load can have a current unbalance of 27.7%. Current unbalance will increase the motor temperature; for every 10°C increase in winding temperature, insulation life is approximately cut in half, which results in significant repair and replacement costs [130]. For U.S. industries, the cost of unbalanced voltage is up to $28 billion a year [130]. In a four-wire (A, B, C, N) system, voltage unbalance can induce neutral current which not only increases power losses but also impacts protection devices [77]. Power loss is one of the major concerns of the utilities.

Three definitions of voltage unbalance (from IEC, NEMA, and IEEE) [105] are commonly used in existing literature: voltage unbalance factor (VUF), line voltage unbalance rate (LVUR), and phase voltage unbalance rate (PVUR):

- $\text{VUF} = \dfrac{\text{negative sequence voltage magnitude}}{\text{positive sequence voltage magnitude}} \times 100$
- $\text{LVUR} = \dfrac{\text{max voltage deviation from average line-to-line voltage}}{\text{average line-to-line voltage}} \times 100$
- $\text{LVUR} = \dfrac{\text{max voltage deviation from average line-to-neutral voltage}}{\text{average line-to-neutral voltage}} \times 100$

In the IEC and ANSI standards [32, 42, 59], these unbalance rates should not exceed 2% or 3%.

There are a variety of strategies to mitigate voltage unbalance. Reconfiguration algorithms can be used to equalize load consumption among phases [21, 115]. Alternatively, voltage balancing can be achieved using power electronic-based static synchronous compensators, passive power filters, or static VAR compensators [29, 77, 101]. However, the former may not be practical because distribution networks often lack automated/remote switching equipment. The latter add additional plant and maintenance costs. Distributed energy resources can also be used to mitigate voltage unbalance. Reference [35] solves an optimization problem to minimize power losses via the control of PEV charging; minimizing losses also improves balance. Reference [45] controls the reactive power injections of PEVs to compensate for negative sequence current. Reference [121] proposes both centralized and distributed real-time strategies that use energy storage to mitigate phase unbalance considering uncertainties.

Control of solar PV systems has also been proposed to help mitigate unbalance. A switching strategy is proposed in [63] to modify the phase assignment of single-phase PV systems in real time to equitably distribute active power injections amongst the three phases to reduce

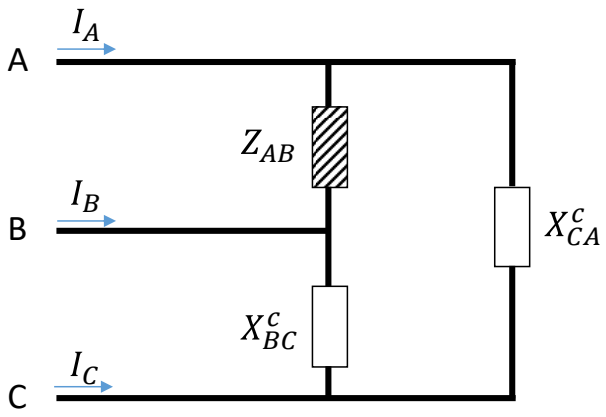

Figure 1.2: Steinmetz compensation circuit for a single-phase load Z_{AB} connected between phase A and phase B.

unbalance. The approach is demonstrated on a small network; however, it may not scale to systems with large numbers of distributed PV systems. Moreover, in real systems, all three phases may not be available at the point of PV connection and additional equipment would need to be installed to enable phase reassignment. Inverter-based control strategies for eliminating unbalanced currents are developed in [33, 55]. These strategies control both active and reactive power injections from the PV systems. However, controlling (i.e., reducing) active power injections would be unacceptable to most PV system owners. Rather, they would like to maximize their active power production so as to minimize their electricity cost and/or maximize their profits from feed-in tariffs.

Most of the strategies proposed for using PV inverters to improve phase unbalance rely on centralized control. For example, [95, 120, 141] solve optimization problems to control active and/or reactive power injections from PV systems to improve unbalance. Centralized control generally requires more information (models, parameters) and communications (time-varying states and inputs) than distributed or decentralized approaches.

1.2.2 Background on Steinmetz Circuit Design and Motivation

Steinmetz proposed a circuit design method to achieve voltage balance by controlling the reactances of three-phase delta-connected constant-impedance loads, as described in [9, 62, 94]. Fig. 1.2 shows a Steinmetz compensation circuit for a single-phase load. Assume that the load, connected between phases A and B, is modeled as a constant impedance load $Z_{AB} = R_{AB} + jX_{AB}$ (its admittance is $Y_{AB} = G_{AB} - jB_{AB}$). Steinmetz circuit design

computes the reactances we should connect to phases BC and CA to make the single-phase load appear as a balanced three-phase load. In [9, 62, 94], analytic expressions of compensated reactances are provided. Steinmetz design has been used to control three-phase delta-connected static VAR compensators to balance traction system loads [128], but its use to control the reactive power injections of single-phase DERs, such as PV systems, is new.

The approach is simple and does not require solving any system-wide optimization problem, and thus is inexpensive to implement compared to centralized control/optimization strategies that require communication and detailed system models. We propose to control the reactive power of distributed solar PV systems without curtailment of real power production to mitigate voltage unbalance based on the idea of Steinmetz circuit design. The capabilities and limitations of Steinmetz circuit design are studied. A key research question is whether Steinmetz circuit design can be applied in a decentralized way. If so, would it be possible to achieve a better unbalance improvement if communication is available. The critical distinguishing challenge that differs from past efforts is that we need to control a large number of distributed single-phase solar PV inverters rather than a single large power electronics device. When we apply the Steinmetz controller to real systems in the presence of time-varying load and PV generation, we will need to overcome a number of practical challenges, namely, inverter reactive power limits, noisy/erroneous measurements, and delayed inputs. In this dissertation, we will consider cases with different load and PV system connection arrangements and control objectives. We will test the performance of the Steinmetz controller on large feeders using real PV data together with realistic load data. Furthermore, we will benchmark the performance of the Steinmetz controller against those of controllers from the literature.

1.3 Contributions and Structure of the Dissertation

The main contributions of this dissertation fall into two categories: the development of computationally tractable solution approaches to the spatio-temporal DR problems with different stability margins and the development of controllers based on Steinmetz design to mitigate voltage unbalance using distributed solar PV systems. The main content of each chapter is described below.

Chapter 2 proposes an optimization problem to maximize the smallest singular value of the power flow Jacobian matrix using DR and solves it via iterative linear programming with

singular value sensitivity. In addition, we compare the performance of demand response to those of generator actions and load shedding. The computation time of the iterative linear programming algorithm is benchmarked against that of an iterative nonlinear programming algorithm from [10].

Chapter 3 considers different types of load models and explores the impact of load models on the optimal solutions.

Chapter 4 presents the formulation of the full "spatio-temporal DR problem". In addition to SSV improvement, the energy payback period is considered. Again, the iterative linear programming algorithm is used to solve the multi-period problem. We conduct case studies using the IEEE 9- and 118-bus systems to determine optimal loading patterns and assess algorithmic performance. Furthermore, we compare the generation cost of spatio-temporal load shifting to that of generator actions.

Chapter 5 chooses the distance to the closest SNB as the measure of voltage stability. A nonlinear nonconvex optimization problem is formulated and then solved through deriving the KKT conditions and solving a set of nonlinear equations using the Newton-Raphson method. We compare the optimal solution to those obtained using other voltage stability metrics including the smallest singular value of the power flow Jacobian and the loading margin, finding that all approaches produce different solutions.

Chapter 6 formulates the optimization problem to improve small-signal characteristics of power system using DR. The problem is solved using iterative linear programming with generalized eigenvalue sensitivity. Different system models are considered in this chapter to investigate the impact on the optimal loading pattern.

Chapter 7 develops a reactive power compensation strategy that uses distributed solar PV inverters to mitigate such voltage unbalance. The proposed strategy takes advantage of Steinmetz design and is implemented via both decentralized and distributed control. The latter coordinates PV inverters through a communication network. We demonstrate the performance of the controllers on the IEEE 13-node feeder and a much larger taxonomy feeder (617 nodes and 1196 triplex nodes) assuming constant load and PV, and consider different connections of loads and PV systems.

Chapter 8 proposes approaches to enhance the Steinmetz controller to cope with a number of practical considerations, namely, inverter reactive power limits, measurement noise and error, and communication delays. Case studies are conducted on the IEEE 13-node feeder with time-varying load and PV generation.

Chapter 9 summarizes the pros and cons of our distributed controller through the compar-

ison with a centralized controller from [47]. In addition, we propose an integrated controller that modifies the design of the distributed controller using the centralized controller results to overcome limitations of the distributed controller. We demonstrate the performance of the integrated controller on the IEEE 13-node feeder and the taxonomy R1 feeder with time-varying load and PV generation.

Chapter 10 concludes the dissertation and discusses a number of future avenues of research.

Note that each chapter is self-contained; mathematical notation is defined in each chapter unless an equation from a different chapter is explicitly referenced.

The following is a list of publications that have resulted from the work described in this dissertation to date.

- M. Yao, J.L. Mathieu, and D.K. Molzahn. "Using demand response to improve power system voltage stability margins". In: *IEEE PowerTech*. 2017.
- M. Yao, D.K. Molzahn, and J.L. Mathieu. "The impact of load models in an algorithm for improving voltage stability via demand response". In: *the Allerton Conference on Communication, Control, and Computing*. 2017 (Invited).
- K. Koorehdavoudi, M. Yao, J.L. Mathieu, and S. Roy. "Using demand response to shape the fast dynamics of the bulk power network". In: *IREP Symposium on Bulk Power System Dynamics and Control*. 2017.
- M. Yao, I.A. Hiskens, and J.L. Mathieu. "Improving power system voltage stability by using demand response to maximize the distance to the closest saddle-node bifurcation". In: *IEEE Conference on Decision and Control*. 2018.
- M. Yao, D.K. Molzahn, and J.L. Mathieu. "An optimal power flow approach to improve power system voltage stability using demand response". In: *IEEE Trans Control of Network Systems*, 6.3 (2019): 1015-1025.
- M. Yao, I.A. Hiskens, and J.L. Mathieu. "Applying Steinmetz circuit design to mitigate voltage unbalance using distributed solar PV". In: *IEEE PowerTech*. 2019.
- M. Yao and J.L. Mathieu. "Overcoming the practical challenges of applying Steinmetz circuit design to mitigate voltage unbalance using distributed solar PV". In: *Power Systems Computation Conference*. 2020.

Chapter 2

Using DR to Improve the Smallest Singular Value

This chapter presents a method for determining the optimal loading pattern that maximize the smallest singular value (SSV). Additionally, we compare the performance of demand response to that of generator actions and load shedding. This chapter is largely based on the following papers.

- M. Yao, J.L. Mathieu, and D.K. Molzahn. "Using demand response to improve power system voltage stability margins". In: *IEEE PowerTech*. 2017.
- M. Yao, D.K. Molzahn, and J.L. Mathieu. "An optimal power flow approach to improve power system voltage stability using demand response". In: *IEEE Trans Control of Network Systems*, 6.3 (2019): 1015-1025.

2.1 Notation

Functions

$\mathcal{F}_n^{\mathrm{P}}(\cdot)$	Real power injection at bus n
$\mathcal{F}_n^{\mathrm{Q}}(\cdot)$	Reactive power injection at bus n
$\mathcal{H}_{nm}(\cdot)$	Line flow for line (n, m)
$f_n^{\mathrm{P}}(\cdot)$	Linearization of $\mathcal{F}_n^{\mathrm{P}}$
$f_n^{\mathrm{Q}}(\cdot)$	Linearization of $\mathcal{F}_n^{\mathrm{Q}}$
$h_{nm}(\cdot)$	Linearization of $\mathcal{H}_{nm}$

Sets

$\mathcal{N}$	Set of all buses
$\mathcal{S}_{\mathrm{PV}}$	Set of all PV buses
$\mathcal{S}_{\mathrm{PQ}}$	Set of all PQ buses
$\mathcal{S}_{\mathrm{G}}$	Set of buses with generators
$\mathcal{S}_{\mathrm{DR}}$	Set of buses with responsive loads

Variables & Parameters

J	Jacobian matrix
l	Left eigenvector
n	Size of $\mathcal{N}$
n_{pv}	Size of $\mathcal{S}_{\mathrm{PV}}$
n_{pq}	Size of $\mathcal{S}_{\mathrm{PQ}}$
n_{dr}	Size of $\mathcal{S}_{\mathrm{DR}}$
$P_{\mathrm{d},n}$	Real power demand at bus n
$P_{\mathrm{g},n}$	Real power generation at bus n
P_{loss}	Total power loss in the system
$Q_{\mathrm{d},n}$	Reactive power demand at bus n
$Q_{\mathrm{g},n}$	Reactive power generation at bus n
r	Right eigenvector
u	Left singular vector
V_n	Voltage magnitude at bus n
w	Right singular vector
ε	Loss management strategy parameter
θ_n	Voltage angle at bus n
λ	Eigenvalue of a matrix
λ_0	Smallest eigenvalue of a matrix
σ	Singular value of a matrix
σ_0	Smallest singular value of a matrix
Σ, U, W	Singular Value Decomposition (SVD) matrices
χ	Operating point

Bold symbols denote vectors including all variables of a type. Overlines and underlines represent the upper and lower limits for variables. Numbers in the parentheses $(\cdot)$ refer to the period number. Subscript 'ref' denotes the slack bus. Superscript '*' denotes the current

value of a variable and superscript 'T' denotes the transpose of a matrix. The notation $X \succeq 0$ means that X is a positive semidefinite matrix. For notational simplicity, we assume that each bus has at most one generator and at most one load. The word 'PV' in Chapter 2-6 denotes as one of the types of power system buses, the real power and voltage magnitude of which are specified.

2.2 Chapter Introduction

In this chapter, we propose an optimal power flow (OPF) approach that uses DR to improve smallest singular value, which serves as a measure of steady-state voltage stability [15, 16, 17, 79, 82, 123, 125, 126]. In contrast to past work that developed load shedding approaches to improve voltage stability [15, 44, 146], we decrease and increase loads while keeping the total loading constant to avoid fluctuation of the system frequency, and we "pay back" the changes to each load so its total energy consumption is unchanged. We envision that such an approach would be used only occasionally, when voltage stability margins are below those desired, but not so small that emergency actions are immediately necessary. DR actions could be executed quickly while ramp-rate-limited generators begin to respond, eventually relieving the loads. Beyond developing the problem formulation and solution algorithm, our objective is to compare the stability margin improvement of load actions to those of generator actions in order to understand both the advantages and disadvantages of the approach. Additionally, we compute the amount of load shedding that would be necessary to achieve the same stability margin improvements as load shifting.

The SSV gives us a measure of how close the Jacobian is to being singular, i.e., power flow infeasibility. Feasibility and stability are closely linked [52]. The advantages of using the SSV as a voltage stability margin are that 1) it captures any direction of changes in power injections and 2) there exist approximate mathematical formulations suitable for inclusion in optimization problems, e.g., [10, 15, 26]. The disadvantages of using the SSV are that 1) it only provides implicit information on the distance to the solvability boundary, 2) it does not capture the impact of all engineering constraints (e.g., reactive power limits could be reached prior to power flow singularity [111]), and 3) it may not be well-behaved, specifically, [72] found that the SSV at voltage collapse varies significantly as function of the loading direction (see Fig. 3 of [72]). Additionally, 4) its numerical value is system-dependent [79] and so the threshold value for a particular system would need to be determined from operator experience. Moreover, 5) the nonlinear programming (NLP) algorithm for solving approximate

mathematical formulation [10] does not scale to realistically-sized system. Despite these issues, we base our approach on the SSV in order to exploit the approximate mathematical formulation [10, 26] and we develop an improved solution algorithm that scales significantly better.

The loading margin is another common voltage stability margin, which is the distance between the current operating point and the maximum loading point [49]. The loading margin is calculated using continuation power flow methods, where the load and generation are usually increased uniformly (in a multiplicative sense) throughout the system [11, 61]. A drawback of this method is that it assumes a single direction of changes in power injections. In this chapter, we will also use DR to maximize the loading margin and compare the results to those with maximum SSV.

The technical contributions of this chapter are as follows:

- We develop an iterative linear programming (LP) solution algorithm using singular value sensitivities [15, 132, 146] to maximize SSV;
- we compare the solutions given by the iterative LP with those of three benchmark approaches - one using a brute force search and two that maximize the loading margin;
- we benchmark the computation time of iterative LP solution algorithm against that of the NLP algorithm in [10];
- and we compare the voltage stability margin improvement of load shifting to that of generator actions and load shedding.

2.3 Problem Description

A conceptual illustration of the problem is shown in Fig. 2.1. The blue shaded region is the feasible/stability region of the power system. The system is initially operating with an adequate stability margin at an operating point (star) determined via unit commitment and economic dispatch. A disturbance happens (e.g., a line goes out of service) causing the operating point to move towards the feasibility/stability boundary (i.e., to Operating Point 0), the system is prone to instability because slight variations in power injections might cause the operating point to leave the stable operating region. The system operator dispatches quick-acting resources including DR to maximize the stability margin (Operating Point 1). After a short period of time, the generators are re-dispatched so that the flexible

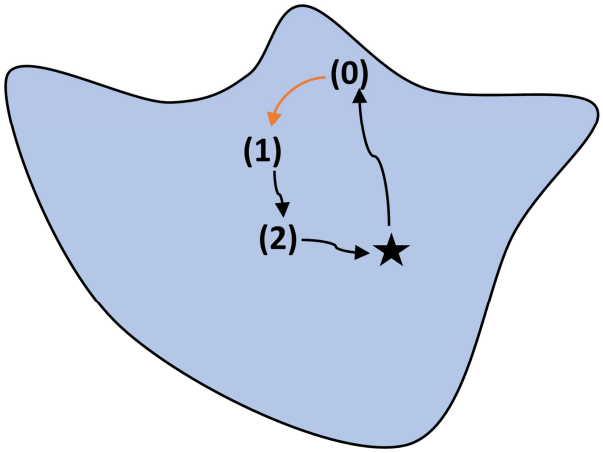

Figure 2.1: Conceptual illustration of the problem.

loads can return to consuming their nominal demands plus/minus some power to "pay back" the energy consumed/not consumed while at Operating Point 1, the operating point then changes (Operating Point 2). Finally, the system returns to its initial operating point, or another point with an adequate stability margin. In this chapter, we develop a method to achieve Operating Point 1 (Period 1), which shown as the orange line in Fig. 2.1, and we will include the payback period in Chapter 4.

During the stability improvement period, we require the total loading to remain unchanged, so as not to affect the system frequency. We assume that the load at certain buses can be decreased or increased within known limits for a short period of time. For example, the responsive loads could be aggregations of heating and cooling loads, such as commercial building heating, ventilation, and air conditioning (HVAC) systems and residential thermostatically controlled loads (TCLs), e.g., air conditioners and refrigerators that cycle on/off within a temperature dead-band. Increases and decreases in load can be achieved through temperature set point adjustments and/or commands to switch TCLs on/off [24]. These types of loads are flexible in their instantaneous power consumption, but energy constrained (i.e., they must consume a certain amount of energy over time), like energy storage units.

In our base case, we use loads alone to improve the stability margin in Period 1. Generator real power injections are held constant with the exception of that associated with the slack bus, which compensates for the small change in system losses resulting from the change in loading pattern (note we could have also assumed a distributed slack). Generator reactive power injections adjust to maintain voltage magnitudes at the PV buses. We model all loads as constant real power loads with constant power factor in this chapter. We will explore the

impact of load models on the results in Chapter 3.

Beyond our base case, we also investigate cases in which we allow (ramp-rate-limited) generator real power injections and voltage magnitudes at PV buses to change in Period 1. We also explore an alternative loss management strategy in which we require the total loading *plus system losses* to remain unchanged so that no generator (including the slack bus) is required to respond in Period 1.

Since we focus on static voltage stability, we ignore power system dynamics. Investigating the dynamic stability implications of changes in operating points is a subject for future research.

2.4 Optimization Model

Let $\mathcal{N}$ be the set of all buses, $\mathcal{S}_{\text{PV}}$ be the set of all PV buses, and $\mathcal{S}_{\text{PQ}}$ be the set of all PQ buses. Additionally, let $\mathcal{S}_{\text{G}}$ be the set of all buses with generators, i.e., all PV buses in addition to the slack bus, and let $\mathcal{S}_{\text{DR}}$ be the set of buses with responsive loads; the buses comprising $\mathcal{S}_{\text{DR}}$ may be PV or PQ buses. In our case studies, we assume that a portion of the existing loads in the network are responsive.

The goal of the optimization problem is to find the Operating Point 1 that maximizes the SSV of power flow Jacobian matrix $J(\boldsymbol{\theta}(1), \boldsymbol{V}(1))$. The general formulation is as follows.

$$\min_{\substack{\boldsymbol{P_g}(1),\boldsymbol{Q_g}(1),\\ \boldsymbol{P_d}(1),\boldsymbol{Q_d}(1),\\ \boldsymbol{V}(1),\boldsymbol{\theta}(1),\sigma_0(1)}} \quad -\sigma_0(1) \quad \text{subject to} \tag{2.1a}$$

$$\sigma_0(1) = \sigma_{\min}\{J(\boldsymbol{\theta}(1), \boldsymbol{V}(1))\} \tag{2.1b}$$

$$\mathcal{F}_n^{\text{P}}(\boldsymbol{\theta}(1), \boldsymbol{V}(1)) = P_{\text{g},n}(1) - P_{\text{d},n}(1) \qquad \forall n \in \mathcal{N} \tag{2.1c}$$

$$\mathcal{F}_n^{\text{Q}}(\boldsymbol{\theta}(1), \boldsymbol{V}(1)) = Q_{\text{g},n}(1) - Q_{\text{d},n}(1) \qquad \forall n \in \mathcal{N} \tag{2.1d}$$

$$\sum_{n \in \mathcal{S}_{\text{DR}}} P_{\text{d},n}(1) = \sum_{n \in \mathcal{S}_{\text{DR}}} P_{\text{d},n}(0) + \varepsilon \left(P_{\text{loss}}(0) - P_{\text{loss}}(1)\right) \tag{2.1e}$$

$$P_{\text{d},n}(1) \cdot \mu_n = Q_{\text{d},n}(1) \qquad \forall n \in \mathcal{N} \tag{2.1f}$$

$$P_{\text{d},n}(1) = P_{\text{d},n}(0) \qquad \forall n \in \mathcal{N} \setminus \mathcal{S}_{\text{DR}} \tag{2.1g}$$

$$\theta_{\text{ref}}(1) = 0 \tag{2.1h}$$

$$\mathcal{H}_{nm}(\boldsymbol{\theta}(1), \boldsymbol{V}(1)) \leq \overline{\mathcal{H}}_{nm} \tag{2.1i}$$

$$\mathcal{H}_{mn}(\boldsymbol{\theta}(1), \boldsymbol{V}(1)) \leq \overline{\mathcal{H}}_{mn} \tag{2.1j}$$

$$\underline{P}_{\mathrm{g},n}(1) \leq P_{\mathrm{g},n}(1) \leq \overline{P}_{\mathrm{g},n}(1) \qquad \forall n \in \mathcal{S}_{\mathrm{G}} \qquad (2.1\mathrm{k})$$

$$\underline{Q}_{\mathrm{g},n}(1) \leq Q_{\mathrm{g},n}(1) \leq \overline{Q}_{\mathrm{g},n}(1) \qquad \forall n \in \mathcal{S}_{\mathrm{G}} \qquad (2.1\mathrm{l})$$

$$\underline{P}_{\mathrm{d},n}(1) \leq P_{\mathrm{d},n}(1) \leq \overline{P}_{\mathrm{d},n}(1) \qquad \forall n \in \mathcal{S}_{\mathrm{DR}} \qquad (2.1\mathrm{m})$$

$$\underline{V}_{n}(1) \leq V_{n}(1) \leq \overline{V}_{n}(1) \qquad \forall n \in \mathcal{N} \qquad (2.1\mathrm{n})$$

Constraint (2.1b) defines the SSV of $J(\boldsymbol{\theta}, \boldsymbol{V})$ where $\sigma_{\min}$ is a function that takes the SSV of a matrix. Constraints (2.1c) and (2.1d) are the nonlinear AC power flow equations [142]. Constraint (2.1e) sets the total system load in Period 1 to be equal its nominal value plus a portion of the change in system losses, where the real power loss is $P_{\mathrm{loss}}(t) = \sum_{n \in \mathcal{N}}(P_{\mathrm{g},n}(t) - P_{\mathrm{d},n}(t))$ and ε is a parameter that defines the loss management strategy (i.e., $0 \leq \varepsilon \leq 1$, where $\varepsilon = 1$ allocates loss management exclusively to the loads, while $\varepsilon = 0$ allocates loss management exclusively to the slack bus). Constraint (2.1f) fixes the power factor of each load, where μ_n is the ratio between the reactive and real demand at bus n. Constraint (2.1g) fixes the non-responsive demand to its nominal value. Constraint (2.1h) sets the slack bus voltage angle. Constraints (2.1i)–(2.1n) limit the line flows, real and reactive power generation at generator buses, real power demand at buses with responsive loads, and voltage magnitudes at all buses. The real power generation limits $\big(\underline{P}_{\mathrm{g},n}(1), \overline{P}_{\mathrm{g},n}(1)\big)$ depend on whether or not the generator is modeled as responsive in Period 1, its minimum/maximum output, its ramp limits, and, for the slack bus, the loss management strategy (i.e., when $\varepsilon = 0$ the slack bus real power generation will be allowed to vary, but when $\varepsilon = 1$ it will be fixed). The real power demand limits $\big(\underline{P}_{\mathrm{d},n}(1), \overline{P}_{\mathrm{d},n}(1)\big)$ depend on the flexibility of the responsive loads. The voltage limits $\big(\underline{V}_{n}(1), \overline{V}_{n}(1)\big)$ depend on whether or not the generator voltages are allowed to adjust in Period 1.

In our base case, the slack bus manages the change in losses, (i.e., $\varepsilon = 0$) but the real power generation of all other generators is fixed in Period 1. Additionally, voltage magnitudes at all generator buses are fixed in Period 1. Specifically,

$$P_{\mathrm{g},n}(1) = P_{\mathrm{g},n}(0) \qquad \forall n \in \mathcal{S}_{\mathrm{PV}}$$

$$\underline{P}_{\mathrm{g,ref}}(1) \leq P_{\mathrm{g,ref}}(1) \leq \overline{P}_{\mathrm{g,ref}}(1)$$

$$V_{n}(1) = V_{n}(0) \qquad \forall n \in \mathcal{S}_{\mathrm{G}}$$

$$\underline{V}_{n}(1) \leq V_{n}(1) \leq \overline{V}_{n}(1) \qquad \forall n \in \mathcal{S}_{\mathrm{PQ}}$$

We investigate seven additional cases in which we vary the decision variables that are al-

lowed to change in Period 1 (specifically, $P_{\mathrm{g,ref}}$, $P_{\mathrm{g},n}\,\forall n \in \mathcal{S}_{\mathrm{PV}}$, $V_n\,\forall n \in \mathcal{S}_{\mathrm{G}}$, and $P_{\mathrm{d},n}, Q_{\mathrm{d},n}\,\forall n \in \mathcal{S}_{\mathrm{DR}}$), the loss management strategy, and, for cases in which generator real power generation is allowed to change in Period 1, whether or not we impose a ramp rate. The cases and associated results, which will be discussed later, are summarized in Table 2.5.

The difficulty in solving (2.1) stems from the existence of the implicit constraint (2.1b). Because the singular values of a matrix A are the square roots of the eigenvalues of $A^T A$, we can replace (2.1b) with

$$J(1)^T J(1) - \lambda_0(1) I \succeq 0 \tag{2.2}$$

$$\sigma_0(1) = \sqrt{\lambda_0(1)} \tag{2.3}$$

where the semidefinite constraint (2.2) forces λ_0 to be the smallest eigenvalue of $J(1)^T J(1)$, I is an identity matrix of appropriate size, and we have simplified the expression for the power flow Jacobian matrix for clarity. The SSV of J is the square root of λ_0, as shown in (2.3).

2.5 Solution Algorithm

2.5.1 Existing Approaches for VSCOPF

A variety of methods have been used to solve problems (i.e., voltage stability constrained optimal power flow (VSCOPF) problems) similar to (2.1). For example, [67] computes the Hessian of (2.1b) and then applies an Interior Point Method to solve the nonlinear optimization problem. However, computation of the second derivatives of singular values is computationally difficult. Specifically, in [67], they are obtained through numerical analysis by applying small perturbations to the operating point. Alternatively, since (2.2) is a semidefinite constraint, we could use semidefinite programming (SDP) by applying a semidefinite relaxation of the AC power flow equations [73, 93]. However, if the relaxation is not tight at the optimal solution, the solution will not be the optimal solution of (2.1) and, moreover, it will not be feasible.

In this section, we develop a new solution approach that overcomes the drawbacks of the aforementioned approaches. Specifically, our approach uses the first derivatives of singular values obtained using singular value sensitivities, reducing the necessary computation as compared to the second-order method in [67]. We also include the full nonlinear AC power

flow equations and solve the resulting optimization problem via an iterative LP algorithm in which 1) the objective function and constraints are linearized such that we can compute a step in the optimal direction using LP, 2) the AC power flow equations are solved for the new operating point (i.e., the original operating point plus the optimal step), and 3) the process is repeated until convergence. The idea of iterative programming has been used to solve many kinds of optimization problems for the power system, for example, it is used to solve the basic AC-OPF problem [142, p. 371] and an iterative quadratic programming approach is proposed to solve a multi-period AC-OPF problem including renewable generators and energy storage [84].

Our approach is an extension of the iterative NLP approach proposed in [10], which we will now describe. It takes advantage of the Singular Value Decomposition (SVD) of the Jacobian, i.e.,

$$J = U\Sigma W^T, \tag{2.4}$$

where Σ is a diagonal matrix, U and W are orthogonal singular vector matrices (i.e., $UU^T = I, WW^T = I$). Around a given operating point, the approximate SSV of J is [10]

$$\widetilde{\sigma}_0 = u_0^T J w_0, \tag{2.5}$$

where u_0, w_0 are the corresponding left and right singular vectors.

Our implicit constraint (2.1b) can be approximated by (2.5) and so we can write our problem as a nonlinear optimization problem

$$\min_{\substack{\boldsymbol{P_g}(1),\boldsymbol{Q_g}(1),\\ \boldsymbol{P_d}(1),\boldsymbol{Q_d}(1),\\ \boldsymbol{V}(1),\boldsymbol{\theta}(1),\widetilde{\sigma}_0(1)}} \quad -\widetilde{\sigma}_0(1) \tag{2.6a}$$

$$\text{s.t} \quad \text{constraints (2.1c)} - \text{(2.1n)}, (2.5) \tag{2.6b}$$

To obtain the solution to our original problem (2.1), we solve (2.6), recompute u_0 and w_0 at the new operating point, and repeat the process until convergence. However, the symbolic matrix multiplication in (2.5) is complex for large systems. Moreover, each iteration requires solving a nonlinear optimization problem. Therefore, the approach does not scale to realistically-sized power systems, as we will show in our case study.

2.5.2 Iterative Linear Programming using Singular Value Sensitivities

Our new solution approach uses iterative linear programming (ILP) where the power flow equations are iteratively linearized around new operating points as in [142, p. 371] and the SSV constraint (2.5) is linearized using singular value sensitivities.

The singular value sensitivity is derived using the perturbation theory. The process works as follows [126]. The first -order Taylor series of the Jacobian matrix:

$$J|_{\chi^*+\Delta\chi} = J|_{\chi^*} + \sum_k \frac{\partial J}{\partial \chi_k}\Big|_{\chi^*} \Delta\chi, \tag{2.7}$$

where k indexes χ and χ^* is the current operating point. The left side of (2.7) can also be presented using the small perturbation matrices ΔU, $\Delta\Sigma$ and ΔW:

$$J|_{\chi^*+\Delta\chi} = (U+\Delta U)(\Sigma+\Delta\Sigma)(W+\Delta W)^T, \tag{2.8}$$

where $(U+\Delta U)(U+\Delta U)^T = I$, $(W+\Delta W)(W+\Delta W)^T = I$ and $\Delta\Sigma$ is a diagonal matrix. Substituting (2.4) and (2.7) into (2.8) (neglect the higher orders):

$$U\Sigma\Delta W^T + U\Delta\Sigma W^T + \Delta U\Sigma W^T = \sum_k \frac{\partial J}{\partial \chi_k}\Big|_{\chi^*} \Delta\chi. \tag{2.9}$$

Using the fact that $(U+\Delta U)(U+\Delta U)^T = I$ and also disregrading the higher order, we have $U\Delta U^T = -(U\Delta U^T)^T$. Similarly, $W\Delta W^T = -(W\Delta W^T)^T$. Therefore, we know that the diagonal entries of matrices $U\Delta U^T$ and $W\Delta W^T$ are zeros. Pre-multiplying (2.9) by U^T and post-multiplying by W, it becomes:

$$\Sigma\Delta W^T W + \Delta\Sigma + U^T\Delta U\Sigma = \sum_k \left(U^T \frac{\partial J}{\partial \chi_k}\Big|_{\chi^*} W^T\right) \Delta\chi. \tag{2.10}$$

Because Σ is a diagonal matrix, the diagonal entries of $\Sigma\Delta W^T W + U^T\Delta U\Sigma$ are zeros. As a result, the change in the i^{th} singular value of Jacobian matrix J due to a small perturbation in the operating point χ is

$$\Delta\sigma_i \approx \sum_k u_i^T \frac{\partial J}{\partial \chi_k}\bigg|_{\chi^*} w_i \Delta\chi_k, \tag{2.11}$$

where u_i and w_i are the left and right singular vectors corresponding to σ_i. Therefore, the

sensitivity of the SSV of J is

$$\Delta\sigma_0 \approx \sum_{n\in\left\{\mathcal{S}_{\mathrm{PV}},\mathcal{S}_{\mathrm{PQ}}\right\}} \left[u_0^T \frac{\partial J}{\partial \theta_n} w_0\right] \Delta\theta_n + \sum_{n\in\mathcal{S}_{\mathrm{PQ}}} \left[u_0^T \frac{\partial J}{\partial V_n} w_0\right] \Delta V_n, \tag{2.12}$$

The resulting linear program solved in each iteration of the ILP algorithm is as follows.

$$\min_{\substack{\boldsymbol{\Delta P}_{\mathbf{g}}(1),\boldsymbol{\Delta Q}_{\mathbf{g}}(1),\\ \boldsymbol{\Delta P}_{\mathbf{d}}(1),\boldsymbol{\Delta Q}_{\mathbf{d}}(1),\\ \boldsymbol{\Delta V}(1),\boldsymbol{\Delta\theta}(1),\Delta\sigma_0(1)}} \quad -\Delta\sigma_0(1) \quad \text{subject to} \tag{2.13a}$$

$$\Delta\sigma_0(1) = \sum_{n\in\left\{\mathcal{S}_{\mathrm{PV}},\mathcal{S}_{\mathrm{PQ}}\right\}} \left[u_0(1)^T \frac{\partial J(\boldsymbol{\theta}(1),\boldsymbol{V}(1))}{\partial \theta_n} w_0(1)\right] \Delta\theta_n(1) + \sum_{n\in\mathcal{S}_{\mathrm{PQ}}} \left[u_0(1)^T \frac{\partial J(\boldsymbol{\theta}(1),\boldsymbol{V}(1))}{\partial V_n} w_0(1)\right] \Delta V_n(1) \tag{2.13b}$$

$$f_n^{\mathrm{P}}(\Delta\boldsymbol{\theta}(1),\Delta\boldsymbol{V}(1)) = \Delta P_{\mathrm{g},n}(1) - \Delta P_{\mathrm{d},n}(1) \qquad \forall n\in\mathcal{N} \tag{2.13c}$$

$$f_n^{\mathrm{Q}}(\Delta\boldsymbol{\theta}(1),\Delta\boldsymbol{V}(1)) = \Delta Q_{\mathrm{g},n}(1) - \Delta Q_{\mathrm{d},n}(1) \qquad \forall n\in\mathcal{N} \tag{2.13d}$$

$$\sum_{n\in\mathcal{S}_{\mathrm{DR}}} \Delta P_{\mathrm{d},n}(1) = -\varepsilon \Delta P_{\mathrm{loss}}(1) \tag{2.13e}$$

$$\Delta P_{\mathrm{d},n}(1)\cdot\mu_n = \Delta Q_{\mathrm{d},n}(1) \qquad \forall n\in\mathcal{N} \tag{2.13f}$$

$$\Delta P_{\mathrm{d},n}(1) = 0 \qquad \forall n\in\mathcal{N}\setminus\mathcal{S}_{\mathrm{DR}} \tag{2.13g}$$

$$\Delta\theta_{\mathrm{ref}}(1) = 0 \tag{2.13h}$$

$$h_{nm}(\Delta\boldsymbol{\theta}(1),\Delta\boldsymbol{V}(1)) \le \overline{h}_{nm} \tag{2.13i}$$

$$h_{mn}(\Delta\boldsymbol{\theta}(1),\Delta\boldsymbol{V}(1)) \le \overline{h}_{mn} \tag{2.13j}$$

$$\underline{P}_{\mathrm{g},n}(1) \le P^*_{\mathrm{g},n}(1) + \Delta P_{\mathrm{g},n}(1) \le \overline{P}_{\mathrm{g},n}(1) \qquad \forall n\in\mathcal{S}_{\mathrm{G}} \tag{2.13k}$$

$$\underline{Q}_{\mathrm{g},n}(1) \le Q^*_{\mathrm{g},n}(1) + \Delta Q_{\mathrm{g},n}(1) \le \overline{Q}_{\mathrm{g},n}(1) \qquad \forall n\in\mathcal{S}_{\mathrm{G}} \tag{2.13l}$$

$$\underline{P}_{\mathrm{d},n}(1) \le P^*_{\mathrm{d},n}(1) + \Delta P_{\mathrm{d},n}(1) \le \overline{P}_{\mathrm{d},n}(1) \qquad \forall n\in\mathcal{S}_{\mathrm{DR}} \tag{2.13m}$$

$$\underline{V}_n(1) \le V^*_n(1) + \Delta V_n(1) \le \overline{V}_n(1) \qquad \forall n\in\mathcal{N} \tag{2.13n}$$

$$\Delta\sigma_0(1) \le \overline{\Delta\sigma_0}, \tag{2.13o}$$

where (2.13b) is the linearized SSV constraint and (2.13c)–(2.13n) correspond to (2.1c)–(2.1n), where $\Delta P_{\mathrm{loss}}(1) = \sum_{n\in\mathcal{N}}(\Delta P_{\mathrm{g},n}(1) - \Delta P_{\mathrm{d},n}(1))$ and superscript '*' denotes the current value of a variable. Constraint (2.13o) limits the change in $\Delta\sigma_0(t)$ since the linearizations are only valid near the current operating point.

The solution algorithm is given in Algorithm 1. We initialize the operating points of Period 1, $\chi^*(1)$, at the operating point of Period 0, $\chi(0)$. Then, we compute the constraints of (2.13) at the current values of the operating point and solve (2.13) to obtain the optimal change in operating point $\Delta\chi^{\text{opt}}(1)$. We use those changes to compute updated operating point estimates $\chi'(1)$. However, in general, $\chi'(1)$ will not be feasible in the AC power flow equations. Therefore, we re-solve the AC power flow equations using components of $\chi'(1)$, specifically, $\boldsymbol{P}_{\text{g}}, \boldsymbol{P}_{\text{d}}, \boldsymbol{Q}_{\text{d}}$, and $V_n \, \forall n \in \mathcal{S}_{\text{G}}$, to obtain the new values of the operating points, $\chi^*(1)$. We use these values to compute the new value of the SSV in Period 1, $\sigma_0^*(1)$. We repeat the process until the absolute value of the change of SSV is less than a threshold (here, 10^{-5}), and the outputs are the final operating point and the SSV.

Algorithm 1 Iterative Linear Programming with Singular Value Sensitivities

Input: The operating point of Period 0, $\chi(0)$

1: $\chi^*(1) = \chi^*(0)$
2: **repeat**
3: Compute (2.13b)–(2.13n) at $\chi^*(1)$
4: Solve (2.13) at $\chi^*(1)$ to obtain to obtain $\Delta\chi^{\text{opt}}(1)$
5: $\chi'(1) = \chi^*(1) + \Delta\chi^{\text{opt}}(1)$
6: Use $\chi'(1)$ to solve AC power flows to obtain a new $\chi^*(1)$.
7: Use $\chi^*(1)$ to calculate $\sigma_0^*(1)$ and the objective function in (2.13a).
8: **until** $|\Delta\sigma_0(1)| < 10^{-5}$

Output: $\chi^*(1)$, $\sigma_0^*(1)$

2.5.3 Iterative Linear Programming using Eigenvalue Sensitivities

As shown in (2.2) and (2.3), the smallest singular value of J is the square root of the smallest eigenvalues of $J^T J$, therefore, the original problem can also be solved by iterative linear programming using eigenvalue sensitivities. In case study, we will also compare the performance of ILP with singular value sensitivities with that of ILP with eigenvalue sensitivities.

Let λ, r and l be the eigenvalues, right eigenvectors, and left eigenvectors of a matrix A:

$$Ar_i = \lambda_i r_i \tag{2.14}$$

$$A^T l_i = \lambda_i l_i \tag{2.15}$$

Differentiating (2.14) with respect to a system state χ_k yields

$$\frac{\partial A}{\partial \chi_k} r_i + A \frac{\partial r_i}{\partial \chi_k} = \frac{\partial \lambda_i}{\partial \chi_k} r_i + \lambda_i \frac{\partial r_i}{\partial \chi_k} \tag{2.16}$$

Pre-multiplying (2.16) by l_i^T, applying (2.15), and using the fact that l_i and r_i are orthogonal ($l_i^T r_i = 1$), the eigenvalue sensitivity is [117]:

$$\frac{\partial \lambda_i}{\partial \chi_k} = l_i^T \frac{\partial A}{\partial \chi_k} r_i, \tag{2.17}$$

so we can approximate the change in λ_0 as

$$\Delta\lambda_0 \approx \sum_{n \in \left\{\mathcal{S}_{\mathrm{PV}}, \mathcal{S}_{\mathrm{PQ}}\right\}} \left[l_0^T \frac{\partial (J^T J)}{\partial \theta_n} r_0 \right] \Delta\theta_n + \sum_{n \in \mathcal{S}_{\mathrm{PQ}}} \left[l_0^T \frac{\partial (J^T J)}{\partial V_n} r_0 \right] \Delta V_n \tag{2.18}$$

where r_0 and l_0 are the right and left eigenvectors corresponding to λ_0.

An equivalent problem to (2.13) is

$$\min_{\substack{\boldsymbol{\Delta P_g}(1), \boldsymbol{\Delta Q_g}(1), \\ \boldsymbol{\Delta P_d}(1), \boldsymbol{\Delta Q_d}(1), \\ \boldsymbol{\Delta V}(1), \boldsymbol{\Delta\theta}(1), \Delta\sigma_0(1)}} \quad -\Delta\sigma_0(1) \quad \text{s.t.} \tag{2.19a}$$

$$\Delta\lambda_0(1) = \sum_{n \in \left\{\mathcal{S}_{\mathrm{PV}}, \mathcal{S}_{\mathrm{PQ}}\right\}} \left[l_0(1)^T \frac{\partial \left(J(1)^T J(1) \right)}{\partial \theta_n} r_0(1) \right] \Delta\theta_n(1) + \sum_{n \in \mathcal{S}_{\mathrm{PQ}}} \left[l_0(1)^T \frac{\partial \left(J(1)^T J(1) \right)}{\partial V_n} r_0(1) \right] \Delta V_n(1) \tag{2.19b}$$

$$\Delta\lambda_0(1) = 2\sigma_0^*(1)\Delta\sigma_0(1) \tag{2.19c}$$

$$\text{constraints (2.13c)} - \text{(2.13o)} \tag{2.19d}$$

2.5.4 Benchmarks

We will benchmark the solution determined by the iterative linear programming against those of three other approaches.

- **Brute force SSV approach**
  We compute the smallest singular value of the Jacobian for all possible loading patterns within a discrete mesh where total load is constant (i.e., using brute force search) and

determine the maximum.

- **Brute force loading margin approach**
  We use MATPOWER's [149] continuation power flow `runcpf` to compute the loading margin for all possible loading patterns within a discrete mesh where total load is constant and determine the maximum. This function does not enforce engineering constraints.

- **Optimal loading margin approach**
  For all possible loading patterns where total load is constant, we use an Optimal-Power-Flow-based Direct Method [11] to maximize the loading factor k subject to both the power flow equations and engineering constraints. Specifically, we solve the following problem, which increases the generation and loading uniformly subject to the power flow equations and engineering constraints:

$$\max_{\substack{\boldsymbol{P_g},\boldsymbol{Q_g},\boldsymbol{P_d},\boldsymbol{Q_d},\boldsymbol{V},\boldsymbol{\theta},\\ \boldsymbol{P_g(1)},\boldsymbol{P_d(1)},\boldsymbol{Q_d(1)},k}} \quad k \quad \text{subject to} \tag{2.20a}$$

$$P_{\mathrm{g},n} = (1+k)P_{\mathrm{g},n}(1) \qquad \forall n \in \mathcal{S}_{\mathrm{PV}} \tag{2.20b}$$

$$P_{\mathrm{d},n} = (1+k)P_{\mathrm{d},n}(1) \qquad \forall n \in \mathcal{S}_{\mathrm{PQ}} \tag{2.20c}$$

$$\mathcal{F}_n^{\mathrm{P}}(\boldsymbol{\theta},\boldsymbol{V}) = P_{\mathrm{g},n} - P_{\mathrm{d},n} \qquad \forall n \in \mathcal{N} \tag{2.20d}$$

$$\mathcal{F}_n^{\mathrm{Q}}(\boldsymbol{\theta},\boldsymbol{V}) = Q_{\mathrm{g},n} - Q_{\mathrm{d},n} \qquad \forall n \in \mathcal{N} \tag{2.20e}$$

$$\textstyle\sum_{n\in\mathcal{S}_{\mathrm{DR}}} P_{\mathrm{d},n}(1) = \sum_{n\in\mathcal{S}_{\mathrm{DR}}} P_{\mathrm{d},n}(0) \tag{2.20f}$$

$$P_{\mathrm{d},n}\cdot\mu_n = Q_{\mathrm{d},n} \qquad \forall n \in \mathcal{N} \tag{2.20g}$$

$$P_{\mathrm{d},n}(1)\cdot\mu_n = Q_{\mathrm{d},n}(1) \qquad \forall n \in \mathcal{N} \tag{2.20h}$$

$$P_{\mathrm{d},n}(1) = P_{\mathrm{d},n}(0) \qquad \forall n \in \mathcal{N}\setminus\mathcal{S}_{\mathrm{DR}} \tag{2.20i}$$

$$P_{\mathrm{g},n}(1) = P_{\mathrm{g},n}(0) \qquad \forall n \in \mathcal{S}_{\mathrm{PV}} \tag{2.20j}$$

$$V_n = V_n(0) \qquad \forall n \in \mathcal{S}_{\mathrm{PV}} \tag{2.20k}$$

$$\theta_{\mathrm{ref}} = 0, V_{\mathrm{ref}} = V_{\mathrm{ref}}(0) \tag{2.20l}$$

$$\mathcal{H}_{nm}(\boldsymbol{\theta},\boldsymbol{V}) \le \overline{\mathcal{H}}_{nm} \tag{2.20m}$$

$$\mathcal{H}_{mn}(\boldsymbol{\theta},\boldsymbol{V}) \le \overline{\mathcal{H}}_{mn} \tag{2.20n}$$

$$\underline{P}_{\mathrm{g},n} \le P_{\mathrm{g},n} \le \overline{P}_{\mathrm{g},n} \qquad \forall n \in \mathcal{S}_{\mathrm{G}} \tag{2.20o}$$

$$\underline{Q}_{\mathrm{g},n} \le Q_{\mathrm{g},n} \le \overline{Q}_{\mathrm{g},n} \qquad \forall n \in \mathcal{S}_{\mathrm{G}} \tag{2.20p}$$

$$\underline{V}_n \le V_n \le \overline{V}_n \qquad \forall n \in \mathcal{S}_{\mathrm{PQ}} \tag{2.20q}$$

Table 2.1: Comparison Between Operating Point 0 and Solution to (2.13) for the 9-bus System

Bus	Original Generation		New Generation	
#	P_g (MW)	Q_g (MVar)	P_g (MW)	Q_g (MVar)
1	71.95	24.07	70.18	3.05
2	163	14.46	163	19.5
3	85	-3.65	85	3.13
Bus	Original Load/Voltage		New Load/Voltage	
#	P_d (MW)	V (p.u.)	P_d (MW)	V (p.u.)
5	90	0.975	74.8	0.989
7	100	0.986	166.68	0.966
9	125	0.958	73.52	0.985

2.6 Results & Discussion

2.6.1 SSV vs Loading Margin

We first demonstrate the performance of the iterative linear programming with SSV sensitivity algorithm on the IEEE 9- and 30-bus systems. We use these small-scale systems to enable visualization of the results. The system data is from MATPOWER [149] and we set $\overline{\Delta\sigma_0} = 0.01$, $\varepsilon = 0$.

9-bus system

We assume the loads at buses 5, 7 and 9 are flexible (total loading = flexible loading = 315 MW). A comparison between the operating point in Period 0 and the solution to (2.13) is given in Table 2.1. As specified by the constraints, the real power generation at buses 2 and 3 does not change, while the load pattern P_d and the slack bus generation changes to maximize the smallest singular value of the power flow Jacobian, which increases from 0.8942 to 0.8995.

To verify the results, we compare the solution of ILP approach to that of the brute force SSV approach. Figure 2.2 shows the SSV as a function of $P_{d,5}$ and $P_{d,7}$ (based on (2.1e),

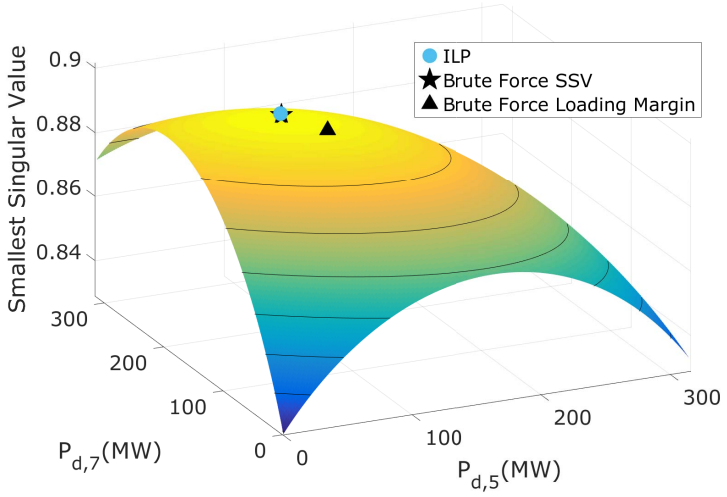

Figure 2.2: Smallest singular value of the power flow Jacobian for the 9-bus system as a function of $P_{\mathrm{d},5}$ and $P_{\mathrm{d},7}$.

$P_{\mathrm{d},9} = 315 - P_{\mathrm{d},5} - P_{\mathrm{d},7}$ MW), using a mesh size of 1 MW. The solution of the iterative sensitivity SSV approach is very near to that of the brute force SSV approach, which has a maximum value that is only 0.00001% larger than that of the iterative sensitivity SSV approach.

Figure 2.3 shows the loading margin as a function of $P_{\mathrm{d},5}$ and $P_{\mathrm{d},7}$. The solutions of the brute force and optimal loading margin approaches are shown. Both approaches produce similar loading patterns (the black dashed line projects the loading pattern corresponding to the optimal loading margin approach to the surface), but different loading margins since the optimal approach includes engineering constraints that reduce the margin from 566 to 257 MW.

Table 2.2 summarizes the results by listing the loading patterns, smallest singular values (SSV), and loading margins (LM) produced by each approach. Note that the loading margins reported for the first two approaches are computed without engineering constraints and so should be compared to the loading margin associated with the brute force loading margin approach. As shown, the loading patterns produced by the loading margin approaches are different than those produced by the SSV approaches. This is unsurprising since the margins are defined differently, the loading margin describes the distance to voltage instability for power injection changes that are restricted to a single profile (i.e., uniform changes at constant power factor), whereas the smallest singular value does not require specification of a power injection profile, but it points to the issue that improving one margin may come at

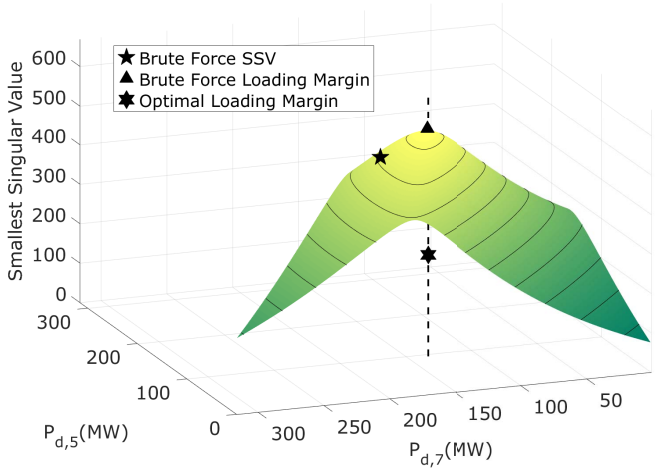

Figure 2.3: Loading margin for the 9-bus system as a function of $P_{\mathrm{d},5}$ and $P_{\mathrm{d},7}$.

Table 2.2: Optimal Loading Patterns for the 9-bus System

Approach	$P_{\mathrm{d},5}$	$P_{\mathrm{d},7}$	$P_{\mathrm{d},9}$	SSV	LM
Iterative Linear Programming	75	167	73	0.8995	516
Brute Force SSV	76	167	72	0.8995	516
Brute Force Loading Margin	97	135	83	0.8984	566
Optimal Loading Margin	95	135	85	0.8984	257

the cost of reducing another.

30-bus system

We assume the loads at buses 7, 8 and 30 are flexible (63.4 MW out of 189.2 MW total). A comparison between the original optimal power flow solution and the solution to (2.13) is given in Table 2.3. Figure 2.4 shows the SSVs (again, using a mesh size of 1 MW) and solutions of two SSV approaches, and Fig. 2.5 shows the loading margins and the solutions of two loading margin approaches. In both cases, the results are plotted as a function of $P_{d,7}$ and $P_{d,8}$, and so, based on (2.1e), $P_{\mathrm{d},30} = 63.4 - P_{\mathrm{d},7} - P_{\mathrm{d},8}$. Table 2.4 summarizes the results.

As shown in Fig. 2.4 and Table 2.4, the result from the iterative sensitivity SSV approach is near the actual maximum. Along the line $P_{\mathrm{d},7} + P_{\mathrm{d},8} = 63$, the smallest singular value slightly increases (from 0.2171 to 0.2187) as the load at bus 7 increases. As shown in Fig. 2.5 and Table 2.4, the loading margin associated with the solution of the optimal loading margin

Table 2.3: Comparison Between Operating Point 0 and Solution to (2.13) for the 30-bus System

Bus	Original Generation		New Generation	
#	P_g (MW)	Q_g (MVar)	P_g (MW)	Q_g (MVar)
1	25.82	-2.46	26.40	-2.87
2	60.97	25.75	60.97	32.27
13	37	10.62	37.00	10.92
22	21.59	37.56	21.59	38.69
23	19.2	7.59	19.20	7.70
27	26.91	8.29	26.91	4.62
Bus	Original Load/Voltage		New Load/Voltage	
#	P_d (MW)	V (p.u.)	P_d (MW)	V (p.u.)
7	22.8	0.971	57.52	0.951
8	30	0.970	5.88	0.978
30	10.6	0.971	0	0.996

Table 2.4: Optimal Loading Patterns for the 30-bus System

Approach	$P_{d,7}$	$P_{d,8}$	$P_{d,30}$	SSV	LM
Iterative Linear Programming	58	6	0	0.2187	209
Brute Force SSV	63	0	0	0.2187	194
Brute Force Loading Margin	24	28	11	0.2173	323
Optimal Loading Margin	25	25	13	0.2172	15

approach is much smaller than that associated with the brute force loading margin approach, again due to the engineering constraints; however, the loading pattern is similar. Also, again, the SSV approaches produce very different loading patterns than the loading margin approaches.

2.6.2 Comparison of Cases

We compare seven cases with different decision variables and/or parameters to the base case in Table 2.5, which defines each case and shows its optimal SSV, percent improvement, and generation cost. For this comparison, we use the IEEE 9-bus system. We assume the system is initially operating at the optimal power flow solution at \$5297/hour (the star in Fig 2.1).

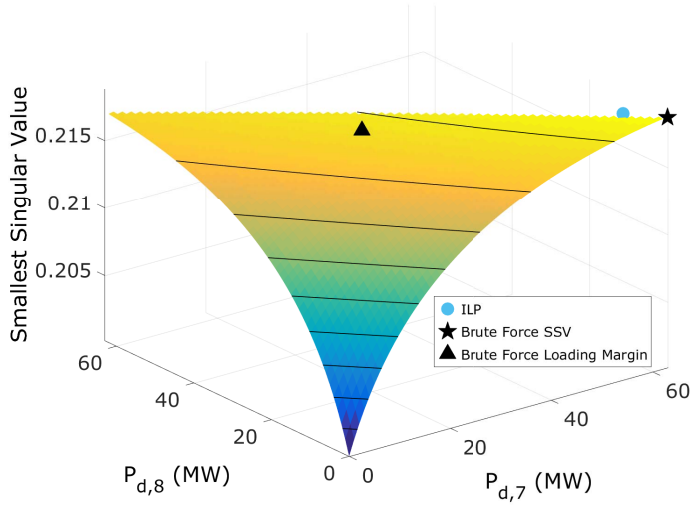

Figure 2.4: Smallest singular value of the power flow Jacobian for the 30-bus system as a function of $P_{\mathrm{d},7}$ and $P_{\mathrm{d},7}$.

A disturbance takes line 4-9 out of service and the SSV drops to 0.4445. Note that the operating point 0 now is different from the point list in Table 2.1.

Case 1 corresponds to our base case. Case 2 uses the loads rather than the slack bus to compensate for the change in system losses. The total loading increases from 315 MW to 319 MW, reducing the optimal SSV slightly. In Cases 3–6, we investigate the achievable change in SSV using generator actions alone (in these cases, ε is irrelevant because there is no DR). The improvement possible through changes to generator real power generation (Case 3) is slightly greater than that of the base case (6.5% vs. 6.1%), but at a significantly higher generation cost. In Case 4, Generators 2 and 3 are modeled as steam turbine plants with 3 MW/minute (1% of capacity [136]) ramp rates, which reduces their ability to respond and the achievable SSV. Case 5 allows real power generation and voltage magnitudes to change. Voltage regulation alone (Case 6) does not improve the SSV very much. The greatest SSV improvement is achieved when we change load, generation, and voltage magnitudes together (Case 7); however, in practice, generators are ramp limited and so we would expect a realistic achievable improvement between that obtained in Case 7 and Case 8, where we have applied the conservative ramp rate used in Case 4.

We also formulated and solved an optimization problem to determine the minimum load shedding needed to achieve the same SSV improvement as obtained in Case 1 (without

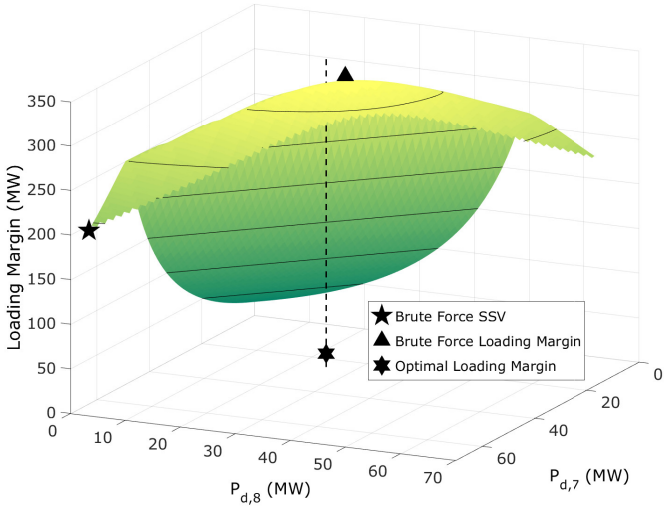

Figure 2.5: Loading margin for the 30-bus system as a function of $P_{\mathrm{d},7}$ and $P_{\mathrm{d},8}$.

system-wide load shedding). The formulation is as follows.

$$\min \quad \sum_{i \in \mathcal{S}_{\mathrm{DR}}} P_{d,i}(0) - \sum_{i \in \mathcal{S}_{\mathrm{DR}}} P_{d,i}(1) \tag{2.21a}$$

$$\sigma_0(1) = \sigma_{\min}\{J(\boldsymbol{\theta}(\mathbf{1}), \boldsymbol{V}(\mathbf{1}))\} \tag{2.21b}$$

$$\mathcal{F}_n^P(\boldsymbol{\theta}(\mathbf{1}), \boldsymbol{V}(\mathbf{1})) = P_{g,n}(1) - P_{d,n}(1) \qquad \forall n \in \mathcal{N} \tag{2.21c}$$

$$\mathcal{F}_n^Q(\boldsymbol{\theta}(\mathbf{1}), \boldsymbol{V}(\mathbf{1})) = Q_{g,n}(1) - Q_{d,n}(1) \qquad \forall n \in \mathcal{N} \tag{2.21d}$$

$$P_{g,n}(1) = P_{g,n}(0) \qquad \forall n \in \mathcal{S}_{\mathrm{PV}} \tag{2.21e}$$

$$\sigma_0(1) \geq 0.4715 \tag{2.21f}$$

$$\underline{P}_{g,\mathrm{ref}}(1) \leq P_{g,\mathrm{ref}}(1) \leq \overline{P}_{g,\mathrm{ref}}(1) \tag{2.21g}$$

$$\underline{Q}_{g,n}(1) \leq Q_{g,n}(1) \leq \overline{Q}_{g,n}(1) \qquad \forall n \in \mathcal{S}_{\mathrm{G}} \tag{2.21h}$$

$$\underline{V}_n(1) \leq V_n(1) \leq \overline{V}_n(1) \qquad \forall n \in \mathcal{S}_{\mathrm{DR}} \tag{2.21i}$$

To solve this problem, we again use iterative linear programming with singular value sensitivities. In [15], the authors formulate a similar problem and also use singular value sensitivities to formulate a linear program. However, they only solve the linear program once and so the solution they obtain does not necessarily satisfy the original problem's constraints. By solving (2.21), we found that the system load would need to drop by at least 17% to

Table 2.5: Decision variables, parameters, optimal SSV, percent improvement, and generation cost for each case

Case	1	2	3	4	5	6	7	8
$P_{\mathrm{g,ref}}$	✓		✓	✓	✓		✓	✓
$P_{\mathrm{g},n} \forall n \in \mathcal{S}_{\mathrm{PV}}$			✓	✓	✓		✓	✓
$V_n \forall n \in \mathcal{S}_{\mathrm{G}}$					✓	✓	✓	✓
$P_{\mathrm{d},n}$, $Q_{\mathrm{d},n} \forall n \in \mathcal{S}_{\mathrm{DR}}$	✓	✓					✓	✓
1% Ramp Rate				✓				✓
ε	0	1	N/A	N/A	N/A	N/A	0	0
Optimal SSV	0.4715	0.4703	0.4732	0.4569	0.4783	0.4469	0.4885	0.4802
Percent improvement	6.1	5.8	6.5	2.3	7.6	0.5	9.9	8.0
Generation cost ($/hr)	5304.6	5424.5	8270.4	5501.6	8502.6	5424.5	7107.8	5428.1

achieve the same stability margin improvement as achieved by spatial load shifting. Load shedding has significant financial and comfort impacts for consumers.

2.6.3 Comparison of Algorithms

In this subsection, we compare the performance of the ILP and INLP algorithms from [10]. Each iteration of the nonlinear optimization problem (2.6) is solved with `fmincon` in MATLAB. Table 2.6 shows the optimal loading pattern and SSV computed using each algorithm for the IEEE 9-bus system with disturbance (line 4-9 is disconnected). The solutions/SSVs produced by the algorithms are close.

Figure 2.6 shows the convergence of SSV of each approach. ILP-E is the iterative linear programming with eigenvalue sensitivity; ILP is the iterative linear programming with singular value sensitivity. The ILP algorithm converges more quickly than the INLP algorithm. The eigenvalue sensitivity in (2.18) requires computing the derivatives of matrix $J^T J$, which is less scalable than computing derivatives of the matrix J in (2.12), therefore, iterative linear programming with singular value sensitivity costs less time than iterative linear programming with eigenvalue sensitivity.

In addition to 9-bus system, we also apply these three algorithms on IEEE 118-bus system. Table 2.7 summarizes the computation times for each algorithm. As shown, the ILP algorithm requires significantly less time than the INLP algorithm,and roughly half as much time as ILP-E. The INLP algorithm does not scale to the 118-bus system.

Table 2.6: Loading Pattern & SSV computed with ILP and INLP for the IEEE 9-bus system with disturbance

Algorithm	Nominal	Optimal	
		ILP	INLP
$P_{d,5}$ (MW)	90	147.93	149.58
$P_{d,7}$ (MW)	100	137.23	135.57
$P_{d,9}$ (MW)	125	29.84	29.85
SSV	0.4445	0.4715	0.4716

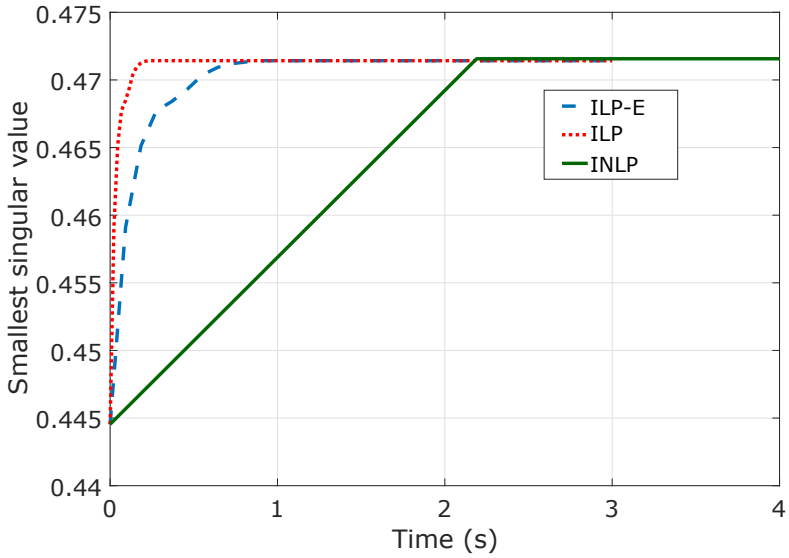

Figure 2.6: Convergence of each approach.

2.7 Chapter Conclusion

We have posed an optimization problem to use DR to improve static voltage stability as measured by the smallest singular value of the power flow Jacobian matrix. In addition to formulating the problem, which increases/decreases loads while holding total load constant in a first period and paying back energy to each load in a second period, we have developed an iterative linear programming algorithm using singular value sensitivities. We demonstrated the performance of the approach on the IEEE 9-, 30-, and 118-bus systems, compared the effectiveness of DR actions to generation actions, and benchmarked our algorithm against an iterative nonlinear programming algorithm from the literature.

The test case results show that demand response actions which shift load between buses,

Table 2.7: Computation Times (s)

	ILP	ILP-E	INLP
IEEE 9-bus system	0.4	1.0	2.5
IEEE 118-bus system	6.5	15.0	-

while keeping the total load constant, can improve voltage stability margins. We also found that our computationally tractable iterative linear programming method produced loading patterns close to the optimum (as determined by a brute force approach). The results further show that we may obtain significantly different loading patterns when maximizing the smallest singular value of the Jacobian versus maximizing the loading margin. This is not surprising since the different margins capture different notions of "distance to instability." However, it means that improving one margin may worsen another, and so the system operator should consider the trade-off between different margins. Moreover, demand response actions can achieve same amount of improvement as generation actions, however, in reality, generators are ramp-limited, therefore, it may still be desirable to deploy DR actions.

Chapter 3

The Impact of Load Models on the Optimal SSV and the Optimal Loading Pattern

In this chapter, we study the impact of load models on a previously proposed iterative linearization algorithm to determine loading patterns that maximize a voltage stability margin, namely, the SSV of the power flow Jacobian matrix. Specifically, we extend the algorithm to enable inclusion of composite load models consisting of both "ZIP" components and a steady-state squirrel-cage induction machine (IM) model. We then investigate the impact of different load models on both the stability margin and the loading pattern. This chapter is largely based on the following paper.

- M. Yao, D.K. Molzahn, and J.L. Mathieu. "The impact of load models in an algorithm for improving voltage stability via demand response". In: *the Allerton Conference on Communication, Control, and Computing*. 2017 (Invited).

3.1 Notation

Sets

$\mathcal{N}$	Set of all buses
$\mathcal{S}_{\text{PV}}$	Set of all PV buses
$\mathcal{S}_{\text{PQ}}$	Set of all PQ buses
$\mathcal{S}_{\text{DR}}$	Set of buses with demand-responsive loads

Functions

$\mathcal{F}_n^{\mathrm{P}}(\cdot)$	Real power injection at bus n
$\mathcal{F}_n^{\mathrm{Q}}(\cdot)$	Reactive power injection at bus n
$\mathcal{F}_n^{ZP}(\cdot)$	Real power demand of ZIP load at bus n
$\mathcal{F}_n^{ZQ}(\cdot)$	Reactive power demand of ZIP load at bus n
$\mathcal{F}_n^{IP}(\cdot)$	Real power demand of IM at bus n
$\mathcal{F}_n^{IQ}(\cdot)$	Reactive power demand of IM at bus n
$\mathcal{H}_{nm}(\cdot)$	Line flow for line (n, m)

Variables & Parameters

a_1, a_2, a_3	ZIP load model real power coefficients
b_1, b_2, b_3	ZIP load model reactive power coefficients
$R_{s,n}$	IM stator's resistance at bus n
$R_{r,n}$	IM rotor's resistance at bus n
$S_{d,n}$	Total complex power demand at bus n
$S_{\mathrm{ZIP},n}$	Complex power demand of ZIP load at bus n
$S_{\mathrm{IM},n}$	Complex power demand of IM at bus n
s_n	Slip of IM at bus n
u	Left singular vector
V_n	Voltage magnitude at bus n
$V_{\mu,n}$	Stator voltage magnitude of IM at bus n
$V_{\rho,n}$	Rotor voltage magnitude of IM at bus n
w	Right singular vector
$X_{ls,n}$	IM stator's leakage reactance at bus n
$X_{lr,n}$	IM rotor's leakage reactance at bus n
$X_{m,n}$	IM mutual reactance at bus n
θ_n	Voltage angle at bus n
$\theta_{\mu,n}$	Stator voltage angle of IM at bus n
$\theta_{\rho,n}$	Rotor voltage angle of IM at bus n
χ	System parameters
κ	Ratio used for the ZIP model

3.2 Chapter Introduction

Proper load models are particularly important in stability studies [53, 64, 102, 110]. This chapter extends the Algorithm 1 to enable inclusion of voltage-dependent load models, specifically ZIP models (i.e., real and reactive demand models with constant impedance, constant current, and constant power components) and steady-state squirrel-cage IM models. Inclusion of these models changes the power flow Jacobian, altering the nominal SSV. We investigate the impact of these models on the optimal SSV and optimal loading pattern. Of course, in practice, we do not choose the load model, but rather identify it using system data, e.g., from Phasor Measurement Units [18, 50, 135]. Given this, our results are useful for two reasons: 1) they help us understand which types of systems (as defined by the load mix) might benefit more or less from using demand response to improve the SSV, and 2) they help us determine the difference in loading pattern and optimality loss we would obtain if we were to use simple load models (e.g., constant power load models) instead of detailed load models within our algorithm.

The technical contributions of this chapter are as follows:

- We extend the SSV maximization problem to include voltage-dependent load models;
- we extend the iterative linear programming approach used in Chapter 2 to solve this problem;
- we compare the solutions and optimal SSVs associated with different types of load models;
- and we discuss difficulties in interpreting the stability margin when the system undergoes structural changes resulting from the use of different load models.

3.3 Load Models

In this section, we describe the voltage-dependent load models - ZIP and induction machine - considered in this chapter. Since we focus on the static voltage stability analysis, we do not consider dynamic load models.

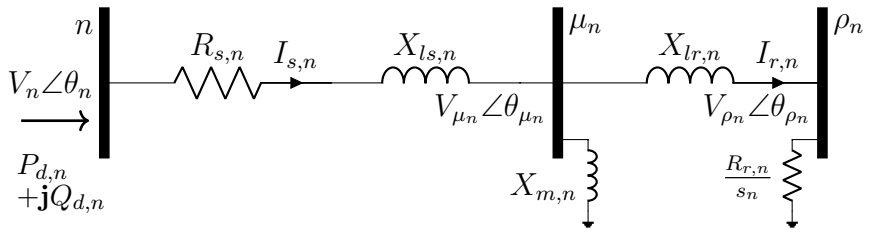

Figure 3.1: Steady-state equivalent circuit of a squirrel-cage induction machine at bus n [92].

3.3.1 Controllable ZIP Model

Typical static loads are represented using a "ZIP" model which has constant impedance ("Z"), constant current ("I"), and constant power ("P") components. To incorporate demand response capabilities into the typical ZIP model, we introduce a scalar variable κ_n that represents the ratio (at a given voltage magnitude) between the controlled and nominal power demands:

$$\mathcal{F}_n^{ZP}(V_n, \kappa_n) = \kappa_n P_{d,n}^0 \left[a_{1,n} \left(\frac{V_n}{V_n^0} \right)^2 + a_{2,n} \left(\frac{V_n}{V_n^0} \right) + a_{3,n} \right], \tag{3.1a}$$

$$\mathcal{F}_n^{ZQ}(V_n, \kappa_n) = \kappa_n Q_{d,n}^0 \left[b_{1,n} \left(\frac{V_n}{V_n^0} \right)^2 + b_{2,n} \left(\frac{V_n}{V_n^0} \right) + b_{3,n} \right], \tag{3.1b}$$

where $\mathcal{F}_n^{ZP}$ and $\mathcal{F}_n^{ZQ}$ are the functions representing the real and reactive power consumption of the controllable ZIP model, $P_{d,n}^0$ and $Q_{d,n}^0$ are the nominal real and reactive demands, and V_n^0 is the nominal voltage magnitude at load bus n. The coefficients $a_{1,n}$, $a_{2,n}$, and $a_{3,n}$ represent constant impedance, constant current, and constant power fractions for real power. Corresponding reactive power coefficients are denoted $b_{1,n}$, $b_{2,n}$, and $b_{3,n}$. These coefficients sum to one, i.e., $\sum_{i=1}^{3} a_{i,n} = 1$ and $\sum_{i=1}^{3} b_{i,n} = 1$ for all n.

3.3.2 Induction Machine Model

Fig. 3.1 shows the equivalent circuit of a squirrel-cage induction machine [70]. An induction machine at bus n is modeled using two additional internal buses denoted μ_n and ρ_n along with a "slip" variable s_n indicating the normalized difference between the electrical frequency and the induction machine's mechanical speed. A slip equal to 1 indicates zero mechanical speed, while a slip equal to 0 indicates that the machine operates at synchronous speed.

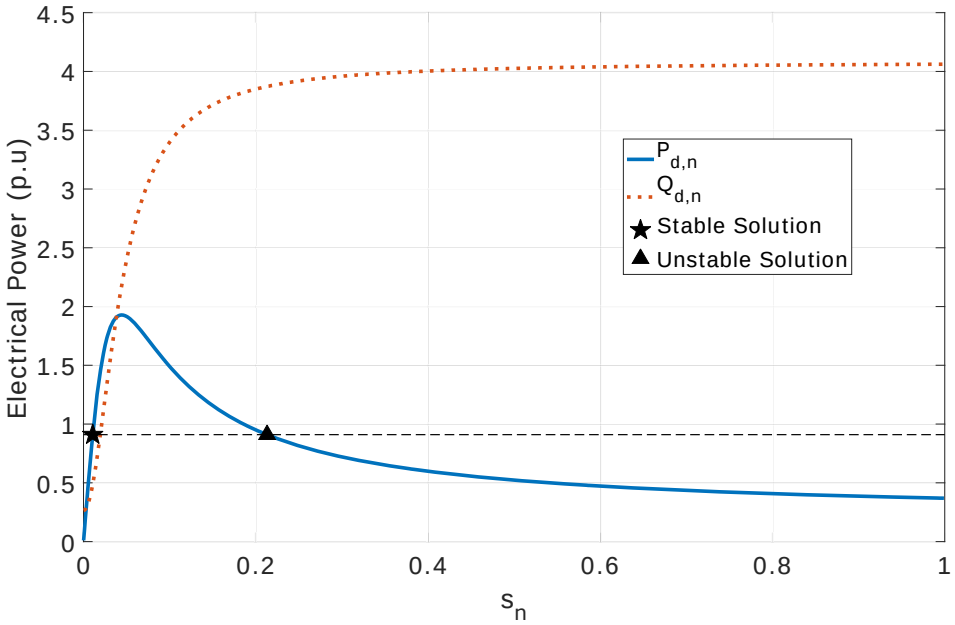

Figure 3.2: The electrical power consumption of an induction machine as a function of the slip.

For both $s_n = 0$ and $s_n = 1$, the induction machine delivers zero mechanical power but may consume electrical power due to losses. Fig. 3.2 shows an induction machine's power consumption as a function of s_n.

Based on the circuit in Fig. 3.1, the real and reactive demands at bus k become functions of the voltage phasors at buses k, μ_n and ρ_n as well as the machine's slip:

$$P_{d,n} + jQ_{d,n} = V_n e^{j\theta_n} \left(\frac{V_{\mu,n} e^{j\theta_{\mu,n}}}{jX_{m,n}} + \frac{V_{\rho,n} e^{j\theta_{\rho,n}} s_n}{R_{r,n}} \right)^*, \tag{3.2}$$

where $j = \sqrt{-1}$. Splitting (3.2) into real and imaginary components yields

$$\mathcal{F}_n^{IP}(\theta_n, V_n, \theta_{\mu,n}, V_{\mu,n}, \theta_{\rho,n}, V_{\rho,n}, s_n) = \frac{V_n V_{\mu,n}}{X_{m,n}} \sin(\theta_{\mu,n} - \theta_n) + \frac{V_n V_{\rho,n} s_n}{R_{r,n}} \cos(\theta_{\rho,n} - \theta_n), \tag{3.3a}$$

$$\mathcal{F}_n^{IQ}(\theta_n, V_n, \theta_{\mu,n}, V_{\mu,n}, \theta_{\rho,n}, V_{\rho,n}, s_n) = \frac{V_n V_{\mu,n}}{X_{m,n}} \cos(\theta_{\mu,n} - \theta_n) - \frac{V_n V_{\rho,n} s_n}{R_{r,n}} \sin(\theta_{\rho,n} - \theta_n). \tag{3.3b}$$

The voltage magnitudes are related by Ohm's law:

$$V_n e^{j\theta_n} - V_{\mu,n} e^{j\theta_{\mu,n}} = (R_{s,n} + jX_{ls,n}) \left(\frac{V_{\mu,n} e^{j\theta_{\mu,n}}}{jX_{m,n}} + \frac{V_{\rho,n} e^{j\theta_{\rho,n}} s_n}{R_{r,n}} \right), \tag{3.4a}$$

$$V_{\mu,n} e^{j\theta_{\mu,n}} = V_{\rho,n} e^{j\theta_{\rho,n}} \left(1 + jX_{lr,n} \frac{s_n}{R_{r,n}} \right). \tag{3.4b}$$

As shown in Fig. 3.2, for a specific value of real power demand $P_{d,k}$ and terminal voltage magnitude V_n (the horizontal dashed line), there can exist multiple possible values for the slip s_n. We choose the smallest slip, which corresponds to stable operation (the star), by imposing the limits $\underline{s}_n \leq s_n \leq \overline{s}_n$. Since the induction machine represents a load, the slip should be greater than zero; therefore, we impose a small nonzero value as the lower limit $\underline{s}_n$. The value of the upper limit $\overline{s}_n$, which must be small enough to preclude unstable solutions, depends on the machine parameters.

We consider a composite load model, which allows for the combination of both ZIP loads and induction machine loads:

$$S_{d,n} = (1-\alpha)S_{\text{ZIP},n} + \alpha S_{\text{IM},n} \tag{3.5}$$

where S_{ZIP} and S_{IM} represent the complex power demands of the ZIP load and the induction machine, respectively, and α is the percentage of induction machine load ($0 \leq \alpha \leq 1$).

3.4 Optimization Model

In Section 2.4, we propose a non-convex optimization formulation for determining loading patterns that improve voltage stability as measured by the SSV of the power flow Jacobian matrix when load is modeled as constant power with fixed power factor. This section introduces ZIP and induction machine models into this formulation.

3.4.1 Jacobian Matrix

The standard AC power flow equations [142] are used to compute the conventional power flow Jacobian matrix:

$$\mathcal{F}_i^P(\boldsymbol{\theta}, \boldsymbol{V}) = V_i \sum_{j \in \mathcal{N}} V_j (G_{ij} \cos\theta_{ij} + B_{ij} \sin\theta_{ij}), \tag{3.6a}$$

$$\mathcal{F}_i^Q(\boldsymbol{\theta}, \boldsymbol{V}) = V_i \sum_{j \in \mathcal{N}} V_j (G_{ij} \sin\theta_{ij} - B_{ij} \cos\theta_{ij}), \tag{3.6b}$$

where $\theta_{ij} = \theta_i - \theta_j$, $G_{ij} = \mathrm{Re}(Y_{ij})$, and $B_{ij} = \mathrm{Im}(Y_{ij})$. The conventional Jacobian matrix is an $m \times m$ matrix, where $m = n_{\mathrm{pv}} + 2n_{\mathrm{pq}}$:

$$J_{\mathrm{cnv}} = \begin{bmatrix} \frac{\partial \mathcal{F}_i^P}{\partial \theta_i} & \frac{\partial \mathcal{F}_i^P}{\partial V_j} \\ \frac{\partial \mathcal{F}_j^Q}{\partial \theta_i} & \frac{\partial \mathcal{F}_j^Q}{\partial V_j} \end{bmatrix}, \tag{3.7}$$

where each term represents a submatrix of partial derivatives over the indices $i \in \{\mathcal{S}_{\mathrm{PV}}, \mathcal{S}_{\mathrm{PQ}}\}$ and $j \in \mathcal{S}_{\mathrm{PQ}}$.

Models of voltage-dependent loads result in modifications to the conventional power flow Jacobian. For a system with ZIP load models, the $m \times m$ Jacobian matrix is

$$J_{\mathrm{ZIP}} = J_{\mathrm{cnv}} + \begin{bmatrix} \mathbf{0}_{n-1 \times n-1} & \frac{\partial \mathcal{F}_i^{ZP}}{\partial V_j} \\ \mathbf{0}_{n_{\mathrm{pq}} \times n-1} & \frac{\partial \mathcal{F}_j^{ZQ}}{\partial V_j} \end{bmatrix}, \tag{3.8}$$

where the new terms are submatrices over the indices $i \in \{\mathcal{S}_{\mathrm{PV}}, \mathcal{S}_{\mathrm{PQ}}\}$ and $j \in \mathcal{S}_{\mathrm{PQ}}$.

The real and reactive power demands of the induction machine model are functions of the variables θ_k, $V_k, \theta_{\mu,k}$, $V_{\mu,k}$, $\theta_{\rho,k}$, $V_{\rho,k}, s_k$, $\forall k \in \mathcal{S}_{\mathrm{DR}}$. The modified $m \times m + 5n_{\mathrm{dr}}$ Jacobian matrix is

$$\begin{aligned} J_{\mathrm{IM}} = &\begin{bmatrix} J_{\mathrm{cnv}} & \mathbf{0}_{m \times 5n_{\mathrm{dr}}} \end{bmatrix} \\ &+ \begin{bmatrix} \frac{\partial \mathcal{F}_i^{IP}}{\partial \theta_i} & \frac{\partial \mathcal{F}_i^{IP}}{\partial V_j} & \frac{\partial \mathcal{F}_i^{IP}}{\partial \theta_{\mu,k}} & \frac{\partial \mathcal{F}_i^{IP}}{\partial V_{\mu,k}} & \frac{\partial \mathcal{F}_i^{IP}}{\partial \theta_{\rho,k}} & \frac{\partial \mathcal{F}_i^{IP}}{\partial V_{\rho,k}} & \frac{\partial \mathcal{F}_i^{IP}}{\partial s_k} \\ \frac{\partial \mathcal{F}_j^{IQ}}{\partial \theta_i} & \frac{\partial \mathcal{F}_j^{IQ}}{\partial V_j} & \frac{\partial \mathcal{F}_j^{IQ}}{\partial \theta_{\mu,k}} & \frac{\partial \mathcal{F}_j^{IQ}}{\partial V_{\mu,k}} & \frac{\partial \mathcal{F}_j^{IQ}}{\partial \theta_{\rho,k}} & \frac{\partial \mathcal{F}_j^{IQ}}{\partial V_{\rho,k}} & \frac{\partial \mathcal{F}_j^{IQ}}{\partial s_k} \end{bmatrix}, \end{aligned} \tag{3.9}$$

where the new terms are submatrices over the indices $i \in \{\mathcal{S}_{\mathrm{PV}}, \mathcal{S}_{\mathrm{PQ}}\}$, $j \in \mathcal{S}_{\mathrm{PQ}}$, and $k \in \mathcal{S}_{DR}$. For example, the partial derivatives $\partial \mathcal{F}_i^{IP}/\partial \theta_{\mu,k}$, $\partial \mathcal{F}_i^{IP}/\partial \theta_{\rho,k}$, $\partial \mathcal{F}_i^{IP}/\partial V_{\mu,k}$, $\partial \mathcal{F}_i^{IP}/\partial V_{\rho,k}$, $\partial \mathcal{F}_i^{IP}/\partial s_k$ are each of size $(n-1) \times n_{\mathrm{dr}}$.

The Jacobian matrix for the composite load model is formed by the weighted sum of J_{ZIP} and J_{IM}:

$$J_{\mathrm{com}} = (1-\alpha) \begin{bmatrix} J_{\mathrm{ZIP}} & \mathbf{0}_{m \times 5n_{\mathrm{dr}}} \end{bmatrix} + \alpha J_{\mathrm{IM}}. \tag{3.10}$$

The SSV of a matrix is closely related to the matrix's dimension. The SSV of the sum of two matrices, as in (3.8), obeys the following inequality [56]:

$$\sigma_{\min}(A+B) \geq \sigma_{\min}(A) - \sigma_{\max}(B) \tag{3.11}$$

where $\sigma_{\min}(\,\cdot\,)$ denotes the SSV and $\sigma_{\max}(\,\cdot\,)$ the largest singular value of the corresponding

matrix. Therefore, we can not say much about the relative size of the SSV of J_{cnv} versus J_{ZIP}. In contrast, appending columns to a matrix, as in (3.9), increases its SSV.

Theorem 3.1. *Let $A \in \mathbb{R}^{m\times n}$, $z \in \mathbb{R}^{m\times 1}$, where $m \leq n$. Then $\sigma_{\min}(\begin{bmatrix} A & z \end{bmatrix}) \geq \sigma_{\min}(A)$.*

Proof. Let $B = \begin{bmatrix} A & z \end{bmatrix}$. Then, $BB^T = \begin{bmatrix} A & z \end{bmatrix}\begin{bmatrix} A & z \end{bmatrix}^T = AA^T + zz^T$. Let v_n be the normalized right eigenvector ($\|v_n\|_2 = 1$) corresponding to the smallest eigenvalue $\lambda_{\min}$ of BB^T, which is equal to the square of the SSV of the matrix B, i.e., $(\sigma_{\min}(B))^2$. Then,

$$\begin{aligned}(AA^T + zz^T)v_n &= (\sigma_{\min}(B))^2 v_n,\\ v_n^T(AA^T + zz^T)v_n &= (\sigma_{\min}(B))^2.\end{aligned}$$

Since zz^T is a positive semidefinite matrix, i.e., $v_n^T zz^T v_n \geq 0$, then

$$\begin{aligned}(\sigma_{\min}(B))^2 &\geq v_n^T AA^T v_n \geq \|v_n^T AA^T v_n\|_2 = \|A^T v_n\|_2^2\\ &\geq (\sigma_{\min}(A^T))^2\|v_n\|_2^2 = (\sigma_{\min}(A))^2,\end{aligned}$$

and therefore $\sigma_{\min}\left(\begin{bmatrix} A & z \end{bmatrix}\right) \geq \sigma_{\min}(A)$. □

Therefore, the SSV of J_{IM} is larger than that of J_{cnv} at the same operating point. We discuss the implication of this result in Section 3.5.2.

3.4.2 Problem Formulation

The objective is to find the loading pattern $\boldsymbol{P_d}(1)$ that maximizes the SSV of the modified power flow Jacobian matrix J_{com} given in (3.10). Here is the mathematical formulation of the optimization problem:

$$\max_{\substack{\boldsymbol{P_g}(1),\boldsymbol{Q_g}(1),\boldsymbol{P_d}(1),\boldsymbol{Q_d}(1),\\ \boldsymbol{V}(1),\boldsymbol{\theta}(1),\boldsymbol{V_\mu}(1),\boldsymbol{\theta_\mu}(1),\\ \boldsymbol{V_\rho}(1),\boldsymbol{\theta_\rho}(1),\boldsymbol{s},\boldsymbol{\kappa},\sigma_0(1)}} \sigma_0(1) \quad \text{subject to} \tag{3.12a}$$

$$\sigma_0(1) = \sigma_{\min}\{J_{\text{com}}(\boldsymbol{\theta}(1), \boldsymbol{V}(1))\} \tag{3.12b}$$

$$\mathcal{F}_n^{\text{P}}(\boldsymbol{\theta}(1), \boldsymbol{V}(1)) = P_{\text{g},n}(1) - P_{\text{d},n}(1) \qquad \forall n \in \mathcal{N} \tag{3.12c}$$

$$\mathcal{F}_n^{\text{Q}}(\boldsymbol{\theta}(1), \boldsymbol{V}(1)) = Q_{\text{g},n}(1) - Q_{\text{d},n}(1) \qquad \forall n \in \mathcal{N} \tag{3.12d}$$

$$(1-\alpha)\mathcal{F}_n^{ZP}(\cdot) + \alpha\mathcal{F}_n^{IP}(\cdot) = P_{\text{d},n}(1) \qquad \forall n \in \mathcal{S}_{\text{DR}} \tag{3.12e}$$

$$(1-\alpha)\mathcal{F}_n^{ZQ}(\cdot) + \alpha\mathcal{F}_n^{IQ}(\cdot) = Q_{\text{d},n}(1) \qquad \forall n \in \mathcal{S}_{\text{DR}} \tag{3.12f}$$

$$V_n(1)\angle\theta_n(1) - V_{\mu,n}(1)\angle\theta_{\mu,n}(1) = (R_{s,n} + jX_{ls,n})\, I_{s,n} \qquad \forall n \in \mathcal{S}_{\mathrm{DR}} \tag{3.12g}$$

$$I_{s,n} = \frac{V_{\mu,n}(1)\angle\theta_{\mu,n}(1)}{jX_{m,n}} + \frac{V_{\rho,n}(1)\angle\theta_{\rho,n}(1)s_n}{R_{r,n}} \qquad \forall n \in \mathcal{S}_{\mathrm{DR}} \tag{3.12h}$$

$$V_{\mu,n}(1)\angle\theta_{\mu,n}(1) = V_{\rho,n}(1)\angle\theta_{\rho,n}(1)\left(1 + j\frac{X_{lr,n}s_n}{R_{r,n}}\right) \qquad \forall n \in \mathcal{S}_{\mathrm{DR}} \tag{3.12i}$$

$$\sum_{n\in\mathcal{S}_{\mathrm{DR}}} P_{\mathrm{d},n}(1) = \sum_{n\in\mathcal{S}_{\mathrm{DR}}} P_{\mathrm{d},n}(0) \tag{3.12j}$$

$$P_{\mathrm{d},n}(1) = P_{\mathrm{d},n}(0) \qquad \forall n \in \mathcal{S}_{\mathrm{PQ}} \setminus \mathcal{S}_{\mathrm{DR}} \tag{3.12k}$$

$$P_{\mathrm{g},n}(1) = P_{\mathrm{g},n}(0) \qquad \forall n \in \mathcal{S}_{\mathrm{PV}} \tag{3.12l}$$

$$V_n(1) = V_n(0) \qquad \forall n \in \mathcal{S}_{\mathrm{PV}} \tag{3.12m}$$

$$V_{\mathrm{ref}}(1) = V_{\mathrm{ref}}(0),\ \theta_{\mathrm{ref}}(1) = 0 \tag{3.12n}$$

$$\mathcal{H}_{nm}(\boldsymbol{\theta}(1), \boldsymbol{V}(1)) \le \overline{\mathcal{H}}_{nm} \tag{3.12o}$$

$$\mathcal{H}_{mn}(\boldsymbol{\theta}(1), \boldsymbol{V}(1)) \le \overline{\mathcal{H}}_{mn} \tag{3.12p}$$

$$\underline{P}_{\mathrm{g,ref}} \le P_{\mathrm{g,ref}}(1) \le \overline{P}_{\mathrm{g,ref}} \tag{3.12q}$$

$$\underline{Q}_{\mathrm{g},n} \le Q_{\mathrm{g},n}(1) \le \overline{Q}_{\mathrm{g},n} \qquad \forall n \in \mathcal{S}_{\mathrm{G}} \tag{3.12r}$$

$$\underline{P}_{\mathrm{d},n} \le P_{\mathrm{d},n}(1) \le \overline{P}_{\mathrm{d},n} \qquad \forall n \in \mathcal{S}_{\mathrm{DR}} \tag{3.12s}$$

$$\underline{s}_n \le s_i \le \overline{s}_n \qquad \forall n \in \mathcal{S}_{\mathrm{DR}} \tag{3.12t}$$

$$\underline{V}_n \le V_n(1) \le \overline{V}_n \qquad \forall n \in \mathcal{S}_{\mathrm{PQ}} \tag{3.12u}$$

Constraints (3.12c) and (3.12d) are the standard nonlinear AC power flow equations. Constraints (3.12e) and (3.12f) are the real and reactive power demands of the demand-responsive loads. Constraints (3.12g)–(3.12i) are the electrical equations for the steady-state induction machine model. While demands at the load buses without demand-responsive loads can be treated using any appropriate load model, our numerical results assume a constant power load model for simplicity. Constraint (3.12j) ensures that the total demand-responsive load is constant, (3.12k)–(3.12n) fix the non-responsive loads' real power demands, the generators' real power production at PV buses, voltage magnitudes at all generator buses, and the voltage angle at the reference bus. Constraints (3.12o)–(3.12u) enforce the upper limits of power flows on the branches (in terms of apparent power) as well as upper and lower limits on real power and reactive power production at all generator buses, real power demands of demand-responsive loads (which is a function of demand flexibility in both the current time period and the payback period), slips of the induction machines, and voltage magnitudes at PQ buses.

We adapt the iterative linear programming algorithm presented in Algorithm 1 to solve (3.12). This algorithm relies on linearizations of the objective function and constraints in (3.12). To get rid of the implict constraint (3.12b), the linear sensitivity of the smallest singular value is derived using singular value sensitivity as shown in Eq. (2.11):

$$\Delta\sigma_i \approx \sum_k u_i^T \frac{\partial J}{\partial \chi_k}\bigg|_{\chi^*} w_i \Delta\chi_k$$

The relevant system states for the ZIP model are

$$\chi_{\text{ZIP}} = [\theta_i, V_j, \varepsilon_k\ ]^T \tag{3.13}$$

and for the IM model are

$$\chi_{\text{IM}} = [\theta_i, V_j, \theta_{\mu,k}, V_{\mu,k}, \theta_{\rho,k}, V_{\rho,k}, s_k]^T, \tag{3.14}$$

where $i \in \{\mathcal{S}_{\text{PV}}, \mathcal{S}_{\text{PQ}}\}$, $j \in \mathcal{S}_{\text{PQ}}$, and $k \in \mathcal{S}_{\text{DR}}$.

In addition to (3.12b), the iterative linear programming algorithm requires linearization of the AC power flow and load model equations, which is accomplished via first-order Taylor expansion.

After evaluating these linearizations at the approximate solution from the previous iteration, each iteration of the algorithm solves the following linear optimization problem:

$$\max_{\substack{\boldsymbol{\Delta P_g}, \boldsymbol{\Delta Q_g}, \\ \boldsymbol{\Delta P_d}, \boldsymbol{\Delta Q_d}, \\ \boldsymbol{\Delta V}, \boldsymbol{\Delta\theta}, \\ \boldsymbol{\Delta V_\mu}, \boldsymbol{\Delta\theta_\mu}, \boldsymbol{V_\rho}, \\ \boldsymbol{\Delta\theta_\rho}, \boldsymbol{\Delta s}, \boldsymbol{\Delta\kappa}, \Delta\sigma_0}} \quad \Delta\sigma_0 \quad \text{subject to} \tag{3.15a}$$

$$\begin{aligned}
\Delta\sigma_0 = &\textstyle\sum_i \left[u_0^T \frac{\partial J_{\text{com}}}{\partial \theta_i} w_0\right] \Delta\theta_i + \sum_j \left[u_0^T \frac{\partial J_{\text{com}}}{\partial V_j} w_0\right] \Delta V_j \\
&+ \textstyle\sum_k \left[u_0^T \frac{\partial J_{\text{com}}}{\partial \theta_{\mu,k}} w_0\right] \Delta\theta_{\mu,k} + \sum_k \left[u_0^T \frac{\partial J_{\text{com}}}{\partial \theta_{\rho,k}} w_0\right] \Delta\theta_{\rho,k} \\
&+ \textstyle\sum_k \left[u_0^T \frac{\partial J_{\text{com}}}{\partial V_{\mu,k}} w_0\right] \Delta V_{\mu,k} + \sum_k \left[u_0^T \frac{\partial J_{\text{com}}}{\partial V_{\rho,k}} w_0\right] \Delta V_{\rho,k} \\
&+ \textstyle\sum_k \left[u_0^T \frac{\partial J_{\text{com}}}{\partial \kappa_k} w_0\right] \Delta\kappa_k + \sum_k \left[u_0^T \frac{\partial J_{\text{com}}}{\partial s_k} w_0\right] \Delta s_k \\
&i \in \{\mathcal{S}_{\text{PV}}, \mathcal{S}_{\text{PQ}}\}, \forall j \in \mathcal{S}_{\text{PQ}}, \forall k \in \mathcal{S}_{\text{DR}}
\end{aligned} \tag{3.15b}$$

Table 3.1: Induction machine parameters (p.u.) [92]

Bus #	R_s	X_{ls}	R_r	X_{lr}	X_m	$\overline{s}$
4	0.012	0.07	0.01	0.17	3.5	0.04
9	0.001	0.23	0.015	0.23	5.8	0.03
14	0.001	0.23	0.015	0.23	5.8	0.03

$$\text{Linearizations of (3.12c)–(3.12u)} \tag{3.15c}$$

$$\Delta\sigma_0 \leq \overline{\Delta\sigma_0} \tag{3.15d}$$

where (3.15b) is the linear eigenvalue sensitivity constraint corresponding to the composite load model. Constraint (3.15d) limits the step size of $\Delta\lambda_0$ to ensure the accuracy of the linearization.

The solution to (3.15) provides an approximation of the change in decision variables that leads to the maximum increase in σ_0, within the region near the linearization point. Each iteration of the algorithm refines an approximate solution to (3.12) by linearizing around the previous operating point, solving (3.15), adding the changes provided by that solution of (3.15) to the previous operating point, and solving the AC power flow equations (3.6) to obtain a new operating point. The algorithm terminates when $\Delta\sigma_0$ is less than a specified threshold (here, 10^{-5}).

3.5 Results & Discussion

This section describes the results of case studies conducted on the IEEE 14-bus system available in MATPOWER [149]. We assume the loads at buses 4, 9, and 14 are demand-responsive resulting in 92.2 MW of responsive demand out of 259 MW of total demand.

We set $\overline{\Delta\sigma_0} = 0.01$ and list the parameters of the induction machine models in Table 3.1. The upper bounds of the slips are determined based on the induction machine parameters. For example, the relationship between the power consumption and slip of the machine at bus 4 is shown in Fig. 3.2. Since the peak real power consumption occurs when the slip equals 0.04 we set $\overline{s}_4 = 0.04$ to ensure the algorithm finds the stable operating point. We set $\underline{s}_k = 0.0001$, $\forall k \in \mathcal{S}_{\text{DR}}$. The ZIP coefficients for a variety of loads typically used for demand response are given in Table 3.2.

The nominal consumption of the loads at buses 4, 9, and 14 along with the SSV of J_{cnv}

Table 3.2: ZIP Load Models Coefficients [18, 50]

Types	a_1	a_2	a_3	b_1	b_2	b_3
Air conditioner	1.17	-1.83	1.66	15.68	-27.15	12.47
Battery charger	3.51	-3.94	1.43	5.80	-7.26	2.46
Baseboard heater	1.00	0.00	0.00	0.00	0.00	0.00
Dryer	1.91	-2.24	1.33	2.51	-2.34	0.83
Refrigerator/freezer	1.19	-0.26	0.07	0.59	0.65	-0.24
Heat pump	0.84	-1.40	1.56	22.92	-40.39	18.47
Washing machine	0.05	0.32	0.63	-0.56	2.20	-0.64

is given in Table 3.4 (see Nominal, Constant Power, J_{cnv}). Modeling the loads as constant power loads with fixed power factors (as in Chapter 2) and applying the ILP algorithm, we obtain the optimal loading pattern shown in Table 3.4 (see Optimal for 3 DR buses, Constant Power, J_{cnv}). All of demand-responsive load is shifted to bus 4, improving the SSV by 0.97%. The remaining values in Table 3.4 will be discussed later.

3.5.1 Controllable ZIP Model

We first consider cases where all demand-responsive loads are modeled as having only one ZIP component. Fig. 3.3 illustrates the results obtained by applying the iterative sensitivity SSV algorithm to each case, where the matrix in the figure defines the cases (e.g., ZIP case #9 corresponds to a constant real/reactive power load model). The nominal SSVs are different since J_{ZIP} is different in each case. The optimal real power loading pattern is the same in all cases: $[P_{d,4}\ P_{d,9}\ P_{d,14}] = [92.2\ 0\ 0]$ MW. However, the reactive power demand at bus 4 is different in each case since the load's power factor is a function of the voltage magnitude in ZIP cases #1-8. Table 3.4 shows the results for case #3 (see Optimal for 3 DR buses, ZIP, J_{ZIP}), which produces the largest SSV. However, ZIP case #9 produces the largest percent improvement: 0.974%.

We next model the demand-responsive loads using the ZIP coefficients in Table 3.2. In each case, we model all demand-responsive load as a single type of load (i.e., using one set of ZIP coefficients). Results are shown in Fig. 3.4. The baseboard heater model produces the largest SSV but the smallest percentage improvement. Again, the constant power load model (corresponding to ZIP case #9) produces the largest percent improvement.

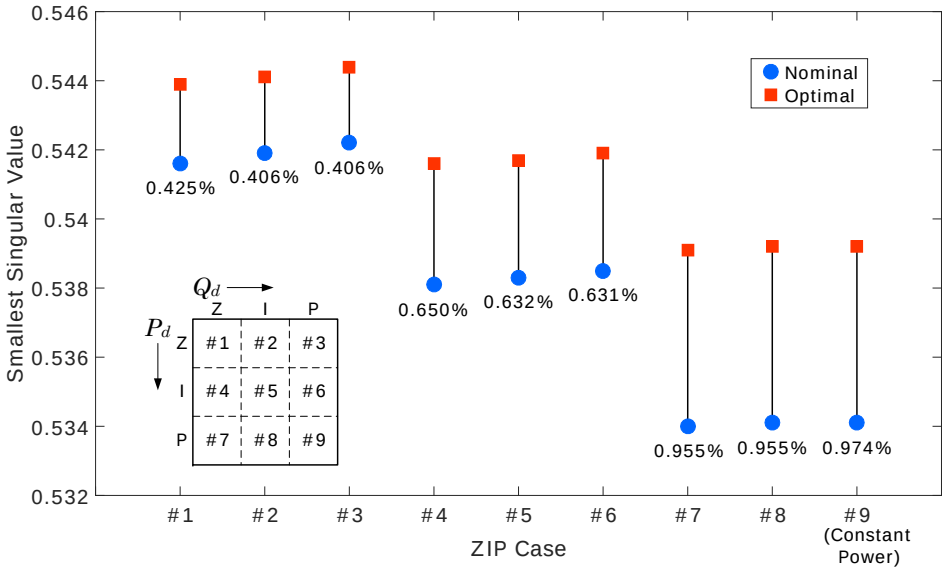

Figure 3.3: The nominal and optimal SSV for different ZIP cases, as shown in the matrix. The values below the blue circles are the percent improvements.

3.5.2 Induction Machine Model

We now model each load as an induction machine (representing the aggregation of a large number of smaller machines) using the parameters given in Table 3.1. The SSV increases from 2.3360 to 2.4533 (5% improvement). The nominal SSV is larger than the nominal SSVs associated with the ZIP loads as expected from Theorem 3.1.

The optimal loading pattern is shown in Table 3.4 (see Optimal for 3 DR buses, IM, J_{IM}). The limits on the induction machines' slips prevent the real power demand at buses 9 and 14 from going to zero, but the optimal loading pattern is similar to the cases with ZIP loads: almost all of the demand-responsive load is shifted to bus 4. However, unlike in the ZIP model cases, the reactive demands at buses 9 and 14 are much greater than zero when the real power demand is close to zero, which is an inherent characteristic of typical induction machines, as shown in Fig. 3.2.

To consider the possibility of disconnecting the induction machines at low consumption levels, we modify the algorithm with the following logical condition: if an induction machine's real power demand at any iteration is less than 0.01 p.u., we disconnect the induction machine by setting its real and reactive power demand to zero prior to continuing the algorithm. Fig. 3.5 illustrates the impacts of this modification. At approximately 50 iterations, P_d at bus 14 is less than 0.01 p.u. (as shown by the vertical dashed lines), so the algorithm disconnects the induction machine at bus 14. After another 15 iterations, the algorithm reaches

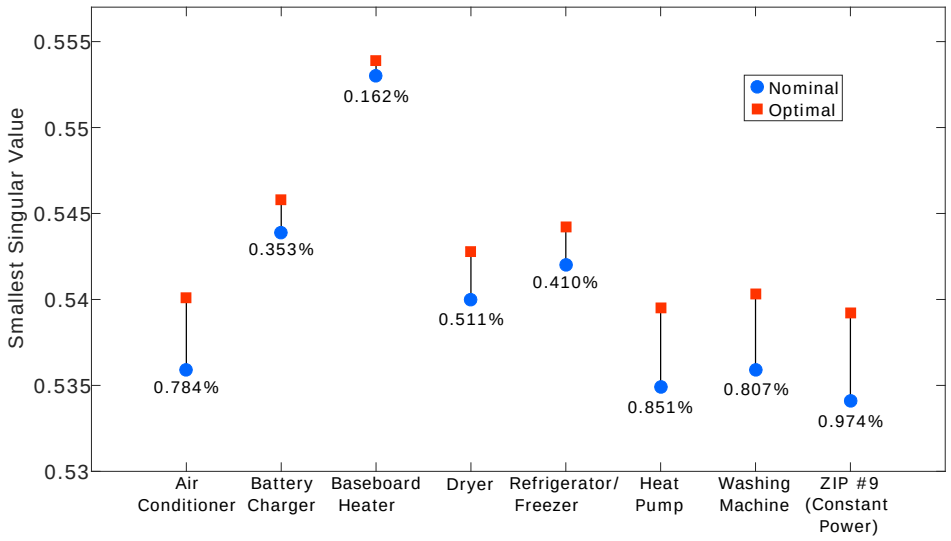

Figure 3.4: The nominal and optimal SSV for common demand-responsive loads. The values below the blue circles are the percent improvements.

the optimum; however, the optimum is not what we would expect given the convergence trajectory before the machine was disconnected. Instead of shifting all load to bus 4, the optimal loading pattern keeps some load at bus 9, as shown in Fig. 3.5 and Table 3.4 (see Optimal for 2 DR buses, IM, J_{IM}), which is different than results obtained using ZIP models within a system with no load at bus 14 and demand-responsive loads at buses 4 and 9 (see Optimal for 2 DR buses, ZIP, J_{ZIP}). Disconnecting the induction machine at bus 14 reduces the number of columns of J_{IM}. According to Theorem 3.1, this leads to a decrease in the the SSV, in this case, from 2.447 to 2.181 prior to converging to a new optimum 2.184, as shown in Fig. 3.5.

3.5.3 Composite Load Model

Table 3.3 summarizes the nominal and optimal SSV results for several ZIP models (including ZIP case #3, which has the largest optimal SSV), the induction machine model, and two composite load models. In addition to the SSVs, we report the absolute improvement (Δ) and percent improvement (%). The case using induction machine models alone has the largest absolute and percent improvement.

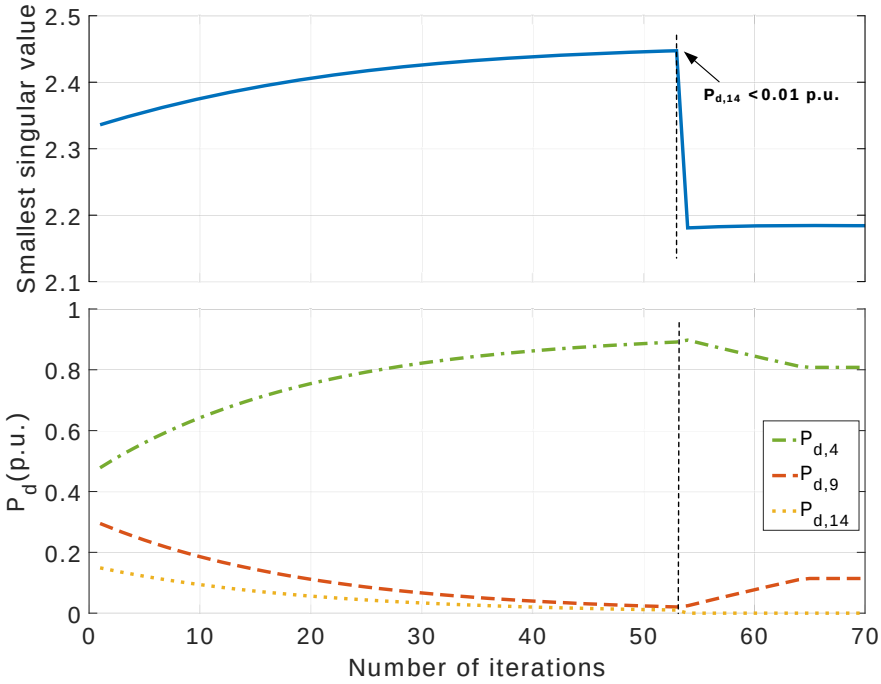

Figure 3.5: Convergence of the SSV and real power demand of the demand-responsive loads if the induction machine at bus 14 is disconnected at low loading.

3.5.4 Difficulties in Interpreting the SSV

It is difficult, if not impossible, to compare the SSVs associated with systems that use different load models. For example, when the SSV drops in Fig. 3.5, it does not necessarily mean that the system is operating closer to instability. The drop is due to structural changes in the Jacobian matrix.

Instead of maximizing the SSV of J_{com}, which is structurally different for each load model, we explore the idea of maximizing the SSV of J_{cnv}, while still using J_{com} to compute the power flow. The benefit of this approach is that the nominal SSVs are identical and the optimal SSVs are comparable. The drawback is that the SSV of J_{cnv} does not reflect the physical system (unless all loads are constant power loads, in which case $J_{\text{com}} = J_{\text{cnv}}$).

Fig. 3.6 shows the results of maximizing J_{cnv} for ZIP cases #1-9, the induction machine model, and a composite load model. The optimal loading patterns corresponding to ZIP case #3 and the induction machine model are shown in Table 3.4 (see Optimal for 3 DR buses, ZIP #3, J_{cnv} and Optimal for 3 DR buses, IM, J_{cnv}). ZIP case #3 yields the same optimal loading patterns regardless of the choice of Jacobian matrix (J_{cnv} or J_{ZIP}) used for

Table 3.3: SSV Comparison

Load Model	Nominal	Optimal	Δ	%
Constant Power (ZIP #9)	0.5341	0.5393	0.0052	0.98
ZIP #3	0.5442	0.5444	0.0002	0.04
Induction Machine	2.3360	2.4533	0.1173	5.02
70% IM + 30% ZIP #3	2.2994	2.4078	0.1084	4.71
30% IM + 70% ZIP #3	2.2402	2.3383	0.0981	4.37

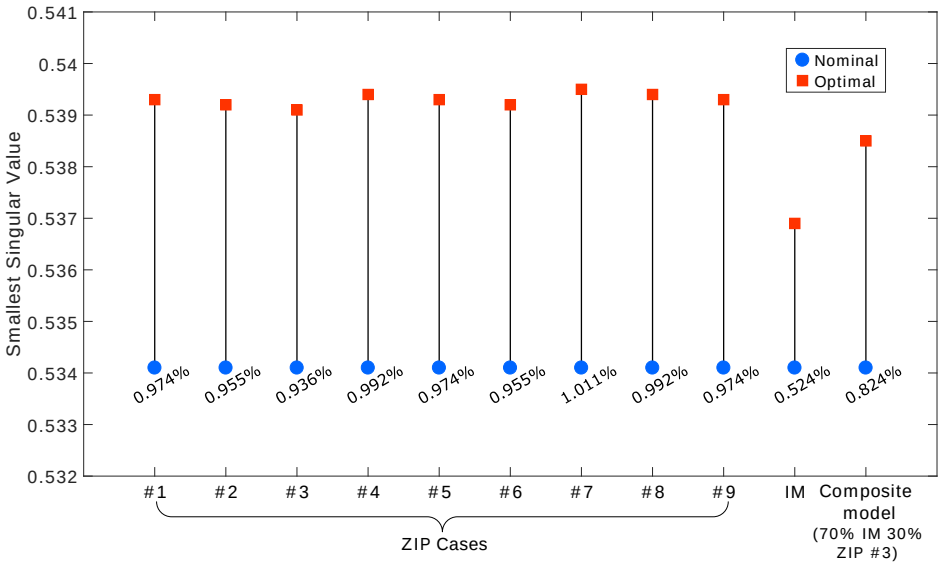

Figure 3.6: The nominal and optimal SSV of the conventional Jacobian matrix. The values below the blue circles are the percent improvement.

the SSV calculation; however, the choice of Jacobian matrix (J_{cnv} or J_{IM}) does affect the optimal loading pattern obtained when using the induction machine model. Interestingly, the SSV percent improvement when maximizing the SSV of J_{cnv} is worst with the induction machine model whereas it was the best when maximizing the SSV of J_{com} (which equals J_{IM} for the induction machine model).

3.5.5 Computation Time

All computations were implemented in MATLAB on a computer with an Intel(R) i5-6600K CPU and 8 GB of RAM. Using the ZIP model, the total time required by the ILP algorithm is less than two seconds for each test case. Using the IM model, the algorithm requires more time (approximately 20 seconds) because 1) the Jacobian matrix is larger requiring more time to compute the singular value sensitivities, and 2) the AC power flow equations are

more complex.

3.6 Chapter Conclusion

This chapter incorporated two voltage-dependent load models into an algorithm for improving a static voltage stability margin based on the SSV of the power flow Jacobian matrix. An iterative linear programming technique was used to determine the optimal loading pattern that maximizes the SSV. Using the IEEE 14-bus system, we studied the impact of the load models on the optimal SSV of the full power flow Jacobian matrix (including terms corresponding to the voltage-dependent load models) and the corresponding optimal loading patterns. We found that use of different ZIP models resulted in the same optimal loading patterns, but use of induction machine models changed the optimal loading pattern, pointing to the importance of properly modeling loads when implementing such an algorithm. Comparing SSVs across systems with different load models proved difficult since structural changes in the power flow Jacobian matrix affect the magnitude of the SSV. Therefore, we also explored the impact of maximizing the SSV of the conventional Jacobian matrix, which is the same for each load model but does not reflect the physical system. This work raises the question of how to compare static voltage stability margins across systems with structural differences.

Table 3.4: Loading Pattern Comparison, P_{d} in MW and Q_{d} in MVar

Load Model Jacobian	Nominal Constant Power J_{cnv}		Optimal for 3 DR buses Constant Power J_{cnv}		ZIP #3 J_{ZIP}		ZIP #3 J_{cnv}		IM J_{IM}		IM J_{cnv}		Optimal for 2 DR buses ZIP #3 J_{ZIP}		IM J_{IM}	
	P_{d}	Q_{d}	P_{d}	Q_{d}	P_{d}	Q_{d}	P_{d}	Q_{d}	P_{d}	Q_{d}	P_{d}	Q_{d}	P_{d}	Q_{d}	P_{d}	Q_{d}
Bus 4	47.80	32.62	92.20	62.90	92.20	63.99	92.20	63.99	90.99	48.90	71.28	39.94	92.20	63.99	80.81	43.94
Bus 9	29.50	20.73	0.00	0.00	0.00	0.00	0.00	0.00	0.62	15.55	20.34	18.50	0.00	0.00	11.39	17.51
Bus 14	14.90	16.39	0.00	0.00	0.00	0.00	0.00	0.00	0.59	15.79	0.59	15.73	-	-	-	-
SSV	0.5341		0.5393		0.5444		0.5391		2.4533		0.5369		0.5444		2.184	

Chapter 4

A Multiperiod OPF to Improve the SSV Using DR

In this chapter, we will take into consideration the energy payback period. The energy payback period maintains the total energy consumption of each load at its nominal value. Now the objective function will balance SSV improvements against generation costs in the energy payback period. This chapter is largely based on the published work:

- M. Yao, D.K. Molzahn, and J.L. Mathieu. "An optimal power flow approach to improve power system voltage stability using demand response". In: *IEEE Trans Control of Network Systems*, 6.3 (2019): 1015-1025.

4.1 Notation

Functions

$\mathcal{C}(\cdot)$	Total generation cost
$\mathcal{F}_n^{\mathrm{P}}(\cdot)$	Real power injection at bus n
$\mathcal{F}_n^{\mathrm{Q}}(\cdot)$	Reactive power injection at bus n
$\mathcal{H}_{nm}(\cdot)$	Line flow for line (n, m)
$f_n^{\mathrm{P}}(\cdot)$	Linearization of $\mathcal{F}_n^{\mathrm{P}}$
$f_n^{\mathrm{Q}}(\cdot)$	Linearization of $\mathcal{F}_n^{\mathrm{Q}}$
$h_{nm}(\cdot)$	Linearization of $\mathcal{H}_{nm}$

Sets

$\mathcal{N}$	Set of all buses
$\mathcal{S}_{\text{PV}}$	Set of all PV buses
$\mathcal{S}_{\text{PQ}}$	Set of all PQ buses
$\mathcal{S}_{\text{G}}$	Set of buses with generators
$\mathcal{S}_{\text{DR}}$	Set of buses with responsive loads
$\mathcal{T}$	Set of time periods within optimization problem

Variables & Parameters

J	Jacobian matrix
n	Size of $\mathcal{N}$
n_{pv}	Size of $\mathcal{S}_{\text{PV}}$
n_{pq}	Size of $\mathcal{S}_{\text{PQ}}$
n_{dr}	Size of $\mathcal{S}_{\text{DR}}$
$P_{\text{d},n}$	Real power demand at bus n
$P_{\text{g},n}$	Real power generation at bus n
P_{loss}	Total power loss in the system
$Q_{\text{d},n}$	Reactive power demand at bus n
$Q_{\text{g},n}$	Reactive power generation at bus n
T_t	Length of time period t
u	Left singular vector
V_n	Voltage magnitude at bus n
w	Right singular vector
α	Weighting factor
ε	Loss management strategy parameter
θ_n	Voltage angle at bus n
σ	Singular value of a matrix
σ_0	Smallest singular value of a matrix
Σ, U, W	Singular Value Decomposition (SVD) matrices
χ	Operating point

4.2 Chapter Introduction

We formulate a multiperiod optimal power flow problem that uses spatio-temporal load shifting to improve voltage stability in this chapter. In the first period, we maximize the

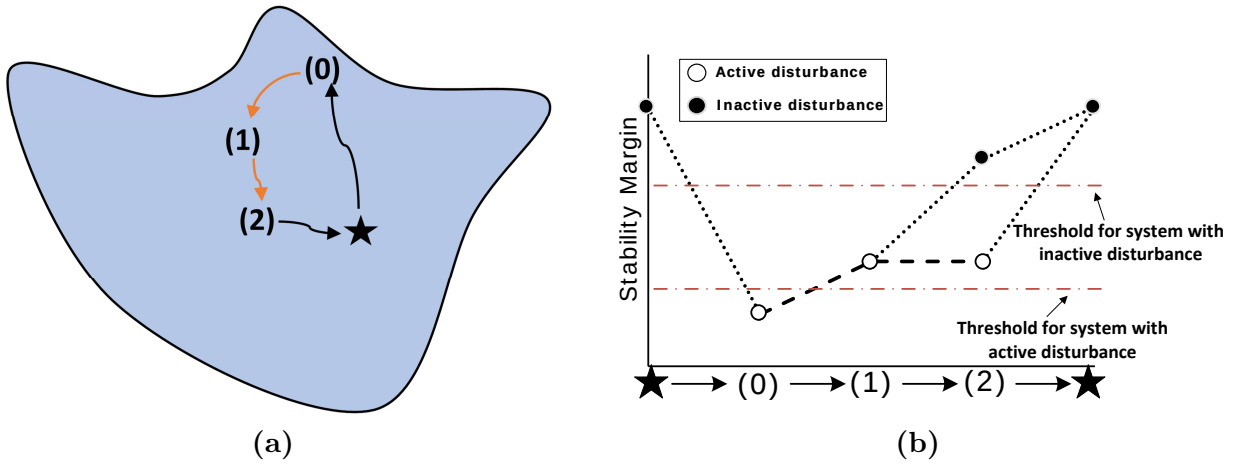

(a) (b)

Figure 4.1: Conceptual illustration of the spatio-temporal load shifting problem.

SSV of the power flow Jacobian by changing the loading pattern subject to the AC power flow equations, engineering limits, and a constraint that forces the total loading to be constant. The second period minimizes the generation cost while paying back energy to each load and maintaining the SSV. We again use the iterative LP solution algorithm using singular value sensitivities to solve the problem and benchmark it against the NLP algorithm in [10]. We conduct case studies using the IEEE 9- and 118-bus systems to determine optimal loading patterns and assess algorithmic performance.

A conceptual illustration of the problem is shown in Fig. 5.1. The initial operating point is denoted as a star that determined via unit commitment and economic dispatch. A disturbance happens resulting in the operating point near the feasibility/stability boundary (i.e., to Operating Point 0) and the stability margin to drop to a point below the stability threshold corresponding to the current system topology (i.e., "threshold for system with active disturbance" shown in the figure). Note that SSVs computed for systems with different topologies are incomparable since the Jacobian changes. This means we cannot compare the SSVs denoted with black circles to those denoted with white circles. Additionally, the system operator would need to determine a stability threshold for each post-disturbance topology.

When the SSV is below its stability threshold, the system is prone to instability. Our algorithm computes a change to the locational distribution of the demand-responsive load. Specifically, we increase some loads and decrease others while ensuring that the total real power consumption of the loads and real power production of each generator (with the exception of the slack bus, which compensates for the change in system losses) is constant so as not to affect the system's frequency stability (Operating Point 1). The reactive power

consumption of the demand-responsive loads changes based on the load model. The reactive power production of the generators adjusts to the new loading pattern in order to keep the voltage magnitudes at generator buses constant. After a short period of time, the system operator determines the minimum cost dispatch of slower-acting generators that relieves the loads, pays back the changes made to each load at Operating Point 1, and maintains/improves the stability margin (Operating Point 2). The payback sets the energy consumed by each load while at Operating Point 2 to its nominal (i.e., baseline) consumption plus/minus the energy not consumed/consumed while at Operating Point 1. As shown in Fig. 4.1(b), at Operating Point 2, the achievable stability margin and associated stability threshold is a function of whether or not the disturbance is still active. When it is no longer active and the energy is paid back, the system returns to its initial operating point, or another point with an adequate stability margin.

Our goal is to determine the optimal dispatches corresponding to Operating Points 1 and 2. Note that we neglect the transition; the path the system takes depends upon how the DR actions are implemented. We pose the problem as a multiperiod optimal power flow problem in which the objective is to minimize a weighted combination of the negative of the stability margin in Period 1 (corresponding to Operating Point 1) and the generation cost in Period 2 (corresponding to Operating Point 2). In each time period, we require the total loading to remain unchanged, so as not to affect the system frequency. For notational simplicity, we assume that each bus has at most one generator and at most one load. We model all loads as constant real power loads with constant power factor.

The technical contributions of this chapter are as follows:

- We formulate a multiperiod optimal power flow problem that uses spatio-temporal load shifting to improve voltage stability. In the first period, we maximize the SSV of the power flow Jacobian by changing the loading pattern subject to the AC power flow equations, engineering limits, and a constraint that forces the total loading to be constant. The second period minimizes the generation cost while paying back energy to each load and maintaining the SSV;

- we conduct case studies using the IEEE 9- and 118-bus systems to determine optimal loading patterns and assess algorithmic performance;

- and we compare the cost and performance of spatio-temporal load shifting to that of generator actions.

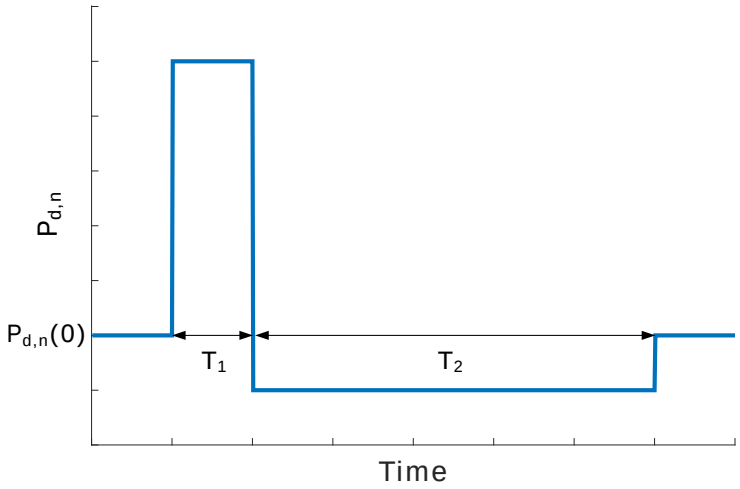

Figure 4.2: Example dispatched demand $P_{\mathrm{d},n}$ at bus n in Periods 1 and 2, where $P_{\mathrm{d},n}(0)$ is its nominal demand. The total energy consumed over both periods is equal to its nominal consumption.

4.3 Multiperiod Optimal Power Flow Problem

Let $\mathcal{T} = \{1, 2\}$ be the set of time periods within the optimization problem, T_1 be the length of Period 1, and T_2 be the length of Period 2. Lengths T_1 and T_2 are not necessarily equal, as shown in Fig. 4.2. For notational simplicity, we assume the real power demand at bus n, $P_{\mathrm{d},n}(t)$, is constant within a time period and the nominal real power demand in all periods is equal to $P_{\mathrm{d},n}(0)$; however, the formulation could be easily extended to incorporate time-varying demands.

Let $\mathcal{N}$ be the set of all buses, $\mathcal{S}_{\mathrm{PV}}$ be the set of all PV buses, and $\mathcal{S}_{\mathrm{PQ}}$ be the set of all PQ buses. Additionally, let $\mathcal{S}_{\mathrm{G}}$ be the set of all buses with generators, i.e., all PV buses in addition to the slack bus, and let $\mathcal{S}_{\mathrm{DR}}$ be the set of buses with responsive loads; the buses comprising $\mathcal{S}_{\mathrm{DR}}$ may be PV or PQ buses. In our case studies, we assume that a portion of the existing loads in the network are responsive.

The multiperiod optimal power flow problem determines the operating points in each time period that balance the two objectives: maximizing the SSV of the power flow Jacobian matrix in Period 1 and minimizing the generation cost in Period 2. The general formulation is as follows.

$$\min_{\substack{\boldsymbol{P}_{\mathbf{g}}(t),\boldsymbol{Q}_{\mathbf{g}}(t),\\ \boldsymbol{P}_{\mathbf{d}}(t),\boldsymbol{Q}_{\mathbf{d}}(t),\\ \boldsymbol{V}(t),\boldsymbol{\theta}(t),\sigma_0(t)}} \quad -\alpha\sigma_0(1) + \mathcal{C}(\boldsymbol{P}_{\mathbf{g}}(2)) \tag{4.1a}$$

$$\text{s.t.} \quad (\forall t \in \mathcal{T})$$

$$\sigma_0(t) = \sigma_{\min}\{J(\boldsymbol{\theta}(t), \boldsymbol{V}(t))\} \tag{4.1b}$$

$$\mathcal{F}_n^{\mathrm{P}}(\boldsymbol{\theta}(t), \boldsymbol{V}(t)) = P_{\mathrm{g},n}(t) - P_{\mathrm{d},n}(t) \qquad \forall n \in \mathcal{N} \tag{4.1c}$$

$$\mathcal{F}_n^{\mathrm{Q}}(\boldsymbol{\theta}(t), \boldsymbol{V}(t)) = Q_{\mathrm{g},n}(t) - Q_{\mathrm{d},n}(t) \qquad \forall n \in \mathcal{N} \tag{4.1d}$$

$$\sum_{n \in \mathcal{S}_{\mathrm{DR}}} P_{\mathrm{d},n}(1) = \sum_{n \in \mathcal{S}_{\mathrm{DR}}} P_{\mathrm{d},n}(0) + \varepsilon \left(P_{\mathrm{loss}}(0) - P_{\mathrm{loss}}(1)\right) \tag{4.1e}$$

$$T_1 P_{\mathrm{d},n}(1) + T_2 P_{\mathrm{d},n}(2) = (T_1 + T_2) P_{\mathrm{d},n}(0) \qquad \forall n \in \mathcal{S}_{\mathrm{DR}} \tag{4.1f}$$

$$P_{\mathrm{d},n}(t) \cdot \mu_n = Q_{\mathrm{d},n}(t) \qquad \forall n \in \mathcal{N} \tag{4.1g}$$

$$P_{\mathrm{d},n}(t) = P_{\mathrm{d},n}(0) \qquad \forall n \in \mathcal{N} \setminus \mathcal{S}_{\mathrm{DR}} \tag{4.1h}$$

$$\theta_{\mathrm{ref}}(t) = 0 \tag{4.1i}$$

$$\sigma_0(2) \geq \sigma_0(1) \tag{4.1j}$$

$$\mathcal{H}_{nm}(\boldsymbol{\theta}(t), \boldsymbol{V}(t)) \leq \overline{\mathcal{H}}_{nm} \tag{4.1k}$$

$$\mathcal{H}_{mn}(\boldsymbol{\theta}(t), \boldsymbol{V}(t)) \leq \overline{\mathcal{H}}_{mn} \tag{4.1l}$$

$$\underline{P}_{\mathrm{g},n}(t) \leq P_{\mathrm{g},n}(t) \leq \overline{P}_{\mathrm{g},n}(t) \qquad \forall n \in \mathcal{S}_{\mathrm{G}} \tag{4.1m}$$

$$\underline{Q}_{\mathrm{g},n}(t) \leq Q_{\mathrm{g},n}(t) \leq \overline{Q}_{\mathrm{g},n}(t) \qquad \forall n \in \mathcal{S}_{\mathrm{G}} \tag{4.1n}$$

$$\underline{P}_{\mathrm{d},n}(t) \leq P_{\mathrm{d},n}(t) \leq \overline{P}_{\mathrm{d},n}(t) \qquad \forall n \in \mathcal{S}_{\mathrm{DR}} \tag{4.1o}$$

$$\underline{V}_n(t) \leq V_n(t) \leq \overline{V}_n(t) \qquad \forall n \in \mathcal{N} \tag{4.1p}$$

The cost function is a linear combination of the SSV σ_0 of the power flow Jacobian matrix $J(\boldsymbol{\theta}, \boldsymbol{V})$ in Period 1 and the generation cost $\mathcal{C}(\cdot)$ in Period 2, where $\alpha \geq 0$ is a weighting factor. Most of constraints are the same as those in 2.1. Constraint (4.1f) enforces energy payback, specifically, that the energy consumed over both periods by each load is equal to its nominal consumption. Constraint (4.1j) ensures that the SSV in Period 2 is greater than or equal to that in Period 1.

Again we use the iterative linear programming to solve 4.1. The resulting linear program solved in each iteration of the iterative LP algorithm is as follows.

$$\min_{\substack{\boldsymbol{\Delta P_{\mathrm{g}}}(t), \boldsymbol{\Delta Q_{\mathrm{g}}}(t), \\ \boldsymbol{\Delta P_{\mathrm{d}}}(t), \boldsymbol{\Delta Q_{\mathrm{d}}}(t), \\ \boldsymbol{\Delta V}(t), \boldsymbol{\Delta \theta}(t), \Delta\sigma_0(t)}} -\alpha \Delta\sigma_0(1) + \sum_{n \in \mathcal{S}_{\mathrm{G}}} \left. \frac{\partial \mathcal{C}(\boldsymbol{P_{\mathrm{g}}}(2))}{\partial P_{\mathrm{g},n}(2)} \right|_{\boldsymbol{P_{\mathrm{g}}^*}(2)} \Delta P_{\mathrm{g},n}(2) \tag{4.2a}$$

$$\text{s.t.} \quad (\forall t \in \mathcal{T})$$

$$\Delta\sigma_0(t) = \sum_{n \in \left\{\mathcal{S}_{\mathrm{PV}}, \mathcal{S}_{\mathrm{PQ}}\right\}} \left[u_0(t)^T \frac{\partial J(t)}{\partial \theta_n} w_0(t) \right] \Delta\theta_n(t)$$

$$+ \sum_{n \in \mathcal{S}_{\mathrm{PQ}}} \left[u_0(t)^T \frac{\partial J(t)}{\partial V_n} w_0(t) \right] \Delta V_n(t) \tag{4.2b}$$

$$\text{Linearizations of (4.1b)} - \text{(4.1p)} \tag{4.2c}$$

$$\Delta\sigma_0(t) \leq \overline{\Delta\sigma_0}, \tag{4.2d}$$

where (4.2b) is the linear smallest singular value sensitivity constraint and (4.2d) limits the maximum change in $\Delta\sigma(t)$ since the linearizations are only valid near the previous operating point.

The solution algorithm is similar to Algorithm 1. We initialize the operating points of Periods 1 and 2, $\chi^*(1), \chi^*(2)$, at the operating point of Period 0, $\chi(0)$. After obtaining a solution to (4.2) and before the next iteration, $\chi'(t)\,\forall t \in \mathcal{T}$ are updated by adding the optimal change in operating point $\Delta\chi^{\mathrm{opt}}(t)\,\forall t \in \mathcal{T}$; the AC power flow is re-solved in each period; and we compute the new values of the SSVs, $\sigma_0^*(t)\,\forall t \in \mathcal{T}$, and the value of the objective function in (4.2a). Iterations are terminated when the absolute value of the objective function in (4.2a) is less than a threshold (here, 10^{-5}), and the outputs are the final operating points and SSVs.

4.4 Case Studies

In this section, we conduct a number of case studies using the IEEE 9- and 118-bus systems. We compare the performance of our iterative LP (ILP) algorithm against the iterative NLP (INLP) algorithm from [10]. Each iteration of the nonlinear optimization problem (2.6) is solved with `fmincon` in MATLAB. All computations are implemented in MATLAB on an Intel(R) i5-6600K CPU with 8 GB of RAM.

For all case studies, we use the system data from MATPOWER [149] and set $\overline{\Delta\sigma_0} = 0.01$. We model the entire load at a bus with responsive demand as flexible, i.e., $0 \leq P_{\mathrm{d},n} \leq 2P_{\mathrm{d},n}(0)\,\forall n \in \mathcal{S}_{\mathrm{DR}}$ in order to get a sense for the maximum achievable change in SSV due to DR. In practice, only a fraction of the load at a particular bus will be responsive. We set $T_1 = 5$ min and choose T_2 as the minimum multiple of 5 min that achieves a feasible solution, though in practice T_1 and T_2 would be a function of the response time of the generators and the flexibility of the loads.

For the IEEE 9-bus system, we assume the system is initially operating at the optimal power flow solution at \$5297/hour. A disturbance takes line 4-9 out of service and the SSV drops to 0.4445, which we assume is below the stability margin threshold. We assume all load

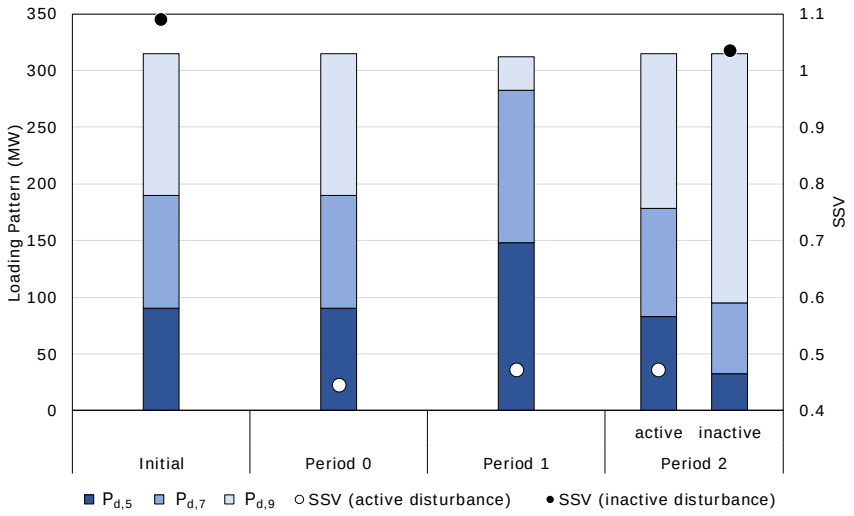

Figure 4.3: Loading pattern and SSV in each period for the IEEE 9-bus system.

is responsive and set $\alpha = 10000$ to prioritize SSV improvement. The effect of the choice of α will be described in the next subsection. If the disturbance is active, we set $T_2 = 8T_1 = 40$ min, while if the disturbance is inactive, we set $T_2 = T_1 = 5$ min.

For the IEEE 118-bus system, we assume the system is initially operating at the optimal power flow solution at \$129627/hour. A disturbance takes line 23-24 out of service and the SSV drops to 0.1534, which we assume is below the stability margin threshold. We assume all load at PQ buses is responsive (1197 MW out a total of 4242 MW of system-wide demand) and set $\alpha = 10000$. Whether or not the disturbance is active, $T_2 = T_1 = 5$ min.

4.4.1 IEEE 9-bus System Results

Figures 4.3 and 4.4 show the loading pattern, SSV, generation dispatch, and generation cost per hour in each period. In Fig. 4.3, we distinguish between SSVs when the disturbance is active and inactive – SSVs denoted with white circles (active) are comparable, SSVs denoted with black circles (inactive) are comparable, but SSVs denoted with white circles are not comparable to those denoted with black circles. In Period 1 the SSV increases by 6.1% due to the DR actions. Note that generation, with the exception of the slack bus, is constant in Periods 0 and 1. Next, we pay back the energy in Period 2. If the disturbance is still active, we maintain the SSV and the generation cost per hour is relatively large, whereas if the disturbance is inactive, the SSV increases due to the change in system topology. The cost per hour is comparable to that in the other periods. The actual generation cost of Period 2 is the cost per hour multiplied by the length of the period, and since T_2 with an active

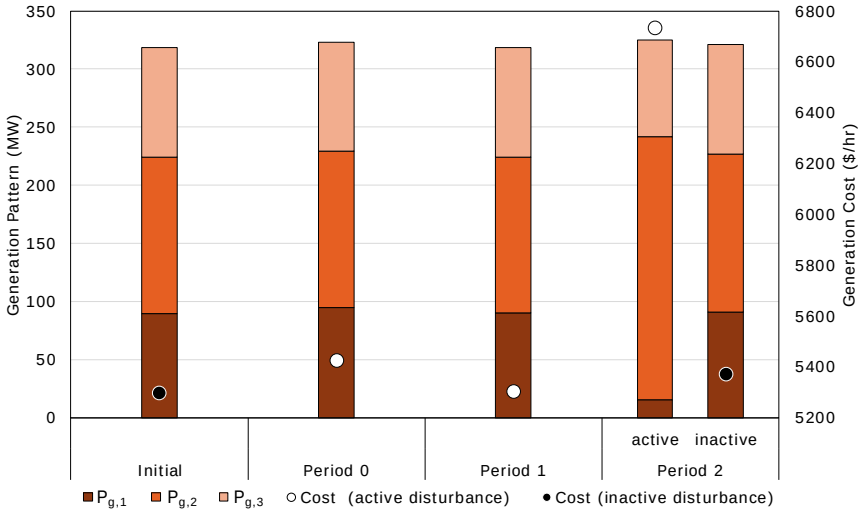

Figure 4.4: Generation dispatch and generation cost per hour in each period for the IEEE 9-bus system.

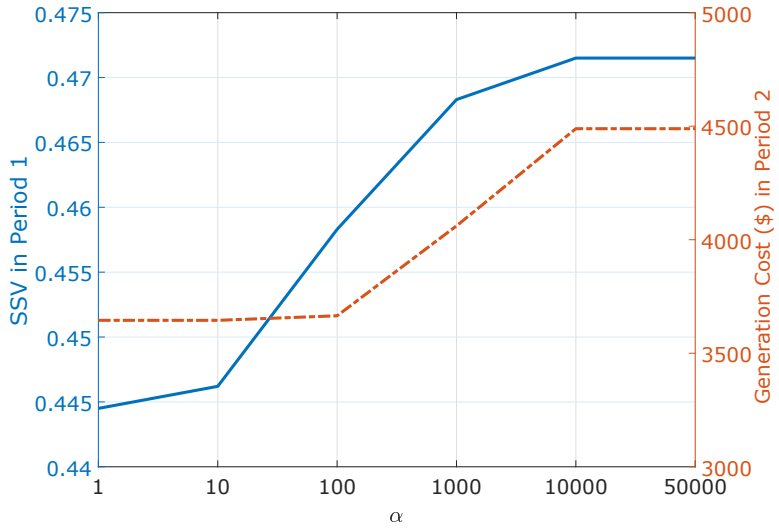

Figure 4.5: Optimal SSV in Period 1 and generation cost in Period 2 as a function of the weighting factor α.

disturbance is much larger than T_2 without, the actual cost difference between the two cases is more extreme than it appears in the figure.

Figure 4.5 shows the SSV in Period 1 and the generation cost in Period 2 as α varies in the case with an active disturbance in Period 2. The weighting factor trades the stability margin improvement for generation cost reduction, and the best choice of α for a particular system is based on operator priorities. For this system, the SSV in Period 1 is maximized when $\alpha \geq 10000$. However, this threshold is system-dependent.

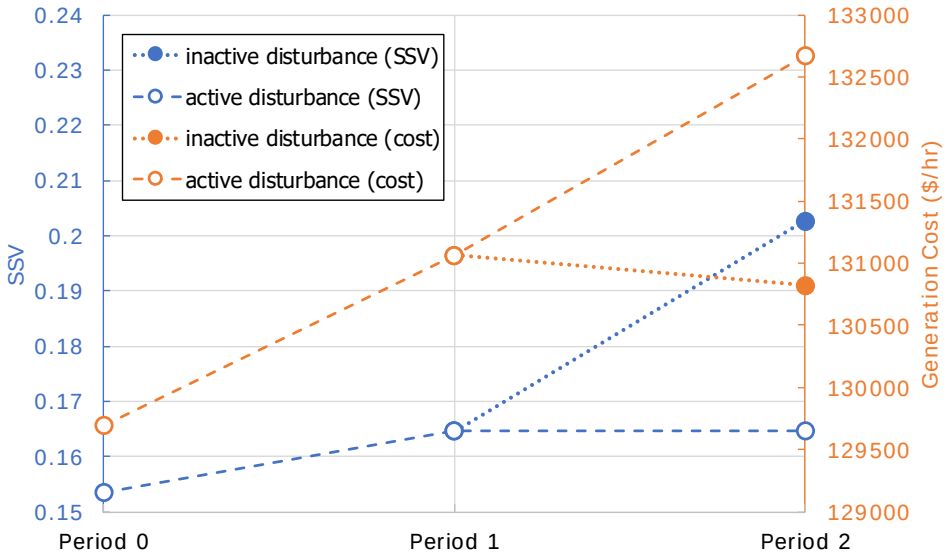

Figure 4.6: SSV and generation cost per hour in each period for the 118-bus system.

4.4.2 IEEE 118-bus System Results

Figure 4.6 shows the SSV and generation cost per hour in each period. The SSV increases by 7.3% due to the DR actions in Period 1. Again, we show two cases in Period 2 and, again, the SSV is higher (due to the change in system topology) and the generation cost is lower if the disturbance is inactive.

Figure 4.7 visualizes the DR actions in Period 1. Red shading in the upper semicircle corresponding to a bus denotes an increase in load, while blue shading in the lower semicircle denotes a decrease in load. The lightning symbol indicates the line removed from service by the disturbance. In this case, the SSV is improved by decreasing the loading in Area 1 and increasing the loading in Area 2.

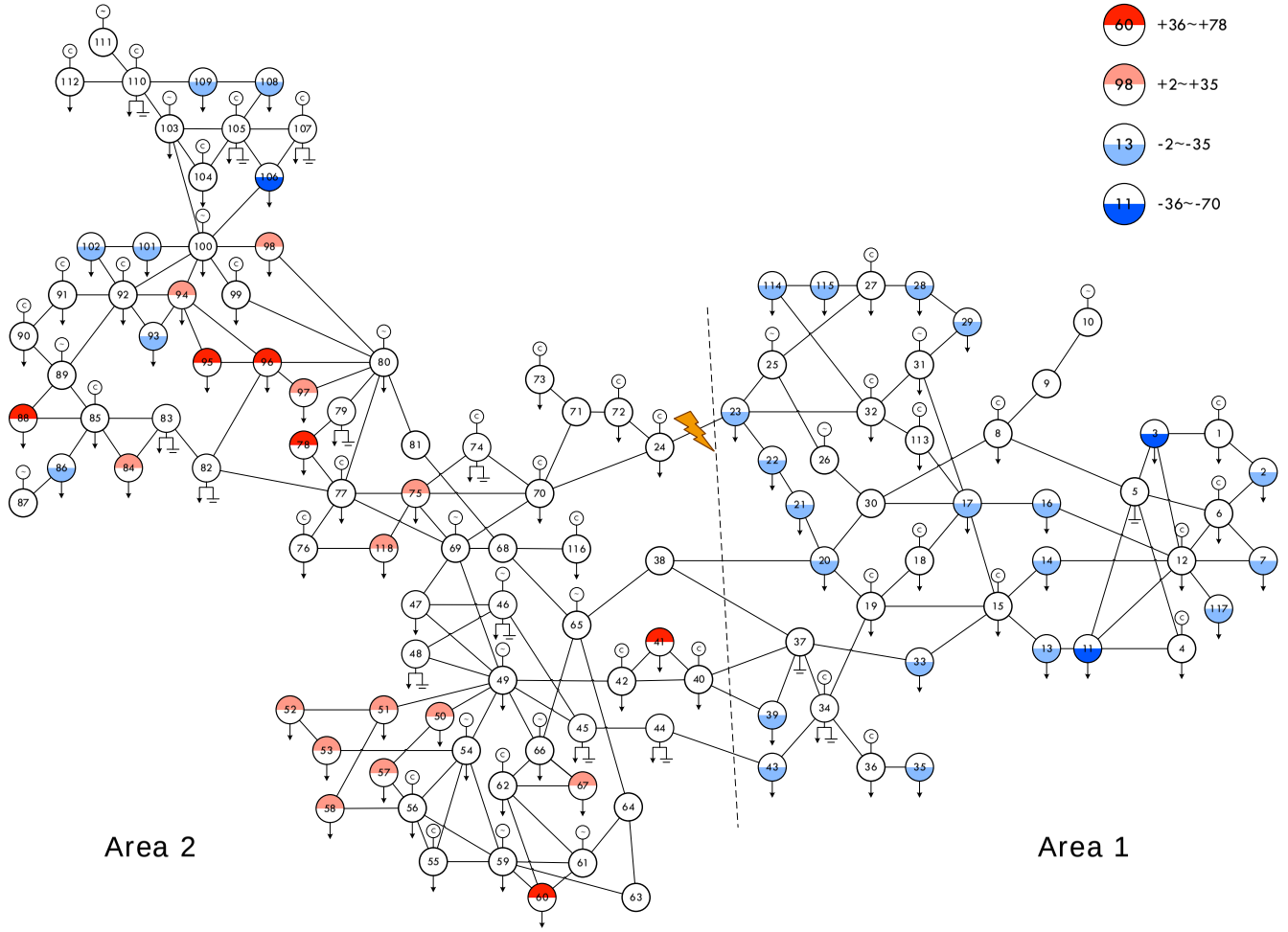

Figure 4.7: Visualization of the DR actions in Period 1 for the IEEE 118-bus system. Figure created with the help of [98].

Table 4.1: Cost over one hour ($) of the multiperiod DR strategy versus generation redispatch to achieve the same SSVs

T_{restored}	Resource	9-bus	118-bus
5 min	DR	5303	129545
	Generation	5360	129905
1 hour	DR	6441	132777
	Generation	6043	132961

4.4.3 Comparison of Costs

Table 4.1 summarizes the cost over one hour of the multiperiod DR strategy (with Period 1 decision variables corresponding to Case 1) for different disturbance restoration times T_{restored}. It also compares the results to the minimum-cost redispatch of generation alone (corresponding to the decision variables in Case 5, i.e., the generators are not limited by ramp rates) to achieve the SSV obtained using DR alone. The cost of each period is computed as the cost per hour times the length of the period, where all periods are 5 min except for the 9-bus system's Period 2 when the disturbance is active, which is 40 min (as a reminder, this was chosen because it is the shortest multiple of 5 min for which we can obtain a feasible solution). When $T_{\text{restored}} = 5$ min, the cost per hour of operating the system beyond Periods 1 and 2 but within the hour is equal to the cost per hour of Period 0. However, when $T_{\text{restored}} = 1$ hr, this cost is equal to the cost of using the generators to maintain the SSV achieved in Periods 1 and 2.

As shown in the table, as T_{restored} increases, the cost of the strategy increases. Comparing the cost of using DR versus generation, we see that the cheaper option is case dependent. In three out of the four cases, DR is cheaper; however, when $T_{\text{restored}} = 1$ hour, generation actions are cheaper than DR actions for the 9-bus system. As described in the previous subsection, DR is always cheaper in Period 1. However, energy payback in Period 2 can be expensive, which is true for the 9-bus system when the disturbance is active, as shown in Fig. 4.4. Moreover, in this case, Period 2 lasts for 40 min.

Note that the generation costs reported in the table may not be realizable in practice because real generators are ramp-limited. Therefore, in cases in which DR is more expensive than generation, it may still be desirable to deploy DR since generation may not respond in time.

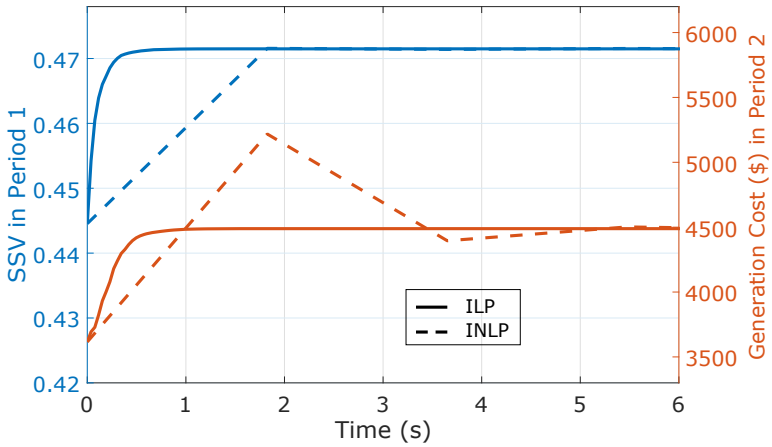

Figure 4.8: Convergence of the SSV in Period 1 and the generation cost in Period 2 using the ILP and INLP algorithms for the IEEE 9-bus system.

4.4.4 Comparison of Algorithms

In this subsection, we compare the performance of the ILP and INLP algorithms. Figure 4.8 shows the convergence of each algorithm on the 9-bus system considering the full multiperiod problem (disturbance active in Period 2). The solid lines are the results of the ILP algorithm and the dashed lines are the results of the INLP algorithm. The ILP algorithm converges more quickly than the INLP algorithm. Similarly, Fig. 4.9 shows the convergence of the ILP algorithm on the 118-bus system considering the full multiperiod problem (disturbance active in Period 2). The INLP algorithm does not scale to the 118-bus system.

The computation times are summarized in Table 4.2. Note that ILP-E refers tp the ILP with eigenvalue sensitivity approach as mentioned in Chapter 2. The overall computation time is a function of the number of iterations needed and the time required for each iteration, where the former depends on the initial operating point and the maximum step size $\overline{\Delta\sigma_0}$ and the latter depends on the size of Jacobian matrix. The time could be reduced through 1) parallel computing of the SSV sensitivities, 2) approximating the SSV sensitivity (4.2b) to only include the system states that most affect the SSV, and/or 3) applying an adaptive maximum step size.

4.5 Chapter Conclusion

This chapter builds on the preliminary work shown in Chapter 2, which developed a single-period formulation that uses DR to maximize the SSV, but does not consider energy payback.

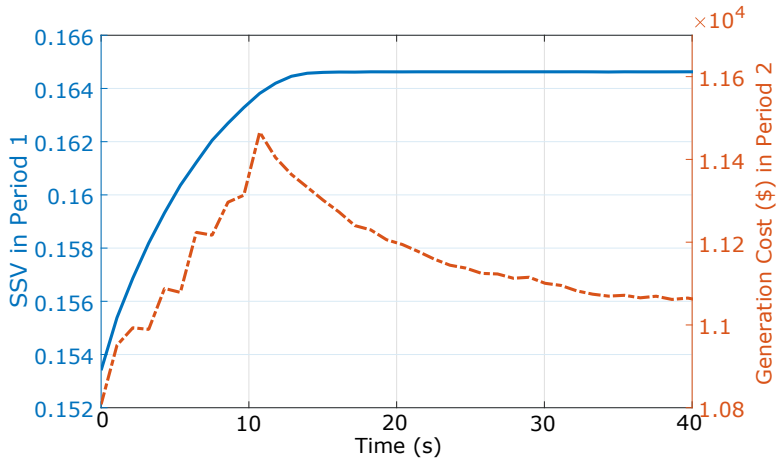

Figure 4.9: Convergence of the SSV in Period 1 and the generation cost in Period 2 using the ILP algorithm for the IEEE 118-bus systems.

Table 4.2: Computation Times (s)

	ILP	ILP-E	INLP
IEEE 9-bus system, Period 1 only	0.4	1.0	2.5
IEEE 9-bus system, Full problem	1.0	2.8	6.0
IEEE 118-bus system, Period 1 only	6.5	15	-
IEEE 118-bus system, Full problem	35	60	-

In this chapter, we have developed a multiperiod optimal power flow approach to use DR to improve static voltage stability while minimizing the generation cost in the energy payback period. The results show that demand response actions can improve static voltage stability, in some cases more cost-effectively than generation actions. We also compared our algorithm's performance to that of an iterative nonlinear programming algorithm from the literature. We find that our approach is approximately 6 times faster when applied to the IEEE 9-bus system, and it is able to be used on the IEEE 118-bus system while the INLP fails to generate results.

Chapter 5

Using DR to Improve the Distance to the Closest SNB

In this chapter, we propose a method to improve power system static voltage stability by maximizing the distance to the closest saddle-node bifurcation of the power flow. Specifically, we formulate a nonlinear nonconvex optimization problem in which we choose loading patterns that maximize this distance while also constraining the total system loading to remain constant (the same as in Chapter 2). This chapter is largely based on the published work:

- M. Yao, I.A. Hiskens, and J.L. Mathieu. "Improving power system voltage stability by using demand response to maximize the distance to the closest saddle-node bifurcation". In: *IEEE Conference on Decision and Control*. 2018.

5.1 Notation

Functions

$\mathcal{F}(\cdot)$: $\mathbb{R}^m \times \mathbb{R}^m \to \mathbb{R}^m$	Standard power flow
$g_1(\cdot)$: $\mathbb{R}^{n_{\mathrm{dr}}} \to \mathbb{R}^{2n_{\mathrm{dr}}}$	Demand response limits
$g_2(\cdot)$: $\mathbb{R}^m \to \mathbb{R}^{n_{\mathrm{e}}}$	Engineering limits
$h(\cdot)$: $\mathbb{R}^{2n_{\mathrm{dr}}} \to \mathbb{R}^{n_{\mathrm{dr}}+1}$	Demand response assumptions

Sets

$\mathcal{S}_{\text{PV}}$	Set of all PV buses
$\mathcal{S}_{\text{PQ}}$	Set of all PQ buses
$\mathcal{S}_{\text{DR}}$	Set of buses with demand responsive loads

Variables & Parameters

θ_i	Voltage angle at bus i
V_i	Voltage magnitude at bus i
P_i	Real power injection at bus i
Q_i	Reactive power injection at bus i
d	Distance to the closest Saddle-Node Bifurcation
x	System state vector
λ	System parameter vector (power injections)
Λ	Feasible set of λ
n_{dr}	Number of buses with demand responsive loads
n_{e}	Number of engineering limits
m	Length of system state and parameter vectors
w	Left eigenvector corresponding to zero eigenvalue
α_i	Ratio between real and reactive demand at bus i
β	Weighting matrix
μ, γ	Lagrange multipliers
ζ	Constant

5.2 Chapter Introduction

The best static voltage stability metric is an open question. Our previous chapters investigated use of the loading margin [49] and the smallest singular value (SSV) of the power flow Jacobian [126] within the spatio-temporal load shifting problem. However, the loading margin specifies the direction of the changes to power injections precipitating an instability and the SSV gives only indirect information about the distance to instability [72].

In this chapter, we explore the use of the distance to the closest saddle-node bifurcation of the power flow as the stability metric we would like to maximize by spatially shifting load across a network within a single time step (we leave the full spatio-temporal problem to future). The distance to the closest saddle-node bifurcation (SNB) is a well-known stability metric [39]. Past work [38] showed that the optimal control direction to move the system

away from instability is antiparallel to the normal vector at the closest SNB. The idea is generalized in [25] for computing the optimal design of system parameters (i.e., shunt and series compensation) to improve this distance. The benefit of this approach is that the resulting optimization problem can be solved by formulating the Karush-Kuhn-Tucker (KKT) conditions, solving the nonlinear system of equations using the Newton-Raphson method, and checking if the solution is a local minimum by using the iterative method proposed in [36]. By reinitializing the nonlinear system solver and repeating this process many times we may find the global minimum, though we have no guarantee. We note that, in practice, limit-induced bifurcations (LIB) may occur before SNBs. We do not consider LIBs here; in future work we will explore algorithmic approaches to maximize the distance to the closest SNB or LIB.

The main contributions of this chapter are as follows.

- We formulate the optimization problem and derive its KKT conditions.
- We conduct case studies using a 4-bus system and the IEEE 9-bus system and explore the performance of the algorithm and the accuracy of the solution. In particular, we find that our algorithm is able to maximize the distance to the globally closest SNB for the 4-bus system but does not find the globally closest SNB for the 9-bus system, instead maximizing the distance to a locally closest SNB. However, the globally closest SNB of the 9-bus system is unrealistic.
- We compare our solution to those obtained by formulations that use other stability metrics. We find that all approaches produce different results and we discuss the implications of this finding.
- Using Kundur's two area system, we explore algorithm convergence issues.

A conceptual illustration of the problem is shown in Fig. 5.1a. The power flow solvability boundary (black curve) is defined by a set of SNBs, where λ denotes power injections. Suppose the initial operating point with injections equal to λ^0 is not sufficiently far from its closest SNB. The system operator would like to increase this distance, which is a measure of static voltage stability. It could do so through generator redisptach, load shedding, and/or spatial load shifting. Here, we only investigate the impact of spatial load shifting.

As we mentioned before, while generators take time to respond to dispatch commands, demand responsive loads can respond quickly if coordinated via low-latency communications

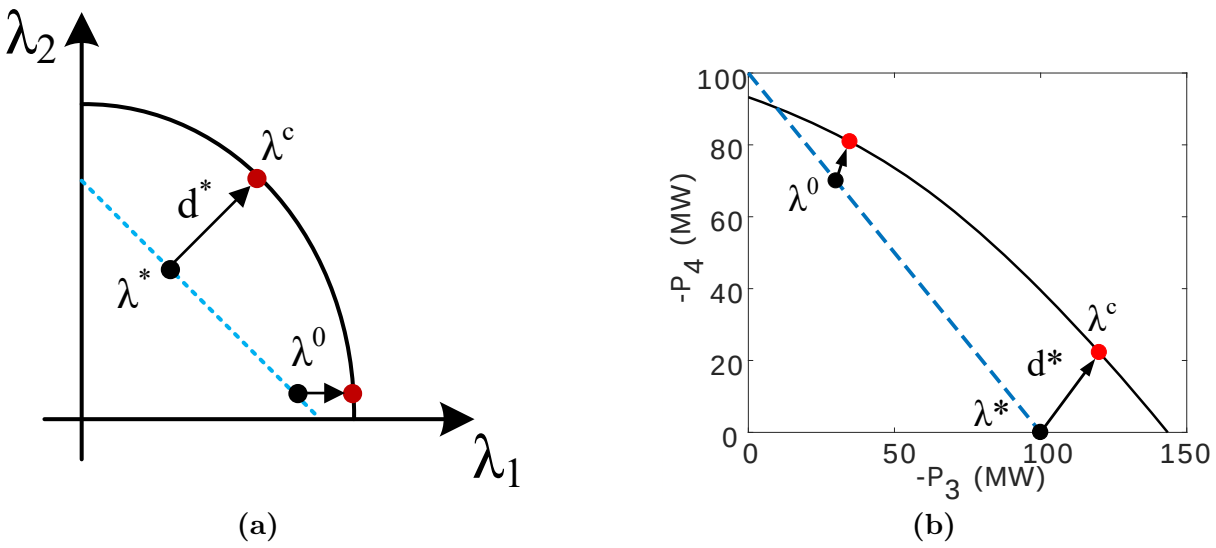

Figure 5.1: Illustration of the problem. (a) Conceptual illustration. (b) 4-bus system example.

systems. Load shedding reduces quality of service to consumers and requires an equivalent decrease in generation to maintain system frequency. In contrast, spatial load shifting decreases and increases loads at various points in the network while maintaining the total loading so as not to affect system frequency. Aggregations of loads such as residential and commercial air conditioning systems can both decrease and increase their power consumption for short periods of time. So long as the energy is "paid back" within a short period of time, quality of service can be maintained. While it would likely be uneconomical to purpose-build demand response capability for this application, it could be one of many services that demand responsive loads could provide in future power networks.

In Fig. 5.1a, the blue dashed line is the feasible range of the injections, including the requirement that the total loading is constant. Our goal is to determine injections $\lambda^\star$ corresponding to the optimal operating point along the blue dashed line that maximize the distance $d^\star$ to the closest SNB λ^c. Figure 5.1b shows an example using a simple four bus system that will be discussed in detail in Section 5.5.1. The optimization problem is:

$$\max_{\lambda^\star \subset \Lambda^\star} \left(\min_{\lambda^c \subset \Lambda^c} ||\lambda^c - \lambda^\star||_2 \right), \tag{5.1}$$

where Λ defines the feasible set of λ.

In our formulation, same as the base case in Chapter 2, we assume that the generator real power outputs do not change with the exception of that of the slack bus, which changes its

output to compensate for the change in system losses that occurs when the load is spatially shifted. Additionally, we assume that PV bus voltages are fixed. Therefore, we choose only the real and reactive power consumption of each demand responsive load, which is modeled as constant power with constant power factor (we do not consider voltage dependent load models as described in Chapter 3 here). In practice, the system operator could simultaneously redispatch generators and demand responsive loads to improve the stability margin, though the generators may be ramp limited. However, here we focus on characterizing the response of demand responsive loads alone.

5.3 Closest Saddle-Node Bifurcation

We first review the approach for computing the closest SNB to a given operating point. The standard power flow equations [142] can be expressed as:

$$\mathcal{F}(x, \lambda) = f(x) - \lambda = 0, \tag{5.2}$$

where $x \in \mathbb{R}^m$ is the system state vector, $\lambda \in \mathbb{R}^m$ is the system parameter vector and $\mathcal{F} : \mathbb{R}^m \times \mathbb{R}^m \to \mathbb{R}^m$. In this chapter, we assume $x = [\theta_{i \in \mathcal{S}_{\text{PV}}};\ \theta_{i \in \mathcal{S}_{\text{PQ}}};\ V_{i \in \mathcal{S}_{\text{PQ}}}]$ and $\lambda = [P_{i \in \mathcal{S}_{\text{PV}}};\ P_{i \in \mathcal{S}_{\text{PQ}}};\ Q_{i \in \mathcal{S}_{\text{PQ}}}]$ (unless otherwise stated). The SNB is reached when the power flow Jacobian becomes singular:

$$\frac{\partial f^T}{\partial x} w = 0, \tag{5.3}$$

where $w \in \mathbb{R}^m$ is a left eigenvector corresponding to the zero eigenvalue of the power flow Jacobian matrix. To obtain a unique solution of w, we normalized the left eigenvector such that $w^T w - 1 = 0$.

As discussed in [39], for a given operating point (x^0, λ^0), if the distance to bifurcation is defined as Euclidean distance $d = ||\lambda^c - \lambda^0||_2$, then the closest SNB can be found by solving the following optimization problem:

$$\min_{x_c, \lambda_c, w} \quad \frac{1}{2}||\lambda^c - \lambda^0||_2^2 \tag{5.4a}$$

$$\text{subject to} \quad \mathcal{F}(x^c, \lambda^c) = 0 \tag{5.4b}$$

$$\frac{\partial f^T}{\partial x}\Big|_{(x = x^c)} w = 0 \tag{5.4c}$$

$$w^T w - 1 = 0. \tag{5.4d}$$

To solve (5.4), we derive the KKT conditions. The Lagrange function is:

$$\mathcal{L} = \frac{1}{2}||\lambda^c - \lambda^0||_2^2 + \mu_1^T \mathcal{F}(x^c, \lambda^c) + \mu_2^T \frac{\partial f^T}{\partial x}\Big|_{(x=x^c)} w + \mu_3(w^T w - 1), \tag{5.5}$$

where $\mu_1 \in \mathbb{R}^m$, $\mu_2 \in \mathbb{R}^m$, $\mu_3 \in \mathbb{R}$ are Lagrange multipliers. Therefore, the KKT conditions are:

$$\frac{\partial \mathcal{L}}{\partial x^c} = \mu_1^T \frac{\partial f}{\partial x}\Big|_{(x=x^c)} + \mu_2^T \frac{\partial}{\partial x}\left(\frac{\partial f^T}{\partial x} w\right)\Big|_{(x=x^c)} = 0 \tag{5.6a}$$

$$\frac{\partial \mathcal{L}}{\partial \lambda^c} = (\lambda^c - \lambda^0)^T + \mu_1^T \frac{\partial \mathcal{F}}{\partial \lambda} = 0 \tag{5.6b}$$

$$\frac{\partial \mathcal{L}}{\partial w} = \mu_2^T \frac{\partial f^T}{\partial x}\Big|_{(x=x^c)} + 2\mu_3 w^T = 0 \tag{5.6c}$$

$$(5.4b) - (5.4d) \tag{5.6d}$$

From (5.6b) we know that $\mu_1^T \partial \mathcal{F}/\partial \lambda \neq 0$. Also, $\partial \mathcal{F}/\partial \lambda = -I$. Therefore, the Lagrange multiplier μ_1 must be nonzero. If we post-multiply (5.6c) by w, the first term becomes zero and since w is not zero, μ_3 must be zero. Then μ_2 is either zero or a right eigenvector corresponding to the zero eigenvalue of the power flow Jacobian (making the first term of (5.6c) zero). Assume μ_2 is a right eigenvector. Post-multiplying (5.6a) by μ_2 results in the first term becoming zero, and therefore the second term, which has quadratic form, must also equal zero. This is only possible if μ_2 lies in the null space of the (symmetric) matrix of that second term. Accordingly, the second term of (5.6a) must equal zero. Alternatively, if $\mu_2 = 0$ then that second term in (5.6a) is zero. In either case, the first term of (5.6a) must equal zero, so μ_1 must be a left eigenvector corresponding to the zero eigenvalue of the power flow Jacobian. Since both μ_1 and w are left eigenvectors corresponding to the zero eigenvalue of the power flow Jacobian, we can set $\mu_1 = \zeta_1 w$, where $\zeta_1 \neq 0$ is a scalar.

Hence, a locally closest SNB must satisfy the following equations:

$$\mathcal{F}(x^c, \lambda^c) = 0 \tag{5.7a}$$

$$\frac{\partial f^T}{\partial x}\Big|_{(x=x^c)} w = 0 \tag{5.7b}$$

$$w^T w - 1 = 0 \tag{5.7c}$$

$$(\lambda^c - \lambda^0) - \zeta_1 w = 0. \tag{5.7d}$$

Reference [39] proposed a similar set of equations, the only difference being that instead of

(5.7d) they use the more general equation $(\lambda^c - \lambda^0) - (\partial \mathcal{F}^T / \partial \lambda) w = 0$ since they allow λ to be any system parameter whereas we define λ as power injections. Equation (5.7) is a set of $3m + 1$ nonlinear equations with $3m + 1$ unknowns. Direct methods, for instance, the Newton-Raphson method, or iterative methods such as the one given in [37] can be used to compute the numerical solutions to (5.7). Note that the KKT conditions are just necessary conditions giving us minima, maxima, and saddle points. Solutions obtained with Newton-Raphson need to be checked to ensure they are minima. In contrast, the iterative method in [37] guarantees that the solution is a local minimum, i.e., a locally closest SNB. The distance to the locally closest SNB is $d = ||\lambda^c - \lambda^0||_2 = ||\zeta_1 w||_2 = |\zeta_1|$. We can attempt to find the globally closest SNB by computing all of the locally closest SNBs using different initializations and determining the minimum d. This may be computationally intractable for large systems and we have no guarantee that we will obtain the globally closest SNB.

5.4 Optimization Formulation

In our problem, we need to determine both the parameters $\lambda^\star$ corresponding to the optimal operating point and the parameters λ^c corresponding to the closest SNB. Since the real power injections at PV buses and the real and reactive power injections at PQ buses without demand responsive loads are unchanged, we divide $\lambda^\star$ into two parts. The controlled power injections $\lambda_1^\star = [P_{i \in \mathcal{S}_{\mathrm{DR}}};\ Q_{i \in \mathcal{S}_{\mathrm{DR}}}]$ are limited by the flexibility of the demand responsive loads:

$$g_1(\lambda_1^\star) = \begin{bmatrix} P_i - \overline{P}_i,\ \forall\, i \in \mathcal{S}_{\mathrm{DR}} \\ -P_i + \underline{P}_i,\ \forall\, i \in \mathcal{S}_{\mathrm{DR}} \end{bmatrix} \leq 0, \tag{5.8}$$

where $g_1 : \mathbb{R}^{2n_{\mathrm{dr}}} \to \mathbb{R}^{2n_{\mathrm{dr}}}$ and $\underline{P}_i, \overline{P}_i$ are the lower and upper limits of the range of allowed changes to the real power consumption of the demand responsive loads. The uncontrolled power injections are $\lambda_2^\star = [P_{i \in \mathcal{S}_{\mathrm{PV}}};\ P_{i \in \mathcal{S}_{\mathrm{PQ}} \setminus \mathcal{S}_{\mathrm{DR}}};\ Q_{i \in \mathcal{S}_{\mathrm{PQ}} \setminus \mathcal{S}_{\mathrm{DR}}}] = \lambda_2^0$.

Our goal is to determine $\lambda_1^\star$ that maximizes the distance to its closest SNB. Therefore, the decision variables of the optimization problem are the system state vectors $x^c, x^\star$, system parameter vectors $\lambda^c, \lambda_1^\star$ and the left eigenvector w. The optimization problem is:

$$\min_{x^c, \lambda^c, x^\star, \lambda_1^\star, w} \quad -\frac{1}{2}(\lambda^c - \lambda^\star)^T \beta (\lambda^c - \lambda^\star) \tag{5.9a}$$

$$\text{subject to} \quad \mathcal{F}(x^c, \lambda^c) = 0 \tag{5.9b}$$

$$\mathcal{F}(x^\star, \lambda^\star) = 0 \tag{5.9c}$$

$$\frac{\partial f^T}{\partial x}\Big|_{(x=x^c)} w = 0 \tag{5.9d}$$

$$w^T w - 1 = 0 \tag{5.9e}$$

$$h(\lambda_1^\star) = 0 \tag{5.9f}$$

$$g_1(\lambda_1^\star) \leq 0 \tag{5.9g}$$

$$g_2(x^\star) \leq 0. \tag{5.9h}$$

The objective (5.9a) maximizes a weighted distance instead of the Euclidean distance ($\beta \succ 0$). Constraints (5.9b) and (5.9c) are the standard power flow equations for the SNB and the optimal operating point, respectively. Constraint (5.9d) implies that (x^c, λ^c) is an SNB. The left eigenvector w is normalized in (5.9e). Equation (5.9f) ensures our demand response assumptions are enforced at $\lambda_1^\star$, specifically, 1) the total loading is constant and 2) the load is modeled as constant power with constant power factor:

$$h(\lambda_1^\star) = \begin{bmatrix} \sum P^\star_{i\in\mathcal{S}_{\mathrm{DR}}} - \sum P^0_{i\in\mathcal{S}_{\mathrm{DR}}} \\ \alpha_i P_i^\star - Q_i^\star,\ \forall\, i \in \mathcal{S}_{\mathrm{DR}} \end{bmatrix} = 0, \tag{5.10}$$

where $h : \mathbb{R}^{2n_{\mathrm{dr}}} \to \mathbb{R}^{n_{\mathrm{dr}}+1}$. The inequality constraint (5.9g) is defined in (5.8). The inequality constraint (5.9h) specifies the engineering limits at $(x^\star, \lambda^\star)$. They include limits on the voltage magnitudes at PQ buses, the reactive power injections at PV buses and the slack bus, and the line flows ($g_2 : \mathbb{R}^m \to \mathbb{R}^{n_{\mathrm{e}}}$). The Lagrange function of (5.9) is:

$$\begin{aligned} \mathcal{L} = &-\frac{1}{2}(\lambda^c - \lambda^\star)^T \beta (\lambda^c - \lambda^\star) + \mu_1^T \mathcal{F}(x^c, \lambda^c) \\ &+ \mu_4^T \mathcal{F}(x^\star, \lambda^\star) + \mu_2^T \frac{\partial f^T}{\partial x}\Big|_{(x=x^c)} w + \mu_3 (w^T w - 1) \\ &+ \mu_5^T h(\lambda_1^\star) + \gamma_1^T g_1(\lambda_1^\star) + \gamma_2^T g_2(x^\star), \end{aligned} \tag{5.11}$$

where $\mu_1, \mu_2, \mu_4 \in \mathbb{R}^m$, $\mu_3 \in \mathbb{R}$, $\mu_5 \in \mathbb{R}^{n_{\mathrm{dr}}+1}$, $\gamma_1 \in \mathbb{R}^{2n_{\mathrm{dr}}}$ and $\gamma_2 \in \mathbb{R}^{n_{\mathrm{e}}}$ are Lagrange multipliers. The KKT conditions are:

$$\frac{\partial \mathcal{L}}{\partial x^c} = \mu_1^T \frac{\partial f}{\partial x}\Big|_{(x=x^c)} + \mu_2^T \frac{\partial}{\partial x}\left(\frac{\partial f^T}{\partial x} w\right)\Big|_{(x=x^c)} = 0 \tag{5.12a}$$

$$\frac{\partial \mathcal{L}}{\partial \lambda^c} = -(\lambda^c - \lambda^\star)^T \beta^T + \mu_1^T \frac{\partial \mathcal{F}}{\partial \lambda} = 0 \tag{5.12b}$$

$$\frac{\partial \mathcal{L}}{\partial x^\star} = \mu_4^T \frac{\partial f}{\partial x}\Big|_{(x=x^\star)} + \gamma_2^T \frac{\partial g_2}{\partial x}\Big|_{(x=x^\star)} = 0 \tag{5.12c}$$

$$\frac{\partial \mathcal{L}}{\partial \lambda_1^\star} = (\lambda_1^c - \lambda_1^\star)^T \beta_1^T + \mu_4^T \frac{\partial \mathcal{F}}{\partial \lambda_1} + \mu_5^T \frac{\partial h}{\partial \lambda_1^\star} + \gamma_1^T \frac{\partial g_1}{\partial \lambda_1^\star} = 0 \tag{5.12d}$$

$$\frac{\partial \mathcal{L}}{\partial w} = \mu_2^T \frac{\partial f^T}{\partial x_1}\Big|_{(x=x^c)} + 2\mu_3 w^T = 0 \tag{5.12e}$$

$$\text{equality constraints (5.9b)} - \text{(5.9f)} \tag{5.12f}$$

$$\gamma_{1,j} g_{1,j}(\lambda_1^\star) = 0, \forall j = 1, ..., 2n_{\text{dr}} \tag{5.12g}$$

$$\gamma_{2,k} g_{2,k}(x^\star) = 0, \forall k = 1, ..., n_{\text{e}} \tag{5.12h}$$

$$\gamma_1 \geq 0, \quad \gamma_2 \geq 0 \tag{5.12i}$$

$$\text{inequality constraints (5.9g)} - \text{(5.9h)} \tag{5.12j}$$

As before, μ_1 equals a constant times w, i.e., $\mu_1 = \zeta_2 w$, the second term of (5.12a) is equal to zero, and $\mu_3 = 0$. Therefore, an optimal solution should satisfy the following equations:

$$\mu_4^T \frac{\partial f}{\partial x}\Big|_{(x=x^\star)} + \gamma_2^T \frac{\partial g_2}{\partial x}\Big|_{(x=x^\star)} = 0 \tag{5.13a}$$

$$-\beta(\lambda^c - \lambda^\star) - \zeta_2 w = 0 \tag{5.13b}$$

$$\beta_1(\lambda_1^c - \lambda_1^\star) + \frac{\partial \mathcal{F}^\mathcal{T}}{\partial \lambda_1}\mu_4 + \frac{\partial h^T}{\partial \lambda_1^\star}\mu_5 + \frac{\partial g_1^T}{\partial \lambda_1^\star}\gamma_1 = 0 \tag{5.13c}$$

$$\text{equality constraints (5.12f)} - \text{(5.12h)} \tag{5.13d}$$

$$\text{inequality constraints (5.12i)} - \text{(5.12j)}, \tag{5.13e}$$

where β_1 is the partition of β corresponding to λ_1. There are $5m + 5n_{\text{dr}} + n_{\text{e}} + 2$ equations and unknowns in (5.13a)-(5.13d). The solution algorithm is as follows. First, we initialize the Newton-Raphson solver to find the solution to (5.13a)-(5.13d). We check to see if the solution also satisfies (5.13e). If so, we check whether λ^c is a locally closest SNB to $\lambda^\star$ by using the iterative method of [37]. If so, then we check whether λ^c is a globally closest SNB to $\lambda^\star$ by testing different initializations within the iterative method to determine if there is a closer SNB to $\lambda^\star$ than λ^c. If we find that λ^c is the globally closest SNB then $\lambda^\star$ is the desired solution. Otherwise, we reinitialize the Newton-Raphson solver in the direction of the globally closest SNB to find a new $\lambda^\star$ and repeat the process.

In our cases studies, we compare the performance of our method to that of a brute force method. Specifically, for all possible loading patterns within a discrete mesh in which the total loading is constant, we compute the distance to the closest SNB via the method of [37]. The optimal loading pattern is the pattern associated with the maximum distance.

5.5 Case Studies

All computation is done in MATLAB and with the help of M ATPOWER [149] on an Intel(R) i7-4720HQ CPU with 16 GB of RAM. The base MVA for all cases is 100 MVA and we set $\beta = I$. The number of the inequality constraints greatly influences the computation time of our method, therefore, we neglect (5.9h) in our case studies. In each case, our initial operating points satisfy (5.9h) and we also find that the optimal solutions we obtain also satisfy (5.9h).

5.5.1 Simple 4-bus System Results

We first apply our method to the simple 4-bus system as shown in Fig. 5.2a. Bus 1 is the slack bus at a voltage of 1 pu, bus 2 is a PV bus outputting 10 MW at a voltage of 1 pu, and buses 3 and 4 are PQ buses with demand responsive loads of 30 MW and 70 MW, respectively. The reactance of the lines are $x_{13} = j0.5, x_{23} = x_{34} = j0.25$ p.u.

When λ only includes the real power injections at the PQ buses (i.e., $\lambda = [P_3;\ P_4]$), the solution is as shown in Fig. 5.1b. Specifically, the black curve is the power flow solvability boundary; the dashed blue line represents the total loading constraint, i.e., $P_3 + P_4 = -100$ MW; and the optimal loading pattern is $\lambda^\star = [-100, 0]$ MW, which maximizes the shortest distance to the boundary.

If we instead define $\lambda = [P_{2-4};\ Q_{3-4}]$, the initial distance to the closest SNB is $d = 0.0879$. The optimal solution determined by our method is $P_3^\star = -63.74$ MW and $P_4^\star = -36.26$ MW, and $d^\star = 0.1264$, which is consistent with the optimal loading pattern obtained via the brute force method, as shown in Fig. 5.2b.

5.5.2 IEEE 9-bus System Results

We next evaluate our method using the IEEE 9-bus system using the data available in MATPOWER [149]. The system has 1 slack bus (bus 1), 2 PV buses (buses 2 and 3), and 6 PQ buses (buses 4-9). We model the entire load at buses 5, 7 and 9 (315 MW) as demand responsive. Hence, the system parameter vector is $\lambda = [P_{2-9}; Q_{4-9}]$ and the controlled power injections are $\lambda_1^\star = [P_5^\star; P_7^\star; P_9^\star; Q_5^\star; Q_7^\star; Q_9^\star]$. We assume the system is initially operating at the operating point given within MATPOWER (see Table 5.3, λ^0).

The optimal solution obtained by our method is given in Table 5.3. The corresponding maximum distance is $d_\beta^\star = 1.6263$, the optimal loading pattern is $P_5 = -108.42$ MW, $P_7 =$

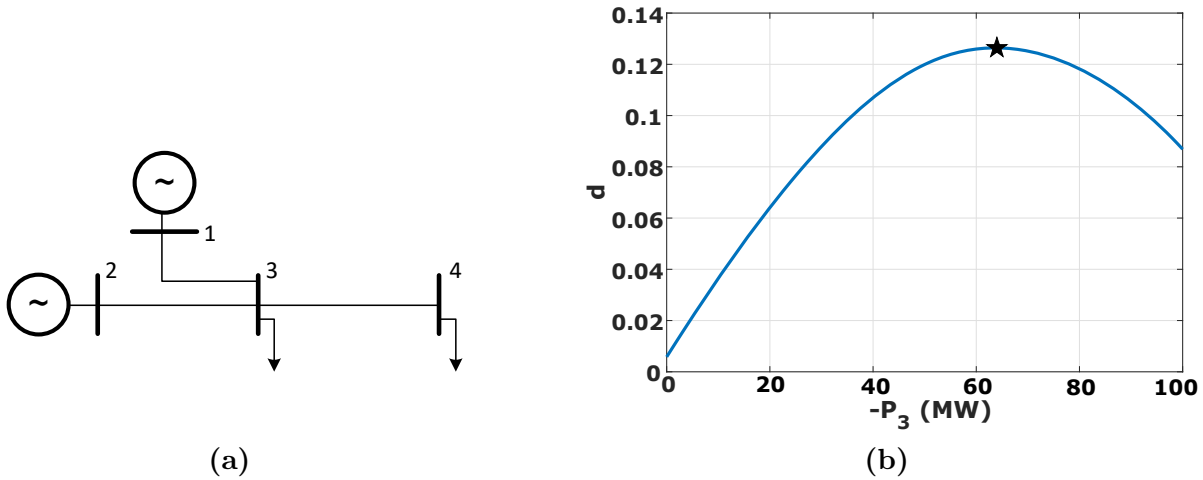

(a) (b)

Figure 5.2: (a) Single line diagram for the 4-bus system. (b) The distance to the closest SNB as a function of P_3.

-73.86 MW, and $P_9 = -132.72$ MW. To verify the results, we compare the solution of our method to that of the brute force method. We use 5000 different directions as initializations of the iterative method of [37] to find locally closest SNB to $\lambda^\star$ and then determine the globally closest SNB. Figure 5.3 shows the distance to the closest SNB as a function of P_5 and P_7 (where $P_9 = -315 - P_5 - P_7$ since the total loading must be constant). The triangle represents the maximum distance obtained by the brute force method: $P_5 = -108$ MW, $P_7 = -74$ MW, $P_9 = -133$ MW and $d = 1.6263$, which is consistent with the solution of our method. There exist discontinuities on the surface in Fig. 5.3 because the feasibility boundary is very likely a folded hypersurface, so the distance is not continuous.

We have verified that λ^c is a locally closest SNB to $\lambda^\star$ but we cannot guarantee that this SNB is the globally closest SNB since the brute force method only explores 5000 random directions. Recently, [143] proposed a new enumeration search strategy to identify multiple local minima to a related optimization problem. Applying this strategy to (5.4), we obtain a closer λ^c to our $\lambda^\star$ with a distance $d = 0.1718$. This solution satisfies the KKT conditions (5.7) and may be the globally closest SNB to $\lambda^\star$. The voltage magnitudes at the PQ buses and the reactive power injections at the buses with generators corresponding to this SNB (SNB 1) and the SNB that our method finds (SNB 2) are given in Table 5.1. For both, the voltage magnitudes are low and the generator reactive power injections are high; however, SNB 1 is particularly unrealistic. Our method moves the system away from the relatively realistic locally closest SNB (SNB 2) but unfortunately there is a closer SNB (SNB 1), which it does not find. This example points to one of the drawbacks of our approach: we cannot

Table 5.1: Voltage and reactive power (p.u.) at the SNBs

	V_4	V_5	V_6	V_7	V_8	V_9	Q_1	Q_2	Q_3
SNB 1	0.5618	0.1593	0.5812	0.0795	0.4969	0.3571	7.8432	8.2343	7.1842
SNB 2	0.7780	0.6907	0.9071	0.8841	0.9009	0.6946	4.9147	1.6245	1.5874

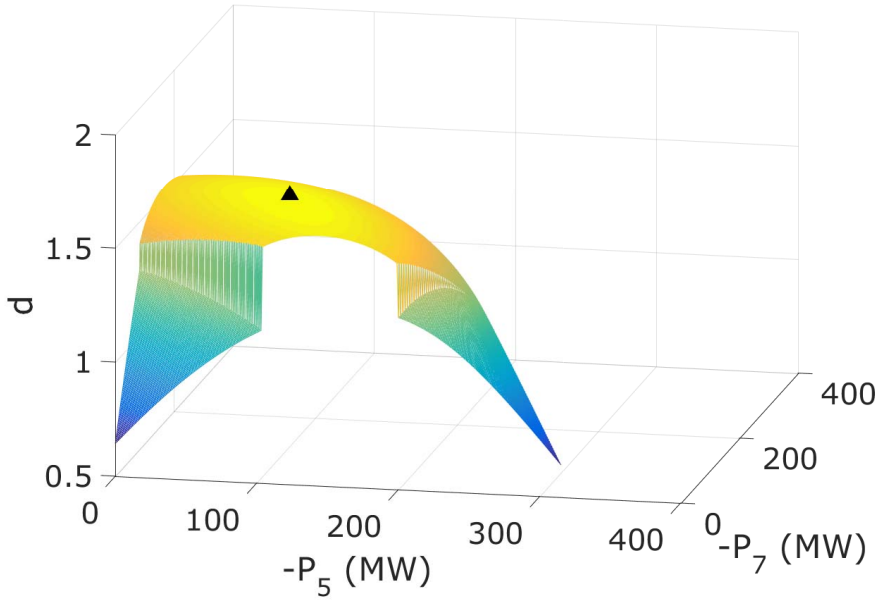

Figure 5.3: The distance to the closest SNB as a function of P_5 and P_7.

guarantee that we will find the globally closest SNB so we might push the system away from a locally closest SNB and end up closer to the globally closest SNB.

We also compared this optimal solution to those obtained using other voltage stability metrics including the smallest singular value (SSV) of the power flow Jacobian and the loading margin (LM). Table 5.2 summarizes the results. The maximum SSV and LM cases are obtained from Table 2.2. The results show that we obtain different loading patterns when maximizing different stability metrics, which is not surprising since the different margins capture different kinds of "distance to instability." The loading margin describes the distance to voltage instability for power injection changes in a single direction, while the SSV and the distance to the closest SNB do not specify the direction. The SSV of the power flow Jacobian describes the distance to the singularity of power flow Jacobian matrix, which is an indirect measure of distance. In contrast, the distance to the closest SNB is a measure of distance in the parameter (power injection) space.

Table 5.2: Optimal loading patterns for different stability metrics

	$-P_5$ (MW)	$-P_7$ (MW)	$-P_9$ (MW)	SSV –	LM (MW)	d (p.u.)
max SSV	75	167	73	0.8995	516	1.5819
max LM	97	135	83	0.8984	566	1.6033
max d	108	74	133	0.8898	408	1.6263

A disadvantage of using our method is that it relies on good initializations, whereas the iterative linear programming method used to maximize the SSV of the power flow Jacobian does not have this issue. The computation time for the 9-bus system is comparable for both approaches; however, it is not yet clear how the computational time/requirements compare for realistically-sized systems. Another disadvantage of our method is that we have no convergence guarantee, as we will show next.

Table 5.3: IEEE 9-bus System: initial and optimal power injections (p.u.)

	P_2	P_3	P_4	P_5	P_6	P_7	P_8	P_9	Q_4	Q_5	Q_6	Q_7	Q_8	Q_9
λ^0	1.6300	0.8500	0.0000	-0.9000	0.0000	-1.0000	0.0000	-1.2500	0.0000	-0.3000	0.0000	-0.3500	0.0000	-0.5000
λ^c	1.0629	0.2508	-0.1248	-1.5821	-0.6003	-1.3436	-0.5726	-1.7980	-0.2961	-0.7620	-0.0638	-0.3343	-0.0741	-0.9325
$\lambda^\star$	1.6300	0.8500	0.0000	-1.0842	0.0000	-0.7386	0.0000	-1.3272	0.0000	-0.3614	0.0000	-0.2585	0.0000	-0.5309

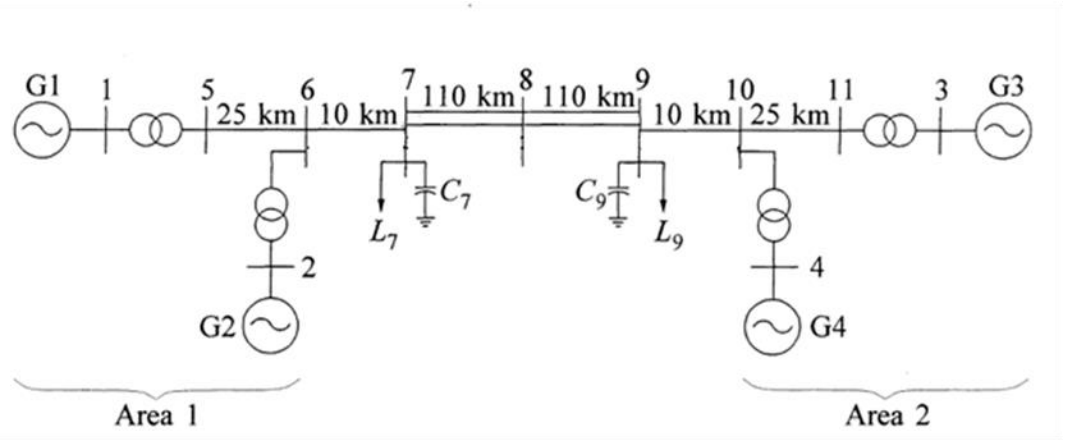

Figure 5.4: Kundur's two area 11-bus test system [70].

5.5.3 Convergence issues: Kundur's Two Area System Results

Kundur's two area system [70] has 4 generators and 2 loads, as shown in Fig. 5.4. We model the entire load at buses 7 and 9 (2134 MW) as demand responsive and set $\lambda = [P_7; P_9]$. The power flow solvability boundary is show in Fig. 5.5. The black dot is the initial operating point $\lambda^0 = [P_7; P_9] = [-967; -1767]$ MW. The shortest distance between the black dot and the boundary (i.e., the distance from the black dot to the black triangle) is $d^0 = 0.5831$. Our method first finds the solution: $\lambda^{\star,1}$ (red dot), $\lambda^{c,1}$ (red upper triangle) with $d^{\star,1} = 5.615$; however, the globally closest SNB to $\lambda^{\star,1}$ is not $\lambda^{c,1}$ but instead the SNB denoted with the red lower triangle with $d = 1.472$. Initializing the Newton-Raphson solver in the direction of the globally closest SNB to $\lambda^{\star,1}$, we find another solution $\lambda^{\star,2}$ (green dot), $\lambda^{c,2}$ (green upper triangle) with $d^{\star,2} = 10.06$. However, $\lambda^{\star,2}$ is on the solvability boundary and so we know that it is not the desired solution. In fact, neither solution is the desired solution. The desired solution is $\lambda^{\star,\text{opt}}$ (pink dot), which has the maximum shortest distance to the boundary; it can not be obtained with our method. Further research is needed to develop approaches to cope with this problem.

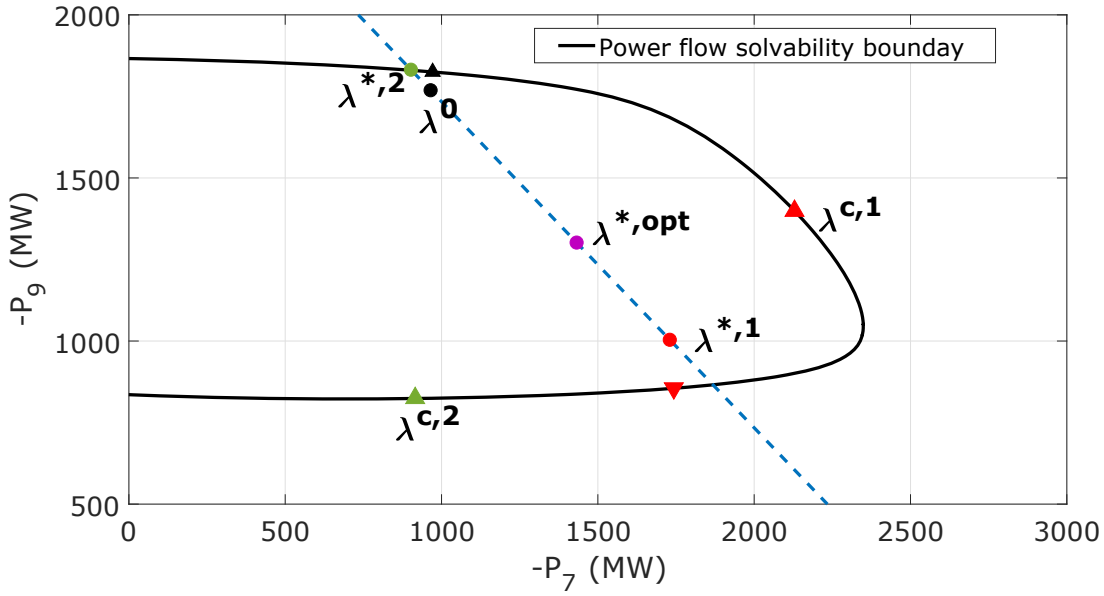

Figure 5.5: The power flow solvability boundary of the Kundur system. The blue dashed line represents the total load constant constraint.

5.6 Chapter Conclusion

In this chapter, we formulated a problem to spatially shift demand responsive load to improve static voltage stability. Specifically, we wish to increase the distance between the operating point and the point corresponding to the closest saddle-node bifurcation, which is a measure of static voltage stability. The problem was posed as a noncovex nonlinear optimization problem and solved by formulating the KKT conditions, applying the Newton-Raphson method to solve them, and checking that the solution is a local minimum. Case study results using a simple 4-bus system and the IEEE 9-bus system showed that the distance to the closest SNB is improved by demand response actions, which increase and decrease individual loads while ensuring the total load is constant. We also noted several issues with our method, specifically, we cannot guarantee that we find the globally closest SNB and, for some systems, we observe convergence issues.

In the future, we would like to develop an improved algorithm that addresses these issues, test our method on larger systems, and compare the magnitude of stability margin improvement achievable with demand response to that achievable with generator redispatch.

Chapter 6

Using DR to Shape the Fast Dynamics of the Power Network

In this chapter, demand-side strategies for shaping the fast dynamics of the bulk power transmission network are explored. The aim is to modulate the network's operating point via demand response so as to achieve desirable small-signal characteristics. The design problem is posed as an optimization problem wherein the total demand responsive load is held constant but shifted between different buses, to improve the small-signal stability. This chapter extends our preliminary work:

- K. Koorehdavoudi, M. Yao, J.L. Mathieu, and S. Roy. "Using demand response to shape the fast dynamics of the bulk power network". In: *IREP Symposium on Bulk Power System Dynamics and Control*. 2017.

6.1 Notation

Functions

$\mathcal{H}_{ij}(\cdot)$	Line flow for line (i, j)
$S_e(\cdot)$	Ceiling function
$f(\cdot)$	System dynamic equations
$g(\cdot)$	System algebraic equations
$h_{ij}(\cdot)$	Linearization of $\mathcal{H}_{ij}$

Variables & Parameters

A_e, B_e	Coefficients of ceiling function
B_{ij}	Susceptance of line ij
D_i	Damping of generator i
G_{ij}	Conductance of line ij
H_i	Inertia of generator i
K_a, K_e, K_f	Parameters of AVR
K_w	Gain of PSS
$i_{d,i}, i_{q,i}$	$d-$ and q-axis currents of generator i
l	Left eigenvalue
$p_{\mathrm{d},i}$	Real power demand at bus i
$p_{\mathrm{g},i}$	Real power generation at bus i
$q_{\mathrm{d},i}$	Reactive power demand at bus i
$q_{\mathrm{g},i}$	Reactive power generation at bus i
r	Right eigenvalue
$r_{a,i}$	Armature resistance of generator i
T_r, T_a, T_e, T_f	Time constants of AVR
T_w, T_1, T_2, T_3, T_4	Time constants of PSS
V_i	Voltage magnitude at bus i
$V_{d,i}, V_{q,i}$	$d-$ and q-axis voltages of generator i
$V_{f,i}$	Field voltages of generator i
$\tilde{V}_f$	Output signal of AVR
V_m	Voltage measured by AVR
V_{r1}, V_{r2}	Internal signals of AVR
V_{si}, V_{so}	Input and output signals of PSS
$V_w; V_p$	Internal signals of PSS
V^{ref}	Reference terminal voltage of AVR
$x'_{d,i}, x'_{q,i}$	$d-$ and q-axis transient reactances of generator i
x	Dynamic state
y	Algebraic state

Variables & Parameters (continued)

α, β	Real and imaginary parts of an eigenvalue
γ	Weighting factor
δ_i	Electrical angle of generator i
η	Damping ratio of an eigenvalue
θ_i	Voltage angle at bus i
λ	Eigenvalue of a matrix
$\psi_{d,i}$, $\psi_{q,i}$	$d-$ and $q-$axis magnetic fluxes of generator i
μ	Ratio between real and reactive power demand
ω_i	Frequency of generator i

Sets

$\mathcal{N}$	Set of all buses
$\mathcal{S}_{\text{PV}}$	Set of all PV buses
$\mathcal{S}_{\text{PQ}}$	Set of all PQ buses
$\mathcal{S}_{\text{G}}$	Set of buses with generators
$\mathcal{S}_{\text{DR}}$	Set of buses with responsive loads
$\mathcal{S}_{\text{PSS}}$	Set of generators with the PSS

6.2 Chapter Introduction

The operating point of the power network can be shaped to ensure that the network's small-signal and transient responses are desirable [138, 139]. Indeed, today's economic dispatch procedures implicitly account for transient and small-signal characteristics, by imposing a stability constraint or margin on the optimal power flow solution. These designs guarantee stability under nominal conditions as well as when any single-component fails, provided that the models for fast dynamics are accurate. However, the constraint-based solutions may not be appealing if variability in renewable generation persistently requires alteration of dispatch to maintain stability, given the possible high economic costs of modifying dispatch. Also, stability-constrained economic dispatch does not consider refined shaping of the fast dynamics (e.g., design of damping or disturbance-response properties), nor account for the dynamics of existing fast controls in the network. As shown in recent work [112], in some cases, OPF can result in operating points that may be poorly damped or even small-signal unstable.

Demand response and other load controls are becoming increasingly practical [24], provid-

ing further degrees of flexibility than generator re-dispatch. Additionally, loads may be able to respond faster and/or more cost-effectively than generators. Thus, demand-side solutions may prove useful to improve transient and small-signal characteristics at both the time of unit commitment and economic dispatch, and at shorter time horizons (e.g. 5-10 minutes) when small-signal or transient stability concerns are detected. Load reduction to reduce flows on tie-lines has been considered in [57], with the aim of improving inter-area mode damping. However, load shedding strategies will have corresponding financial and comfort impacts on consumers. To avoid this, the focus of this chapter is on load dispatch at shorter time horizons using spatial load shifting that keeps total load constant so as not to affect the system frequency. Since the total demand responsive load is constrained to be constant, the generator outputs are fixed at the results determined previously via the unit commitment and economic dispatch algorithms over the time frame of interest, with the exception of the reference generator, which compensates for the change in system losses resulting from the change in load pattern.

The process of determining the optimal dispatch of demand responsive loads is described briefly here. First, we build the mathematical models of the power system and derive the linear state-space model to assess the small-signal characteristics of the system, detailed in Section 6.3. In Section 6.4, three common stability metrics are introduced. Then, we formulate a nonlinear optimization problem with the objective to maximize a performance metric, detailed in Section 6.5. Next, we propose the solution algorithm in Section 6.6, specifically, we approximate the change of stability metrics using generalized eigenvalue sensitivities and linearize other nonlinear constraints so that we can apply iterative linear programming to obtain the optimal loading pattern that improves small-signal stability.

Our previous work [68] showed that the small-signal and transient characteristics of Kundur's two-area system are improved by shifting load from area 2 to area 1 while the total load is constant. However, we modeled the load as constant impedance in [68], resulting in the damping ratio being improved by both the change of load impedance and the load shifting instead of the load shifting only. To focus on the investigation of the effectiveness of spatial load shifting, we model the load as constant power in this chapter. In addition, in [68], we solved the optimization problem by applying iterative linear programming with the eigenvalue sensitivity of the reduced system matrix. Special numerical analysis is needed to compute the eigenvalue sensitivities, therefore, we instead use generalized eigenvalue sensitivity within the iterative linear programming in this chapter to overcome the computation complexity of eigenvalue sensitivity. Automatic voltage regulators (AVRs) and power system

stabilizers (PSSs) are also not considered in [68], but they are commonly used to enhance power system stability and damping of oscillations [27, 40] in practice, thus we also explore the possibility of using demand-side strategies when the system has AVRs and PSSs.

The main contributions of this chapter are as follows.

- We develop an iterative linear programming solution algorithm using generalized eigenvalue sensitivities to maximize a performance metric to improve the small-signal stability;
- we consider different small-signal characteristics and conduct case studies on different systems with and without AVR and PSS;
- we compare the performance of spatio-temporal load shifting to those of generation actions and load shedding; and
- we investigate the impact on voltage stability when improving the small-signal stability.

6.3 System Model

To analyze the system small-signal or transient behavior, we need dynamic models of all components of a power system. In this section, the models of transmission network, load, and generator and its excitation system are first introduced. Next, we present the linear state-space model that used to determine the eigenvalues of the system.

We consider a bulk power transmission system with n buses, labeled $1, \ldots, n$, belonging to set $\mathcal{N}$. A subset of the buses, labeled $1, \ldots, m$, belonging to set $\mathcal{S}_G$, have synchronous machines associated with them. One is modeled as a slack bus while the others are modeled as PV buses belonging to set $\mathcal{S}_{\text{PV}}$. A second subset is load-only and is modeled as PQ buses belonging to set $\mathcal{S}_{\text{PQ}}$. Of all buses $\mathcal{N}$, a portion contains demand responsive loads and belongs to set $\mathcal{S}_{\text{DR}}$.

6.3.1 Network and Load Model

The AC power flow equations [142] are used as the algebraic equations of the network. For $i \in \mathcal{N}$, we define the algebraic state associated with power balance as $\boldsymbol{y_{pf,i}} = [V_i;\ \theta_i]$, which

are the voltage magnitude and angle of bus i. The power flow balance equations are:

$$0 = V_i \sum_{j \in \mathcal{N}} V_j (G_{ij} \cos(\theta_i - \theta_j) + B_{ij} \sin(\theta_i - \theta_j)) - p_{\mathrm{g},i} + p_{\mathrm{d},i} \tag{6.1a}$$

$$0 = V_i \sum_{j \in \mathcal{N}} V_j (G_{ij} \sin(\theta_i - \theta_j) - B_{ij} \cos(\theta_i - \theta_j)) - q_{\mathrm{g},i} + q_{\mathrm{d},i} \tag{6.1b}$$

where G_{ij}, B_{ij} are the conductance and susceptance of line ij. The subscript g represents the generation and d represents the demand. For PQ buses, we have $p_{\mathrm{g}} = q_{\mathrm{g}} = 0$. We neglect the dynamics and voltage dependence etc. of loads in this chapter, but these can be easily included in the future. All loads are modeled as constant power load with real and reactive power demand as p_{d} and q_{d}.

6.3.2 Synchronous Machine Model

The classical model [88] of synchronous machine is used. For $k \in \mathcal{S}_G$, we define the dynamic state vector as $\boldsymbol{x_{G,k}} = [\delta_k;\ \omega_k]$, and algebraic state vector as $\boldsymbol{y_{G,k}} = [i_{d,k};\ i_{q,k};\ V_{d,k};\ V_{q,k};\ p_{\mathrm{g},k};\ q_{\mathrm{g},k};\ \psi_{d,k};\ \psi_{q,k};\ V_{f,k}]$, where δ_k is the rotor angle; ω_k is the rotor frequency; $i_{d,k},\ i_{q,k}$ are the $d-$ and $q-$axis currents; $V_{d,k},\ V_{q,k}$ are the $d-$ and $q-$axis voltages; $p_{\mathrm{g},k},\ q_{\mathrm{g},k}$ are the real and reactive power generation; $\psi_{d,k},\ \psi_{q,k}$ are the $d-$ and $q-$axis magnetic fluxes; and $V_{f,k}$ is the field voltage.

Mechanical differential equations are:

$$\dot{\delta}_k = \omega_k \tag{6.2a}$$

$$\dot{\omega}_k = \frac{1}{2H_k} \left(P_{m,k} - (\psi_{d,k} i_{q,k} - \psi_{q,k} i_{d,k}) - D_k \omega_k\right) \tag{6.2b}$$

Algebraic equations are:

$$0 = V_k \sin(\delta_k - \theta_k) - V_{d,k} \tag{6.3a}$$

$$0 = V_k \cos(\delta_k - \theta_k) - V_{q,k} \tag{6.3b}$$

$$0 = V_{d,k} i_{d,k} + V_{q,k} i_{q,k} - p_{\mathrm{g},k} \tag{6.3c}$$

$$0 = V_{q,k} i_{d,k} - V_{d,k} i_{q,k} - q_{\mathrm{g},k} \tag{6.3d}$$

$$0 = \psi_{d,k} + r_a i_{q,k} + x'_{d,k} i_{d,k} - V_{f,k} \tag{6.3e}$$

$$0 = \psi_{q,k} + x'_{q,k} i_{q,k} \tag{6.3f}$$

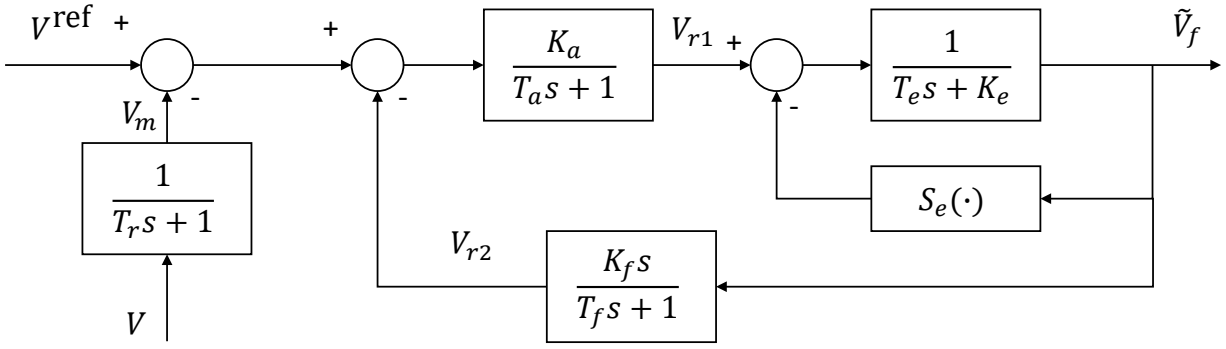

Figure 6.1: Automatic voltage regulator control diagram [88].

$$0 = -\psi_{d,k} + V_{q,k} + r_{a,k} i_{q,k} \tag{6.3g}$$

$$0 = \psi_{q,k} + V_{d,k} + r_{a,k} i_{d,k} \tag{6.3h}$$

$$0 = V_{f,k} - V_{f,k}^0 \tag{6.3i}$$

where H_k, D_k, $r_{a,k}$, $x'_{d,k}$, and $x'_{q,k}$ are the inertia constant, damping coefficient, armature resistance, d-axis transient reactance, and q-axis transient reactance of the k-th generator. The quantity $P_{m,k}$ is the mechanical power input and $V_{f,k}^0$ is the setpoint of the field voltage. Park's transformation converts the original three-phase frames of reference into a dq frame in which the new variables for voltages, currents, and fluxes can be viewed as space vectors. The link between the terminal voltage phasor $V\angle\theta$ and machine voltages V_d, V_q is shown in (6.3a) and (6.3b). The real and reactive power injections are functions of currents and voltages in the dq frame as shown in (6.3c) and (6.3d). The rest show the relationships between fluxes and voltages and currents.

6.3.3 Automatic Voltage Regulator Model

An Automatic Voltage Regulator (AVR) is used to realize primary voltage control. The control diagram of an AVR is shown in Fig. 6.1. We assume each synchronous machine has one AVR connected. For $k \in \mathcal{S}_G$, we define the dynamic state vector of the AVR as $\boldsymbol{x_{R,k}} = [V_{m,k};\ V_{r1,k}; V_{r2,k}; \tilde{V}_{f,k};]$, where $V_{m,k}$ is the measured voltage, $V_{r1,k}$ and $V_{r2,k}$ are the internal signals, and $\tilde{V}_{f,k}$ is the AVR output signal to the machine; the algebraic state only includes $\boldsymbol{y_{R,k}} = [V_k^{\text{ref}}]$, where V_k^{ref} is the reference terminal voltage. Based on the control

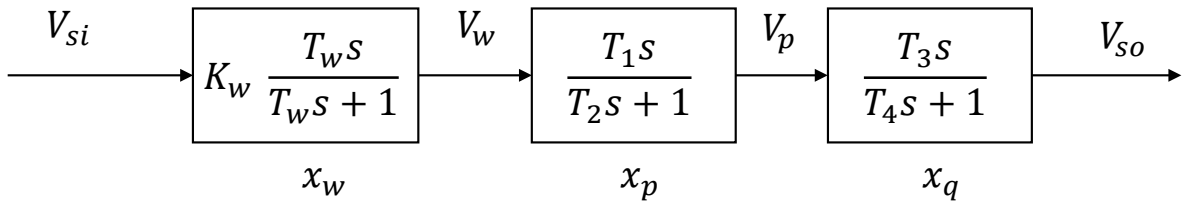

Figure 6.2: Power system stabilizer control diagram [70].

diagram, we can write the differential equations as follows:

$$\dot{V}_{m,k} = \frac{1}{T_{r,k}}(V_k - V_{m,k}) \tag{6.4a}$$

$$\dot{V}_{r1,k} = \frac{1}{T_{a,k}}(K_{a,k}(V_k^{\text{ref}} - V_{m,k} - V_{r2,k}) - V_{r1,k}) \tag{6.4b}$$

$$\dot{\tilde{V}}_{f,k} = \frac{1}{T_{e,k}}(V_{r1,k} - K_{e,k}\tilde{V}_{f,k} - S_e(\tilde{V}_{f,k})) \tag{6.4c}$$

$$\dot{V}_{r2,k} = \frac{1}{T_{f,k}}(K_{f,k}\dot{\tilde{V}}_{f,k} - V_{r2,k}) = \frac{1}{T_{f,k}}\left(\frac{K_{f,k}}{T_{e,k}}(V_{r1,k} - K_{e,k}\tilde{V}_{f,k} - S_e(\tilde{V}_{f,k})) - V_{r2,k}\right) \tag{6.4d}$$

where $T_{r,k}$, $T_{a,k}$, $T_{e,k}$, $T_{f,k}$ are time constants and $K_{a,k}$, $K_{e,k}$, $K_{f,k}$ are AVR parameters. The ceiling function S_e is defined as $S_e(\tilde{V}_{f,k})) = A_{e,k}e^{B_{e,k}|\tilde{V}_{f,k}|}$, where A_e and B_e are the ceiling coefficients.

When a machine has an AVR, $V_{f,k}$ in (6.3i) is set to be equal to the output of the AVR; therefore, (6.3i) is modified to be

$$0 = \tilde{V}_{f,k} - V_{f,k}; \tag{6.5}$$

we have another algebraic equation:

$$0 = V_k^{\text{ref}} - V_k^{\text{ref0}} \tag{6.6}$$

where V_k^{ref0} is the setpoint value of the regulated generator voltage magnitude.

6.3.4 Power System Stabilizer Model

A Power System Stabilizer (PSS) is used to add damping to the generator rotor oscillations. The first block serves as a high-pass filter and the following two blocks are phase compensators. Figure 6.2 shows a typical control diagram of a PSS. For machine k that has the PSS ($k \in \mathcal{S}_{\text{PSS}}$), we define its dynamic state as $\boldsymbol{x_{S,k}} = [x_{w,k};\ x_{p,k};\ x_{q,k}]$, which are the internal

states for each block; the algebraic state is defined as $\boldsymbol{y_{S,k}} = [V_{si,k};\ V_{so,k};\ V_w;\ V_{p,k}]$, where $V_{si,k}$, $V_{so,k}$ are the input and output signals of the PSS, and $V_w, V_{p,k}$ are internal signals.

The differential equations are:

$$\dot{x}_{w,k} = \frac{1}{T_{w,k}} V_{w,k} \tag{6.7a}$$

$$\dot{x}_{p,k} = V_{w,k} - V_{p,k} \tag{6.7b}$$

$$\dot{x}_{q,k} = V_{p,k} - V_{so,k} \tag{6.7c}$$

The algebraic equations are:

$$0 = V_{si,k} - K_{w,k}\omega \tag{6.8a}$$

$$0 = V_{si,k} - V_{w,k} - x_{w,k} \tag{6.8b}$$

$$0 = V_{p,k}T_{2,k} - V_{w,k}T_{1,k} - x_{p,k} \tag{6.8c}$$

$$0 = V_{so,k}T_{4,k} - V_{p,k}T_{3,k} - x_{q,k} \tag{6.8d}$$

where $T_{w,k}$, $T_{1,k}$, $T_{2,k}$, $T_{3,k}$, and $T_{4,k}$ are time constants and $K_{w,k}$ is the gain of the stabilizer.

The output signal $V_{so,k}$ of the PSS is a signal that modifies the reference voltage V^{ref} of the AVR, and as a result, (6.6) becomes

$$0 = V_k^{\text{ref0}} - V_k^{\text{ref}} + V_{so,k} \tag{6.9}$$

6.3.5 Linear State-space Model

A power system can be described as a set of non-linear differential algebraic equations:

$$\begin{cases} \dot{\boldsymbol{x}} = f(\boldsymbol{x}, \boldsymbol{y}) \\ 0 = g(\boldsymbol{x}, \boldsymbol{y}) \end{cases} \tag{6.10}$$

When system models are different, the states and equations of (6.10) will be different. Table 6.1 summarizes the states and equations for the systems with and without AVRs and PSSs. When the system has no AVR and PSS, the state vector $\boldsymbol{x} = [\boldsymbol{x_{G,k\in\mathcal{S}_G}}]$, the algebraic vector $\boldsymbol{y} = [\boldsymbol{y_{pf,i\in\mathcal{N}}};\ \boldsymbol{y_{G,k\in\mathcal{S}_G}}]$. Function f only includes the mechanical differential equations of the machines (6.2) and function g includes (6.1), and (6.3). When the system has AVRs and PSSs, the state vector $\boldsymbol{x} = [\boldsymbol{x_{G,k\in\mathcal{S}_G}};\ \boldsymbol{x_{R,k\in\mathcal{S}_G}};\ \boldsymbol{x_{S,l\in\mathcal{S}_{PSS}}}]$, the algebraic vector

Table 6.1: Summary of the state-space model without and with AVR and PSS

	without	with
f	(6.2)	(6.2), (6.4), (6.7)
g	(6.1), (6.3)	(6.1), (6.3a)-(6.3h), (6.5), (6.6), (6.8), (6.9)
$\boldsymbol{x}$	$\boldsymbol{x_{G,k\in\mathcal{S}_G}}$	$\boldsymbol{x_{G,k\in\mathcal{S}_G}}$, $\boldsymbol{x_{R,k\in\mathcal{S}_G}}$, $\boldsymbol{x_{S,l\in\mathcal{S}_{PSS}}}$
$\boldsymbol{y}$	$\boldsymbol{y_{pf,i\in\mathcal{N}}}$, $\boldsymbol{y_{G,k\in\mathcal{S}_G}}$	$\boldsymbol{y_{pf,i\in\mathcal{N}}}$, $\boldsymbol{y_{G,k\in\mathcal{S}_G}}$, $\boldsymbol{y_{R,k\in\mathcal{S}_G}}$, $\boldsymbol{y_{S,l\in\mathcal{S}_{PSS}}}$

$\boldsymbol{y} = [\boldsymbol{y_{pf,i\in\mathcal{N}}};\ \boldsymbol{y_{G,k\in\mathcal{S}_G}};\ \boldsymbol{y_{R,k\in\mathcal{S}_G}};\ \boldsymbol{y_{S,l\in\mathcal{S}_{PSS}}}]$. Function f combines the differential equations (6.2), (6.4), and (6.7); function g combines the algebraic equations (6.1), (6.3a)-(6.3h), (6.5), (6.6), (6.8) and (6.9).

Linearizing the nonlinear equations around an operating point yields the following model:

$$\begin{bmatrix} \dot{\Delta}x \\ 0 \end{bmatrix} = \underbrace{\begin{bmatrix} f_x & f_y \\ g_x & g_y \end{bmatrix}}_{A} \begin{bmatrix} \Delta x \\ \Delta y \end{bmatrix} \tag{6.11}$$

where f_x, f_y, g_x, and g_y are the partial derivatives $\dfrac{\partial f}{\partial x}$, $\dfrac{\partial f}{\partial y}$, $\dfrac{\partial g}{\partial x}$, and $\dfrac{\partial g}{\partial y}$ respectively. Define $B = \begin{bmatrix} I & 0 \\ 0 & 0 \end{bmatrix}$, (6.11) can be rewritten as

$$B \begin{bmatrix} \dot{\Delta}x \\ \dot{\Delta}y \end{bmatrix} = A \begin{bmatrix} \Delta x \\ \Delta y \end{bmatrix} \tag{6.12}$$

We are interested in designing the small-signal characteristics of the power system, which are based on the finite eigenvalues of the general eigenvalue problem (A, B).

6.4 Stability Metrics

The attenuation of small disturbances, whether impulsive or persistent, is one natural metric for the network's dynamic performance. The damping of the network is one measure of disturbance attenuation and considered in this chapter. The smallest damping ratio (SDR) is one of the common indices used in literature, $\eta_S = \min\left(-\alpha/\sqrt{\alpha^2+\beta^2}\right)$, where α and β are the real part and imaginary part of λ, which are the finite eigenvalues of the generalized eigenvalue problem (A, B). Another common index is the damping of the critical inter-area

mode, $\eta_I = -\alpha_I/\sqrt{\alpha_I^2 + \beta_I^2}$, where α_I and β_I are the real part and imaginary part of the eigenvalue of the critical inter-area mode (electromechnical oscillations in the range of less than 1 Hz). It is worth noting that congestion or stress in the power network sometimes promotes low-frequency wide-area responses (i.e., the network becomes more "springy"), which may not always be directly related to the damping ratio.

Similar to the distance to the closest SNB, the distance to the Hopf bifurcation could also be used to measure the small-signal stability, which is known as the oscillatory stability margin [48, 81]. Alternatively, we could use the largest of the real parts of the eigenvalues ($\alpha_1 = \max(\alpha)$) [82] to approximate the distance to the small-signal stability boundary.

The transient stability margin of the system is another natural performance measure for the fast dynamics of the power network. Several specific definitions have been proposed for the transient stability margin, including the distance from the operating point to the boundary of the region of attraction [133], the power-transfer limit, and the critical fault clearing time for a specified set of contingencies [148]. However, each of these metrics is rather difficult to compute, which makes the optimization of a transient stability metric challenging. For this reason, the transient stability margin is not considered further in this work.

6.5 Optimization Formulation

In this section, we present the formulation of load dispatch optimization problem to maximize the stability metric. Although the loading pattern $\boldsymbol{p_d}$ does not appear explicitly in the system matrix A, any re-dispatch of $\boldsymbol{p_d}$ will change the operating point at which the system is evaluated and thus affect the system matrix A as well as its eigenvalues. The full optimization problem is:

$$\max \quad \gamma_1\eta_S + \gamma_2\eta_I - \gamma_3\alpha_1 \ \text{ subject to} \tag{6.13a}$$

$$\eta_S = \min\left(\frac{-\alpha}{\sqrt{\alpha^2+\beta^2}}\right) \tag{6.13b}$$

$$\eta_I = \frac{-\alpha_I}{\sqrt{\alpha_I^2+\beta_I^2}} \tag{6.13c}$$

$$\alpha_1 = \max(\alpha) \tag{6.13d}$$

$$\alpha_I = \mathrm{Re}\{\lambda_I\} \tag{6.13e}$$

$$\beta_I = \mathrm{Im}\{\lambda_I\} \tag{6.13f}$$

$$\alpha = \mathrm{Re}\{\lambda\} \tag{6.13g}$$

$$\beta = \mathrm{Im}\{\lambda\} \tag{6.13h}$$

$$\lambda = \mathrm{eig}(A, B) \tag{6.13i}$$

$$A = \begin{bmatrix} f_x & f_y \\ g_x & g_y \end{bmatrix}, B = \begin{bmatrix} I & 0 \\ 0 & 0 \end{bmatrix} \tag{6.13j}$$

$$g(\boldsymbol{x}, \boldsymbol{y}) = 0 \tag{6.13k}$$

$$\sum_{i \in \mathcal{S}_{\mathrm{DR}}} p_{\mathrm{d},i} = \sum_{i \in \mathcal{S}_{\mathrm{DR}}} p^0_{\mathrm{d},i} \tag{6.13l}$$

$$\mu_i p_{\mathrm{d},i} = q_{\mathrm{d},i} \qquad \forall i \in \mathcal{N} \tag{6.13m}$$

$$p_{\mathrm{d},i} = p^0_{\mathrm{d},i} \qquad \forall i \in \mathcal{N} \setminus \mathcal{S}_{\mathrm{DR}} \tag{6.13n}$$

$$p_{\mathrm{g},i} = p^0_{\mathrm{g},i} \qquad \forall i \in \mathcal{S}_{\mathrm{PV}} \tag{6.13o}$$

$$V_i = V^0_i \qquad \forall i \in \mathcal{S}_{\mathrm{G}} \tag{6.13p}$$

$$\theta_{\mathrm{slack}} = 0 \tag{6.13q}$$

$$\mathcal{H}_{ij}(\boldsymbol{\theta}, \boldsymbol{V}) \leq \overline{\mathcal{H}}_{ij} \tag{6.13r}$$

$$\mathcal{H}_{ji}(\boldsymbol{\theta}, \boldsymbol{V}) \leq \overline{\mathcal{H}}_{ji} \tag{6.13s}$$

$$\underline{p}_{\mathrm{g,slack}} \leq p_{\mathrm{g,slack}} \leq \overline{p}_{\mathrm{g,slack}} \tag{6.13t}$$

$$\underline{q}_{\mathrm{g},i} \leq q_{\mathrm{g},i} \leq \overline{q}_{\mathrm{g},i} \qquad \forall i \in \mathcal{S}_G \tag{6.13u}$$

$$\underline{p}_{\mathrm{d},i} \leq p_{\mathrm{d},i} \leq \overline{p}_{\mathrm{d},i} \qquad \forall i \in \mathcal{S}_{\mathrm{DR}} \tag{6.13v}$$

$$\underline{q}_{\mathrm{d},i} \leq q_{\mathrm{d},i} \leq \overline{q}_{\mathrm{d},i} \qquad \forall i \in \mathcal{S}_{\mathrm{DR}} \tag{6.13w}$$

$$\underline{V}_i \leq V_i \leq \overline{V}_i \qquad \forall i \in \mathcal{N} \tag{6.13x}$$

The objective is to maximize a performance metric, which is a linear combination of the smallest damping ratio, the damping of critical inter-area mode, and the maximum real part of all eigenvalues; and γ_1, γ_2, and γ_3 are the weighting factors. Constraints (6.13b)-(6.13j) define η_S as the smallest damping ratio of the generator modes, η_I as the damping of critical inter-area mode (λ_I), and α_1 as the maximum real part. Constraint (6.13k) includes all algebraic equations. Note that (6.13j) and (6.13k) will be different for the systems with or without AVRs and PSSs, details can be found in Table 6.1. The assumption of the total loading remaining constant is given in (6.13l). Superscript '0' denotes the nominal value. Constraint (6.13m) models loads as constant power factor loads and (6.13n)-(6.13q) fix the

real power demand of inflexible loads, the real power generation of all PV buses , the voltage magnitudes of buses with generators, and the voltage angle of the slack bus to their nominal values. The remaining constraints are engineering concerns, including the line flow, real and reactive generation, demand responsive load flexibility, and voltage magnitude limits.

6.6 Solution Algorithm

The optimization problem (6.13) is challenging due to the non-linear, non-convex constraints. To solve this problem, we again take advantage of using *iterative linear programming*. The process works as follows. At each iteration, we first linearize the cost and each of the nonlinear constraints at the current operating point. We harness the generalized eigenvalue sensitivity to approximate $\Delta\eta_S$, $\Delta\eta_I$, and $\Delta\alpha_1$. Then we solve the resulting linear program (6.17), where the new decision variables are the *changes* in the original decision variables ($\boldsymbol{\Delta p_g}, \boldsymbol{\Delta q_g}, \boldsymbol{\Delta p_d}, \boldsymbol{\Delta q_d}$). We bound the changes because the linearization is only valid in a small region around the original operating point. This yields an estimate of the solution for the original nonlinear program. For this solution estimate, the new operating point is computed by solving the AC power flow equations. The process is then iterated: i.e., the nonlinear program is re-linearized around the new operating point to obtain a linear program, and this linear program is solved to get another estimate of the solution. The algorithm is continued until the solution estimate converges, either to the global optimal solution of the nonlinear problem or at least a local maxima. In this section, we first introduce the generalized eigenvalue sensitivity and then present the formulation of the linear optimization problem that we solved at each iteration.

6.6.1 Generalized Eigenvalue Sensitivity

For any system state χ that matrices A and B depend on, the derivative of λ with respect to χ can be found as:

$$\frac{\partial \lambda}{\partial \chi} = \frac{l^T(\frac{\partial A}{\partial \chi} - \lambda \frac{\partial B}{\partial \chi})r}{l^T B r} \tag{6.14}$$

where r and l are the corresponding right and left eigenvectors. This formula is utilized to deign the HVDC damping controllers in [117], and FACTS devices in [60]. Here, $\dfrac{\partial B}{\partial \chi} = 0$,

the generalized eigenvalue sensitivity formulation is presented as:

$$\frac{\partial \lambda}{\partial \chi} = \frac{l^T \frac{\partial A}{\partial \chi} r}{l^T B r} \tag{6.15}$$

and so we can approximate the change in λ around current steady-state values (x^*, y^*) as:

$$\Delta\lambda = \sum_i \left. \frac{l^T \frac{\partial A}{\partial x_i} r}{l^T B r} \right|_{(x^*,y^*)} \Delta x_i + \sum_j \left. \frac{l^T \frac{\partial A}{\partial y_j} r}{l^T B r} \right|_{(x^*,y^*)} \Delta y_j \tag{6.16}$$

Note that x, y will be different for different system models, see Table 6.1 for the details.

Because there exist infinite eigenvalues when solving the general eigenvalue problem (A, B), the modes of the generators are generally obtained via eliminating Δy and computing the eigenvalue of a reduced linear matrix $A^\star$, where $A^\star = f_x - f_y(g_y)^{-1} g_x$. The eigenvalue sensitivity of matrix $A^\star$ is widely used for power system small-signal stability analysis [31, 57], which we also used in [68]. But special numerical procedures are need to be implemented to obtain $\dfrac{\partial A^\star}{\partial \chi}$ and to compute the eigenvalue sensitivity, resulting in a significant increase in computations for large systems. In contrast, the generalized eigenvalue sensitivity can be obtained through analytic analysis. In [83, 85, 86], the electromechanical modes without AVR and PSS are obtained through solving a quadratic eigenvalue problem. The eigenvalue sensitivity formulation is different than the generalized eigenvalue sensitivity, but the computation complexity is the same. Moreover, the method used in [83, 85, 86] requires the system to be lossless and only allows the reactive power of load modelling to be voltage magnitude depended; however, the generalized eigenvalue sensitivity method has no limit on the system models.

6.6.2 Linear Program Solved at Each Iteration

The linear program to be solved during each step of the iterative linear programming algorithm is as follows:

$$\max \quad \gamma_1 \Delta\eta_S + \gamma_2 \Delta\eta_I - \gamma_3 \Delta\alpha_1 \quad \text{subject to} \tag{6.17a}$$

$$\Delta\eta_S = \frac{(-\beta_S^2 \Delta\alpha_S + \alpha_S \beta_S \Delta\beta_S)}{(\alpha_S^2 + \beta_S^2)^{\frac{3}{2}}} \tag{6.17b}$$

$$\Delta\eta_I = \frac{(-\beta_I^2 \Delta\alpha_I + \alpha_I \beta_I \Delta\beta_I)}{(\alpha_I^2 + \beta_I^2)^{\frac{3}{2}}} \tag{6.17c}$$

$$\Delta\lambda_S = \sum_i \frac{l_S^T \frac{\partial A}{\partial x_i} r_S}{l_S^T B r_S} \Delta x_i + \sum_j \frac{l_S^T \frac{\partial A}{\partial y_j} r_S}{l_S^T B r_S} \Delta y_j \tag{6.17d}$$

$$\Delta\lambda_I = \sum_i \frac{l_I^T \frac{\partial A}{\partial x_i} r_I}{l_I^T B r_I} \Delta x_i + \sum_j \frac{l_I^T \frac{\partial A}{\partial y_j} r_I}{l_I^T B r_I} \Delta y_j \tag{6.17e}$$

$$\Delta\lambda_1 = \sum_i \frac{l_1^T \frac{\partial A}{\partial x_i} r_1}{l_1^T B r_1} \Delta x_i + \sum_j \frac{l_1^T \frac{\partial A}{\partial y_j} r_1}{l_1^T B r_1} \Delta y_j \tag{6.17f}$$

$$\Delta\alpha_S = \mathrm{Re}\{\Delta\lambda_S\} \tag{6.17g}$$

$$\Delta\beta_S = \mathrm{Im}\{\Delta\lambda_S\} \tag{6.17h}$$

$$\Delta\alpha_I = \mathrm{Re}\{\Delta\lambda_I\} \tag{6.17i}$$

$$\Delta\beta_I = \mathrm{Im}\{\Delta\lambda_I\} \tag{6.17j}$$

$$\Delta\alpha_1 = \mathrm{Re}\{\Delta\lambda_1\} \tag{6.17k}$$

$$\sum_i \frac{\partial g}{\partial x_i} \Delta x_i + \sum_j \frac{\partial g}{\partial y_i} \Delta y_j = 0 \tag{6.17l}$$

$$\sum_{i \in \mathcal{S}_{\mathrm{DR}}} \Delta p_{\mathrm{d},i} = 0 \tag{6.17m}$$

$$\mu_i \Delta p_{\mathrm{d},i} = \Delta q_{\mathrm{d},i} \qquad \forall i \in \mathcal{N} \tag{6.17n}$$

$$\Delta p_{\mathrm{d},i} = 0 \qquad \forall i \in \mathcal{N} \setminus \mathcal{S}_{\mathrm{DR}} \tag{6.17o}$$

$$\Delta p_{\mathrm{g},i} = 0 \qquad \forall i \in \mathcal{S}_{\mathrm{PV}} \tag{6.17p}$$

$$\Delta V_i = 0 \qquad \forall i \in \mathcal{S}_{\mathrm{G}} \tag{6.17q}$$

$$\Delta\theta_{\mathrm{slack}} = 0 \tag{6.17r}$$

$$h_{ij}(\boldsymbol{\Delta\theta}, \boldsymbol{\Delta V}) \leq \overline{h}_{ij} \tag{6.17s}$$

$$h_{ji}(\boldsymbol{\Delta\theta}, \boldsymbol{\Delta V}) \leq \overline{h}_{ji} \tag{6.17t}$$

$$\underline{p}_{\mathrm{g,slack}} \leq p^*_{\mathrm{g,slack}} + \Delta p_{\mathrm{g,slack}} \leq \overline{p}_{\mathrm{g,slack}} \tag{6.17u}$$

$$\underline{q}_{\mathrm{g},i} \leq q^*_{\mathrm{g},i} + \Delta q_{\mathrm{g},i} \leq \overline{q}_{\mathrm{g},i} \qquad \forall i \in \mathcal{S}_G \tag{6.17v}$$

$$\underline{p}_{\mathrm{d},i} \leq p^*_{\mathrm{d},i} + \Delta p_{\mathrm{d},i} \leq \overline{p}_{\mathrm{d},i} \qquad \forall i \in \mathcal{S}_{\mathrm{DR}} \tag{6.17w}$$

$$\underline{q}_{\mathrm{d},i} \leq q^*_{\mathrm{d},i} + \Delta q_{\mathrm{d},i} \leq \overline{q}_{\mathrm{d},i} \qquad \forall i \in \mathcal{S}_{\mathrm{DR}} \tag{6.17x}$$

$$\underline{V}_i \leq V_i^* + \Delta V_i \leq \overline{V}_i \qquad \forall i \in \mathcal{N} \tag{6.17y}$$

$$\underline{\Delta} \leq \Delta\alpha_S, \Delta\beta_S, \Delta\alpha_I, \Delta\beta_I, \Delta\alpha_1 \leq \overline{\Delta} \tag{6.17z}$$

where λ_S is the generator mode with the smallest damping ratio, λ_I is the critical inter-area mode, and λ_1 is the generator mode with the largest real part; r_s, l_s are the right and left eigenvectors corresponding to λ_S; r_I, l_I are the right and left eigenvectors corresponding to λ_I; r_1, l_1 are the right and left eigenvectors corresponding to λ_1. Constraints (6.17b) - (6.17k) represent the sensitivities of these stability metrics. Constraints (6.17l) - (6.17y) are the linearization of (6.13k) - (6.13x); superscript '*' denotes the current operating point. To ensure the accuracy of the linearization, (6.17z) is added to limit the step size of the change of the stability metrics, where $\underline{\Delta}$ and $\overline{\Delta}$ are user-chosen parameters.

After solving the linear problem, we will update $(\boldsymbol{p}_{\mathbf{g}}^*, \boldsymbol{q}_{\mathbf{g}}^*, \boldsymbol{p}_{\mathbf{d}}^*, \boldsymbol{q}_{\mathbf{d}}^*)$ with the optimal change $(\boldsymbol{\Delta p}_{\mathbf{g}}^*, \boldsymbol{\Delta q}_{\mathbf{g}}^*, \boldsymbol{\Delta p}_{\mathbf{d}}^*, \boldsymbol{\Delta q}_{\mathbf{d}}^*)$. It is possible that when we change the loading pattern to improve the damping of the most critical mode, it has negative effect on the damping of another mode, to the extent that the latter becomes the most critical. Therefore, the new stability metrics $(\eta_S, \eta_I, \alpha_1)$ and eigenvalues $(\lambda_S, \lambda_I, \lambda_1)$ are re-computed at the new operating point. The algorithm is terminated when the absolute value of the objective function in (6.17a) goes below a small threshold (here, we use 10^{-4}).

6.7 Case Studies

In this section, we apply the iterative algorithm to Kundur's two area system, the 39-bus New England system, and the 14-bus system. Table 6.2 shows the models and stability metrics we consider in each system. AVRs and PSSs are not included in the first two systems; in the 14-bus system, we will consider two cases: with and without AVRs and PSSs. The main purposes of testing on each system are also summarized in the table. The purposes of the case studies conducted on Kundur's system are: 1) to correct the results in [68] with constant power load model and investigate the performance of spatial load shifting; 2) to compare the optimal loading patterns with different stability metrics. Since Kundur's system is small and only has two load buses, a larger system, the 39-bus system, is then used to test the scalability of our iterative algorithm. Using the 14-bus system, we compare the optimal loading patterns with and without AVR and PSS. For all three systems, we compare the improvement of the SDR achieved by DR actions with that achieved by generation actions. For the 14-bus system, we also compare the performance of cases with the real power demand of flexible loads controlled, the reactive power demand controlled, and both controlled. Moreover, we investigate the minimum load shedding needed to achieve the same SDR improvement as obtained by spatial load shifting. Finally, the impact on the voltage

Table 6.2: System model, stability metric, and main purpose of each case study

System	AVR/PSS	Stability Metric	Main Purpose
Kundur	without	η_S, η_I, α_1	Correction of the results in [68] Comparison of different metrics
39-bus	without	η_S	Scalability
14-bus	without and with	η_S	Comparison of different models

Table 6.3: Power flow solution of the nominal Kundur's two area system

Bus	P (MW)	Q (MVar)	V (p.u.)
1	709	132	1.030
2	700	102	1.010
3	719	63	1.030
4	700	-69	1.010
7	-967	-100	1.000
9	-1767	-100	1.051

stability when we improve the small-signal stability is explored.

6.7.1 Kundur's Two-Area System Results

We first apply the iterative algorithm to Kundur's two-area 11-bus test system shown in Fig. 5.4. The power flow solution for the nominal system is shown in Table 6.3. We choose generator 1 as the reference generator. The inertias, dampings, amateur resistance and transient reactances of the remaining generators are $H_{2-4} = [58.5\ 55.6\ 55.6]$ p.u., $D_{2-4} = [200\ 100\ 200]$ p.u., and $r_a = 0, x'_d = x'_q = 0.0472$ p.u. The three electromechanical eigenvalues, damping ratios, and swing profiles are shown in Table 6.4. The swing profile indicates which two generators are involved in the intermachine mode corresponding to the eigenvalue as determined by the participation factors [114, p. 229]. The first pair of the eigenvalues is the mode with the smallest damping ratio and maximum real part ($\lambda_S = \lambda_1 = -0.6517 \pm 6.3161j$). We assume the second pair of the eigenvalues is the critical inter-area mode ($\lambda_I = -0.8536 \pm 5.4333j$).

Table 6.5 summarizes the optimal loading pattern, SDR, damping of the critical inter-area mode, and maximum real part of eigenvalues when we maximize each stability metric at a time. We first investigate the influence of demand response on the SDR of the generator modes. We set $\gamma_1 = 1, \gamma_2 = \gamma_3 = 0$. The solution to (6.13) is $p_{\mathrm{d},7} = 1455$ MW, $p_{\mathrm{d},9} = 1279$

Table 6.4: Eigenvalues of the nominal Kundur's system

Eigenvalues (rad/s)	Frequency(Hz)	Damping (%)	Swing Profile
$-0.6517 \pm 6.3161j$	1.01	10.26	$G2 \leftrightarrow G3, G4$
$-0.8536 \pm 5.4333j$	0.86	15.52	$G2 \leftrightarrow G3, G4$
$-0.6989 \pm 1.1743j$	0.19	51.14	$G3 \leftrightarrow G4$

Table 6.5: Results of different stability metrics when $D_{2-4} = [200\ 100\ 200]$

	$p_{\mathrm{d},7}$	$p_{\mathrm{d},9}$	η_S	η_I	α_1
max η_S	1456	1278	10.77	15.01	-0.6668
max η_I	947	1787	10.19	15.59	-0.0716
max $-\alpha_1$	1092	1642	10.56	15.20	-0.6761

MW. By increasing the power consumption at bus 7 and decreasing that at bus 9, the SDR of the generator modes increases from 10.26% to 10.77%. The convergence of the algorithm is shown in Fig. 6.3. To verify the results, we compare the solution of the iterative approach to that of a brute force approach. We compute the SDR of the generator modes for all possible loading patterns with a 1 MW mesh size. Figure 6.4 shows the SDR as a function of the real power demand at bus 7 $p_{\mathrm{d},7}$ (based on (6.13l), $p_{\mathrm{d},9} = 2734 - p_{\mathrm{d},7}$ MW). The maximum SDR (star) is 10.77% when $p_{\mathrm{d},7} = 1456$ MW, $p_{\mathrm{d},9} = 1278$ MW. The solution of the iterative approach is very near to the optimum determined by the brute force method. We then investigate the performance of the generation action. The optimal SDR through changes to generator real power generation is 12.33%. For this small system, demand response does not significantly improve the SDR as compared to generation re-dispatch.

Next, we maximize the damping of the critical inter-area mode ($\gamma_2 = 1, \gamma_1 = \gamma_3 = 0$). The optimal loading patter is $p_{\mathrm{d},7} = 947$ MW, $p_{\mathrm{d},9} = 1787$ MW. We also notice that the maximum real part of the eigenvalues reduces significantly when we improve η_I. Finally, we choose the maximum real part of eigenvalues as the stability margin ($\gamma_3 = 1, \gamma_1 = \gamma_2 = 0$), and we obtain another different optimal loading pattern $p_{\mathrm{d},7} = 1092$ MW, $p_{\mathrm{d},9} = 1642$ MW with the maximum real part of the eigenvalues as -0.6761.

We then change the damping of the generators to $D_{2-4} = [200\ 100\ 70]$. Figure 6.5 shows the trajectories of the eigenvalues when we decrease the loading at bus 7 and increase the loading at bus 9. The eigenvalues in blue are the critical eigenvalues with the SDR. As we can see, the SDR keeps increasing when the load at bus 7 decreases. However, one of the real

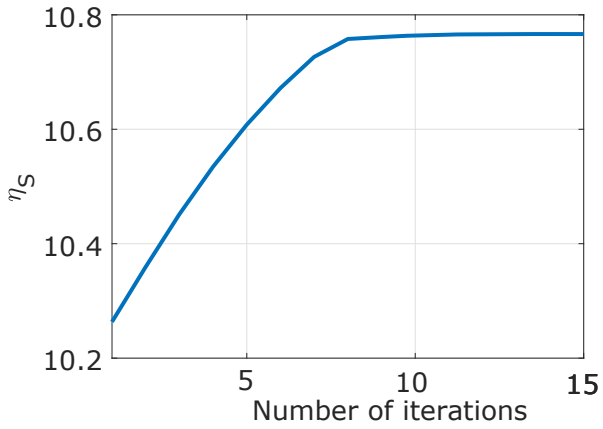

Figure 6.3: The convergence of the smallest damping ratio of the generator modes for the Kundur system.

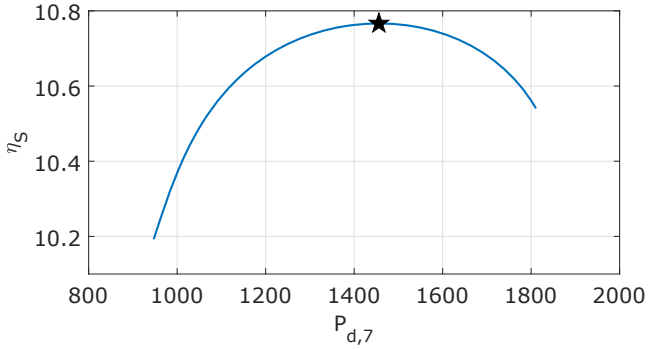

Figure 6.4: Smallest damping ratio of the generator modes as a function of the loading at bus 7 when $D_{2-4} = [200\ 100\ 200]$.

part of the eigenvalues in red becomes positive when $p_{\mathrm{d},7}$ is smaller than 947 MW. Although the SDR of the system is improved, the system is prone to instability.

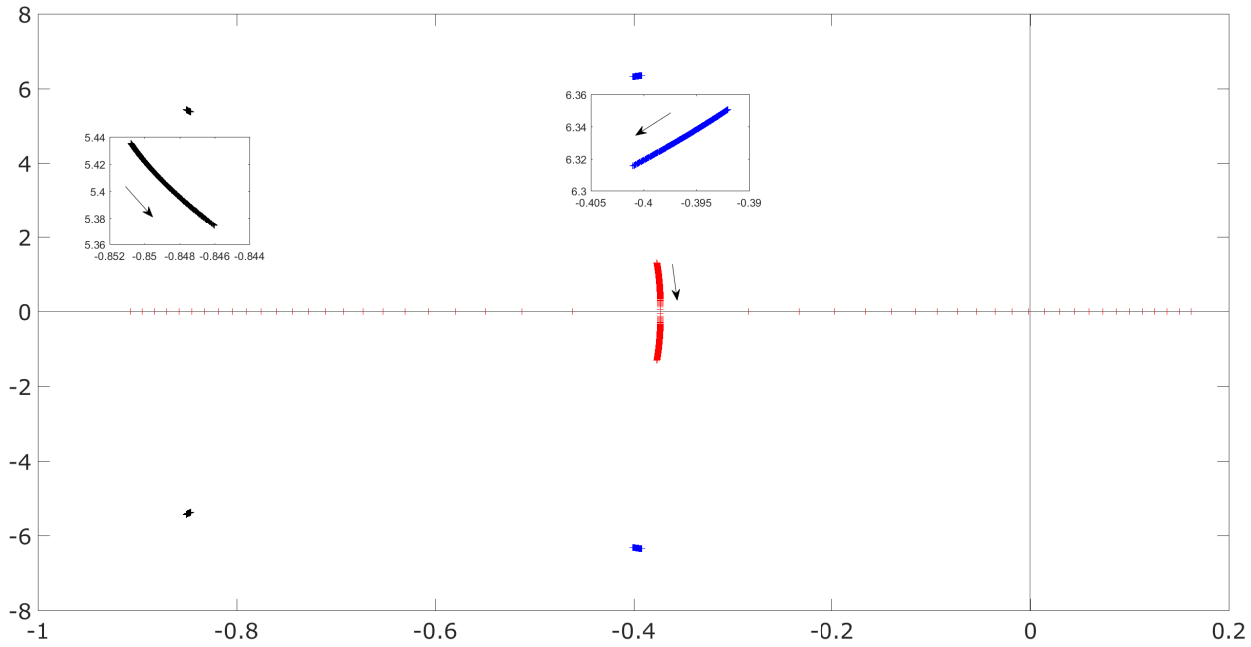

Figure 6.5: Root locus plot when $p_{\mathrm{d},7}$ changes from 967 MW to 945 MW when $D_{2-4} = [200\ 100\ 70]$.

Table 6.6: Eigenvalues of the nominal 39-bus system

Eigenvalues (rad/s)	Damping(%)	Swing Profile
$-0.0512 \pm 4.2360j$	1.2094	G10
$-0.0514 \pm 9.6176j$	0.5343	G1,G4,G8
$-0.0596 \pm 9.7159j$	0.6137	G4,G6,G7
$-0.0725 \pm 9.2591j$	0.7829	G4,G5
$-0.0074 \pm 6.1395j$	$^{\diamond}$0.1211	G5 G10
$-0.0325 \pm 6.5629j$	0.4951	G2,G3,G5,G9
$-0.0513 \pm 7.2053j$	0.7123	G6,G7
$-0.0517 \pm 8.0477j$	0.6429	G1,G8
$-0.0525 \pm 7.9760j$	0.6584	G2,G3

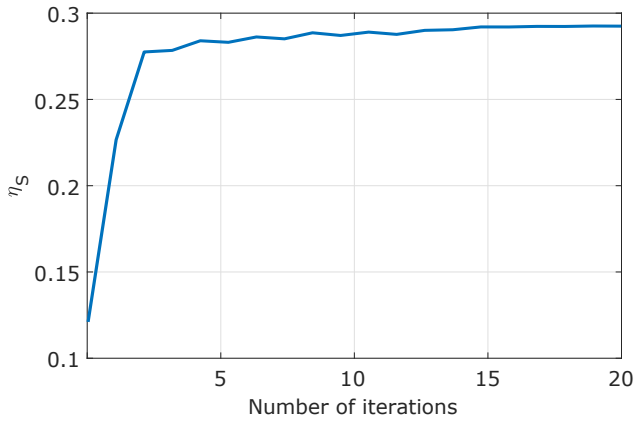

Figure 6.6: The convergence of the smallest damping ratio of the generator modes for the 39-bus system.

6.7.2 New England 39-bus System Results

We next apply the iterative algorithm to the New England 39-bus system. Again, AVR and PSS are not considered in this system. The generator parameters can be found in [86] and the rest of the data is provided in [103]. The swing profiles of the nominal system are given in Table 6.6. We only use the SDR as the stability metric. The critical eigenvalue is $\lambda_S = -0.0074 \pm 6.1395j$ and the nominal SDR is 0.12%.

We assume 5771.8 MW of total 6097.1 MW total load is demand responsive and the change range of these load as $0 \leq p_{\mathrm{d}} \leq 2p_{\mathrm{d}}(0)$. The convergence of the algorithm is shown in Fig. 6.6. The SDR increases from 0.12% to 0.29%. The algorithm converges in less than 3 seconds. Most of the load is shifted to bus 39 to improve the damping ratio. Alternatively,

Table 6.7: Nominal and optimal loading patterns for cases with and without AVRs and a PSS

Bus #	2	3	5	6	9	10	11	12	13	14
Nominal	21.70	94.20	7.60	11.20	29.50	9.00	3.50	6.10	13.50	14.90
without AVR/PSS	0.00	124.29	35.90	8.13	0.00	0.00	0.00	36.75	3.43	2.69
with AVR/PSS	25.36	60.60	69.61	32.98	9.74	9.96	1.69	0.00	0.00	1.26

if we redispatch the generation, the maximum SDR is 0.27% and this is achieved when we decrease the generation of G10 at bus 39. One possible explanation is that the critical mode is sensitive to G5 (at bus 34) and G10 (at bus 39), so increasing the load at bus 39 or decreasing the generation at bus 39 will improve the SDR.

6.7.3 IEEE 14-bus System Results

In this system, we consider two cases: 1) there is no AVR or PSS connected to the synchronous machines; 2) the system includes AVRs for each synchronous machine and a PSS is connected to the synchronous machine at bus 1. The system data and generator parameters can be found in [88]. The parameters of the PSS are set as follows: $K_w = 1$, $T_1 = T_3 = 0.28$, $T_2 = T_4 = 0.02$. Again, we assume 211.2 MW of total 259 MW total load (81.5%) is demand responsive and the change range of these load as $0 \leq p_{\mathrm{d}} \leq 2p_{\mathrm{d}}(0)$. The DR buses and the nominal loading pattern are given in Table 6.7.

We apply the iterative algorithm to both cases and choose the SDR as the stability metric. The nominal SDR without AVR is 0.66% and the optimal SDR we obtain is 0.69%. The nominal SDR with AVR is 0.51% and the optimal SDR is 0.70%. The optimal loading patterns for each case are shown in Table 6.7. We notice that both the nominal SDR and the optimal loading pattern are different when we have different system models. Compared with the case without AVR, the size of matrix A of the case with AVRs and a PSS increases, but the ILP algorithm can converge within few iterations (10 seconds), as shown in Fig. 6.7.

Next, we compare six cases with different decision variables and/or constraints to the base case (6.13) in Table 6.8, which defines each case and shows its optimal SDR, and percent improvement. Note that all following cases include the AVRs and a PSS in the system. Case 1 corresponds to our base case, where the total demand responsive load remains constant and the load is modeled as constant power factor load. Case 2 only spatially shifts the real power of demand responsive loads, and we achieve a slightly better optimal η_S. In Case 3,

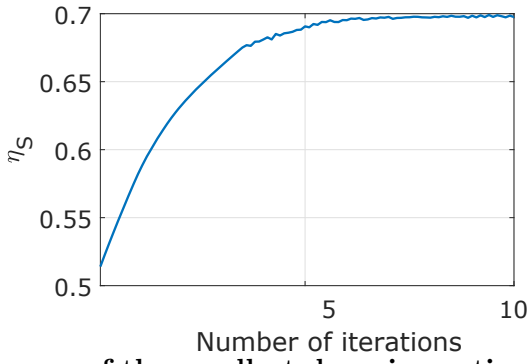

Figure 6.7: The convergence of the smallest damping ratio of the generator modes for the 14-bus system with AVRs and a PSS.

Table 6.8: Decision variables, parameters, optimal smallest damping ratio η_S, and percent improvement for each case

Case	1	2	3	4	5	6	7
p_g						✓	✓
p_d	✓	✓		✓	✓		✓
q_d	✓		✓	✓	✓		✓
Constraint (6.13m)	✓						
$\lvert\Delta q_d\rvert \leq 100$MVar			✓	✓			
$\lvert\Delta q_d\rvert \leq 20$MVar					✓		✓
Optimal η_S	0.6989	0.7018	0.6380	0.7203	0.7036	0.7258	0.7683
Percent improvement	36.0	36.5	24.1	40.1	36.9	41.2	49.5

we investigate the achievable change in η_S by controlling the reactive power of demand responsive loads and we assume that the reactive power of each demand responsive load can increase/decrease by 100 MVar. As shown, optimizing the reactive power demand does not improve η_S as much as optimizing the real power demand. Next, we consider changing both the real and reactive power demand independently in Case 4 and the SDR is greatly improved. In Cases 3 and 4, allowable change in the reactive power demand has a large range. In practice, the flexibility of reactive power demand might be constrained. Therefore, in Case 5, we constrain that the change in reactive power demand to $\pm$ 20, resulting in a slightly lower maximum SDR than that of Case 4. Compared with Case 1, which assumed constant power factor loads (i.e., the real and reactive power demand cannot be changed independently), Case 5 offers more flexibility of reactive power demand and thus achieves a higher optimal η_S. In Case 6, we explore the performance of generation actions alone and find

that they have a slightly better performance than the demand actions have. The greatest SDR improvement is achieved when we change load and generation together (Case 7). In this case, the SDR is improved by around 50%.

We also formulate and solve an optimization problem to determine the minimum load shedding needed to achieve the same SDR improvement as obtained in Case 1 (without system-wide load shedding). The formulation is as follows.

$$\min \quad \sum_{i \in \mathcal{S}_{\mathrm{DR}}} (p_{\mathrm{d},i}^{0} - p_{\mathrm{d},i}) \quad \text{subject to} \tag{6.18a}$$

$$\eta_S \geq 0.6989 \tag{6.18b}$$

$$\text{Constraints (6.13b), (6.13h)} - \text{(6.13k)} \tag{6.18c}$$

$$\text{Constraints (6.13m)} - \text{(6.13x)} \tag{6.18d}$$

To solve this problem, we again use iterative linear programming with generalized eigenvalue sensitivities. We found that the system load would need to drop by at least 13% to achieve the same SDR improvement as achieved by spatial load shifting.

6.7.4 Impact on Voltage Stability

Here, we investigate the impact of improving small signal stability on voltage stability using Kundur's system and the 14-bus system. The SSV of the power flow is used as measure of voltage stability.

Figure 6.8 depicts the SDR and the SSV as a function of the loading at bus 7 when $D_{2-4} = [200\ 100\ 70]$ for Kundur's system. As we can see, the maximum SDR and the maximum SSV points are totally different. When we improve the voltage stability, we will adversely impact the small-signal stability.

We then compare the optimal solution of (6.13) with that of (2.1) for the 14-bus system. We first assume the loads of bus 4, 9, and 14 are demand responsive and find that the optimal solutions of both problems are identical. Both the SDR and the SSV are maximized when we shift all demand to bus 4. Next, we assume all PQ buses belong to $\mathcal{S}_{\mathrm{DR}}$. The maximum SSV is 0.56 and it is achieved by shifting all demand to bus 4; the SDR of the maximum SSV point is 0.58%. Meanwhile, the maximum η_S is achieved when we shift all demand except the load at bus 4 to bus 5. The maximum η_S is 0.64% and the SSV of this point is 0.56. For the 14-bus system, we observe that the voltage stability is not influenced when we improve the small-signal stability.

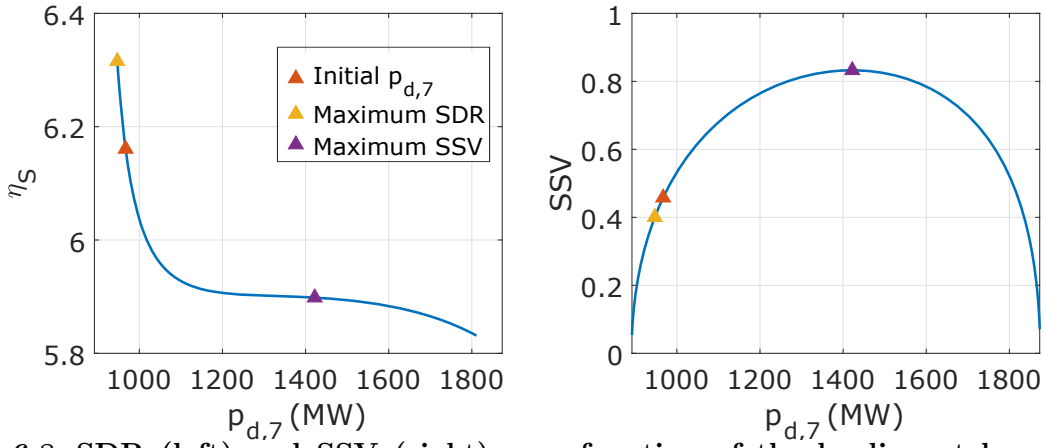

Figure 6.8: SDR (left) and SSV (right) as a function of the loading at bus 7 when $D_{2-4} = [200\ 100\ 70]$. Red triangle represents the initial $p_{d,7}$; yellow triangle represents $p_{d,7}$ with the maximum SDR point; purple triangle represents $p_{d,7}$ with the maximum SSV point.

6.8 Chapter Conclusion

This chapter has presented a method to improve power system small-signal performance using demand response. We formulated an optimization model and solved it with iterative linear programming using generalized eigenvalue sensitivities.

The test case results show that demand response actions can improve small-signal stability performance. However, it may happen that when we improve the smallest damping ratio, it will have adverse impact on other stability metrics, for example, the maximum real part of eigenvalues, to the extent that one of the eigenvalues moves across the imaginary axis and thus making the system unstable. Similarly, we notice that the voltage stability margin is reduced when we improve power system small-signal performance in Kundur's system, although case-dependent, this suggests that the choice of stability metric is critical and will greatly influence the optimal loading pattern.

In Kundur's system, our demand response action does not achieve the same improvement as the generation action. However, there are more generator buses than demand buses in this example, which is atypical. In both the 14-bus and the 39-bus systems, the demand response actions have similar or even better performance than the generation actions have. Moreover, in practice, ramp limits would prevent the generators from responding fast, which makes the demand response strategy more effective.

Future work will involve incorporate tuning of the stabilizers together with the demand responsive loads to further improve the small-signal stability.

Chapter 7

Mitigating Voltage Unbalance using Distributed Solar PV

In this chapter, we shift our focus from transmission system stability analysis to power quality in distribution systems. Specifically, we investigate methods to improve voltage unbalance via controlling the reactive power of distributed solar PV systems. We focus on developing controllers based on Steinmetz design. This chapter is largely based on a manuscript that has been submitted to a journal:

- M. Yao, I.A. Hiskens, and J.L. Mathieu. "Mitigating voltage unbalance using distributed solar photovoltaic inverters". (submitted to *IEEE Transactions on Power Systems*)

The preliminary work is published in:

- M. Yao, I.A. Hiskens, and J.L. Mathieu. "Applying Steinmetz circuit design to mitigate voltage unbalance using distributed solar PV". In: *IEEE PowerTech*. 2019.

7.1 Chapter Introduction

This chapter develops a simple-to-implement strategy to control PV inverter reactive power injections to improve voltage balance in distribution networks. While voltage unbalance can be improved through control of real and reactive power injections, we only consider reactive power control since we assume the owners of the PV systems would like to maximize the real power output of their devices. The strategy is based on Steinmetz design [62, 94]. We first explore the capabilities and limitations of Steinmetz circuit design applied to distributed PV

systems. After that, we develop two control schemes, one that is completely decentralized and the other a distributed controller that coordinates PV inverters through a communication network. We demonstrate the performance of both controllers through case studies. In contrast to centralized optimization-based formulations, our approach does not require detailed information about the feeder nor significant computational resources. It relies only on local measurements and simple calculations (though the distributed controller requires a simple communication network to broadcast commands to distributed PV systems). Therefore, our approach is scalable to large feeders and inexpensive to implement, though suboptimal relative to centralized optimization-based approaches with perfect information.

The main contributions of this chapter are as follows.

- We extend the use of Steinmetz circuit design to distributed solar PV systems to achieve voltage balance. Past work has also commonly used Steinmetz circuit design to balance the voltage at the bus that the controllable device is connected to. Here, we also explore the ability of PV systems to balance upstream buses.

- We propose the reactive power strategies considering cases with different load and PV system connection arrangements, and show that the controller is able to reduce multiple forms of unbalance, depending upon the PV system connections and the control objective.

- We first test the controllers on a toy system to investigate whether the Steinmetz method can be applied in a completely decentralized way, or if coordination between systems is necessary. We then evaluate the performance of the controllers on large feeders with high penetration of distributed PV systems. We choose the IEEE 13-node feeder and the GridLAB-D taxonomy feeder R1-12.47-1 (617 nodes and 1196 triplex nodes), which is based on a real distribution feeder in the U.S. [28, 106], as our test feeders.

- We compare the performance of our proposed controller to that of a model-free controller [12] and discuss the trade-offs associated with different unbalance improvement objectives.

7.2 Problem Description and Controller Overview

Recall that positive-sequence voltage V_1, negative-sequence voltage V_2, and zero-sequence voltage V_0 can be computed using the Fortescue transformation,

$$\begin{bmatrix} V_0 \\ V_1 \\ V_2 \end{bmatrix} = \begin{bmatrix} 1 & 1 & 1 \\ 1 & a^2 & a \\ 1 & a & a^2 \end{bmatrix}^{-1} \begin{bmatrix} V_A \\ V_B \\ V_C \end{bmatrix}, \tag{7.1}$$

where $a = e^{j2\pi/3} = 1\angle 120^{\text{o}}$, and $V_A,\ V_B,\ V_C$ are phase-to-neutral voltages. Voltage unbalance factors are used to quantify voltage unbalance. The negative-sequence voltage unbalance factor is defined as $\text{VUF}_2\,(\%) = 100|V_2|/|V_1|$ and the zero-sequence voltage unbalance factor is defined as $\text{VUF}_0\,(\%) = 100|V_0|/|V_1|$. We consider two different unbalance improvement objectives, reducing the negative-sequence unbalance and reducing the zero-sequence unbalance.

Distribution networks are experiencing a steady increase in the number of single-phase PV systems distributed along feeders, as illustrated in Fig. 7.1. Voltage unbalance occurs due to unbalanced components (e.g., unbalanced lines, loads, and/or distributed generation, unequal regulator taps) connected to the feeder, leading to three-phase voltages with unequal magnitudes and/or angle differences. For large three-phase transformers and induction motors, voltage unbalance causes high temperatures, lower efficiencies, and shortened lifespans. To protect these devices from damage, our goal is to balance the three-phase voltages at the nodes where they are connected, referred to as *critical nodes*. This goal is achieved by controlling the reactive power injections of PV systems without altering their active power injections. We make the realistic assumption that PV systems are often operating below their rating, enabling them to provide reactive power to a limit determined by their apparent power rating S^{rate} and the active power they are providing P. For PV system i, reactive power at time t must satisfy the limit,

$$Q_{i,t}^{\text{lim}} = \pm\sqrt{(S_i^{\text{rate}})^2 - (P_{i,t})^2}. \tag{7.2}$$

Steinmetz design has been used to control three-phase delta-connected static VAR compensators to balance traction system loads [128], but its use to control the reactive power injections of single-phase DERs, such as PV systems, is new. The method computes the three-phase line-to-line capacitance required at a critical node to make the load at that node

together with the total load further out on the distribution feeder (including network losses), collectively referred to as the *downstream load*, appear balanced. However, voltage unbalance at a critical node is also a function of unbalance upstream of that node. If the upstream unbalance is significant, balancing the downstream load will not be sufficient to balance the voltage at that node and, in some cases, could increase the unbalance. Thus, it is important for network operators to determine which portions of the network contribute most to unbalance and apply the method only to critical nodes where the unbalance is primarily due to the downstream load, such as nodes relatively close to substations.

Steinmetz design cannot be applied directly to control PV systems because, 1) they are typically single-phase devices that may be connected line-to-neutral or line-to-line, 2) they are not all connected to the critical node but are distributed along the feeder, 3) they do not control capacitance but rather reactive power injection, and 4) their reactive power injection capacity is limited and time varying. To address these challenges, Steinmetz design is extended in Section 7.4 to enable computation of reactive power injections for networks with delta- and/or wye-connected PV systems. In Section 7.5, we propose two different controllers that address the distributed nature of PV systems.

A conceptual illustration of the **decentralized** controller is provided in Fig. 7.1a. PV systems at different nodes are controlled separately with no coordination between them[1]. Consider the PV system connected to node X as an example. The controller at node X receives a measurement of the three-phase complex voltage V^m at node X and the three-phase complex power $S^m = P^m + jQ^m$ flowing into that node (composed of the load at node X together with the total load further out on the feeder). It uses Steinmetz design to compute the three-phase reactive power injection that would balance that total load. The computed reactive power could be either the total amount or the change of reactive power that PV systems should provide, detailed in Section 7.5. Distribution-level PV systems are typically not three-phase, nor do they have unlimited reactive power capability. Therefore the controller commands the PV system to change its reactive power by an amount that is as close as physically possible to Q^c, as dictated by its connection arrangement and reactive power limits. Hence, if a single-phase PV system is connected to node X, it will inject only into the phase to which it is connected. Controllers at other nodes perform their equivalent actions, and in so doing achieve an overall balancing effect. In this paper, we assume all controllers act simultaneously.

[1]Where multiple PV systems are connected to the same node, they are jointly regulated by a common controller.

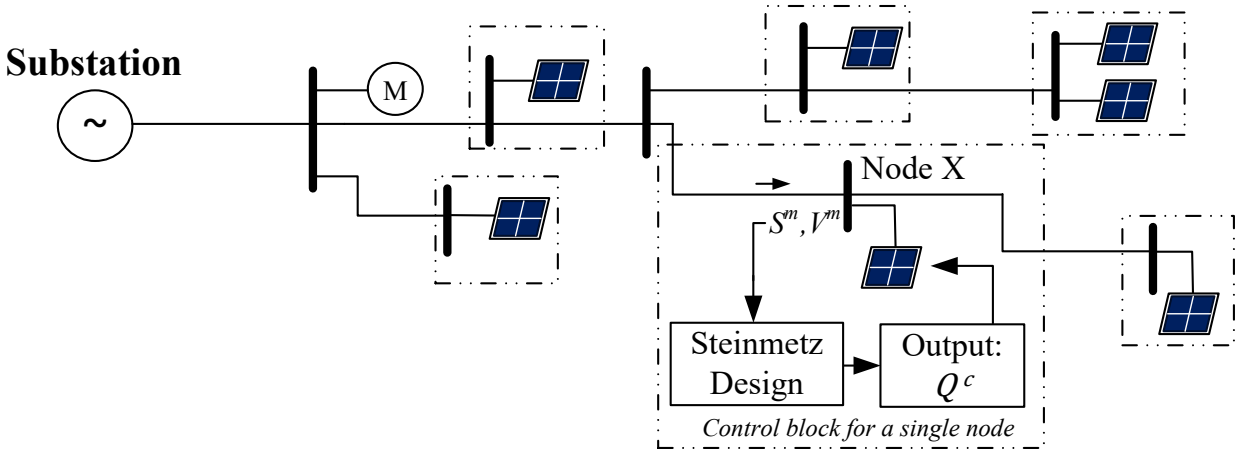

(a) Decentralized Controller

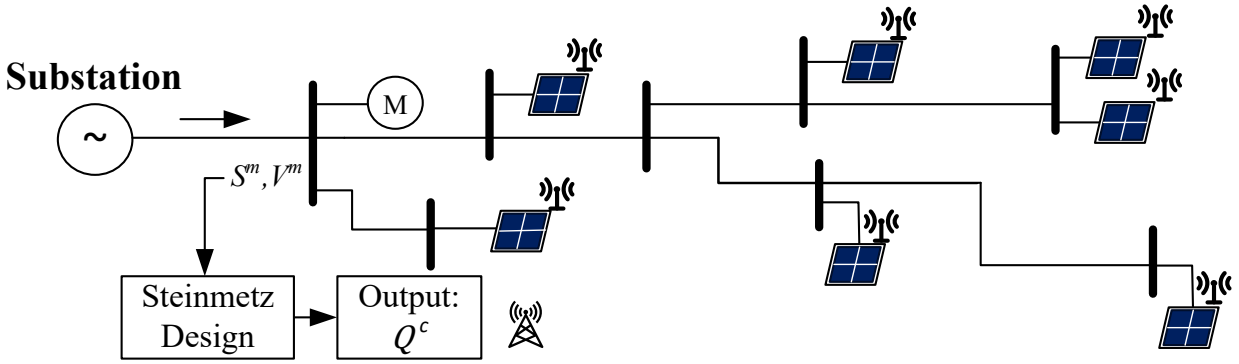

(b) Distributed Controller

Figure 7.1: Conceptual illustrations of the proposed controllers. Single-phase PV systems are distributed along a radial feeder. We wish to balance a critical node, in this case the one with a three-phase motor (M). (a) Decentralized controller: each node uses the same control scheme as shown in the block around node X. (b) Distributed controller: measurements are taken at the critical node and commands are broadcast to downstream PV systems.

Fig. 7.1b shows a conceptual illustration of the **distributed** controller. The controller receives a measurement of the three-phase complex voltage V^m at the critical node and the three-phase complex power $S^m = P^m + jQ^m$ flowing into the critical node. It uses Steinmetz design to compute the change Q^c in three-phase reactive power injection that would balance the node. It then commands downstream PV systems to adjust their reactive power injections by broadcasting commands through a communication network. In this paper, we assume communication is one-way, from the controller to the PV systems, and all PV systems receive the commands without delay. We further assume the controller knows each downstream PV system's phase connection and rating S^{rate}, and sends commands to each PV system.

The feeder's voltage profile and power losses change after distributed PV systems inject reactive power. Load and PV generation are also continually changing. Therefore, the process repeats periodically, acquiring measurements, computing the latest injections, and implementing those commands.

7.3 Conventional Steinmetz Design

In this section, we first review the process of conventional Steinmetz design to derive the compensating reactances to balance a single-phase constant impedance load and then derive the compensating reactive power injections to balance a single-phase constant power load.

Figure 7.2 shows a Steinmetz compensation circuit for a single-phase load. Assume that the load, connected between phases A and B, is modeled as a constant impedance load $Z_{AB} = R_{AB} + jX_{AB}$ (the admittance is $Y_{AB} = G_{AB} - jB_{AB}$). Steinmetz circuit design computes the reactances we should connect to phases BC and CA to make the single-phase load appear as a balanced three-phase load. The circuit is balanced when the negative sequence components are eliminated. The reactances that should be connected (X^c_{BC}, X^c_{CA}) are computed as follows [62].

According to Kirchoff's current law:

$$\begin{bmatrix} I_A \\ I_B \\ I_C \end{bmatrix} = \begin{bmatrix} 1 & 0 & -1 \\ -1 & 1 & 0 \\ 0 & -1 & 1 \end{bmatrix} \begin{bmatrix} I_{AB} \\ I_{BC} \\ I_{CA} \end{bmatrix}. \tag{7.3}$$

The symmetrical components of the line currents are obtained with the Fortescue trans-

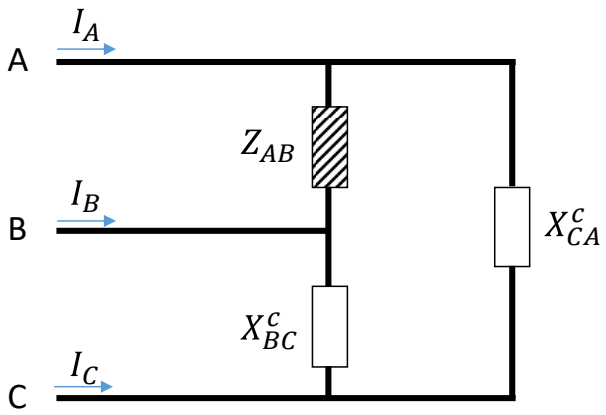

Figure 7.2: Steinmetz compensation circuit for a single-phase load Z_{AB} connected between phase A and phase B.

formation:

$$\begin{bmatrix} I_0 \\ I_1 \\ I_2 \end{bmatrix} = \begin{bmatrix} 1 & 1 & 1 \\ 1 & a^2 & a \\ 1 & a & a^2 \end{bmatrix}^{-1} \begin{bmatrix} I_A \\ I_B \\ I_C \end{bmatrix} \tag{7.4}$$

where $a = e^{j2\pi/3}$ and I_0, I_1, I_2 are the zero sequence, positive sequence, and negative sequence current, respectively. When the circuit is balanced, the negative sequence current is zero:

$$3I_2 = (1 - a^2)I_{AB} + (a^2 - a)I_{BC} + (a - 1)I_{CA} = 0 \tag{7.5}$$

Since $I = VY$, we can replace I_{AB}, I_{BC}, I_{CA} with their corresponding voltage and admittance:

$$(1 - a^2)V_{AB}Y_{AB} + (a^2 - a)V_{BC}(-jB^c_{BC}) + (a - 1)V_{CA}(-jB^c_{CA}) = 0. \tag{7.6}$$

When the circuit is balanced,

$$V_{BC} = a^2 V_{AB}, \quad V_{CA} = aV_{AB}. \tag{7.7}$$

Multiply (7.6) with V_{AB} and split it into its real and imaginary parts:

$$-\frac{3}{2}B_{AB} + \frac{\sqrt{3}}{2}G_{AB} + \frac{3}{2}B^c_{BC} = 0 \tag{7.8a}$$

$$\frac{\sqrt{3}}{2}B_{AB} + \frac{3}{2}G_{AB} + \frac{\sqrt{3}}{2}B^c_{BC} - \sqrt{3}B^c_{CA} = 0 \tag{7.8b}$$

Table 7.1: Susceptance compensation for single-phase constant impedance load

Location	B^c_{AB}	B^c_{BC}	B^c_{CA}
Phase AB	0	$-G_{AB}/\sqrt{3}+B_{AB}$	$G_{AB}/\sqrt{3}+B_{AB}$
Phase BC	$G_{BC}/\sqrt{3}+B_{BC}$	0	$-G_{BC}/\sqrt{3}+B_{BC}$
Phase CA	$-G_{CA}/\sqrt{3}+B_{CA}$	$G_{CA}/\sqrt{3}+B_{CA}$	0

Table 7.2: Reactive power compensation for single-phase constant power load

Location	Q^c_{AB}	Q^c_{BC}	Q^c_{CA}
Phase AB	0	$-P_{AB}/\sqrt{3}+Q_{AB}$	$P_{AB}/\sqrt{3}+Q_{AB}$
Phase BC	$P_{BC}/\sqrt{3}+Q_{BC}$	0	$-P_{BC}/\sqrt{3}+Q_{BC}$
Phase CA	$-P_{CA}/\sqrt{3}+Q_{CA}$	$P_{CA}/\sqrt{3}+Q_{CA}$	0

Therefore, the susceptances (reactances) are:

$$\frac{1}{X^c_{BC}} = B^c_{BC} = -\frac{G_{AB}}{\sqrt{3}} + B_{AB}, \quad \frac{1}{X^c_{CA}} = B^c_{CA} = \frac{G_{AB}}{\sqrt{3}} + B_{AB}. \tag{7.9}$$

If the load is in another phase, the process to determine the reactances is the same. The equations are summarized in Table 7.1.

When the load is modeled as constant power $S_{AB} = P_{AB} + jQ_{AB}$, we replace I_{AB}, I_{BC}, I_{CA} in (7.5) with their corresponding power and voltage and derive the compensating reactive power injections using the same process. The equations are summarized in Table 7.2.

When the load is three-phase, we can divide the three-phase load into three single-phase loads. For each single-phase load, computed reactive power reactances/injections on the other two phases based on Table 7.1 or 7.2. Finally, we sum the reactances/injections to determine the three-phase compensation strategy for the original three-phase load. Complete compensation of an unbalanced three-phase constant impedance load can be obtained as follows:

$$\begin{aligned} B^c_{AB} &= \frac{G_{BC}}{\sqrt{3}} + B_{BC} - \frac{G_{CA}}{\sqrt{3}} + B_{CA}, \\ B^c_{BC} &= \frac{G_{CA}}{\sqrt{3}} + B_{CA} - \frac{G_{AB}}{\sqrt{3}} + B_{AB}, \\ B^c_{CA} &= \frac{G_{AB}}{\sqrt{3}} + B_{AB} - \frac{G_{BC}}{\sqrt{3}} + B_{BC}, \end{aligned} \tag{7.10}$$

and for an unbalanced three-phase constant power load:

$$
\begin{aligned}
Q^c_{AB} &= \frac{P_{BC}}{\sqrt{3}} + Q_{BC} - \frac{P_{CA}}{\sqrt{3}} + Q_{CA}, \\
Q^c_{BC} &= \frac{P_{CA}}{\sqrt{3}} + Q_{CA} - \frac{P_{AB}}{\sqrt{3}} + Q_{AB}, \\
Q^c_{CA} &= \frac{P_{AB}}{\sqrt{3}} + Q_{AB} - \frac{P_{BC}}{\sqrt{3}} + Q_{BC}.
\end{aligned}
\tag{7.11}
$$

While (7.11) produces unique solutions and balances the voltage, the resulting injections may impact the system power factor and voltage profile. Moreover, (7.11) can only be applied to delta-connected systems, which are relatively uncommon in the U.S. In the following section, we propose a better reactive power strategy and consider different load and PV connection configurations.

7.4 Computing Reactive Power Injections Using Steinmetz Design

In this section, we derive the three-phase reactive power injections required to improve voltage unbalance for various connections of three-phase loads and PV systems.

Table 7.3 summarizes the specific cases we explore. The first two rows list the types of load and PV system connections and the third row lists the unbalance improvement objective. Steinmetz design has usually been applied to three-wire systems with delta-connected loads [128]. Therefore, Case 1 assumes delta-connected loads and PV systems, and seeks to reduce negative-sequence voltage unbalance. (Recall that there is no zero-sequence unbalance in a three-wire system.) Cases 2–5 assume four-wire systems with a mixture of delta- and wye-connected loads. When the PV systems are delta-connected, only negative-sequence voltage unbalance can be reduced (Case 2). When the PV systems are wye-connected, either negative- or zero-sequence voltage unbalance can be reduced (Cases 3 and 4). When both delta- and wye-connected PV systems are on the same network, negative- and/or zero-sequence voltage unbalance can be reduced. Case 5 seeks to reduce both simultaneously.

For each case, we derive the reactive power injections assuming, i) the upstream network is balanced, ii) the downstream load, including actual load, line losses, and distributed generation, can be approximated as constant power (i.e. independent of voltage), and iii) reactive power compensation is provided by a three-phase PV system at the critical node, or a col-

Table 7.3: Case Summary

Case	1	2	3	4	5
Load	Δ	Δ & Y	Δ & Y	Δ & Y	Δ & Y
PV	Δ	Δ	Y	Y	Δ & Y
Objective	VUF_2	VUF_2	VUF_2	VUF_0	VUF_2 & VUF_0

lection of single-phase PV systems distributed across all three phases at the critical node. Because Steinmetz design balances the downstream load, if the upstream network is not balanced, the approach will not exactly balance the voltage at the critical node. (We show in Section 7.6, though, that it can still significantly improve unbalance.) If the downstream load is not constant power and/or the PV systems are distributed across the network, a single application of Steinmetz design will not exactly balance the critical-node voltage. However, the proposed feedback process described in Section 7.5 will do so.

Case 1: Delta Load and Delta PV, Eliminate V_2

We first consider the case in which the load and PV system are both delta connected, as shown in Fig. 7.3a. Suppose the measured line-to-neutral voltages at the critical node are V_A^m, V_B^m, V_C^m, and the complex power measured on each phase is S_A^m, S_B^m, S_C^m. Then, the line currents are $I_A^m = (S_A^m/V_A^m)^*$, $I_B^m = (S_B^m/V_B^m)^*$, $I_C^m = (S_C^m/V_C^m)^*$. The delta-load currents can be expressed to an arbitrary (unknowable) constant K as,

$$\begin{bmatrix} I_{AB}^{tot} \\ I_{BC}^{tot} \\ I_{CA}^{tot} \end{bmatrix} = \begin{bmatrix} I_{AB}^{eq} \\ I_{BC}^{eq} \\ I_{CA}^{eq} \end{bmatrix} + K \begin{bmatrix} 1 \\ 1 \\ 1 \end{bmatrix} = \frac{1}{3} \begin{bmatrix} 1 & -1 & 0 \\ 1 & 2 & 0 \\ -2 & -1 & 0 \end{bmatrix} \begin{bmatrix} I_A^m \\ I_B^m \\ I_C^m \end{bmatrix} + K \begin{bmatrix} 1 \\ 1 \\ 1 \end{bmatrix}. \tag{7.12}$$

The line-to-line voltages are $V_{AB}^m = V_A^m - V_B^m$, $V_{BC}^m = V_B^m - V_C^m$, $V_{CA}^m = V_C^m - V_A^m$, so the equivalent delta-load demand can be written,

$$\begin{aligned} S_{AB}^{tot} &= V_{AB}^m (I_{AB}^{eq} + K)^* = S_{AB}^{eq} + V_{AB}^m K^*, \\ S_{BC}^{tot} &= V_{BC}^m (I_{BC}^{eq} + K)^* = S_{BC}^{eq} + V_{BC}^m K^*, \\ S_{CA}^{tot} &= V_{CA}^m (I_{CA}^{eq} + K)^* = S_{CA}^{eq} + V_{CA}^m K^*. \end{aligned}$$

Zero VUF_2, or equivalently zero V_2, can be achieved by driving the negative-sequence current I_2 to zero (assuming the upstream network is balanced). To do so, the reactive power injections of delta-connected PV systems are changed by $Q_{AB}^{c,\Delta}$, $Q_{BC}^{c,\Delta}$, $Q_{CA}^{c,\Delta}$. The resulting

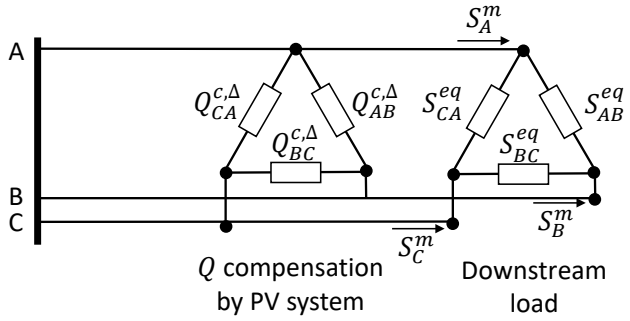

(a) Case 1.

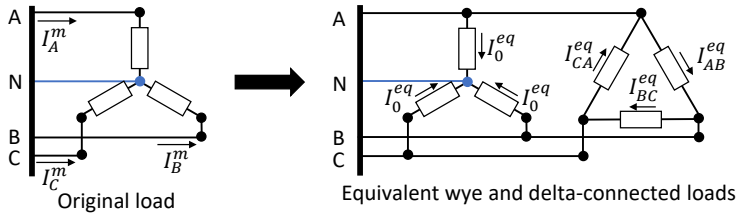

(b) Case 2 load transformation.

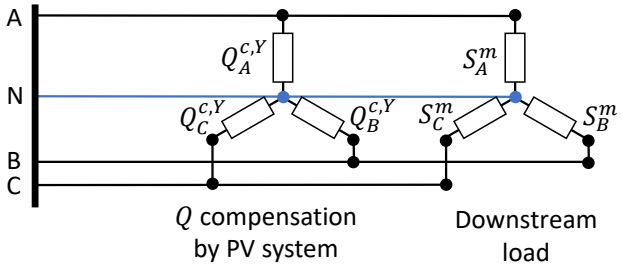

(c) Cases 3 and 4.

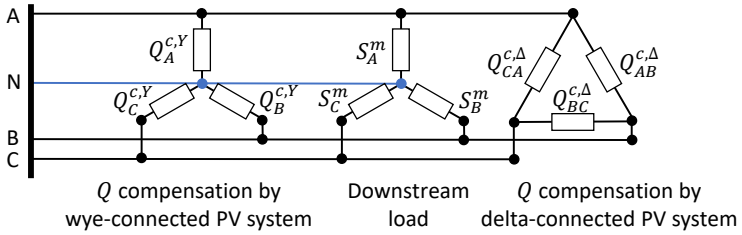

(d) Case 5.

Figure 7.3: Reactive power compensation by three-phase PV systems. "Downstream load" refers to the equivalent three-phase load at the critical node and further out on the feeder, including the PV system active power injections at the critical node. (a) Case 1: Delta-connected PV system used to eliminate negative-sequence unbalance. (b) Case 2: Transformation from a wye-connected load to equivalent wye- and delta-connected loads. (c) Cases 3 and 4: Wye-connected PV system used to eliminate negative- or zero-sequence unbalance. (d) Case 5: Delta- and wye-connected PV systems used to eliminate negative- and zero-sequence unbalance.

delta-load currents for the compensated system are given by,

$$I_{AB}^{c,tot} = \Big(\frac{S_{AB}^{eq} + V_{AB}^{m}K^{*} + jQ_{AB}^{c,\Delta}}{V_{AB}^{c}}\Big)^{*} = I_{AB}^{c} + K\Big(\frac{V_{AB}^{m}}{V_{AB}^{c}}\Big)^{*}, \tag{7.13a}$$

$$I_{BC}^{c,tot} = \Big(\frac{S_{BC}^{eq} + V_{BC}^{m}K^{*} + jQ_{BC}^{c,\Delta}}{V_{BC}^{c}}\Big)^{*} = I_{BC}^{c} + K\Big(\frac{V_{BC}^{m}}{V_{BC}^{c}}\Big)^{*}, \tag{7.13b}$$

$$I_{CA}^{c,tot} = \Big(\frac{S_{CA}^{eq} + V_{CA}^{m}K^{*} + jQ_{CA}^{c,\Delta}}{V_{CA}^{c}}\Big)^{*} = I_{CA}^{c} + K\Big(\frac{V_{CA}^{m}}{V_{CA}^{c}}\Big)^{*}, \tag{7.13c}$$

where $V_{AB}^{c}, V_{BC}^{c}, V_{CA}^{c}$ are the line-to-line voltages of the compensated system. The corresponding sequence currents I_0^c, I_1^c, I_2^c can be computed using the Fortescue transformation and Kirchoff's current law,

$$\begin{bmatrix} I_0^c \\ I_1^c \\ I_2^c \end{bmatrix} = \begin{bmatrix} 1 & 1 & 1 \\ 1 & a^2 & a \\ 1 & a & a^2 \end{bmatrix}^{-1} \begin{bmatrix} 1 & 0 & -1 \\ -1 & 1 & 0 \\ 0 & -1 & 1 \end{bmatrix} \begin{bmatrix} I_{AB}^{c,tot} \\ I_{BC}^{c,tot} \\ I_{CA}^{c,tot} \end{bmatrix}. \tag{7.14}$$

Solving for I_2 in (7.14) and setting the result to zero yields,

$$\begin{aligned} 3I_2^c = {} & (1-a^2)I_{AB}^{c} + (a^2-a)I_{BC}^{c} + (a-1)I_{CA}^{c} \\ & + K\Big[(1-a^2)\Big(\frac{V_{AB}^{m}}{V_{AB}^{c}}\Big)^{*} + (a^2-a)\Big(\frac{V_{BC}^{m}}{V_{BC}^{c}}\Big)^{*} + (a-1)\Big(\frac{V_{CA}^{m}}{V_{CA}^{c}}\Big)^{*}\Big] = 0. \end{aligned} \tag{7.15}$$

Note though that because the controller is seeking to balance V_{AB}^m, V_{BC}^m, V_{CA}^m, we have $\frac{V_{AB}^m}{V_{AB}^c} \approx \frac{V_{BC}^m}{V_{BC}^c} \approx \frac{V_{CA}^m}{V_{CA}^c}$, so the term multiplying K is effectively zero. We shall use that observation in subsequent analysis. Additionally, when the node is balanced, we have (7.7). Using (7.13) and (7.7) to simplify (7.15) and then splitting into real and imaginary parts gives,

$$Q_{AB}^{c,\Delta} + Q_{BC}^{c,\Delta} - 2Q_{CA}^{c,\Delta} = -\sqrt{3}(P_{AB}^{eq} - P_{BC}^{eq}) - (Q_{AB}^{eq} + Q_{BC}^{eq}) + 2Q_{CA}^{eq}, \tag{7.16a}$$

$$Q_{AB}^{c,\Delta} - Q_{BC}^{c,\Delta} = \frac{1}{\sqrt{3}}(P_{AB}^{eq} + P_{BC}^{eq} - 2P_{CA}^{eq}) - (Q_{AB}^{eq} - Q_{BC}^{eq}), \tag{7.16b}$$

where $P_\phi^{eq} + jQ_\phi^{eq} = S_\phi^{eq}$ ($\phi \in \{AB, BC, CA\}$). These equations must be satisfied to balance the critical node. However, we have three unknowns, $Q_{AB}^{c,\Delta}$, $Q_{BC}^{c,\Delta}$, $Q_{CA}^{c,\Delta}$, and only two equations, so there are an infinite number of solutions. An additional constraint is required to obtain a unique set of injections. Three choices are presented in [77], 1) enforce unity power factor at the node, 2) minimize the quadratic sum of the changes in reactive power

injections, or 3) set the sum of the changes in reactive power injections equal to zero. To avoid altering the reactive power demand of the system and significantly changing its voltage profile, the third option,

$$Q_{AB}^{c,\Delta} + Q_{BC}^{c,\Delta} + Q_{CA}^{c,\Delta} = 0, \tag{7.17}$$

is preferable. Combining (7.16) and (7.17) gives the final three-phase reactive power compensation strategy,

$$Q_{AB}^{c,\Delta} = \tfrac{1}{3}\big(Q_{CA}^{eq} + Q_{BC}^{eq} - 2Q_{AB}^{eq} + \sqrt{3}(P_{BC}^{eq} - P_{CA}^{eq})\big), \tag{7.18a}$$

$$Q_{BC}^{c,\Delta} = \tfrac{1}{3}\big(Q_{AB}^{eq} + Q_{CA}^{eq} - 2Q_{BC}^{eq} + \sqrt{3}(P_{CA}^{eq} - P_{AB}^{eq})\big), \tag{7.18b}$$

$$Q_{CA}^{c,\Delta} = \tfrac{1}{3}\big(Q_{BC}^{eq} + Q_{AB}^{eq} - 2Q_{CA}^{eq} + \sqrt{3}(P_{AB}^{eq} - P_{BC}^{eq})\big). \tag{7.18c}$$

Case 2: Delta and Wye Load, Delta PV, Eliminate V_2

When some or all loads are wye-connected, (7.18) can still be applied to eliminate V_2. However, the wye-connected loads must first be transformed into equivalent delta-connected loads with delta-load currents I_{AB}^{eq}, I_{BC}^{eq}, I_{CA}^{eq} together with wye-connected loads with zero-sequence current $I_0^{eq} = (I_A^m + I_B^m + I_C^m)/3$ flowing in each phase, as shown in Fig. 7.3b. Then, V_2 can be eliminated by balancing the equivalent delta-connected load.

Case 3: Wye PV, Eliminate V_2

We next consider the case in which PV systems are wye-connected, as shown in Fig. 7.3c, and the goal is to eliminate negative-sequence voltage unbalance V_2. Again, we need to drive I_2 to zero, but in this case we must compute the change in reactive power injections needed from wye-connected PV systems, $Q_A^{c,Y}$, $Q_B^{c,Y}$, $Q_C^{c,Y}$. Using the Fortescue transformation, we derive an equation equivalent to (7.15) but in terms of the line currents for the compensated system,

$$3I_2^c = I_A^c + a^2 I_B^c + a I_C^c = 0, \tag{7.19}$$

where

$$I_A^c = \Big(\frac{S_A^m + jQ_A^{c,Y}}{V_A^c}\Big)^*, \tag{7.20a}$$

$$I_B^c = \Big(\frac{S_B^m + jQ_B^{c,Y}}{V_B^c}\Big)^*, \tag{7.20b}$$

$$I_C^c = \Big(\frac{S_C^m + jQ_C^{c,Y}}{V_C^c}\Big)^*. \tag{7.20c}$$

Eliminating V_2 balances the line-to-line voltages but does not necessarily balance the line-to-neutral voltages, as zero-sequence voltage V_0 may be nonzero. Nevertheless, if we assume line-to-neutral voltages are balanced,

$$V_B^c = a^2 V_A^c, \quad V_C^c = aV_A^c. \tag{7.21}$$

and set the sum of the changes in reactive power injections to zero, we derive the reactive power compensation strategy,

$$Q_A^{c,Y} = \tfrac{1}{3}\big(Q_C^m + Q_B^m - 2Q_A^m + \sqrt{3}(P_B^m - P_C^m)\big), \tag{7.22a}$$
$$Q_B^{c,Y} = \tfrac{1}{3}\big(Q_A^m + Q_C^m - 2Q_B^m + \sqrt{3}(P_C^m - P_A^m)\big), \tag{7.22b}$$
$$Q_C^{c,Y} = \tfrac{1}{3}\big(Q_B^m + Q_A^m - 2Q_C^m + \sqrt{3}(P_A^m - P_B^m)\big). \tag{7.22c}$$

If the zero-sequence voltage V_0 is non-negligible, (7.21) may not be a good approximation. In such cases, it may be better to approximate the line-to-neutral voltages for the compensated system with the measured voltages,

$$V_A^c = V_A^m, \quad V_B^c = V_B^m, \quad V_C^c = V_C^m. \tag{7.23}$$

Then, the three-phase reactive power compensation strategy is given by the solution of,

$$\mathrm{Re}\{I_2^c\} = \mathrm{Im}\{I_2^c\} = 0, \tag{7.24a}$$
$$Q_A^{c,Y} + Q_B^{c,Y} + Q_C^{c,Y} = 0. \tag{7.24b}$$

Because of the approximation (7.21) or (7.23), the change in reactive power injections will not perfectly eliminate V_2. However, V_2 generally converges close to zero with feedback.

Case 4: Wye PV, Eliminate V_0

Case 4 assumes the same connections as Case 3 (see Fig. 7.3c) but drives the zero-sequence current to zero,

$$3I_0^c = I_A^c + I_B^c + I_C^c = 0. \tag{7.25}$$

If we assume the voltages are balanced (7.21), then the reactive power compensation strategy is given by,

$$Q_A^{c,Y} = \tfrac{1}{3}\big(Q_C^m + Q_B^m - 2Q_A^m + \sqrt{3}(P_C^m - P_B^m)\big), \tag{7.26a}$$
$$Q_B^{c,Y} = \tfrac{1}{3}\big(Q_A^m + Q_C^m - 2Q_B^m + \sqrt{3}(P_A^m - P_C^m)\big), \tag{7.26b}$$
$$Q_C^{c,Y} = \tfrac{1}{3}\big(Q_B^m + Q_A^m - 2Q_C^m + \sqrt{3}(P_B^m - P_A^m)\big). \tag{7.26c}$$

However, eliminating V_0 may increase V_2, resulting in unbalanced line-to-line voltages and, subsequently, unbalanced line-to-neutral voltages. Alternatively, we can set the voltages to their measured values, as in (7.23). Then, the compensation strategy has the same form as (7.24) but with (7.24a) replaced by,

$$\mathrm{Re}\{I_0^c\} = \mathrm{Im}\{I_0^c\} = 0. \tag{7.27}$$

Because of the voltage approximation, feedback is again used to drive V_0 close to zero.

Case 5: Delta and Wye PV, Eliminate V_2 and V_0

Finally, Case 5 uses delta- and wye-connected PV systems, as shown in Fig. 7.3d, to eliminate both zero- and negative-sequence unbalance. In this case, both line-to-line and line-to-neutral voltages are balanced, and so both (7.7) and (7.21) are satisfied. Setting the negative- and zero-sequence currents equal to zero, applying (7.7) and (7.21), setting the sum of the reactive power injections to zero, and solving the resulting system of equations, we obtain the reactive power compensation strategy,

$$Q_A^{c,Y} = \tfrac{1}{3}\big(Q_C^m + Q_B^m - 2Q_A^m + \sqrt{3}(P_C^m - P_B^m)\big), \tag{7.28a}$$
$$Q_B^{c,Y} = \tfrac{1}{3}\big(Q_A^m + Q_C^m - 2Q_B^m + \sqrt{3}(P_A^m - P_C^m)\big), \tag{7.28b}$$
$$Q_C^{c,Y} = \tfrac{1}{3}\big(Q_B^m + Q_A^m - 2Q_C^m + \sqrt{3}(P_B^m - P_A^m)\big), \tag{7.28c}$$
$$Q_{AB}^{c,\Delta} = \tfrac{2}{\sqrt{3}}\big(P_B^m - P_A^m\big), \tag{7.28d}$$
$$Q_{BC}^{c,\Delta} = \tfrac{2}{\sqrt{3}}\big(P_C^m - P_B^m\big), \tag{7.28e}$$
$$Q_{CA}^{c,\Delta} = \tfrac{2}{\sqrt{3}}\big(P_A^m - P_C^m\big). \tag{7.28f}$$

7.5 Feedback Controllers for Distributed PV

In this section, we first introduce two command strategies; we then detail the design of decentralized and distributed feedback controllers which implement the reactive power compensation strategies of Section 7.4. Recall that the strategies were derived assuming that reactive power compensation is provided by a three-phase PV systems at the critical node, or an equivalent collection of single-phase PV systems. We heuristically apply these strategies to control single-phase PV systems distributed across the network. Section 7.5.4 describes the model-free controller from [12], which is used as a benchmark.

7.5.1 Command Strategy

In this work, we propose two different command strategies as follows.

- **Direct command strategy**: The command is the *total* amount of reactive power that the PV system should provide. If the PV systems have already injected reactive power in the previous time step, the measured power demand includes those injections, thus, they should be excluded when we use the reactive power compensation strategies of Section 7.4. The controller will exclude the previous command when we compute the new command.

- **Differential command strategy**: The command is the *change* of reactive power that the PV system should provide. Specifically, we do not subtract the previous command, but instead determine the change in reactive power injections needed to balance the bus.

The two command strategies are identical if we have (7.17) and ignore inverter reactive power limits. The proof is provided in Section 8.2.2. When we consider the limits, the differential command strategy works better. Again, an example will be shown in Section 8.4.2. Instead of (7.17), we can set the total injected reactive power to any specific value. For example, the total reactive power injection of (7.11) is not zero, in that case, the direct command strategy should be used.

In this chapter, since the reactive power compensation strategies of Section 7.4 are derived based on (7.17), we will use the the differential command strategy unless we explicitly state that the direct command strategy is used. When we use the differential command strategy,

the reactive power injections are sent to each PV system in proportion to its ratings, i.e.,

$$Q_i^c = Q_\phi^c \times \frac{S_i^{\text{rate}}}{\sum_{j \in \Omega_\phi} S_j^{\text{rate}}}, \tag{7.29}$$

where Q_ϕ^c is the change in reactive power injection required from phase ϕ and Ω_ϕ is the set of downstream PV systems that are connected to phase ϕ.

7.5.2 Decentralized Controller

The decentralized controller attempts to balance all three-phase nodes simultaneously, thereby balancing the critical node. Applying the compensation strategies from Section 7.4 will, in general, not achieve perfect balance because, i) reactive power injections are limited by PV phase connections and time-varying reactive power limits (7.2), and ii) Steinmetz design is applied at multiple nodes simultaneously instead of just the critical node. Each three-phase node with a participating PV system undertakes the same actions:

- Use local measurements S^m and V^m to compute Q^c corresponding to PV system phase connections and balancing objective by applying the appropriate compensation strategy from Section 7.4.
- Use local PV systems to change reactive power injections by Q^c or, if impossible because of the PV system phase connections and/or reactive power limits, a quantity as close as physically possible to Q^c. In cases with multiple PV systems at a node, Q^c can be allocated to individual systems based on apparent power ratings as in (7.29) and/or reactive power limits.
- Repeat this process periodically with the latest local measurements.

If the unbalance is large and each PV system's reactive power injection capabilities are small, this approach works well, as discussed in Section 7.6. However, it can also lead to over-injection. For example, two nearby nodes will calculate similar Q^c but only one node's injection needs to change by Q^c to approximately balance both nodes. Responses at both nodes may result in overcompensation of the VUF and lead to oscillations in the feedback process. Heuristic methods to address this issue include decreasing the number of participating PV systems and/or ensuring asynchronous adjustments across nodes.

7.5.3 Distributed Controller

The distributed controller seeks to balance the critical node using PV systems downstream of the critical node. This scheme is more consistent with the assumptions underpinning the compensation strategies of Section 7.4 than is the decentralized controller. Perfect balancing is still not possible, though, because the effective changes in reactive power injections seen at the critical bus will not exactly match Q^c due to reactive power losses on the lines between the critical node and the downstream PV systems. Implementing the controller within a feedback loop can, however, eliminate this issue. Specifically, the critical node completes the following actions:

- Use measurements S^m and V^m at the critical node to compute Q^c corresponding to PV system phase connections and balancing objective by applying the appropriate compensation strategy from Section 7.4.
- Allocate Q^c to each participating PV system using (7.29) and send commands via the communication network. Each PV system implements its change in reactive power injection Q_i^c or, if impossible, sets its reactive power injection equal to its reactive power limit $Q_{i,t}^{\max}$.
- Repeat this process periodically with the latest measurements.

In general, the distributed controller performs better than the decentralized controller, as shown in Section 7.6.

7.5.4 Benchmark: Model-free Controller

We compare the performance of our controllers with that of the model-free controller proposed in [12]. The objective of the model-free controller is to equalize the line-to-line voltage magnitudes or line-to-neutral voltage magnitudes by injecting (consuming) reactive power into the phases with voltage magnitudes lower (higher) than the average. We assume conditions consistent with those of the distributed controller, namely measurements are taken at the critical node and then changes in reactive power injections are computed and allocated to downstream PV systems using (7.29). This sequence is implemented as a feedback loop. However, instead of using the compensation strategies derived in Section 7.4, the strategy in this case is given by,

$$Q_\phi^c = k(|V_\phi^m| - \overline{V}), \quad \forall \phi, \tag{7.30}$$

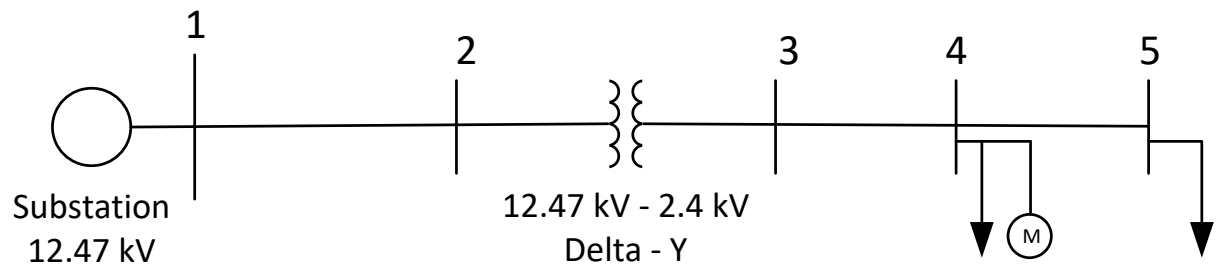

Figure 7.4: One-line diagram of a 5-bus distribution system.

where $\phi \in \{AB, BC, CA\}$ and $\overline{V} = (|V^m_{AB}| + |V^m_{BC}| + |V^m_{CA}|)/3$ for line-to-line connected PV systems, or $\phi \in \{A, B, C\}$ and $\overline{V} = (|V^m_A| + |V^m_B| + |V^m_C|)/3$ for line-to-neutral connected PV systems, and $k > 0$ is a scalar gain.

7.6 Case Studies

In this section, we first test the performance of Steinmetz design on a small delta-connected system (Case 1). Next, We conducted case studies using the IEEE 13-node feeder [58] and the taxonomy feeder R1-12.47-1 [107]. Both feeders are four-wire systems with a mixture of delta- and wye-connected loads, so we are able to explore Cases 2–5. We first provide feeder details and then use the 13-node feeder to assess and compare the performance of controllers. The controllers are then tested on the R1-12.47-1 feeder, and the impact on system losses is assessed.

7.6.1 Toy System

We first conduct a number of studies on a simple five bus radial distribution system shown in Fig. 7.4. We assume that the voltage source is balanced (12.47 kV line-to-line), a delta-grounded wye transformer is connected between buses 2 and 3 (2000 kVA, 12.47 kV - 2.4 kV, $Z = 1 + j6$ pu), all line segments are balanced ($Z_{l,1-2} = 0.0924 + j0.2128\ \Omega, Z_{l,3-4} = Z_{l,4-5} = 0.3061 + j0.627\ \Omega$), unbalanced three-phase delta-connected loads are connected to buses 4 and 5 (modeled as either constant impedance or constant power loads), and a three-phase compensator (three-phase controllable reactances or three-phase PV system with controllable reactive power injections) is connected to bus 4 or 5. We wish to balance bus 4 since we assume some equipment sensitive to voltage unbalance, such as a three-phase

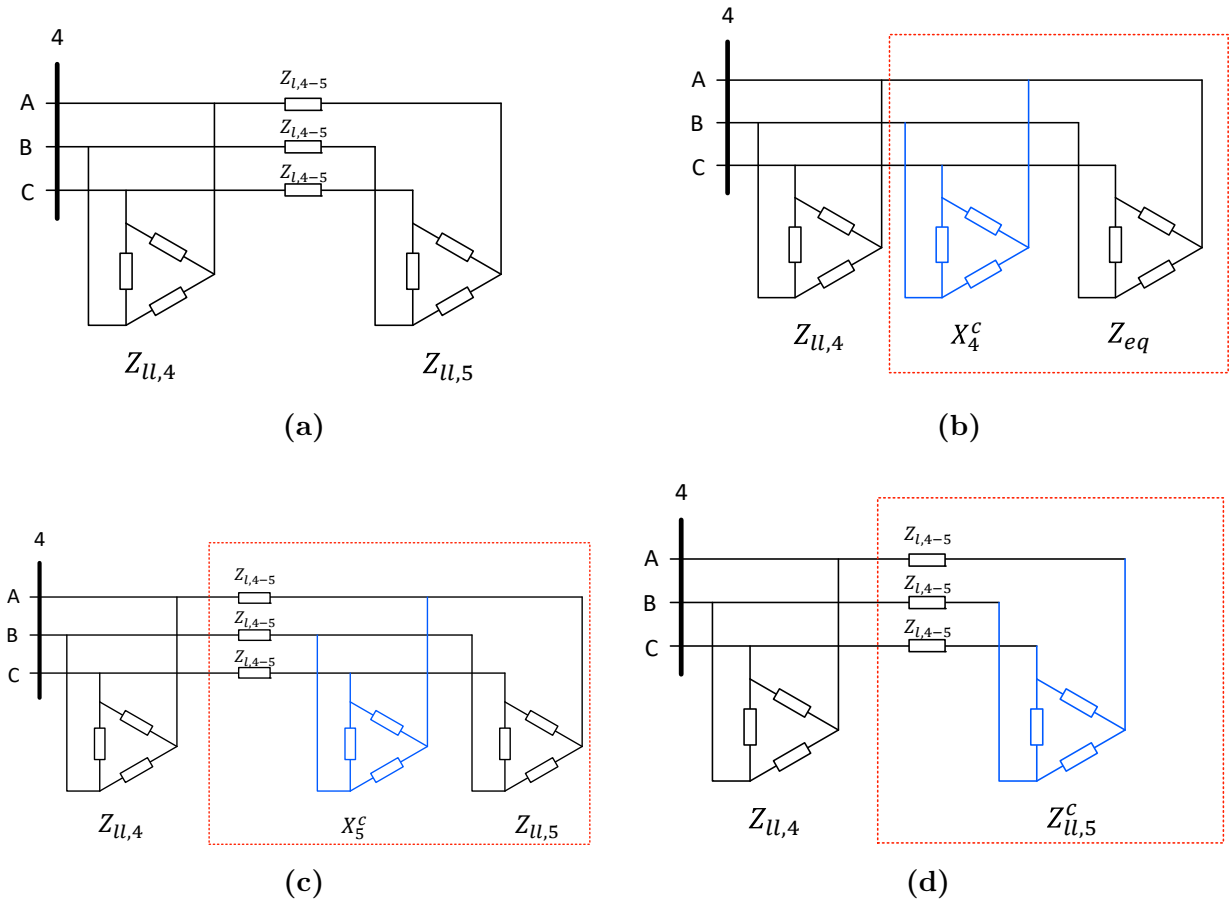

Figure 7.5: Three-phase system as seen from bus 4. (a) the base case. (b) balancing equipment at bus 4. (c) balancing equipment at bus 5. (d) equivalent circuit to (b) needed to compute X_5^c.

motor, is connected to this bus. We do not model voltage regulators. We also assume that the compensator reactances or reactive power injections are unconstrained. We use (7.10) to compute reactances and (7.11) to compute reactive power. The direct command strategy is used for the feedback control. Note that in this example, VUF refers to negative sequence voltage unbalance factor VUF_2, the subscript represents the bus number.

Compensator with three-phase controllable reactances: constant impedance load

We first show how to apply the Steinmetz circuit design to balance the voltage at bus 4 when we control the reactances (X^c). We assume that the loads are constant impedance

loads with three-phase impedances[2] $Z_{ll,4} = [300 + j150; 520 + j250; 200 + j760]\,\Omega, \quad Z_{ll,5} = [220 + j130; 320 + j180; 250 + j430]\,\Omega$. Without compensation, $VUF_4\% = 0.262\%$. The three-phase load connections and line are shown in Fig. 7.5a.

Scenario 1: Compensator at bus 4. When the controllable reactances are connected to bus 4, as shown in Fig. 7.5b, the equivalent impedance of the downstream circuit Z_{eq} can be computed using the delta-wye transformation, and then the total unbalanced load at bus 4 can be obtained. The compensating reactances are:

$$X_4^c = [j152.8; j278.95; j151.1]\ \Omega,$$

which completely balances the voltage at bus 4.

Scenario 2: Compensator at bus 5. When the controllable reactances are connected at bus 5, as shown in Fig. 7.5c, the computation of X_5^c works as follows. From Scenario 1, we know the equivalent impedeance of the load in the red box in Fig. 7.5b. We can use it to compute the impedance $Z_{ll,5}^c$ shown in Fig. 7.5d. The difference between $Z_{ll,5}^c$ and $Z_{ll,5}$ is what should be compensated at bus 5 to balance the voltage at bus 4. However, the difference may not be purely reactance so the voltage unbalance at bus 4 may not be completely eliminated because the compensator is not able to provide resistance. Applying this procedure, we obtain:

$$Z_{ll,5}^c = [38.8 + j99.78; 78.6 + j163.4; 13.4 + j116.1]\ \Omega$$

$$\frac{1}{X_5^c} = \text{Im}\left\{\frac{1}{Z_{ll,5}^c} - \frac{1}{Z_{ll,5}}\right\}$$

$$X_5^c = [148.95; 275.04; 147.92]\ \Omega$$

which results in $VUF_4\% = 0.0041\%$.

Compensator with three-phase controllable reactive power: constant impedance load

We next use a three-phase PV inverter to balance the voltage at bus 4 assuming constant impedance loads. We first compute the compensating reactances and then use them together

[2]Impedances are given in the order AB, BC, CA.

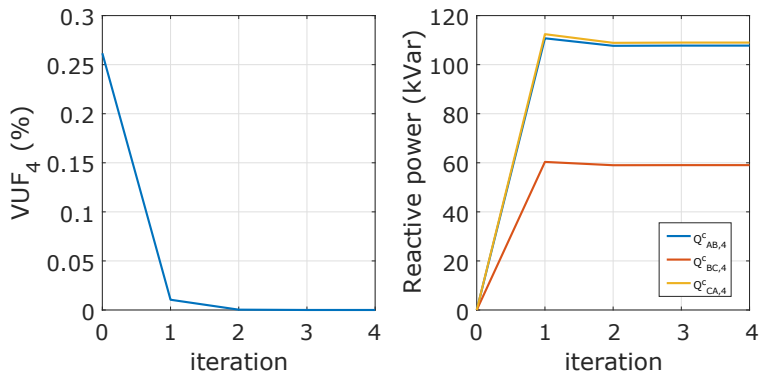

Figure 7.6: Convergence of voltage unbalance factor (VUF) at bus 4 and reactive power injections at bus 4 when load is modeled as constant impedance.

with measurements of the line to line voltages to obtain the reactive power injections:

$$Q^c_{AB,m} = \frac{|V_{AB,m}|^2}{X^c_{AB,m}} \; Q^c_{BC,m} = \frac{|V_{BC.m}|^2}{X^c_{BC,m}} \; Q^c_{CA,m} = \frac{|V_{CA,m}|^2}{X^c_{CA,m}} \tag{7.31}$$

where m refers to the bus where the PV system is connected.

Scenario 3: Compensator at bus 4. Using X^c_4 from Scenario 1 and the measured voltages at bus 4, the compensating reactive power injections in kVAr are:

$$[Q^c_{AB,4};\; Q^c_{BC,4};\; Q^c_{CA,4}] = [110.7424;\; 60.3547;\; 112.4241].$$

which results in $VUF_4\% = 0.0104\%$.

Scenario 4: Compensator at bus 5. Using X^c_5 from Scenario 2 and measured voltages at bus 5, the compensating reactive power injections in kVAr are:

$$[Q^c_{AB,5};\; Q^c_{BC,5};\; Q^c_{CA,5}] = [112.4583;\; 60.4614;\; 113.8552].$$

which results in $VUF_4\% = 0.0225\%$.

In both scenarios, Steinmetz circuit design fails to balance the voltage at bus 4. This is because we use the measured voltage to compute the reactive power injections but the voltage changes after we inject the reactive power.

Scenario 5: Compensator at bus 4, feedback control. Figure 7.6 shows the convergence of VUF and reactive power injections if the PV system is located at bus 4. As we can see, the voltage unbalance at bus 4 is completely eliminated using feedback control. The

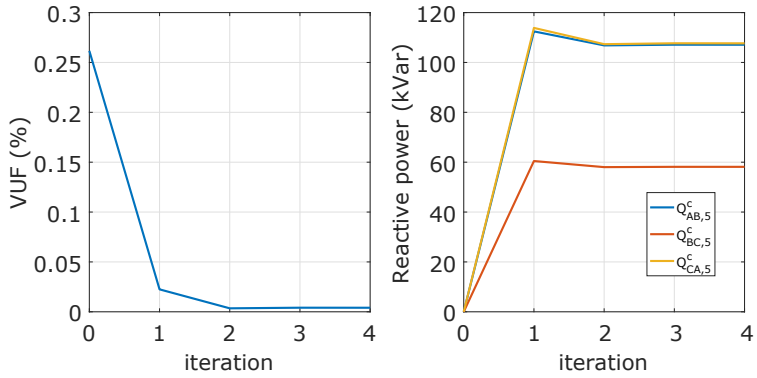

Figure 7.7: Convergence of voltage unbalance factor (VUF) at bus 4 and reactive power injections at bus 5 when load is modeled as constant impedance.

Table 7.4: Constant Power Loads at Buses 4 and 5

Bus 4	$\|S\|$	Power factor	Bus 5	$\|S\|$	Power factor
S_{AB}	40 kVA	0.95 lagging	S_{AB}	50 kVA	0.85 lagging
S_{BC}	20 kVA	0.80 lagging	S_{BC}	30 kVA	0.90 lagging
S_{CA}	70 kVA	0.85 lagging	S_{CA}	100 kVA	0.95 lagging

compensating reactive power injections in kVAr are:

$$[Q^c_{AB,4};\ Q^c_{BC,4};\ Q^c_{CA,4}] = [107.7651;\ 59.0437;\ 108.9941].$$

Scenario 6: Compensator at bus 5, feedback control. Figure 7.7 shows the convergence of VUF and reactive power injections if the PV system is located at bus 5. The compensating reactive power injections in kVAr are:

$$[Q^c_{AB,5};\ Q^c_{BC,5};\ Q^c_{CA,5}] = [107.1048;\ 58.1325;\ 107.6737],$$

However, like in Scenario 2, the PV inverters can not completely balance the voltage because they only inject reactive, not real, power. As in Scenario 2, $VUF_4\% = 0.0041\%$.

Compensator with three-phase controllable reactive power: constant power load

Next, we use a three-phase PV inverter to balance the voltage at bus 4 assuming constant power loads, given in Table 7.4. Without compensation, $VUF_4\% = 0.5495\%$.

Scenario 7: Compensator at bus 4. The compensating reactive power injections in

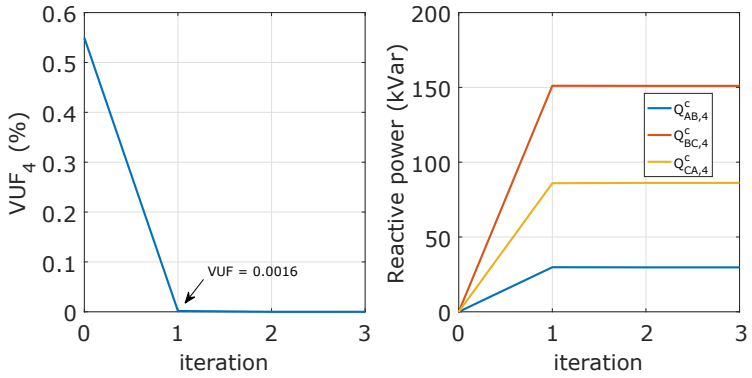

Figure 7.8: Convergence of voltage unbalance factor (VUF) at bus 4 and reactive power injections at bus 4 when load is modeled as constant power.

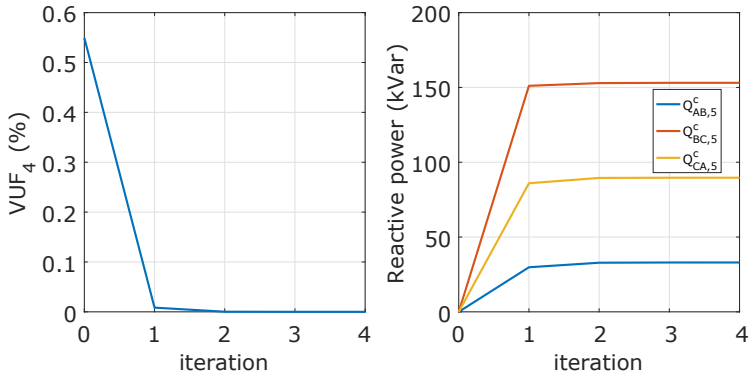

Figure 7.9: Convergence of voltage unbalance factor (VUF) at bus 4 and reactive power injections at bus 5 when load is modeled as constant power.

kVAr are:

$$[Q^c_{AB,4};\ Q^c_{BC,4};\ Q^c_{CA,4}] = [29.7865;\ 151.0846;\ 85.9497]$$

which results in $VUF_4\% = 0.00016\%$. Steinmetz circuit design fails to balance the voltage at bus 4 because network losses change after the reactive power is injected. In Scenario 9 we show how feedback control can be used to eliminate the unbalance.

Scenario 8: Compensator at bus 5. When the loads are modeled as constant power loads, the procedure we used in Scenario 2 to compute the equivalent impedance (which was used in Scenarios 4 and 6 to determine the compensating reactive power injections) no longer works. Therefore, here, we simply apply the compensating reactive power injections we computed in Scenario 7 to bus 5 rather than bus 4, effectively neglecting the impact of the line impedance. This results in $VUF_4\% = 0.0084\%$.

Scenario 9: Compensator at bus 4, feedback control. Since Scenarios 7 and 8 show that Steinmetz circuit design fails to achieve balance for constant power loads, we again use feedback control strategy. Figure 7.8 shows the convergence of VUF and reactive power injections if the PV system is located at bus 4. As before, feedback control completely eliminates unbalance at bus 4. The compensating reactive power injections in kVAr are:

$$[Q^c_{AB,4};\ Q^c_{BC,4};\ Q^c_{CA,4}] = [29.6925;\ 151.0270;\ 86.1694].$$

Scenario 10: Compensator at bus 5, feedback control. Figure 7.9 shows the convergence of VUF and reactive power injections if the PV system is located at bus 5. The compensating reactive power injections in kVAr are:

$$[Q^c_{AB,5};\ Q^c_{BC,5};\ Q^c_{CA,5}] = [32.9862;\ 153.0851;\ 89.6489]$$

which completely eliminates the unbalance at bus 4.

Scenario 6 (modified): Compensator at bus 5, feedback control. As shown in Scenario 10, Steinmetz circuit design within a feedback control is able to balance an upstream bus using the downstream PV system; therefore, it is possible that we can also achieve perfect balance in Scenario 6. Unlike computing the compensating reactive power based on the computed compensating reactances, we alternatively model loads as constant power (even though they are constant impedance models) and measure the voltages and currents to compute the overall unbalanced power demand at bus 4. The feedback is then applied as in Scenario 10. Figure 7.10 shows the convergence of VUF, bus 4 now is balanced compared to Fig. 7.7. The compensating reactive power injections in kVAr are:

$$[Q^c_{AB,5};\ Q^c_{BC,5};\ Q^c_{CA,5}] = [109.5717;\ 61.5492;\ 110.6029].$$

Table 7.5 summarizes the scenario descriptions and results. As shown, Steinmetz circuit design is only able to perfectly balance the voltage at the bus the compensator is connected to and only if the loads are modeled as constant impedance loads. However, it can significantly improve balance in all Scenarios. In contrast, use of Steinmetz circuit design within a feedback controller can achieve perfect balance in all scenarios. As shown in the Figs. 7.6 - 7.10, the feedback controller quickly converges.

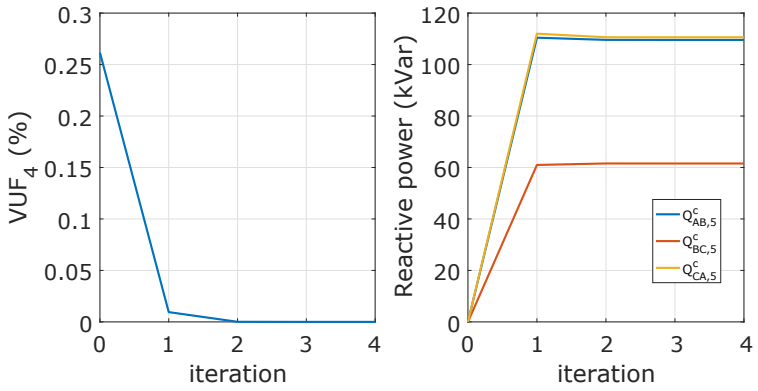

Figure 7.10: Convergence of voltage unbalance factor (VUF) at bus 4 and reactive power injections at bus 5 when we model constant impedance load as constant power.

Table 7.5: Summary of scenario descriptions and results

Scenario #	Load model	Compensator Type	Compensator Bus	Strategy	Initial $VUF_4\%$	Final $VUF_4\%$
1		X^c	4	Steinmetz		0
2		X^c	5	Steinmetz		0.0043
3		Q^c	4	Steinmetz		0.0085
4	Z	Q^c	5	Steinmetz	0.2798	0.0221
5		Q^c	4	feedback (Z)		0
6		Q^c	5	feedback (Z)		0.0043
6*		Q^c	5	feedback (P)		0
7		Q^c	4	Steinmetz		0.0018
8	P	Q^c	5	Steinmetz	0.5891	0.0091
9		Q^c	4	feedback (P)		0
10		Q^c	5	feedback (P)		0

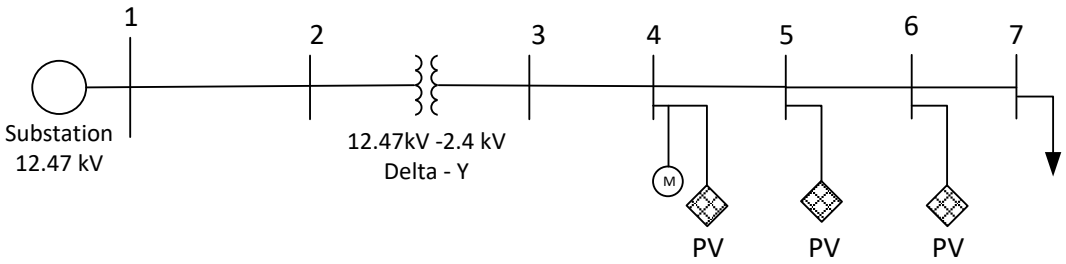

Figure 7.11: One-line diagram of a 7-bus distribution system.

Steinmetz Circuit Design Applied to Distributed Solar PV

Lastly, we explore the performance of Steinmetz circuit design on a network with distributed single phase PV systems. Figure 7.11 shows the seven bus distribution system we use, with single-phase PV systems connected to buses 4, 5, and 6. We assume that the voltage source is balanced (12.47 kV line-to-line), a delta-grounded wye transformer is connected between buses 2 and 3 (2000 kVA, 12.47 kV - 2.4 kV, $Z = 1 + j6$ pu), the impedance of all line segments is $0.0924 + j0.2128\ \Omega$, the PV system at bus 4 is connected AB and generating 50 kW, the PV system at bus 5 is connected BC and generating 80 kW, and the PV system at bus 6 is connected CA and generating 100 kW. Bus 7 has an unbalanced three-phase constant power load ($|S_{AB,7}| = 200$ kVA at 0.8 lagging, $|S_{BC,7}| = 50$ kVA at 0.9 lagging, $|S_{CA,7}| = 300$ kVA at 0.95 lagging) and, as before, we wish to balance bus 4. Initially, $VUF_4\% = 0.6455\%$.

With the decentralized controller, $VUF\% = 0.071\%$. The VUF at bus 4 is completely eliminated using the distributed controller, as shown in Fig. 7.12. As seen from this example, Steinmetz circuit design is able to significantly reduce voltage unbalance in a completely decentralized manner, and we can further reduce the unbalance when communication is available.

7.6.2 Feeder Description

Fig. 7.13 shows the one-line diagram of the IEEE 13-node feeder [58], with system data available in [66]. To accentuate unbalance, the loading at each node was increased by 10%. We chose the critical node to be 632. Upstream unbalance was eliminated by setting the regulator taps to be identical (to tap 11) in each phase and transposing line 630-632 (with self phase impedance $0.2124 + j0.6422\ \Omega$/km and mutual phase impedance $0.0968 + j0.2714\ \Omega$/km). We

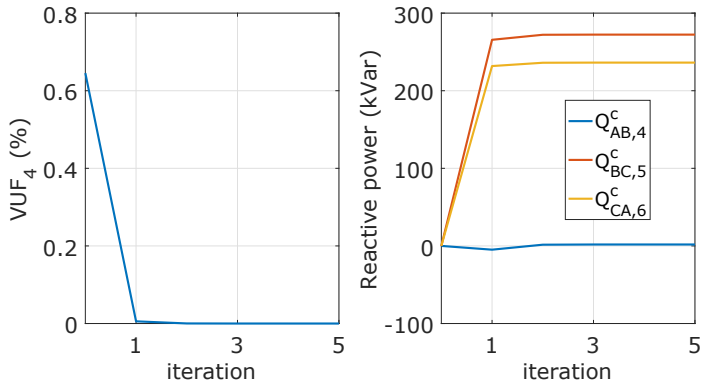

Figure 7.12: Convergence of voltage unbalance factor (VUF) at bus 4 and reactive power injection at each distributed PV.

Table 7.6: Single-phase PV systems added to 13-node feeder

#	1	2	3	4	5	6	7	8	9	10	11
Location	632	633	634	645	646	671	652	611	680	692	675
Phase	2	1	1	2	2	1	3	3	2	3	1
P (kW)	100	150	60	100	100	50	100	50	50	100	110

also changed lines 684-652 and 684-611 to three-phase lines to enable addition of line-to-line connected PV systems at nodes 611 and 652. For those lines, we used the same configuration and parameters as line 671-684.

Eleven single-phase PV systems were added as shown in Fig. 7.13. The location, phase, and active power output of each PV system is listed in Table 7.6, where the phase identifiers 1, 2, 3 refer to AB, BC, CA, respectively, for PV systems connected line-to-line, or A, B, C, respectively, for PV systems connected line-to-neutral. When exploring the different cases summarized in Table 7.3, the PV connections were changed to match the case, i.e., for Cases 1 and 2 the single-phase PV systems were connected line-to-line, and for Cases 3 and 4, they were connected line-to-neutral. For Case 5, PV systems 1 to 7 were connected line-to-line and PV systems 8 to 11 were connected line-to-neutral. Nodes 645, 646, 652, and 611 are not three-phase nodes and so PV systems at those nodes were not controlled by the decentralized controller. All PV systems are rated at $S^{\text{rate}} = 300$ kVA and operate at unity power factor when uncontrolled. The total active power generation is 970 kW, which is around 25% of the system load (3813 kW).

Fig. 7.14 shows the one-line diagram of the R1-12.47-1 feeder, which is representative of

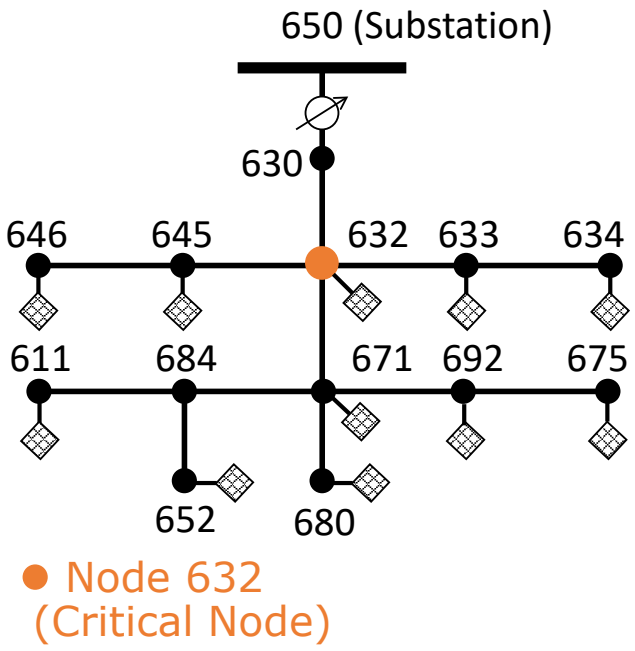

Figure 7.13: IEEE 13-node feeder[58] with single-phase PV system added.

a moderately populated suburban and rural area. System data can be found in [107]. The critical node is 359. To increase unbalance, 961 kW of load representing seasonal agricultural pumping was added to phase C. This increased the system load to 8237 kW. PV systems were added to 598 single family residences, with 265, 150, and 183 of those systems connected to phases AB, BC, CA for Case 2, or to phases A, B, C for Cases 3 and 4. For Case 5, all PV systems downstream of node 216 were connected line-to-line and the rest line-to-neutral. All PV systems were rated at $S^{\text{rate}} = 10$ kVA. Their active power output was randomly selected from the range 1 to 5 kW, and they operate at unity power factor when uncontrolled. The total active power generation is 1773 kW, which is around 21.5% of the system load. Full details of all the feeder modifications are available in the feeder file [144].

For all simulations, we assumed the net load at each node was constant. We ran the controllers until the unbalance converged. This is reasonable since the controllers converge quickly.

7.6.3 IEEE 13-node Feeder Results

We first use the distributed controller to compare the results of Cases 2 to 5. Table 7.7 summarizes the initial and final VUF_2 and VUF_0 at the critical node, and reports the total

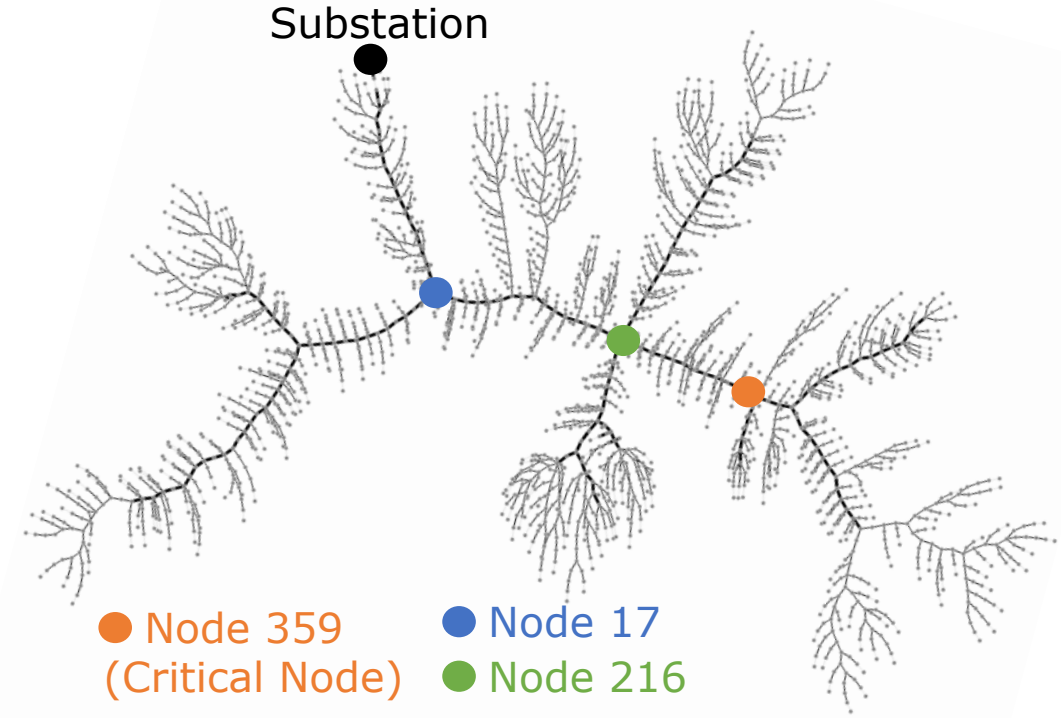

Figure 7.14: Taxonomy feeder R1-12.47-1 [107] visualized using [99].

reactive power injections for each case. The initial VUFs differ for different PV system connections. Cases 2 and 3 only seek to eliminate negative-sequence unbalance but zero-sequence unbalance remains unaddressed. The opposite is true for Case 4. Case 5 eliminates both forms of unbalance. Despite the differences between the assumptions underlying the compensation strategies and the actual controller implementation, the controllers are able to exactly meet their unbalance objectives because of feedback. Note that the results for Cases 3 and 4 were generated using the measured voltages (7.23). Compensation strategies (7.22) and (7.26) used within feedback loops significantly decrease the unbalance but do not drive it exactly to zero.

We next compare the performance of the decentralized, distributed, and model-free controllers for Case 2. Results for the other cases are similar. Fig. 7.15 shows the VUF_2 of all three-phase nodes initially and after applying the controllers. The initial VUF_2 at the critical node (node 632) is 0.79% and the line-to-line voltage magnitudes are 1.035, 1.042, and 1.028 pu. The decentralized controller reduces the VUF_2 at the critical node to 0.46% and both the distributed and the model-free controllers (gain $k = 5$) reduce it to 0% with line-to-line voltage magnitudes of 1.035 pu. While the decentralized controller is able to

Table 7.7: Unbalance and Reactive Power Injections by Case

Case	VUF_2 (%)		VUF_0 (%)		Q^c (kVar)			
	Initial	Final	Initial	Final				
2	0.79	0.00	1.68	1.57	$Q^{c,\Delta} =$	[-133.15	403.68	270.53]
3	0.77	0.00	3.93	3.24	$Q^{c,Y} =$	[-341.80	315.35	26.45]
4	0.77	1.03	3.93	0.00	$Q^{c,Y} =$	[161.581	66.21	-227.79]
5	0.70	0.00	1.46	0.00	$Q^{c,\Delta} =$	[-365.05	402.75	-37.70]
					$Q^{c,Y} =$	[61.23	145.76	-207.00]

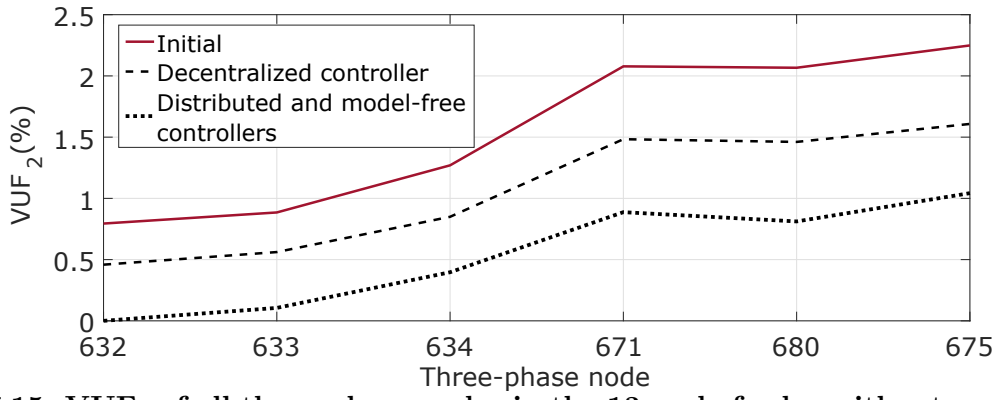

Figure 7.15: VUF_2 of all three-phase nodes in the 13-node feeder without control (initial) and after applying the controllers of Case 2.

significantly reduce voltage unbalance with only local measurements, the distributed and model-free controllers are able to completely eliminate it, but both require a communication network. In all cases, since the sum of the reactive power injections is zero, the voltage profiles of the controlled systems are similar to that of the uncontrolled system, and the regulator taps do not change.

Fig. 7.16 shows the convergence of VUF_2 and three-phase reactive power injections for each controller. The distributed and model-free controllers converge to the same reactive power injections. The distributed controller converges faster but requires voltage phasor measurements rather than just voltage magnitude measurements. The convergence of the model-free controller is sensitive to the choice of k, though large k does not necessarily lead to faster convergence. For $k = 20$, the controller requires more iterations to converge, with the high gain inducing oscillations in the reactive power injections, as seen in Fig. 7.17.

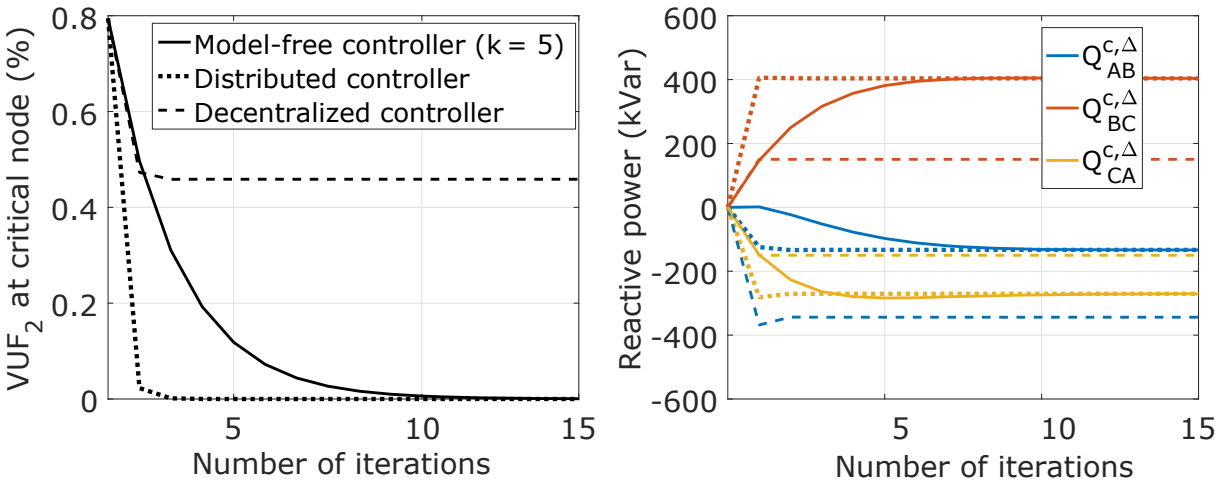

Figure 7.16: Convergence of VUF_2 at the critical node (left) and the reactive power injections (right) using different controllers.

7.6.4 Taxonomy R1-12.47-1 Feeder Results

Fig. 7.18 shows the VUF_2 of all three-phase nodes initially and after applying the controllers of Case 2. The initial VUF_2 at the critical node is 3.19%. The distributed controller implemented at the critical node reduced the VUF_2 at that node to 2.54%. Since the node is far from the substation, there are only 124 downstream PV systems and so there is insufficient reactive power capacity to balance the downstream load. Moreover, there is significant upstream unbalance and so the critical node would remain unbalanced even if it were possible to completely balance the downstream load. Since balancing upstream nodes generally improves downstream unbalance, as shown in Fig. 7.15, we implemented the distributed controller at node 17 (shown in Fig. 7.14) and achieved a much better result. VUF_2 at node 17 decreased from 1.63% to 0.39%, and at the critical node to 1.02%. Convergence was achieved in 3 iterations. Fig. 7.18 also shows the results of the decentralized controller, which achieved VUF_2 at the critical node of 1.57%.

7.6.5 Impact of Balancing on Losses

Table 7.8 summarizes the VUF_2, zero-sequence current $|I_0|$ at the critical node (due to local plus downstream current), and power losses before and after implementing the distributed controller. For the R1-12.47-1 feeder, we use the controller implemented at node 17. Losses decrease with a reduction in zero-sequence current or a reduction in VUF_2; however, when

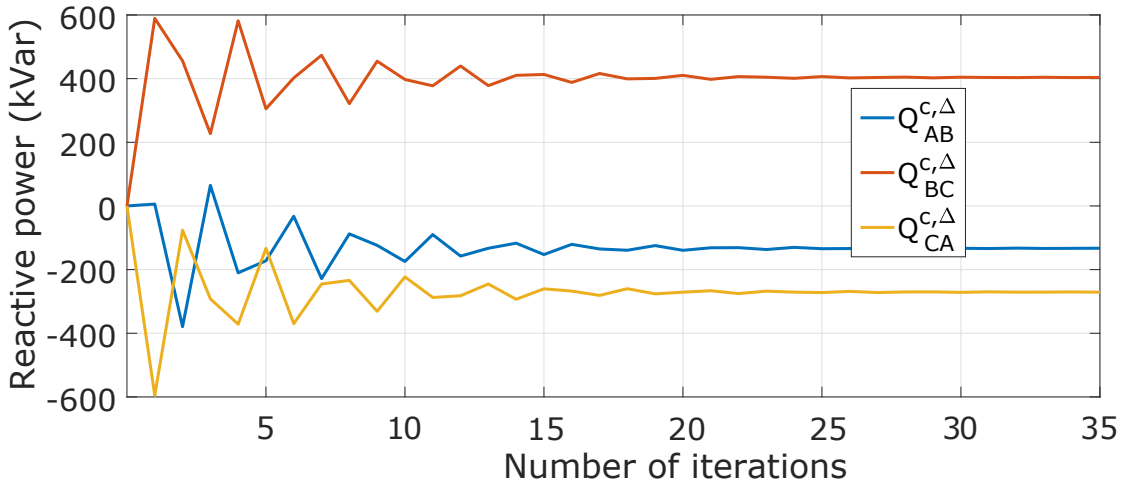

Figure 7.17: Convergence of reactive power injections using the model-free controller with $k = 20$.

Table 7.8: Impact on Zero-Sequence Current and Losses

Feeder	Case	VUF_2 (%)		$\lvert I_0 \rvert$ (A)		Losses (kW)	
		Initial	Final	Initial	Final	Initial	Final
13-node	2	0.79	0.00	54.69	51.14	95.30	91.58
	3	0.77	0.00	50.72	105.55	91.84	97.73
	4	0.77	1.03	50.72	0.00	91.84	90.61
	5	0.70	0.00	47.42	0.00	91.72	86.00
R1-12.47-1	2	3.19	1.02	30.25	27.96	401.08	382.60
	3	3.06	1.24	29.28	52.60	352.42	432.25
	4	3.06	4.45	29.28	4.34	352.42	408.01
	5	3.12	1.93	35.10	24.4	377.65	368.53

one increases and one decreases, the effect is complicated. When the PV systems are delta-connected (Case 2), the controller reduces the VUF_2 and does not introduce additional zero-sequence current and so losses decrease. When the PV systems are wye-connected and the goal is to reduce the VUF_2 (Case 3), the VUF_2 decreases, but zero-sequence current increases. For both feeders, losses increase. When the PV systems are wye-connected and the goal is to reduce the VUF_0 (Case 4), the VUF_2 increases, but zero-sequence current decreases significantly. The 13-node feeder experiences a small decrease in losses, but the R1-12.47-1 feeder sees an increase. In Case 5, both VUF_2 and zero-sequence current decrease and so losses decrease.

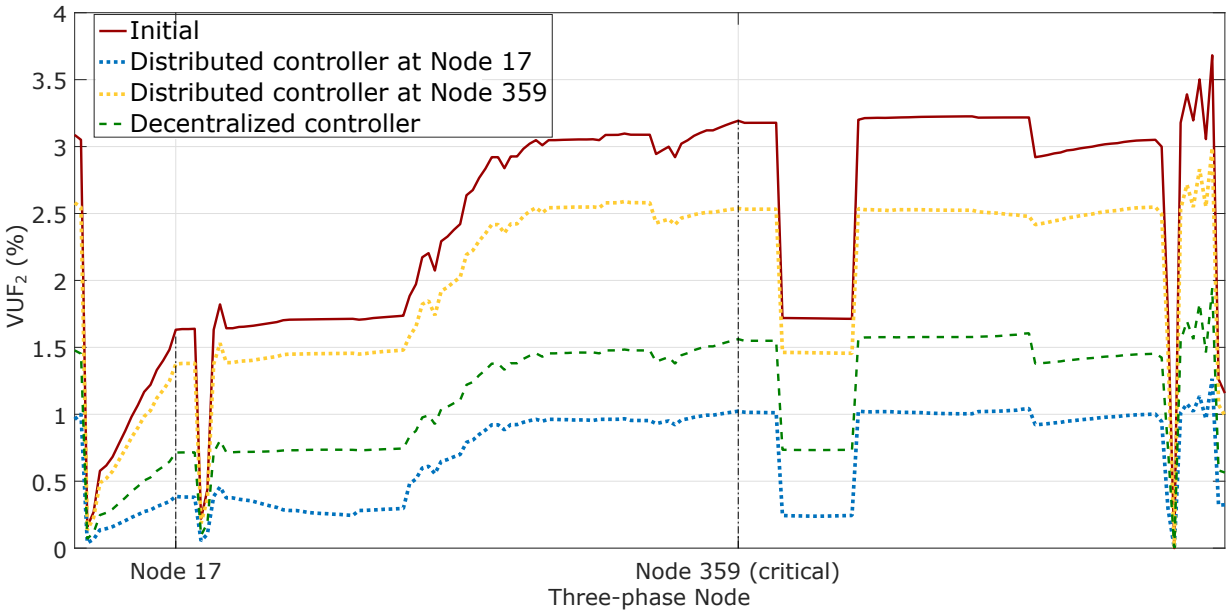

Figure 7.18: VUF_2 at all three-phase nodes in the R1-12.47-1 feeder without control (initial) and after applying the controllers of Case 2.

7.7 Chapter Conclusion

This chapter has proposed several controllers for mitigating voltage unbalance. They exploit Steinmetz design to control the reactive power injections of distributed single-phase PV systems. Performance has been demonstrated on small- and large-scale feeders. Feedback control is required to achieve better unbalance improvement. In contrast to feedback control approaches that drive voltages to predefined setpoints, our feedback control approach achieves voltage balance without the need for establishing voltage setpoints. The results suggest that the approach can be applied in a completely decentralized manner. Distributed control offers improved performance but requires communication infrastructure. Our case study indicated that when the critical node is far from the substation, rather than implementing the distributed controller at the critical node, better performance can be achieved by implementing the controller at an upstream node. The case study also highlighted trade-offs arising from different balancing objectives.

Chapter 8

Overcoming the Practical Challenges of Applying the Distributed Controller

In Chapter 7, we have shown that the Steinmetz approach is linear and uses only local measurements to compute the required compensating reactive power. The computation time is short and, therefore, the controller responds quickly to changes in operating point. The controller works well in ideal situations. In this chapter, we extend this controller to cope with a number of practical considerations, namely, inverter reactive power limits, noisy/erroneous measurements, and delayed inputs in the presence of time-varying load and PV generation. This chapter is largely based on the following paper.

- M. Yao and J.L. Mathieu. "Overcoming the practical challenges of applying Steinmetz circuit design to mitigate voltage unbalance using distributed solar PV". In: *Power Systems Computation Conference*. 2020.

8.1 Chapter Introduction

The goal of this chapter is to develop approaches that overcome the practical challenges of applying the distributed controller to real systems. The first challenge is managing PV inverter limitations, specifically, reactive power injection limits, which are a function of real power injections. Here, we will show that neglecting them significantly impacts the performance of the controller. The second challenge is managing measurement error/noise and communication delays. The approach requires local measurements of voltage and current

phasors; different measurement methods (e.g., distribution phasor measurement units (D-PMUs) versus using measurements from traditional meters to measure magnitudes and then compute phasors) lead to different measurement error/noise. We will show how measurement error/noise impacts the results. Additionally, the approach requires communication networks to send commands to downstream PV systems. In the previous chapter, we assume constant load and PV generation. We will show that large delays can lead to instability when load and PV generation are time-varying.

To address these practical challenges, we enhance the Steinmetz controller via improved algorithms. The main contributions of this chapter are as follow.

- We develop an approach to cope with inverter reactive power limits and strategies to cope with communication delays in the presence of time-varying load and PV real power generation; and
- we demonstrate the issues that can arise and the performance of the enhanced controller on a modified IEEE 13-node system, which has more severe unbalance than the original system [66], using real PV data (specifically, two different solar irradiation cases) together with realistic load data.

8.2 Controller Overview

In this chapter, Steinmetz controller refers to the distributed controller in Chapter 7. Moreover, PV systems are connected in delta configuration (Case 2 in Table 7.3), and thus, the unbalance factor is given by:

$$VUF = \frac{|V_A + a^2 V_B + a V_C|}{|V_A + a V_B + a^2 V_C|}, \tag{8.1}$$

where $a = e^{j2\pi/3}$ and V_A, V_B, V_C are the line-to-neutral voltage phasors.

8.2.1 Problem Description

A conceptual illustration of the problem is shown in Fig. 8.1. The goal of the Steinmetz controller is to mitigate voltage unbalance at buses with three-phase motors (referred to as critical buses) by controlling reactive power injections from distributed PV systems. We assume that the unbalance upstream of a critical bus is not the main cause of unbalance

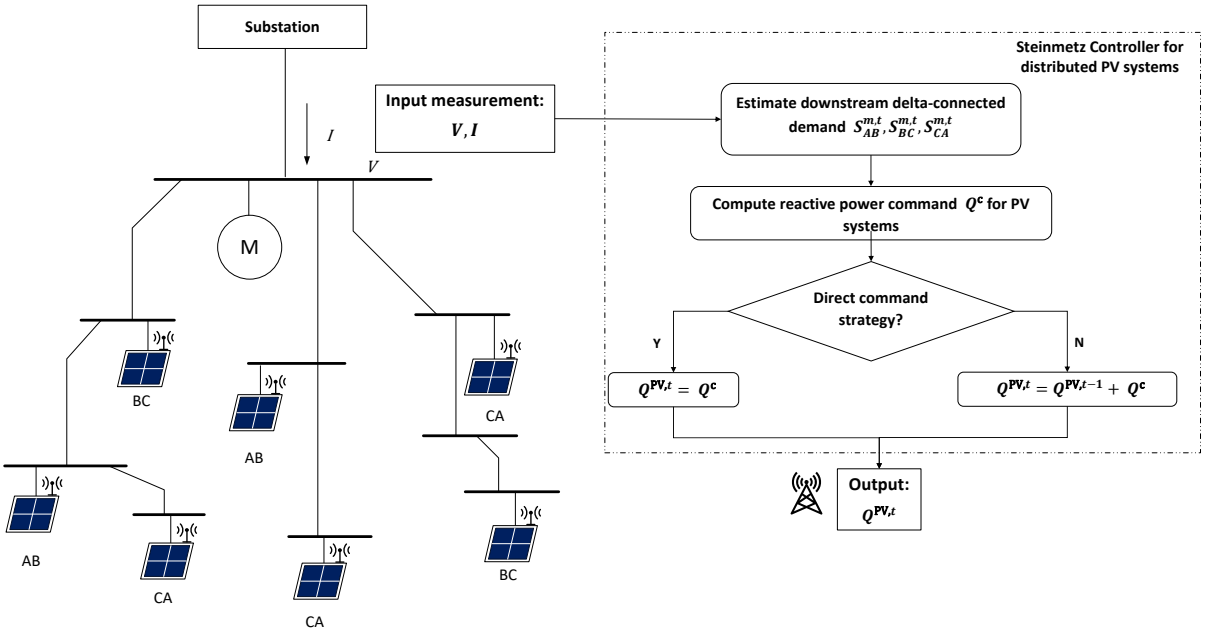

Figure 8.1: A radial distribution feeder (left) with single-phase PV systems. The phases to which PV systems are connected are labeled below each PV system. The flowchart (right) shows the Steinmetz controller. The measurements are taken at the critical bus, here, a bus with a 3-phase motor (M). The control signals are sent to each PV system through a simple communication system.

and, therefore, voltage unbalance at the critical bus will be reduced after applying Steinmetz circuit design to eliminate downstream unbalance. One Steinmetz controller works to mitigate unbalance at one specific critical bus; however, most buses in the network see a reduction in unbalance after the control actions are applied. Multiple Steinmetz controllers can operate on the same network, for example, mitigating unbalance at critical buses on different laterals; however, in this chapter we will only explore cases with a single Steinmetz controller per network.

The flowchart providing an overview of the steps taken by the Steinmetz controller is shown on the right side of Fig. 8.1. First, three-phase voltage and line current phasors are measured with D-PMUs or computed from traditional meter measurements at the critical bus. The measurements are used to compute the downstream power demand. Then, using Steinmetz circuit design, we can determine the reactive power injections required to balance the critical bus voltage. We use either a direct or differential command strategy to request reactive power injections from all downstream PV systems. Requests are sent through a simple communication network. PV systems provide the requested reactive power, up to

their capacity. We assume communication is one-way from the controller to distributed PV systems and so PV systems cannot report their actual injections back to the controller. The process is repeated until the voltage unbalance is within a tolerance.

This process can be regarded as system-wide feedback control. The feeder's voltage profile and power losses will change due to the reactive power injections and also due to time-varying load consumption and PV real power generation. Therefore, the compensating reactive power should be recomputed based on the latest measurements. If the measurements are accurate, the communication system is perfect, the reactive power injections are unlimited, and the load and PV real power generation are constant, we find that the controller converges quickly and can achieve zero unbalance at the critical bus.

As derived in Section 7.4, the unique reactive power compensation solution (7.18) is:

$$\begin{aligned}
Q^c_{AB} =& \frac{1}{3}(Q_{BC} + Q_{CA} - 2Q_{AB} + \sqrt{3}(P_{BC} - P_{CA})),\\
Q^c_{BC} =& \frac{1}{3}(Q_{AB} + Q_{CA} - 2Q_{BC} + \sqrt{3}(P_{CA} - P_{AB})),\\
Q^c_{CA} =& \frac{1}{3}(Q_{AB} + Q_{BC} - 2Q_{CA} + \sqrt{3}(P_{AB} - P_{BC})).
\end{aligned}$$

Let $\boldsymbol{p} = \begin{bmatrix} P_{AB} & P_{BC} & P_{CA} \end{bmatrix}^T$, $\boldsymbol{q} = \begin{bmatrix} Q_{AB} & Q_{BC} & Q_{CA} \end{bmatrix}^T$, and $\boldsymbol{q}^c = \begin{bmatrix} Q^c_{AB} & Q^c_{BC} & Q^c_{CA} \end{bmatrix}^T$, then (7.18) can be rewritten:

$$\boldsymbol{q}^c = f(\boldsymbol{p}, \boldsymbol{q}) = C_P \boldsymbol{p} + C_Q \boldsymbol{q} \tag{8.2}$$

where $C_P = \frac{\sqrt{3}}{3} \begin{bmatrix} 0 & 1 & -1 \\ -1 & 0 & 1 \\ 1 & -1 & 0 \end{bmatrix}$, $C_Q = \frac{1}{3} \begin{bmatrix} -2 & 1 & 1 \\ 1 & -2 & 1 \\ 1 & 1 & -2 \end{bmatrix}$.

8.2.2 Note on Command Strategies

For simplicity assume PV systems that are not being controlled operate at unity power factor, though our approach also works in the case of non-unity factors. Denote the set of PV systems connected to each phase as $\mathcal{N}_{\text{AB}}$, $\mathcal{N}_{\text{BC}}$, and $\mathcal{N}_{\text{CA}}$. We use bold symbols to denote vectors containing variables associated with different phases in the order AB, BC, CA. Suppose the measured line-to-line voltages and the line currents at time step t are $V^t_{AB}, V^t_{BC}, V^t_{CA}$ and I^t_A, I^t_B, I^t_C. We first convert the currents into equivalent delta-load

currents using the following transformation:

$$\begin{bmatrix} I_{AB}^{\mathrm{eq}} \\ I_{BC}^{\mathrm{eq}} \\ I_{CA}^{\mathrm{eq}} \end{bmatrix} = \frac{1}{3} \begin{bmatrix} 1 & -1 & 0 \\ 1 & 2 & 0 \\ -2 & -1 & 0 \end{bmatrix} \begin{bmatrix} I_A^t \\ I_B^t \\ I_C^t \end{bmatrix}. \tag{8.3}$$

Then, the measured delta-connected power demand of downstream of the critical bus is:

$$\boldsymbol{s}^{m,t} = \begin{bmatrix} V_{AB}^t (I_{AB}^{\mathrm{eq}})^* & V_{BC}^t (I_{BC}^{\mathrm{eq}})^* & V_{CA}^t (I_{CA}^{\mathrm{eq}})^* \end{bmatrix}^T. \tag{8.4}$$

Using $\boldsymbol{s}^{m,t}$ as the load within (8.2) and a strategy to allocate the total injections to each PV systems, we can compute the reactive power command for each PV system i and send out the signal $Q_i^{\mathrm{c},t}$. Then, each PV system injects $Q_i^{\mathrm{PV},t}$ equal to $Q_i^{\mathrm{c},t}$ or its reactive power limit $\pm Q_i^{\mathrm{max},t}$. We consider two strategies to determine the command; the direct command strategy and the differential command strategy that copes with inverter reactive power limits.

Direct command strategy

The command is the *total* amount of reactive power that the PV system should provide. First, we define the vector of reactive power injections as

$$\boldsymbol{q}^{\mathrm{PV},t} = \begin{bmatrix} \sum_{i \in \mathcal{N}_{\mathrm{AB}}} Q_i^{\mathrm{PV},t} & \sum_{i \in \mathcal{N}_{\mathrm{BC}}} Q_i^{\mathrm{PV},t} & \sum_{i \in \mathcal{N}_{\mathrm{CA}}} Q_i^{\mathrm{PV},t} \end{bmatrix}^T.$$

If the PV systems have already injected reactive power in the previous time step, the measured power demand includes those injections, i.e., $\boldsymbol{q}^{\mathrm{PV},t-1}$. Thus, the computation of the reactive power injections for the current time step t using (8.2) should exclude $\boldsymbol{q}^{\mathrm{PV},t-1}$. However, the operator does not know the actual reactive power injections $\boldsymbol{q}^{\mathrm{PV},t-1}$, only its commands $\boldsymbol{q}^{c,t-1} = \begin{bmatrix} \sum_{i \in \mathcal{N}_{\mathrm{AB}}} Q_i^{\mathrm{c},t-1} & \sum_{i \in \mathcal{N}_{\mathrm{BC}}} Q_i^{\mathrm{c},t-1} & \sum_{i \in \mathcal{N}_{\mathrm{CA}}} Q_i^{\mathrm{c},t-1} \end{bmatrix}^T$. and so it computes the new command as follows:

$$\boldsymbol{q}^{c,t} = f(\boldsymbol{p}^{m,t}, \boldsymbol{q}^{m,t} - \boldsymbol{q}^{c,t-1}). \tag{8.5}$$

We assume $\boldsymbol{q}^{c,t}$ is allocated to each PV system in proportion to its rated apparent power capacity S_i^{PV} (see (7.29)). However, its reactive power capacity is time-varying and unknown to the controller $Q_i^{\mathrm{max},t} = \sqrt{(S_i^{\mathrm{PV}})^2 - (P_i^{\mathrm{PV},t})^2}$, where $P_i^{\mathrm{PV},t}$ is its real power generation.

Therefore, actual injection is:

$$Q_i^{\mathrm{PV},t} = \begin{cases} Q_i^{\max,t}, & \text{if } Q_i^{\mathrm{c},t} > Q_i^{\max,t} \\ -Q_i^{\max,t}, & \text{if } Q_i^{\mathrm{c},t} < -Q_i^{\max,t} \\ Q_i^{\mathrm{c},t}, & \text{otherwise,} \end{cases} \tag{8.6}$$

which could be significantly different than the command.

Differential command strategy

The command is the *change* of reactive power that the PV system should provide. Specifically, we do not subtract the previous command, but instead determine the change in reactive power injections needed to balance the bus:

$$\Delta \boldsymbol{q}^{c,t} = f(\boldsymbol{p}^{m,t}, \boldsymbol{q}^{m,t}). \tag{8.7}$$

We assume $\Delta \boldsymbol{q}^{c,t}$ is allocated to each PV system in proportion to its rated apparent power (see (7.29)) and:

$$Q_i^{\mathrm{PV},t} = \begin{cases} Q_i^{\max,t}, & \text{if } Q_i^{\mathrm{PV},t-1} + \Delta Q_i^{\mathrm{c},t} > Q_i^{\max,t} \\ -Q_i^{\max,t}, & \text{if } Q_i^{\mathrm{PV},t-1} + \Delta Q_i^{\mathrm{c},t} < -Q_i^{\max,t} \\ Q_i^{\mathrm{PV},t-1} + \Delta Q_i^{\mathrm{c},t}, & \text{otherwise.} \end{cases} \tag{8.8}$$

The two command strategies are identical if we ignore inverter reactive power limits. The proof is as follows. Consider that PV inverters do not have reactive power limits, for the direct command strategy, we will have: $\boldsymbol{q}^{\mathrm{PV}_D,t-1} = \boldsymbol{q}^{c,t-1}$. Substituting this constraint into (8.5), we get:

$$\boldsymbol{q}^{c,t} = f(\boldsymbol{p}^{m,t}, \boldsymbol{q}^{m,t} - \boldsymbol{q}^{c,t-1}) = f(\boldsymbol{p}^{L,t}, \boldsymbol{q}^{m,t} - \boldsymbol{q}^{\mathrm{PV}_D,t-1}) = f(\boldsymbol{p}^{L,t}, \boldsymbol{q}^{L,t}). \tag{8.9}$$

For the differential command strategy, we have $\Delta \boldsymbol{q}^{\mathrm{PV}_\Delta,t} = \Delta \boldsymbol{q}^{c,t}$, and together with (8.7), $q^{\mathrm{PV}_\Delta,t}$ can be presented as:

$$\boldsymbol{q}^{\mathrm{PV}_\Delta,t} = \boldsymbol{q}^{\mathrm{PV}_\Delta,t-1} + f(\boldsymbol{p}^{m,t}, \boldsymbol{q}^{m,t}). \tag{8.10}$$

Since f is a linear function, the second part of (8.10) can be rewritten as:

$$f(\boldsymbol{p}^{m,t}, \boldsymbol{q}^{m,t}) = f(\boldsymbol{p}^{L,t}, \boldsymbol{q}^{L,t} + \boldsymbol{q}^{\mathrm{PV}_\Delta,t-1}) = f(\boldsymbol{p}^{L,t}, \boldsymbol{q}^{L,t}) + C_Q \boldsymbol{q}^{\mathrm{PV}_\Delta,t-1}, \tag{8.11}$$

From $Q^c_{AB} + Q^c_{BC} + Q^c_{CA} = 0$, we can easily obtain

$$C_Q \boldsymbol{q}^{\mathrm{PV}_\Delta,t-1} = -\boldsymbol{q}^{\mathrm{PV}_\Delta,t-1} \tag{8.12}$$

Finally, by substituting (8.11) and (8.12) into (8.10), we obtain:

$$\boldsymbol{q}^{\mathrm{PV}_\Delta,t} = \boldsymbol{q}^{\mathrm{PV}_\Delta,t-1} + f(\boldsymbol{p}^{L,t}, \boldsymbol{q}^{L,t}) - \boldsymbol{q}^{\mathrm{PV}_\Delta,t-1} = f(\boldsymbol{p}^{L,t}, \boldsymbol{q}^{L,t}) = \boldsymbol{q}^{\mathrm{PV}_D,t}. \tag{8.13}$$

The above equation proves that the reactive power provided using the two strategies are identical. The identity is valid if and only if the reactive power saturation of PV systems is neglected and the sum of total compensating reactive power is zero. In reality, the reactive power capacity of PV systems could be very small at noon when the systems are generating peak real power. When this happens, the inverters may not be able to follow reactive power commands and the direct command strategy will lead to an accumulation error between past commands and actual responses. This can lead to divergence of the controller. In contrast, since the differential command strategy only uses measures from time step t, it works better in this case. An example will be shown in Section 8.4.2.

8.3 Further Challenges

8.3.1 Measurement Error and Noise

Following the PMU measurement error model in [1] and PMU noise model in [22], the measured voltage phasor with errors and noises can be written:

$$\tilde{V} = (1+\gamma)|V|e^{j(\delta+\Delta\delta)} + \epsilon_V e^{j\phi_V} \tag{8.14}$$

where $|V|,\ \delta$ are the true magnitude and angle of the voltage phasor, error quantities γ and $\Delta\delta$ are random variables following uniform distributions, and model noise quantities ϵ_V and ϕ_V are random variables following zero-mean Gaussian distributions [22]. To quantify the noise level of the signal, the signal-to-noise ratio (SNR) is used, and for a normalized signal with unit energy, the SNR in dB is given by: $\mathrm{SNR}_{\mathrm{dB}} = 20\log(\frac{1}{\sigma})$, where σ is the standard

deviation of the random variable. The measured current phasor with errors and noises, $\tilde{I}$, can be expressed similarly to (8.14).

Both the error and noise quantities in the voltage and current measurements will contribute to the error in the estimate of downstream delta-connected power demand, and as a result, we will obtain inaccurate reactive power injections, which may increase unbalance. When we do not have a measurement of the phasors, e.g., from D-PMUs, but instead need to estimate them from measurements taken from traditional meters, our estimate of the downstream delta-connected power demand will generally be less accurate. We can obtain such an estimate by using measurements of the line-to-line and line-to-neutral voltage magnitudes along with real and reactive power flows at the critical bus to compute the voltage phase angles and line current phasors, from which we can compute $\boldsymbol{s}^{m,t}$. Moreover, traditional meters generally have larger measurement errors and noises than D-PMUs. The impact of measurement error/noise will be investigated in Section V.

8.3.2 Communication Delays

We assume that communication delays follow a Gamma distribution [118], specifically, that the time delay for the command to PV i at time t is $\tau_i^t = \Gamma(\alpha, \beta)$, where $E[\tau] = \alpha/\beta, Var[\tau] = \alpha/\beta^2$. Because of the delays, the reactive power injections will not be as expected and the controller will continue sending reactive power commands while the unbalance persists. This could result in an over-response which could worsen the unbalance. One way to mitigate this issue is to slow down the commands. Our first strategy, referred to as the conditional triggered strategy, is to send a new input only when the change of VUF with respect to the previous time step is larger than a threshold m:

$$|VUF^t - VUF^{t-1}|/VUF^{t-1} > m. \tag{8.15}$$

One disadvantage of the strategy is that when the message is completely lost, the controller will never be activated and the unbalance will not be mitigated.

Our second strategy to cope with delays is to add a proportional gain $k = [0, 1]$ to the controller, i.e., we down-scale the command in order to reduce the response. The gain can either be constant or time-varying. When it is constant, we also assume it is identical for all phases. Alternatively, it could be adaptive, e.g., the gain for phase AB could be computed

as

$$k_{AB}^{t} = \frac{|\Delta V_{AB}^{t} - \Delta V_{AB}^{t-1}|}{\Delta V_{AB}^{0}}, \tag{8.16}$$

where ΔV_{AB}^{t} is the absolute value of the difference between the voltage magnitude in phase AB and the average voltage magnitude across all phases and $t = 0$ corresponds to the time step in which we begin to use Steinmetz controller. Assuming unbalance decreases while we are using the Steinmetz controller, which is true when unbalance at the critical bus is primarily due to downstream unbalance, normalizing by ΔV_{AB}^{0} ensures that the gain is smaller than 1. The gain for the other phases could be can similarly. When PV systems fail to respond adequately, the gain will be small and the next command will be small mitigating the chance of requesting too much reactive power from the PV systems.

8.4 Case Studies

In this section, we conduct a number of case studies using the IEEE 13-node feeder modified to include distributed PV systems, as shown in Fig. 7.13.

8.4.1 Setup

We use system data for the IEEE 13-node feeder from [66]. The load data is assumed to be the base power consumption of each load. Bus 632 is assumed to be the critical bus with a three-phase motor, and therefore the objective is to balance the voltage at Bus 632. We make some modifications to the original feeder: 1. The taps of the regulator are set to be identical in each phase; 2. line 630-632 is changed to be balanced (self phase impedance is $0.3418 + 1.0335j$ Ω/mile, mutual phase impedance is $0.1558 + 0.4367j$ Ω/mile); and 3. the configurations of Line 684-632 and Line 684-611 are changed to be same as that of Line 671-684. The reason for the first two changes is that we want to exclude the impact of the voltage source unbalance (the taps are unequal) and the upstream line unbalance (Line 630-632 is not transposed) on the voltage unbalance of Bus 632. With these changes we are able to achieve zero unbalance at Bus 632 when we balance the downstream loading via Steinmetz circuit design. The last change is made because we want to add delta-connected PV systems to Buses 611 and 632. Originally, Line 684-632 and Line 684-611 are single-phase.

We connect 11 single-phase delta-connected PV systems to different buses in the feeder, the details of the location, the base PV real power generation $P_{\text{base}}^{\text{PV}}$ (kW), and the apparent power rating S^{PV} (kVA) of each PV are provided in Table 8.1. The PV real power generation

Table 8.1: Details of single-phase PV systems

Bus	632	633	634	645	646	671	652	611	680	692	675
Phase	BC	AB	AB	BC	BC	AB	CA	CA	BC	CA	AB
$P_{\text{base}}^{\text{PV}}$	200	80	80	200	200	50	100	60	50	100	200
S^{PV}	340	135	135	340	340	90	170	110	90	170	340

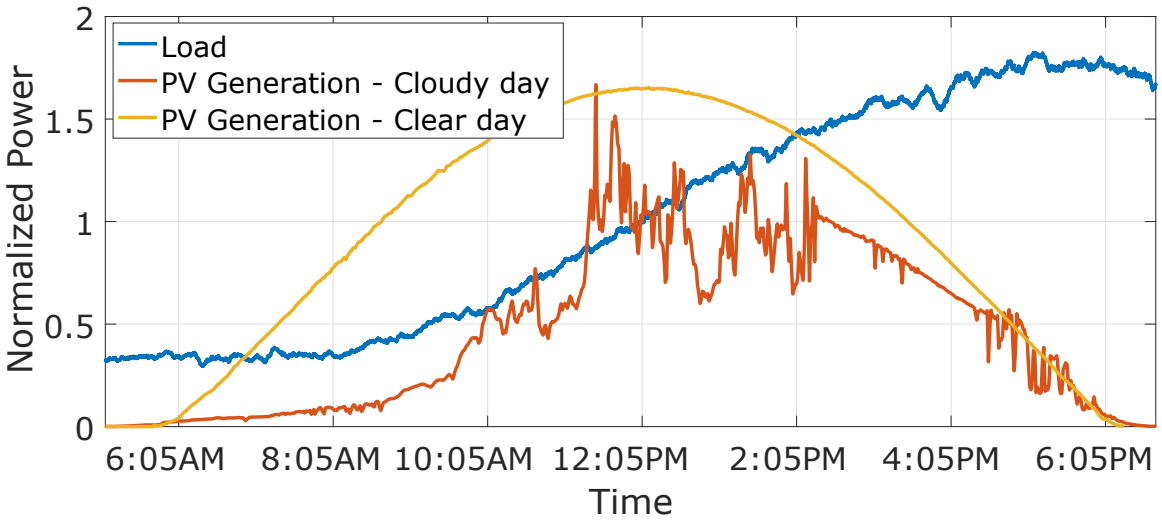

Figure 8.2: Normalized real power generation of PV systems and real power consumption of loads from sunrise to sunset.

is simulated based on irradiance data from the National Renewable Energy Laboratory's Measurement and Instrumentation Data Center [100]. We pick a clear day and a cloudy day using data from Los Angeles, CA on April 4 and May 4, 2016, respectively. We linearly interpolate the data from one-minute interval to two-second interval. The irradiance data is normalized by the value at 12 PM on May 4 and shown in Fig. 8.2. We use a two-second interval residential profile from [74] and normalized it by dividing by the value at 12 PM. We assume all PV systems and loads follow the same trends. We set the real power output of each PV system equal to its base real power generation multiplied by the normalized PV data and the load equal to its base power consumption multiplied by the normalized load data. Total base power consumption of load is 3466 kW and total base real power generation of PV is 1320 kW. The total real power generation of PV systems does not exceed the power demand of load at any time in this case.

Figure 8.3 shows the impact of deployment of single-phase PV systems in the feeder on

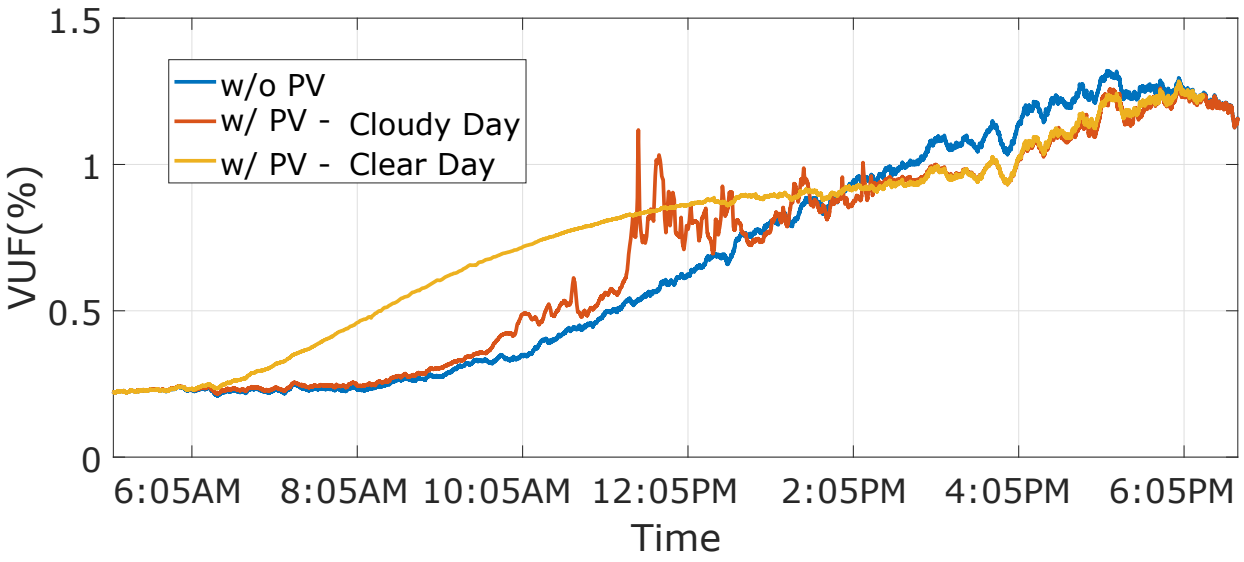

Figure 8.3: The impact of distributed solar PV systems on the VUF at Bus 632.

the VUF at Bus 632. It is observed that VUF significantly increases at noon when we have high PV generation. The VUF oscillates on cloudy days due to the intermittency of PV generation. The largest VUFs occur during when the demand peaks; at that time PV generation is small, which indicates that the reactive power capacity of PV systems is large. Therefore, controlling the PV inverter reactive power injections is a compelling method to mitigate voltage unbalance in the evening.

8.4.2 PV Inverter Reactive Power Limits

We first assume perfect measurements and delay-free communication networks so that we can compare the direct and differential command strategies. The results are shown in Fig. 8.4a, where the solid yellow line is the VUF without control, the red dashed line is the VUF using the direct command strategy, and the green dotted line is the VUF using the differential command strategy. All PV inverters reach their maximum reactive power limits between 9 AM and 2 PM. As we can see, both strategies are able to achieve zero unbalance before 9 AM and can reduce VUF from 9 AM to 2 PM identically as the PV inverters are generating their maximum reactive power output. However, after 2 PM, the VUF resulting from the direct command strategy increases, becoming even higher than that of the initial case. The main reason can be seen from the reactive power output of the single-phase PV at bus 652, as shown in Fig. 8.4b. The command given by the direct command strategy contains the accumulated error between the previous commands and responses. Thus, the command

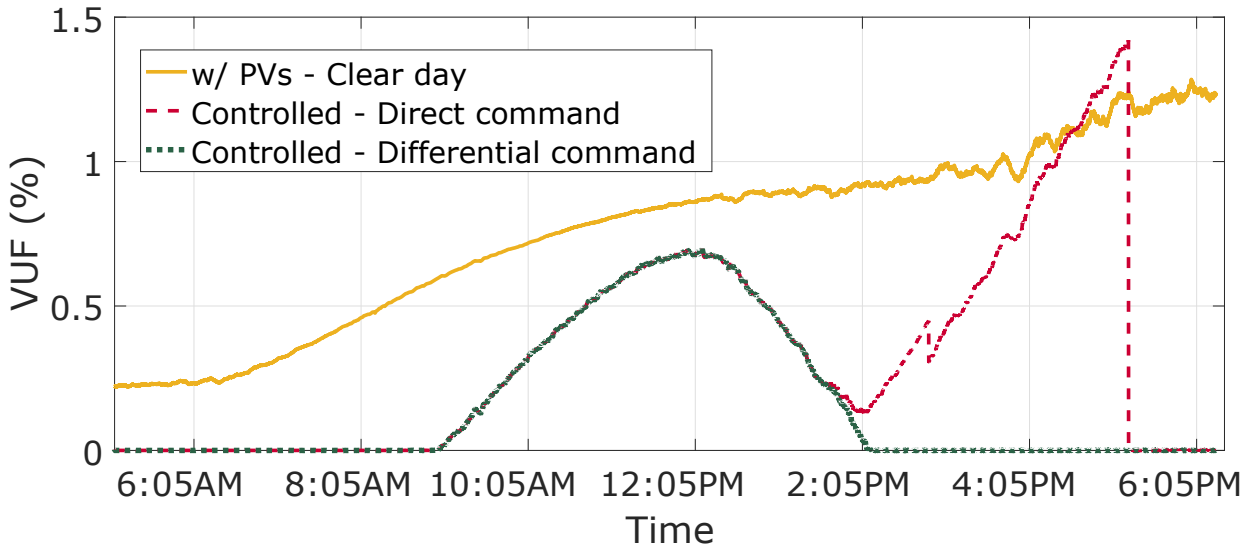

(a)

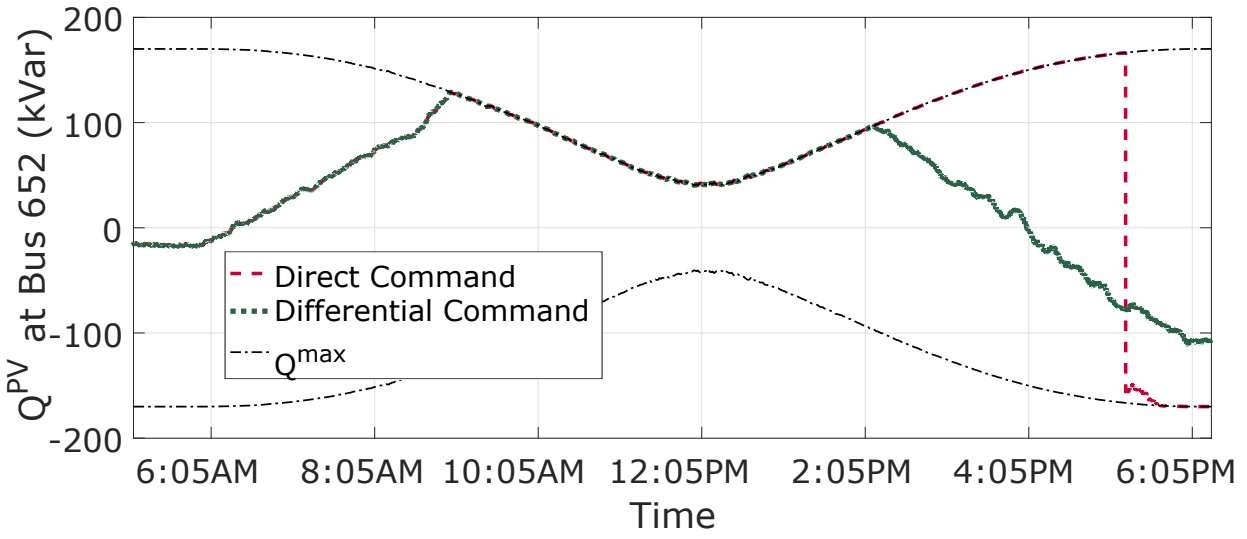

(b)

Figure 8.4: (a) The VUF and (b) the reactive power output of the PV system at Bus 652 using different command strategies on a clear day.

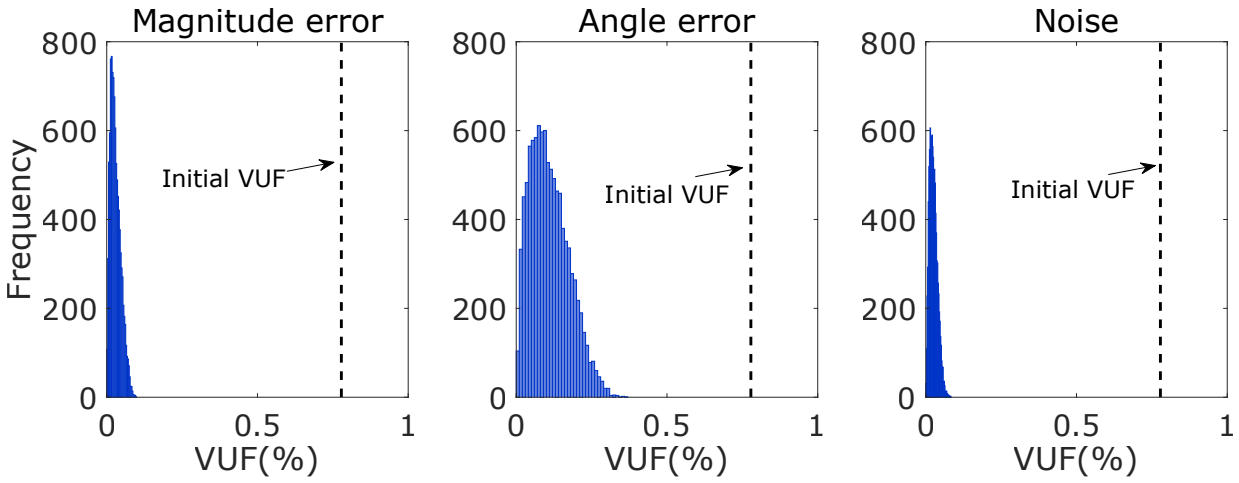

Figure 8.5: Histograms of the final VUF for 10,000 samples only considering magnitude error, angle error, or noise. The initial VUF $= 0.7783\%$**.**

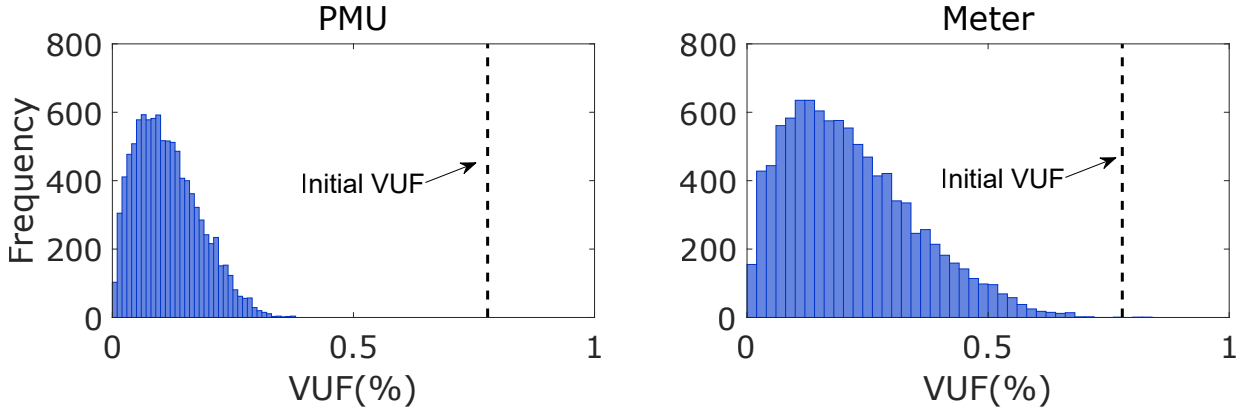

Figure 8.6: Histograms of the final VUF (%) **with 10000 samples when using PMUs versus traditional meters. The initial VUF** $=0.7783\%$**.**

diverges significantly from the required reactive power injection and becomes much larger than the reactive power limit. This results in PV inverters consistently producing maximum reactive power, which eventually leads to an increase in the VUF. On the other hand, the differential command strategy is able to compute the required reactive power injections resulting in a VUF of zero after 2 PM. The remaining results use the differential command strategy.

8.4.3 Measurement Error and Noise

Next, we assume perfect communication but inaccurate and noisy measurements. We only test on t =12 PM of the cloudy day to explore the impact of measurement errors and noises on

the final VUF after applying the Steinmetz controller. The initial VUF at 12 PM is 0.7783%. For other time steps, the impact of measurement error and noise on the performance of the Steinmetz controller is similar.

We first consider the case when D-PMUs are available. We assume inaccurate voltage and current phasor measurements are used to estimate downstream power demand and so measurement errors and noises are incorporated into the computation of Steinmetz compensating reactive power, leading to the final VUF being greater than 0. The maximum amplitude error is set to 2% and the maximum phase angle error is set to 5°. According to [22], we use SNR = 45 dB to simulate the noises in measurements. The base line-to-line voltage magnitude 4160 V and the base apparent power 1 MVA are used to compute the variance of the noises. Figure 8.5 shows the distribution of the final VUF over 10,000 samples when we only consider magnitude error, angle error, or noise at one time. We find that the angle error has the most impact on the final VUF. It can also be seen that we can considerably reduce the unbalance when we have 2% magnitude error and 45 dB SNR (which are realistic).

Next, we assess the impact of errors and noise combined, and we also compare the results of using D-PMU measurements versus traditional meter measurements. We assume that the meters have 5% maximum magnitude errors and SNR = 35 dB, i.e., they are more inaccurate and noisier than D-PMUs. The VUF distributions are shown in Fig. 8.6. The mean VUF using D-PMUs is 0.1146% while the mean VUF using traditional meters is 0.2150%.

8.4.4 Communication Delays

Next, we consider the impact of communication delays. We assume the commands sent to all PV systems (except the PV system at Bus 632, which is where the controller is located) have a random delay following the Gamma distribution: $\Gamma(\alpha = 10, \beta = 5/6)$. We pick a 15-minute interval ($T = 900s$) on the cloudy day. The VUF without control and net feeder demand are shown in Fig. 8.7. The average value of the VUF over this 15-minute interval is 0.8089%. Figure 8.8 shows an example of the VUF after applying the Steinmetz controller over a communication network with delays (red line). Note the significant oscillations in the VUF and how, at some points, the controller worsens the unbalance.

We tested each delay compensation strategy by conducting 100 simulations of this 15-minute interval. For the conditional triggered strategy, the mean VUF for different threshold values are 0.4004% ($m = 0.1$), 0.1963% ($m = 0.2$), and 0.1553% ($m = 0.5$). As m increases, PV systems have more time to respond, which results in better unbalance improvement. For

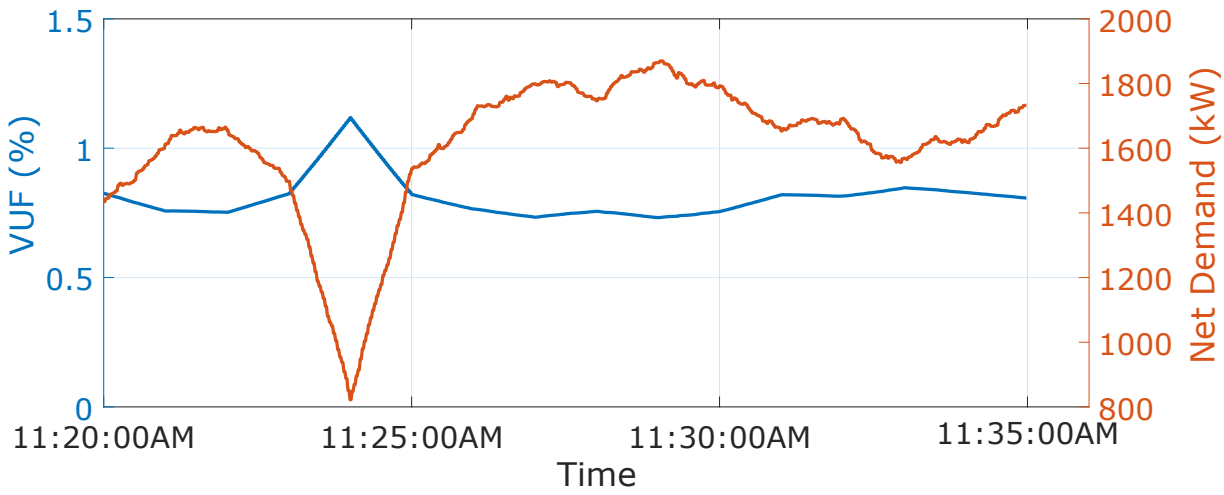

Figure 8.7: The VUF without control and net feeder demand ($P^L - P^{\mathbf{PV}}$) from 11:20 AM to 11:35 AM on a cloudy day.

the proportional controller with the constant gain, the mean VUF for different gains are 0.0636% ($k = 0.2$), 0.1882% ($k = 0.5$), and 0.3487% ($k = 0.8$). Smaller gains results in lower mean VUFs. For the proportional controller with the adaptive gain described in (8.16), the mean is 0.1079%. Examples of the VUF with different delay compensation strategies are shown in Fig. 8.8. All strategies are able to improve the Steinmetz controller and reduce the unbalance during the interval. The spike near 11:25 AM is because the PV systems are at their reactive power limit. If the delay distribution changes, e.g., $\beta = 1/3$, then $k = 0.2$ is not enough to achieve same unbalance reduction as when $\beta = 5/6$. Specifically, the mean VUF becomes 0.2036%. Using the proportional controller with the adaptive gain the mean VUF becomes 0.1307% and using the conditional triggered strategy ($m = 0.5$) the mean VUF becomes 0.1606%. Therefore, the conditional triggered strategy and the proportional controller with the adaptive gain appear less sensitive to the distribution of the delay.

8.5 Chapter Conclusion

In this chapter, we investigated a number of practical issues that would complicate the application of a Steinmetz circuit design-based feedback controller to mitigate voltage unbalance in distribution networks using reactive power injections from distributed PV systems. Specifically, we explored the impact of reactive power limits, measurement errors/noise, and communication delays given time-varying load and PV generation. We find that using the differential command strategy can significantly reduce voltage unbalance even when PV sys-

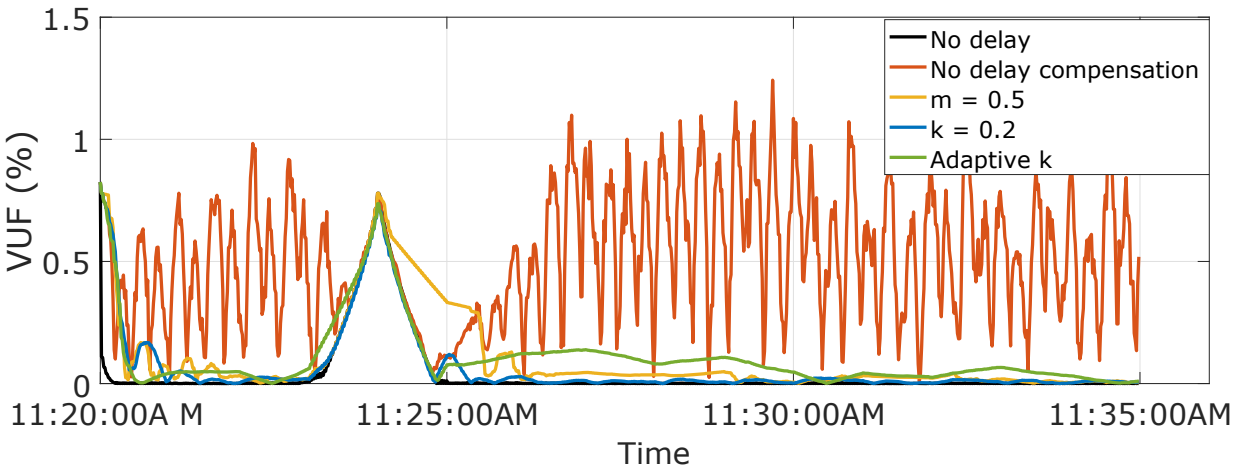

Figure 8.8: The VUF with control from 11:20 AM to 11:35 AM on a cloudy day.

tems reach their reactive power limits. Additionally, our results show that measurement error and noise do not have a large impact on the controller but communication delays may worsen the unbalance. However, with our proposed strategies to cope with communication delay, the Steinmetz controller is able to effectively mitigate voltage unbalance.

In future work, instead of communication delays, we will also consider missing/bad data. We plan to develop a robust algorithm to deal with these communication issues.

Chapter 9

Centralized and Steinmetz Controllers: Comparison and Integration

9.1 Chapter Introduction

Previous literature has sought to achieve the best improvement to unbalance by solving optimization problems to centrally control the real and/or reactive power of distributed PV systems [8, 47, 95, 120, 141]. The computation of the optimal solution with respect to a large unbalanced distributed system is generally complex. To overcome this issue, [121] proposed a distributed algorithm to decompose the centralized three-phase optimization problem into three single-phase subproblems. Although the distributed algorithm speeds up the convergence of the centralized controller, it still requires solving optimization problems. As an alternative, we developed a distributed controller based on Steinmetz circuit design [62] in Chapter 7, which we refer to as a Steinmetz controller, to mitigate voltage unbalance without solving an optimization problem. This approach uses only local measurements at the node that is being balanced, which is referred to as the critical node, and then solves a set of linear equations to compute the required compensating reactive power. The computation time is short and, therefore, the controller responds quickly to changes in the operating point. Reactive power requests are sent to distributed PV systems downstream of the critical node through a communication network.

The major limitation of the Steinmetz controller is that it does not consider any engineering limits. Therefore, in this chapter, we propose two types of strategies to reduce the

possibility of violating engineering limits when using our Steinmetz controller: 1) a heuristic decentralized approach; and 2) using the optimal solutions from the centralized controller. An integrated controller is then developed based on the second type of strategy. The main objective of this chapter is to explore proper ways to utilize the solutions of the centralized controller within the distributed controller and compare the performance in a variety of scenarios.

In Chapter 7, we compared the performance of the Steinmetz controller with a model-free controller. In Chapter 8, we showed that the Steinmetz controller can effectively mitigate voltage unbalance on a small system with time-varying load and PV generation when the critical node is close to the substation. However, we have not yet studied the performance of the Steinmetz controller on a large feeder with time-varying load and PV generation, nor have we compared the Steinmetz controller with a centralized controller. As such, in this chapter, we evaluate and compare the performance of the centralized controller, the Steinmetz controller, and the integrated controller, with the critical node being either close to or far from the substation, through time-varying case studies on the 13-node feeder and the GridLAB-D taxonomy feeder R1-12.47-1 with a high penetration of distributed PV systems.

The main contributions of this chapter are as follows:

- We test the Steinmetz controller on a large feeder with time-varying load and PV generation, and demonstrate the limitations of the Steinmetz controller.
- We summarize the pros and cons of the distributed controller and the centralized controller.
- We propose two heuristic strategies to improve the performance of the distributed controller.
- We propose an integrated controller that modifies the design of the Steinmetz controller to use centralized controller results and compare its performance with those of a centralized controller and a distributed controller acting individually.

9.2 Controller Overview

In this section, we first describe the formulation of the centralized controller from [47]. Next, we review the design of the Steinmetz-based distributed controller and discuss the

limitations of the distributed controller. We then propose two heuristic strategies to improve the performance of the distributed controller. Finally, the integrated controller is introduced.

The objective is to improve the negative-sequence voltage unbalance; thus, the unbalanced factor is defined as:

$$\text{VUF}(\%) = 100 \times \frac{|V_2|}{|V_1|} \tag{9.1}$$

where V_2 and V_1 are the negative-sequence and positive-sequence voltages.

9.2.1 Centralized Controller

When the centralized controller is used to mitigate unbalance, the reactive power injections of PV systems are determined by solving an optimization problem. The objective is to minimize the unbalance factor VUF at the critical node n ($n \in \mathcal{N}_{3\phi}$, where $\mathcal{N}_{3\phi}$ is the set of the three-phase nodes in the feeder), subject to various engineering constraints in three-phase, unbalanced distribution grids. The optimization problem is formulated as:

$$\begin{aligned} \text{minimize} \quad & \text{VUF}_n \\ \text{subject to} \quad & \text{AC power flow equations}, \\ & \text{Voltage magnitude limits}, \\ & \text{Inverter limits}, \\ & \text{VUF}_k^{\text{final}} \leq \text{VUF}_k^{\text{initial}}, \forall k \in \mathcal{N}_{3\phi}. \end{aligned} \tag{9.2}$$

The equality constraints of (9.2) are the three-phase AC power flow equations; modeling of distribution lines, transformers, voltage regulators, and ZIP loads are introduced in detail in [47]. The rest of the constraints are engineering limits. The inverter limits are the reactive power capacity of each PV inverter, determined by its apparent power rating and the active power generation it is providing. Suppose the power rating of the PV system i is S_i^{rated}, and the active power it generates at time t is $P_{i,t}$, the reactive power limit of the PV system i at time t is:

$$Q_{i,t}^{\text{lim}} = \pm\sqrt{(S_i^{\text{rate}})^2 - (P_{i,t})^2} \tag{9.3}$$

The final constraint is to ensure that we do not increase the unbalance at noncritical nodes when improving the unbalance at the critical node.

The optimization problem (9.2) is a large-scale, non-convex, nonlinear problem, and thus is solved using a nonlinear programming solver. We denote the optimal reactive power

injections of PV systems determined by (9.2) as $\boldsymbol{Q}^{\text{PV, ctr}} = [Q_i^{\text{PV, ctr}}, \forall i \in \Omega_{\text{PV}}]$, where $Q_i^{\text{PV, ctr}}$ is the reactive power injection of the PV system i and Ω_{PV} is the set of all PV systems.

9.2.2 Distributed Controller

The distributed controller uses local measurements to compute the required compensating reactive power based on Steinmetz design and then sends out the commands to each downstream PV system through a communication network. Here, we briefly review how the command values are determined, using wye-connected PV systems as an example. For delta-connected PV systems, the procedure is similar.

When we apply Steinmetz design to compute the reactive power compensation, we assume that the upstream network of the critical node is balanced; as a result, the negative-sequence voltage is eliminated when we balance the load by reducing the negative-sequence current I_2 to zero. Suppose that the measured three-phase voltages and power demand are V_A^m, V_B^m, V_C^m and S_A^m, S_B^m, S_C^m. Using the Fortescue transformation, the negative-sequence current is derived as:

$$3I_2^c = I_A^c + a^2 I_B^c + a I_C^c = 0, \tag{9.4}$$

where

$$I_A^c = \Big(\frac{S_A^m + jQ_A^{c,Y}}{V_A^c}\Big)^*, \tag{9.5a}$$

$$I_B^c = \Big(\frac{S_B^m + jQ_B^{c,Y}}{V_B^c}\Big)^*, \tag{9.5b}$$

$$I_C^c = \Big(\frac{S_C^m + jQ_C^{c,Y}}{V_C^c}\Big)^*, \tag{9.5c}$$

where V_A^c, V_B^c, V_C^c are the phase-to-neutral voltages when the negative-sequence voltage is eliminated. As discussed in Section 7.4, it may not be good to assume that V_A^c, V_B^c, V_C^c are balanced when V_2 is zero, so we again use the measured voltages to approximate the line-to-neutral voltages in (9.5):

$$V_A^c = V_A^m, \quad V_B^c = V_B^m, \quad V_C^c = V_C^m. \tag{9.6}$$

By splitting (9.4) into its real and imaginary parts, we obtain two equations, however we have three unknowns; one more constraint is needed to reach a unique reactive power compensation solution. Therefore, we add a constraint that requires the sum of the changes

in reactive power injections to be a specific value $\hat{Q}$:

$$Q_A^{c,Y} + Q_B^{c,Y} + Q_C^{c,Y} = \hat{Q}. \tag{9.7}$$

Now, we solve the problem:

$$\mathrm{Re}\{I_2^c\} = 0 \tag{9.8a}$$
$$\mathrm{Im}\{I_2^c\} = 0 \tag{9.8b}$$
$$Q_A^{c,Y} + Q_B^{c,Y} + Q_C^{c,Y} = \hat{Q} \tag{9.8c}$$

Let $\boldsymbol{S} = \begin{bmatrix} S_A^m & S_B^m & S_C^m \end{bmatrix}^T$, $\boldsymbol{V} = \begin{bmatrix} V_A^m & V_B^m & V_C^m \end{bmatrix}^T$, and $\boldsymbol{Q^c} = \begin{bmatrix} Q_A^{c,Y} & Q_B^{c,Y} & Q_C^{c,Y} \end{bmatrix}^T$, then the three-phase reactive power compensation strategy of the distributed controller $\boldsymbol{Q^c}$ that given by the solution of (9.8) can be presented as:

$$\boldsymbol{Q^c} = f(\boldsymbol{S}, \boldsymbol{V}, \hat{Q}) \tag{9.9}$$

Next, we assign $\boldsymbol{Q^c}$ to each PV system:

$$Q_i^{\mathrm{PV},c} = \gamma_i Q_\phi^{c,Y}, \tag{9.10}$$

where $\phi \in \{A, B, C\}$ is the phase to which the PV system i is connected and γ_i is the contribution ratio of this PV system. In addition, we have the following constraint:

$$\sum_{i \in \Omega_\phi} \gamma_i = 1, \quad \forall \phi \in \{A, B, C\} \tag{9.11}$$

where Ω_ϕ is the set of downstream PV systems that are connected to phase ϕ.

Because of the approximation (9.6) and varying load and PV generation, the distributed controller is implemented periodically. The command value (9.10) will be re-computed based on the updated measurements.

In Chapter 7, $\hat{Q}$ was set to zero so that the total power demand in the system remained constant and the voltage profile did not change significantly. In addition, we simply allocated $\boldsymbol{Q^c}$ in proportion to each PV system's apparent power rating:

$$\gamma_i = \frac{S_i^{\mathrm{rate}}}{\sum_{j \in \Omega_\phi} S_j^{\mathrm{rate}}} \tag{9.12}$$

Chapters 7 and 8 showed that the above design significantly improved the unbalance at critical nodes close to the substation. However, the design has two major limitations:

- The distributed controller does not work well when the critical node is far from the substation. This is because the number of controllable downstream PV systems is small, and upstream unbalance will still cause the voltage at the critical bus to be unbalanced, even the downstream loading is able to be balanced.
- The distributed controller does not consider engineering limits. If the distributed controller commands PV systems to inject reactive power, the voltage magnitudes at nodes with PV systems will increase, and may exceed the upper limit when the initial values are already close to the limit. In addition, the goal of the distributed controller is to mitigate unbalance at one specific node; the controller does not account for the unbalance of other nodes.

9.2.3 Heuristic Strategies to Improve the Distributed Controller

We propose two strategies to alleviate the adverse impacts caused by the distributed controller. The first strategy uses a grouped controller to deal with the first limitation. The term 'grouped controller' refers to multiple distributed controllers deployed in the following way: the feeder is partitioned into several groups, and for each group, a distributed controller is used to control the PV systems in this group. Local communication exists within groups, but not between groups.

When the critical node is far from the substation, instead of having only one distributed controller at the critical node, multiple distributed controllers are applied to upstream nodes in order to improve the unbalance of the upstream network. An example of the grouped controller is presented in Fig. 9.1. The objective is to mitigate voltage unbalance at Node Y. All PV systems are divided into two groups: one includes all the downstream PV systems of the critical node (Group Y), and the other includes the upstream PV systems (Group X). The downstream PV systems form the downstream distributed controller, which is utilized to balance the load downstream of the critical node; the upstream PV systems form the upstream distributed controller, which aims to balance the load downstream of Node X in order to reduce the unbalance at Node X. We expect the grouped controller to reduce unbalance both upstream and downstream of the critical node, which will improve the voltage unbalance at the critical node. Although in practice more than two groups can be used,

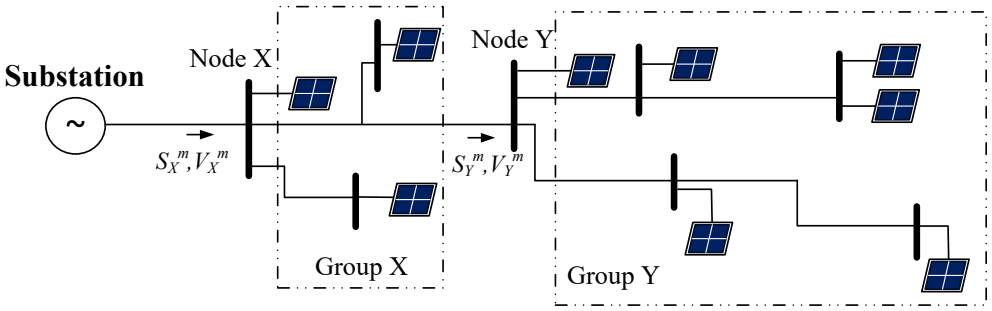

Figure 9.1: A conceptual illustration of the grouped controller. The critical node is Node Y and we divide all PV systems into two groups.

more groups would require extra measurements. Therefore, in this chapter we only consider grouped controllers with two groups; in addition, we assume the two controllers act simultaneously.

The second strategy, referred to as the local PV strategy, is proposed to reduce the violations of voltage magnitude limits. The fundamental idea behind this second strategy is that if the voltage magnitude is larger than the upper limit ($\overline{V}$), PV systems should consume reactive power; if the voltage magnitude is smaller than the lower limit ($\underline{V}$), PV systems should inject reactive power. Consequently, the command value sent by the distributed controller is modified to:

$$Q_i^{\mathrm{PV},c} = \begin{cases} -Q_i^{\mathrm{PV},c}, & \text{if } (V_i^m - \overline{V})Q_i^{\mathrm{PV},c} \text{ or } (V_i^m - \underline{V})Q_i^{\mathrm{PV},c} > 0 \\ Q_i^{\mathrm{PV},c}, & \text{otherwise.} \end{cases} \tag{9.13}$$

where V_i^m is the voltage magnitude of the node to which the PV system i is connected. If the voltage magnitude is greater than the upper limit and the command is to inject reactive power ($Q_i^{\mathrm{PV},c} > 0$), in order to avoid increasing the voltage magnitude, the command will change to request the PV system to consume reactive power. The amount of reactive power consumption is arbitrary, and here we simply change the sign of the command. Similarly, when the voltage magnitude is smaller than the lower limit and the command is to consume reactive power ($Q_i^{\mathrm{PV},c} < 0$), the command will change to inject reactive power.

Due to the local PV strategy, the total injected reactive power in each phase of the current time step does not equal its desired value. However, in the following time steps, the distributed controller will command other PV systems to compensate for this difference: PV systems change their injections to make the total injected reactive power as close as possible to the desired value to improve the unbalance at the critical node.

Note that both strategies are heuristic; the grouped controller can achieve better unbalance reduction compared to the single distributed controller, but there is no guarantee that the local PV strategy can eliminate the voltage violations. Moreover, neither strategy can be used to reduce the unbalance at noncritical nodes like the centralized controller does with the constraint $\text{VUF}^{\text{final}} \leq \text{VUF}^{\text{initial}}$.

9.2.4 Integrated Controller

The choice of $\hat{Q}$ and γ in (9.9) and (9.10) will affect the voltage profile of the system after compensating reactive power. Based on local measurements, $\hat{Q}$ and γ cannot be determined to avoid violations of the engineering limits; however, since the centralized controller knows the system details, it can provide us $\hat{Q}$ and γ respect the engineering limits. Therefore, we propose to integrate the centralized controller results into the distributed controller in order to mitigate voltage limit violations and increases in voltage unbalance at noncritical nodes. The new controller is referred to as the integrated controller.

Based on the centralized controller results at current time step t, assuming that PV systems do not compensate any reactive power in the previous time step, the sum of the changes in reactive power injections $\hat{Q}_t$ is set as:

$$\hat{Q}_t = \sum_{i \in \Omega_{\text{Dis}}} Q_{i,t}^{\text{PV,ctr}}, \tag{9.14}$$

where Ω_{Dis} is the set of PV systems controlled by the distributed controller and $Q_{i,t}^{\text{PV,ctr}}$ is the optimal reactive power injection of the PV system i determined by the centralized controller at time step t. The contribution ratio of the PV system i at time t based on centralized results is given by,

$$\gamma_{i,t}^{\text{ctr}} = \frac{Q_{i,t}^{\text{PV,ctr}}}{\sum_{j \in \Omega_\phi} Q_{j,t}^{\text{PV,ctr}}}. \tag{9.15}$$

One disadvantage of computing the ratio based on the centralized results is that the magnitude of the ratio may become very large when the denominator of (9.15) is very small. This could happen when some PV systems in one phase are consuming reactive power while others are injecting reactive power. A large ratio means a large command value, which would easily cause PV systems to operate at their maximum reactive power capacity. When a large amount of PV systems reach their reactive power limits, they would not be able to provide the desired reactive power to mitigate unbalance.

Table 9.1: Integrated Controller Configurations

Controller #	Strategy	γ	Local PV Strategy
1	Indirect	Centralized	N
2		PV rating	Y
3	Direct	Centralized	N
4		PV rating	Y

We will now introduce different configurations of the integrated controller. First, we propose a strategy that indirectly uses the centralized results, referred to as the 'Indirect Strategy'. Two integrated controllers are designed under this strategy, as summarized in Table 9.1 (see Strategy Indirect). The integrated controller #1 uses the centralized ratio (9.15) to allocate the reactive power to each PV system while controller #2 uses the ratio based on PV rating (9.12). In addition, controller #2 will use the local PV strategy. For both controllers, in the time step t at which we receive the centralized controller results, we compute the three-phase reactive power compensation $\boldsymbol{Q}_t^{\boldsymbol{c}}$ by plugging (9.14) into (9.9). For the rest of time steps, we do not change the total injected reactive power. The requested sum of the changes in reactive power injections is set to zero because we do not have centralized results to know how to change the total injected reactive power. An approach to determine $\hat{Q}$ based on the forecasts of load and PV generation is needed when the centralized controller is not available, which is a subject for future research.

Controller #1 is only suitable for cases where the critical node is close to the substation due to the fact that its allocation of reactive power to each phase ($Q_A^{c,Y}, Q_B^{c,Y}, Q_C^{c,Y}$) is similar (but not the same due to the approximation in (9.6)) to the allocation obtained by the centralized controller. This is due to the fact that centralized control minimizes the VUF by balancing the downstream load, which is also the goal of the distributed controller. Using the same centralized ratio (9.15), the reactive power injections of controller #1 will be similar to those of the centralized controller, and therefore it can satisfy the engineering limits. However, when the critical node is far from the substation, minimizing the VUF is not equivalent to balancing downstream load. This will result in a different allocation of reactive power to each phase than what we get from the centralized controller. Thus, we cannot guarantee that controller #1 can reduce the violations of the engineering limits. In this case, we should use controller #2. An example will be shown in Section 9.3.4.

Next, we propose another strategy that directly utilizes the centralized controller results,

referred to as the 'Direct Strategy'. As shown in Table 9.1 (see Strategy Direct), two controllers are designed: controller #3 uses the centralized ratio while controller # 4 uses the ratio based on PV rating with the local PV strategy. Under this strategy, for the time step t at which we receive the centralized controller results, we directly send out $\boldsymbol{Q}_t^{\mathrm{PV,ctr}}$ from the centralized controller to each PV system. At the same time, we record the power demand at the measured node of the distributed controller $\boldsymbol{S}^{\mathrm{ctr}}$. In the following time steps, the objective of the integrated controller is to eliminate the change of the negative-sequence voltage introduced by the change of load and PV generation. The three-phase reactive power compensation is calculated as follows:

$$\boldsymbol{Q_t^c} = f(\boldsymbol{S_t^m} - \boldsymbol{S}^{\mathrm{ctr}}, \boldsymbol{V_t^m}, 0). \tag{9.16}$$

Again, $\hat{Q}_t = 0$ because we have no information on how to change the total injected reactive power. The term $\boldsymbol{S_t^m} - \boldsymbol{S}^{\mathrm{ctr}}$ represents the change of net demand with respect to that at the time when we directly apply the centralized controller results.

9.3 Case Studies

In this section, we present several case studies on the IEEE 13-node feeder [58] and the taxonomy feeder R1-12.47-1 [107]. We first define the performance metrics for the controller evaluation. We then provide the details of the feeders and the real-time simulations. The centralized controller is implemented in Julia using JuMP and solved using a nonlinear programming solver `Ipopt`, and the distributed controller and the integrated controller are implemented in MATLAB. Next, we compare the performance of the centralized controller and the distributed controller, considering both static and time-varying cases. The pros and cons of each controller are then discussed. In addition, we test the performance of the heuristic strategies introduced in Section 9.2.3. Lastly, we present the results of the integrated controller.

Assume the number of the time steps is T and the number of the nodes is N. We set the upper and lower limits of the voltage magnitude as $\overline{V} = 1.1, \underline{V} = 0.9$. The performance of each controller is evaluated based on the following aspects:

- Unbalance improvement: for static cases, we will compare the final VUF at the critical node n (VUF_n) achieved by each controller; for time-varying cases, the mean VUF at the critical node n over the day ($\overline{\mathrm{VUF}}_n = \sum_t \mathrm{VUF}_{n,t}/T$) is compared.

- Violation of the voltage limits: The percent violation of the voltage limits (α) is defined as

$$\alpha = 100 \times \frac{\sum_t \sum_n a_{n,t}}{NT} \tag{9.17}$$

where $a_{n,t}$ is a binary variable indicating the voltage limit violation at node n and time step t:

$$a_{n,t} = \begin{cases} 1, & \text{if } V_n^m > \overline{V} \text{ or } V_n^m < \underline{V} \\ 0, & \text{otherwise} \end{cases} \tag{9.18}$$

- Violation of the limit $\text{VUF}_n^{\text{final}} \leq \text{VUF}_n^{\text{initial}}, \forall n \in \mathcal{N}_{3\phi}$: The percent violation of this limit (β) is defined as

$$\beta = 100 \times \frac{\sum_t \sum_n b_{n,t}}{NT} \tag{9.19}$$

where $b_{n,t}$ is a binary variable indicating whether the unbalance at a three-phase node n and time step t becomes worse or not after implementing a controller:

$$b_{n,t} = \begin{cases} 1, & \text{if } \text{VUF}_{n,t}^{\text{final}} > \text{VUF}_{n,t}^{\text{initial}} \\ 0, & \text{otherwise} \end{cases} \tag{9.20}$$

9.3.1 Simulation Setup

We simulate the feeders using a 1-minute resolution load and PV data, and we assume that load and PV generation remain constant for the duration of one minute. The PV real power generation is simulated based on 1-minute irradiance data from the National Renewable Energy Laboratory's Measurement and Instrumentation Data Center [100]. We use the 1-minute or 15-minute data from Pecan Street [119] to generate the load profiles. The 1-minute and 15-minute data are collected at different locations and on different days. The details of PV and load profiles for each feeder are discussed below.

Fig. 9.3 shows the one-line diagram of the IEEE 13-node feeder [58], with system data available in [66]. Similar to what had been done in Chapters 7 and 8, we balance the upstream network of 632, as discussed in Section 7.6.2. We connect 15 houses into the feeder: for each house, we assume there are 5 residential loads and 5 PV inverters. Instead of using the available 1-minute load data, we linearly interpolate the 15-minute load data to a 1-minute interval. This is because we did not observe any violation of the engineering limits of the distributed controller using the 1-minute data, however the interpolated 15-minute load data

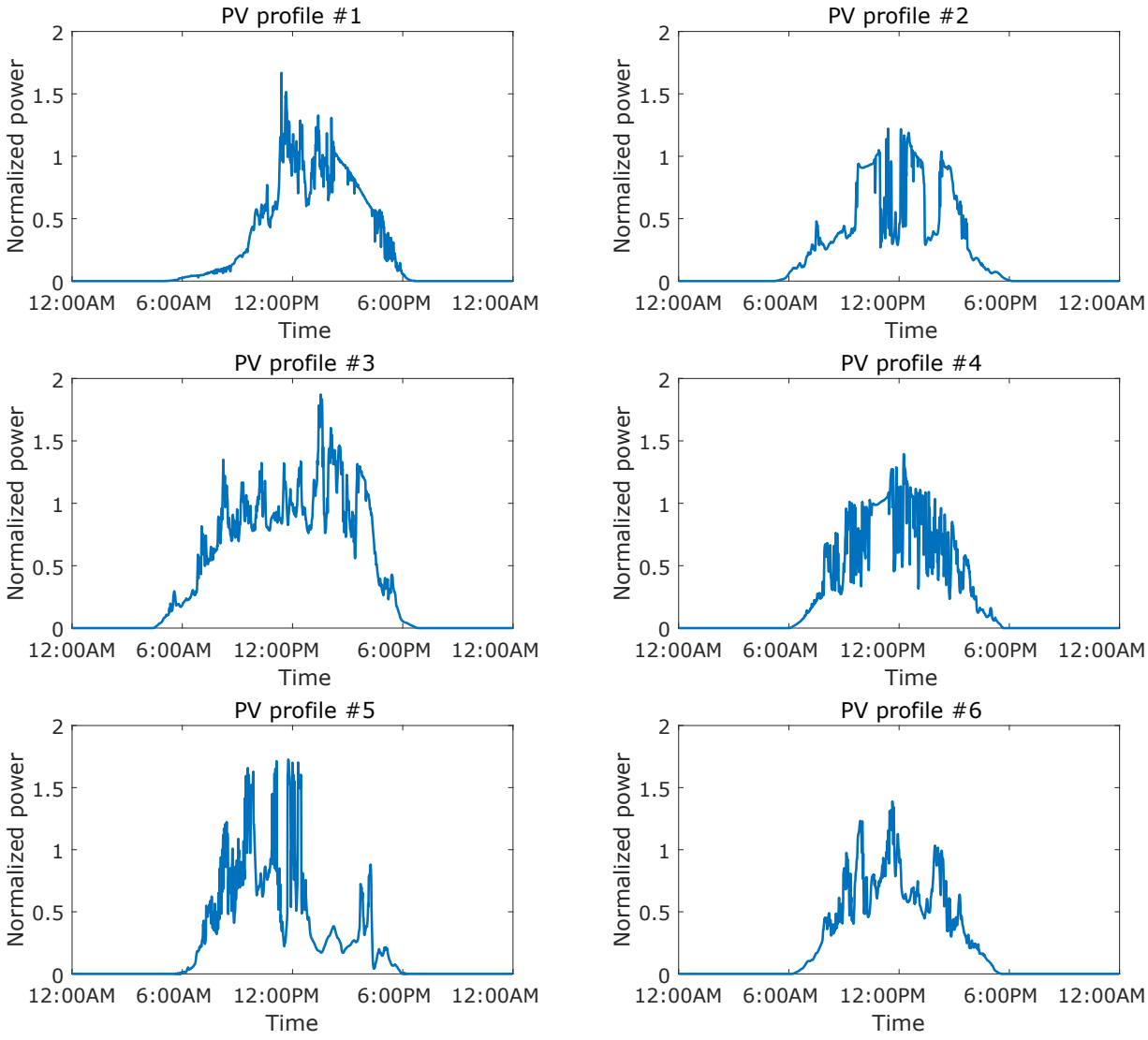

Figure 9.2: Normalized real power generation profiles of PV systems.

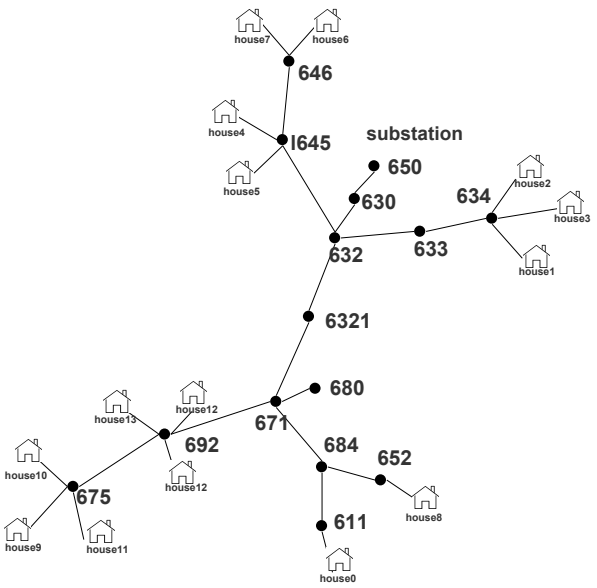

Figure 9.3: IEEE 13-node feeder [58] with houses connected visualized using [134] .

did expose the disadvantages of the distributed controller. The feeder has 75 PV systems, 20, 25, and 30 of those systems connected to phases A, B, C, respectively. All PV systems are rated at $S^{\text{rate}} = 35$ kVA and their base real power generation are randomly generated from the range of 15 to 20 kW. We pick the irradiance data collected on a cloudy day in January 2020 in Las Vegas, NV and normalized the data by the irradiance value at 12 PM, as shown in Fig. 9.2 (see PV profile #1). We assume all 75 PV systems follow the same trend as PV profile #1. We set the real power output of each PV system to be equal to its base real power generation multiplied by the normalized PV data, and set 632 and 671 as the critical nodes.

Fig. 9.4 shows the one-line diagram of the R1-12.47-1 feeder. PV systems are added to 598 single family residences, with 265, 150, and 183 of those systems connected to phases A, B, C, respectively. All PV systems are rated at $S^{\text{rate}} = 20$ kVA and their base real power generation are randomly selected from the range of 8 to 13 kW. We divide the feeder into six different areas as shown in Fig. 9.4. PV systems in the same area have the same PV profile, and each area has a different PV profile. To create the PV profiles of the entire feeder on one day, six PV profiles are required; they are generated based on irradiance data collected on six cloudy days from January to June 2020 (one day per month) in Las Vegas, NV. Each set of data is normalized by its value at 12:00 PM, as shown in Fig. 9.2. Again, the real power output of each PV system is set equal to its base real power generation multiplied by

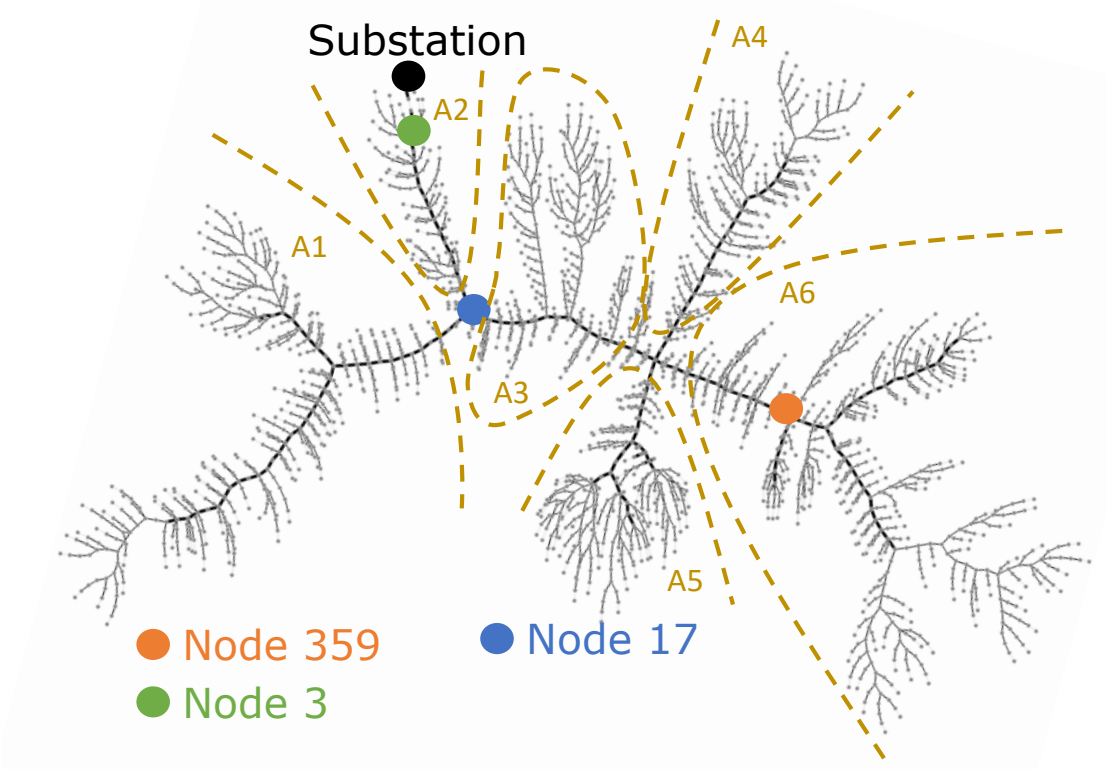

Figure 9.4: Taxonomy feeder R1-12.47-1 [107] visualized using [99].

the normalized PV data. We pick 598 1-minute resolution load profiles randomly out of 750 available ones from [119]. We choose two nodes, 17 and 359, as the critical nodes: 17 is close to the substation and 359 is far from the substation.

9.3.2 Comparison between Centralized Controller and Distributed Controller

We first consider the **static cases** where the load and PV generation remain constant during the computation of the reactive power compensation. The centralized controller and the distributed controller are evaluated using the load and PV generation at 12:00 PM, mainly to compare the computation time of each controller. For the distributed controller, we keep it running until a stable VUF is reached. The final VUF at the critical node, violation of engineering limits, and computation time are summarized in Table 9.2. During the simulation, we do not observe the increase of unbalance at any node, resulting $\beta = 0$; therefore, we only show the percent violation of voltage limits (α) in the table. The abbreviations 'Ctr.' and

Table 9.2: Comparison of the results: constant load and PV

Feeder	Case #	Critical Node	VUF (%) Int.	VUF (%) Ctr.	VUF (%) Dis.	α (%) Int.	α (%) Ctr.	α (%) Dis.	Comp. time (s) Ctr.	Comp. time (s) Dis.
13-node	I	632	0.5562	0.0000	0.0000	0.000	0.000	0.000	0.2	0.2
	II	671	1.6713	0.0000	0.7674	0.000	0.000	0.000		
R1	III	17	0.8629	0.1369	0.0125	0.408	0.000	24.183	1500.0	3.0
	IV	359	1.7185	0.1713	0.8295	0.408	0.000	13.747		

Table 9.3: Comparison of the results: time-varying load and PV

Feeder	Case #	Critical Node	$\overline{\text{VUF}}$ (%) Int.	$\overline{\text{VUF}}$ (%) Ctr.	$\overline{\text{VUF}}$ (%) Dis.	α (%) Int.	α (%) Ctr.	α (%) Dis.	β (%) Ctr.	β (%) Dis.
13-node	I	632	0.5394	0.0000	0.0000	0.422	0.000	0.446	0.000	1.668
	II	671	1.7370	0.0000	0.9922	0.422	0.000	16.908	0.000	29.236
R1	III	17	0.8602	0.1256	0.0085	0.087	0.003	7.036	0.000	0.000
	IV	359	1.7459	0.1764	0.8988	0.087	0.025	5.145	0.000	0.000

'Dis.' represent the centralized controller and the distributed controller, respectively. For each feeder, we consider two cases with different critical nodes. In each case, the objective is to minimize VUF at the critical node. The initial VUF at the critical nodes and percent violation of voltage limits are also presented in Table 9.2 (see Int.).

As indicated in Table 9.2, both controllers can reduce the unbalance at the critical node. The distributed controller is only able to perfectly eliminate the unbalance when network upstream of the critical node is balanced. When the critical nodes are far from the substation (see Critical Node 671, 359), the distributed controller cannot achieve the same unbalance improvement as the centralized controller. When we reduce the unbalance at node 17 in the R1-12.47-1 feeder, the final VUF by the distributed controller is lower than that by the centralized controller; however, the distributed controller has significantly more voltage violations. In all cases, the centralized controller does not violate any limit while the distributed controller sometimes results in very large percent violations. Regarding the computation time, the distributed controller is fast (3 seconds), while the centralized controller needs 25 minutes to obtain the optimal solutions for the R1-12.47-1 feeder.

Next, we consider the **time-varying cases** where the load and PV generation are changing

following the 24-hour profiles discussed in Section 9.3.1. We have four cases; the objective of each case is to reduce the unbalance at the critical node. Since the computation time of the distributed controller is short, we assume the distributed controller operates every 10 seconds. For the R1-12.47-1 feeder, the centralized controller takes approximately 16-30 minutes to obtain a solution. Therefore, we assume for every 30-minute period, the centralized controller takes measurements of load and PV generation at the beginning of the period, and then uses the entire period to compute the reactive power injections of each PV system. At the end of the period, PV systems will receive the results of the centralized controller and inject reactive power as commanded.

Table 9.3 summarizes the mean VUF of the whole day ($\overline{\text{VUF}}$) at the critical nodes, percent voltage violation (α), and percent violation of the limit $\text{VUF}^{\text{final}} \leq \text{VUF}^{\text{initial}}$ (β) for different cases. Similar to the results of the static cases, both controllers reduce the mean VUF at the critical nodes. In Case III, the distributed controller achieves lower mean VUF than the centralized controller does, but the percent violation of the engineering limits is relatively high. Another finding is that the centralized controller cannot satisfy the engineering limits for the R1-12.47-1 feeder. This is because the reactive power injections generated by the centralized controller are computed using outdated measurements. However much lower α and β values are achieved using the centralized controller than using the distributed controller. In addition, the centralized controller reduces the violation of the voltage limits compared with that of the initial cases with uncontrolled PV systems (see α, Int. versus Ctr.).

Fig. 9.5 shows the VUF at all three-phase nodes in the 13-node feeder when the objective is to reduce the unbalance of 632 (Case I in Table 9.3), and Fig. 9.6 shows the voltage magnitudes of all nodes in the 13-node feeder after applying the distributed controller. As shown in Fig. 9.5, the distributed controller achieves perfect balance at the critical node, as does the centralized controller throughout the entire day. However, unlike the centralized controller, the unbalance at 634, 671, 692, and 675 become worse around 6 - 7 PM. Moreover, we observe that the voltage magnitudes of some nodes around that period are also below 0.9 p.u., as shown in Fig. 9.6. In contrast to the distributed controller, the centralized controller has zero values for both α and β. Similar results can be observed in Table 9.3 when the critical node is 671.

Based on the comparisons of the results for both static and time-varying cases, we summarize the pros and cons of the centralized controller and the distributed controller in Table 9.4. In all cases, the centralized controller can significantly reduce the unbalance, and has low

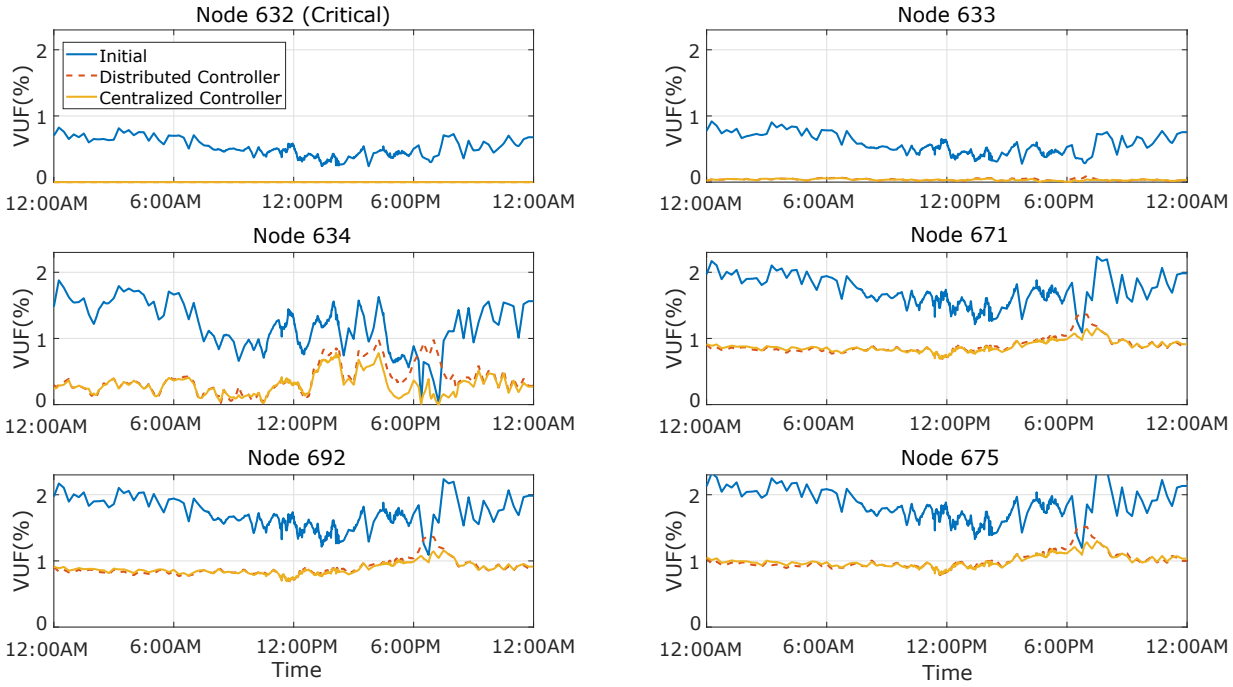

Figure 9.5: VUF at the three-phase nodes in the 13-node feeder without control (initial) and after applying the controllers.

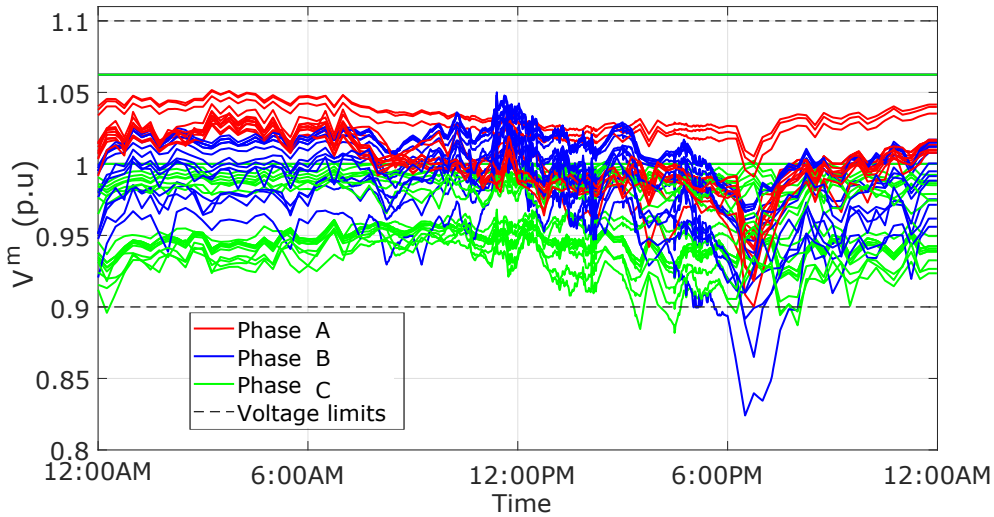

Figure 9.6: Voltage magnitudes of all nodes in the 13-node feeder after applying the distributed controller.

Table 9.4: Comparison between centralized controller and distributed controller

	Centralized Controller	Distributed Controller
Pros	Directly minimizes VUF; Considers engineering limits	Does not require system model; Requires few local measurements; Requires simple broadcast communication system; Computationally simple
Cons	Requires detailed system model; Requires load and PV measurements at every node; Requires two-way communication system; Computationally heavy	Reduces V_2 to improve VUF via balancing the downstream load; Does not consider engineering limits

or even zero percent violation of the engineering limits. However, the centralized controller requires a detailed system model, accurate load and PV generation inputs, two-way communication system, and is computationally heavy. The major advantages of the distributed controller are that it is computationally simple, and does not require pervasive sensing and communication networks. Since the distributed controller is designed based on Steinmetz design, one drawback is that the goal of the distributed controller is to balance the downstream load. As we can see from the results of the cases where the critical nodes are far from the substation, the distributed controller cannot significantly improve the unbalance, implying that balancing downstream load is not always an effective approach to mitigate unbalance.

9.3.3 Heuristic Strategy Results

Next, we test the performance of the grouped controller and the local PV strategy. We notice that when the critical nodes are far from the substation, the distributed controller cannot significantly improve the unbalance at the critical node. Therefore, we use the grouped controller to reduce unbalance. When the critical node is 671 in the 13-node feeder, all 75 PV systems are divided into two groups; group 1 includes PV systems at houses 1-8 and group 2 includes all the remaining PV systems. The grouped controller has two distributed controllers, one at 632 and the other at 671. Similarly for 359 in the R1-12.47-1 feeder, the grouped controller has two distributed controllers, one at 3 and the other at 359, so that all

Table 9.5: Comparison between distributed controller and grouped controller

Feeder	Critical Node	$\overline{\text{VUF}}$ (%)		α (%)		β (%)	
		Dis.	Grp.	Dis.	Grp.	Dis.	Grp.
13-node	671	0.9992	0.4608	16.908	6.705	29.236	15.521
R1	359	0.8988	0.0428	5.145	17.321	0.000	0.000

Table 9.6: Mean VUF and percent violation of the voltage limits with and without the local PV strategy

Feeder	Critical Node	$\overline{\text{VUF}}$ (%)		α (%)	
		Without	With	Without	With
13-node	632	0.0000	0.0000	0.446	0.232
	671	0.4608	0.4644	6.705	4.034
R1	17	0.0085	0.0085	7.036	0.302
	359	0.0428	0.1653	17.321	3.702

PV systems are controlled by the grouped controller. The results of the distributed controller and the grouped controller with time-varying load and PV are compared in Table 9.5. The abbreviation 'Grp.' represents the grouped controller. In both feeders, the grouped controller has a lower mean VUF. Although the grouped controller reduces the percent violation of the engineering limits for the 13-node feeder, that is not the case for the R1-12.47-1 feeder.

Next, the performance of the local PV strategy is explored. Table 9.6 reports the mean VUF and the percent violation of the voltage limits with time-varying load and PV before and after applying the local PV strategy. The results of the cases where 671 and 359 are the critical nodes are generated using the grouped controller. When the critical nodes are close to the substation, the values of α are reduced and the mean VUFs are not influenced after using the local PV strategy; however, when the critical nodes are far from the substation, the mean VUF becomes larger than those without the local PV strategy. This is because the unbalance of the critical nodes that are far from the substation is severe and a large amount of reactive power is required to reduce the unbalance, causing many PV systems to operate at their maximum reactive power capacity. When we continue to apply the local PV strategy, the difference between the actual responses and the desired reactive power compensation becomes larger. PV systems do not have enough reactive power capacity to compensate the difference, and thus the mean VUF increases when the value of α decreases.

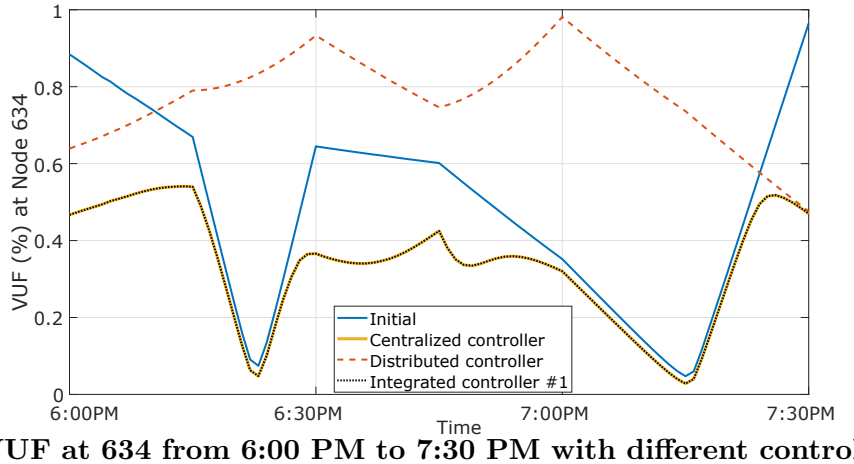

Figure 9.7: VUF at 634 from 6:00 PM to 7:30 PM with different controllers when the critical node is 632.

9.3.4 Integrated Controller Results

In this section, we test the performance of the integrated controllers with the different configurations introduced in Section 9.2.4. First, we will show an example illustrating that the integrated controller #1 is only suitable for the cases where the critical nodes are close to the substation. We test the performance of the integrated controller #1 on the 13-node feeder. We assume the centralized controller can provide its optimal results to the integrated controller every 1 minute. Recall in Fig. 9.5 that the distributed controller will violate the engineering limit $\text{VUF}^{\text{final}} \leq \text{VUF}^{\text{initial}}$ at around 6 - 7 PM, and such violation is the most serious at 634. In what follows, we will compare the VUF achieved using different controllers at 634.

Fig. 9.7 shows the comparison among different controllers when the objective is to mitigate the unbalance at the critical node 632. The blue solid line is the VUF without control ($\text{VUF}^{\text{initial}}$), the red dashed line is the VUF using the distributed controller. We can easily tell that, when the distributed controller is used, the corresponding VUF is larger than $\text{VUF}^{\text{initial}}$ in most of the time during this period. The yellow solid line is the VUF using the centralized controller and the black dotted line is the VUF using the integrated controller #1. The overlapping of these two lines shows that using both the total injected reactive power and the contribution ratio from the centralized results, the integrated controller #1 achieves the same performance as the centralized controller.

The VUF at 634 acquired using different controllers to reduce the unbalance at 671 is illustrated in Fig. 9.8. The grouped controller (red dashed line) still increases the unbalance at 634 when reducing the unbalance at 671, while the centralized controller does not (yellow

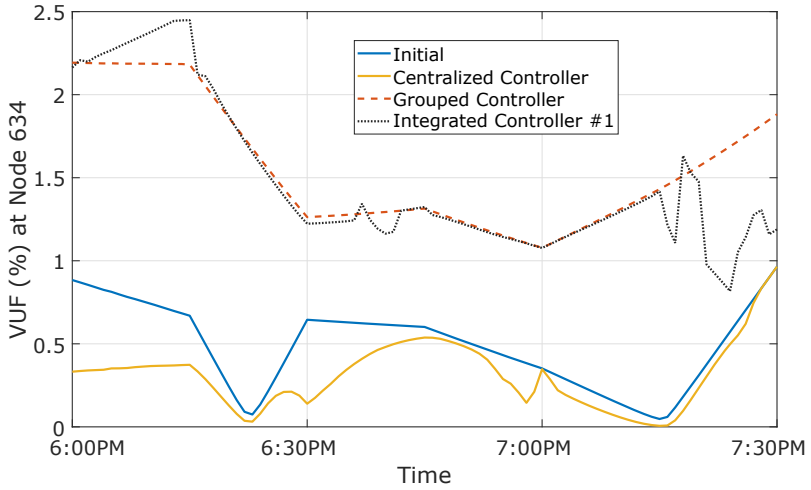

Figure 9.8: VUF at 634 from 6:00 PM to 7:30 PM with different controllers when the critical node is 671.

Table 9.7: Performance metrics for the centralized controller for the 13-node feeder when implemented every 1 minute or 60 minutes

Critical Node	1 minute $\overline{\text{VUF}}$ (%)	1 minute α (%)	1 minute β (%)	60 minutes $\overline{\text{VUF}}$ (%)	60 minutes α (%)	60 minutes β (%)
632	0.0000	0.00	0.00	0.1316	0.14	1.40
671	0.0000	0.00	0.00	0.2201	1.51	8.28

solid line). In this case, the integrated controller using the centralized controller results (black dashed line) does not yield a better performance than that of the grouped controller. Even though the integrated controller knows the total injected reactive power from the centralized controller, it cannot obtain the same allocation of reactive power to each phase as the centralized controller does, because the centralized controller does not minimize the VUF at 671 by balancing the load downstream and upstream of 671. The reactive power injections of the integrated controller are totally different from those of the centralized controller, so the integrated controller still worsens the unbalance at 634.

Next, we consider a more realistic circumstance in which the centralized controller is activated every 60 minutes. Table 9.7 compares the performance of the centralized controller on the 13-node feeder when the controller is implemented every 1 minute and every 60 minutes. It is shown that all performance metrics become worse when the centralized controller runs infrequently. For the R1-12.47-1 feeder, when the period of the centralized controller is 60 minutes, the mean VUF always increases. However, α decreases when the critical node is

Table 9.8: Performance metrics for the centralized controller for the R1-12.47-1 feeder when implemented every 30 minutes or 60 minutes

Critical Node	30 minutes $\overline{\text{VUF}}$ (%)	30 minutes α (%)	60 minutes $\overline{\text{VUF}}$ (%)	60 minutes α (%)
17	0.1256	0.003	0.1503	0.004
359	0.1764	0.025	0.2315	0.019

Table 9.9: Comparison of controllers when the critical node is 671 of the 13-node feeder

Controller		$\overline{\text{VUF}}$ (%)	α (%)	β (%)
Integrated	#1	0.5592	10.33	15.53
	#2	0.4754	3.60	13.98
	#3	0.0775	1.35	6.17
	#4	0.0743	0.56	5.00
Centralized (every 60 minutes)		0.2201	1.51	8.28
Grouped with local PV strategy		0.4644	4.03	14.70

359, as shown in Table 9.8. For the large feeder, the solutions of the centralized controller are always solved based on the outdated measurements despite the length of the implementation period, so it is hard to tell whether the percent violation of the voltage limits will increase or not.

The following studies focus on investigating whether the integrated controller can improve the performance of the centralized controller. We compare the results of the integrated controller with those of the centralized controller, as well as the grouped controller with the local PV strategy when the critical nodes are far from the substation.

For the 13-node feeder, the objective of all controllers is to mitigate the unbalance at 671. Table 9.9 summarizes the mean VUF and the percent violation of the engineering limits of different controllers. As discussed above, the integrated controller #1 does not work well when the critical node is far from the substation, even when the centralized controller runs frequently, so it is not surprising that the integrated controller #1 has the worst performance. The integrated controller #2 has lower values in all three aspects than the integrated controller #1. Using the integrated controller #3 and #4, we can further reduce the mean VUF and the values of α and β. In addition, the performance of the integrated controller #4 is

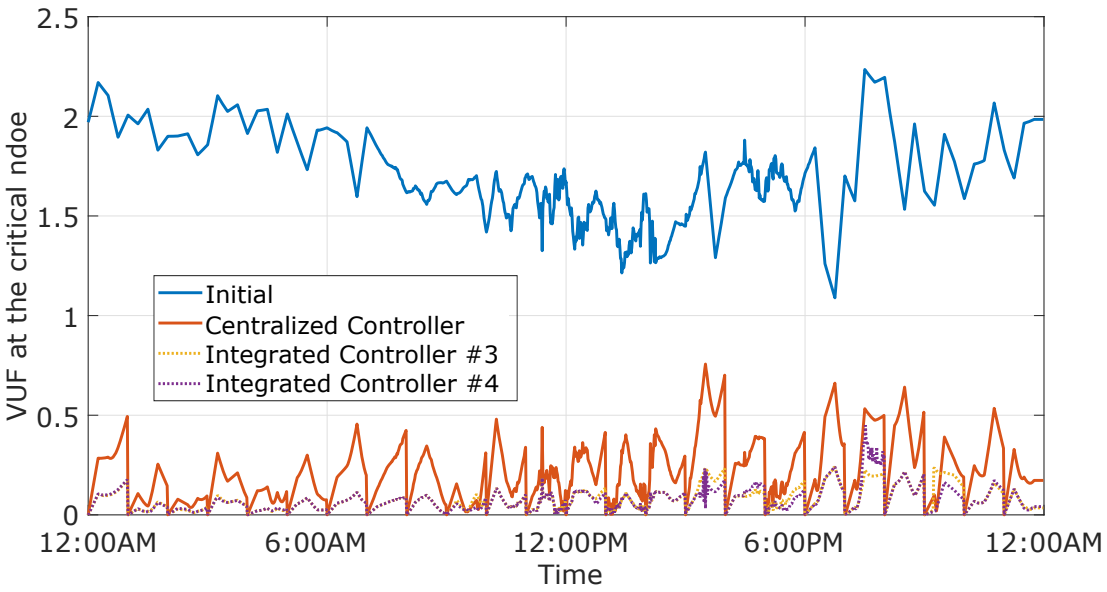

Figure 9.9: VUF at node 671 with different controllers

better than that of the controller #3 in every aspect: this is because the centralized ratio from the centralized controller using the measurements at one specific time may not be suitable for another time. Even though the centralized controller runs every 60 minutes, it still has a better performance than the grouped controller. Among all controllers, the integrated controller #4 has the best performance.

Our results show that the integrated controller with the Direct Strategy has better performance than with the Indirect Strategy, so we focus on comparing the VUF achieved by the centralized controller and the integrated controller with the Direct Strategy. Fig. 9.9 depicts the VUF at 671 before and after applying the centralized controller, the integrated controller #3, and the integrated controller #4. The blue solid line is the initial VUF. The red solid line is the results of using the centralized controller. The yellow and purple dotted lines are the results of using the integrated controller #3 and #4, respectively. When the measurements of the centralized controller are not updated every 1 minute, the VUF will not remain zero when the load and PV generation are changing. On the other hand, the integrated controller #3 and #4 can recognize such operating point changes based on local measurements, and can effectively reduce the negative-sequence voltage caused by the change in load and PV generation, thus improving the unbalance.

For the R1-12.47-1 feeder, the objective of all controllers is to mitigate the unbalance at 359. Table 9.10 reports the resulting mean VUF and the percent violation of the voltage

limits. Again, the integrated controller #1 does not have good performance compared with all other controllers. Although the integrated controller #2 has the lowest mean VUF, it has a larger α compared with the centralized controller. Similar to the results of the 13-node feeder, the integrated controller #3 and #4 yield a lower mean VUF than the centralized controller, and the integrated controller #4 is still better than controller #3.

The details of the VUF at the critical node after using the centralized controller, the integrated controller #3, and the integrated controller #4 are depicted in Fig. 9.10. Different from the observation in Fig. 9.9, the results in Fig. 9.10 reveal that the integrated controller with Direct Strategy cannot always reduce the VUF. For example, from 1:20 PM to 2:00 PM, we observe that the integrated controller produces a larger VUF than using centralized controller alone at the critical node. The reason is that the integrated controller with Direct Strategy is trying to maintain the negative-sequence voltage of the centralized controller, but in this situation the negative-sequence voltage would naturally decrease with uncontrolled PV systems; thus applying the integrated controller will result in an increase of the VUF. We then propose a heuristic strategy in which the integrated controller will only send out new commands when it detects an increase in the VUF with respect to the VUF of the centralized controller. The performance of the integrated controller with the heuristic strategy is illustrated using the integrated controller #4, shown as the green dotted line in Fig. 9.10. Using this strategy, we can ensure that the integrated controller does not negatively impact the VUF achieved by the centralized controller. As shown in Table 9.10, the integrated controller #4 with heuristic strategy has a lower mean VUF than those acquired without it. However, the integrated controller cannot achieve a similar percent voltage violation level to that obtained by the centralized controller acting alone. The violation of voltage limits happens primarily during the first hour when we do not have any information from the centralized controller. If we only compute α for the remaining 23 hours, the percent violation is only 0.08%.

Considering every performance metric, the integrated controller with the Direct Strategy is better than that with the Indirect Strategy, because directly using the centralized controller results ensures a good starting point with low unbalance and fewer violations of the engineering limits for the integrated controller. Since the integrated controller can respond quickly to the change of load and PV, the mean VUF of the integrated controller with the Direct Strategy is always lower than that of the centralized controller. We have also demonstrated the effect of integrating the centralized controller results into the Steinmetz controller. Through the above comparison, we find that using the centralized ratio does

Table 9.10: Comparison of controllers when the critical node is 359 of the R1-12.47-1 feeder

Controller		$\overline{\text{VUF}}$ (%)	α (%)
Integrated	#1	0.2711	11.58
	#2	0.0936	1.65
	#3	0.1459	0.59
	#4	0.1394	0.33
	#4 - Heuristic	0.1161	0.33
Centralized (every 60 minutes)		0.2315	0.02
Grouped with local PV strategy		0.1653	3.70

not perform better than using the ratio based on the PV rating if the centralized controller cannot run frequently. The integrated controllers have a lower α than the grouped controller under most conditions, suggesting that setting the total injected reactive power equal to that computed by the centralized controller helps to reduce the violation of the voltage limits.

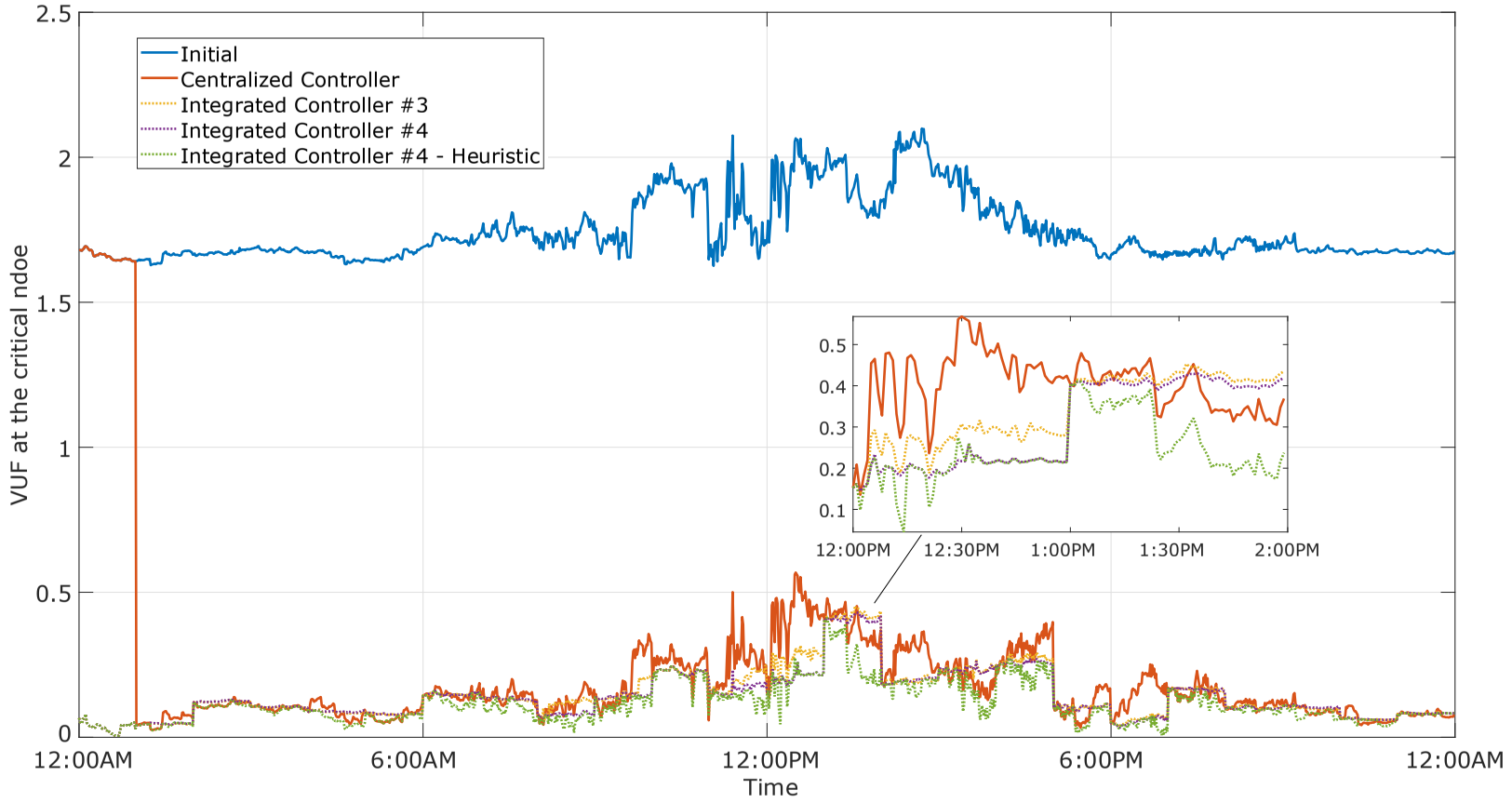

Figure 9.10: VUF at node 359 with different controllers

9.4 Chapter Conclusion

In this chapter, we compared the performance of the distributed controller with that of the centralized controller, and the pros and cons of each controller were discussed. The major drawback of the distributed controller is that it may negatively impact on the voltage profile and the unbalance on other nodes. In addition, balancing load is not an effective way to mitigate the unbalance when the critical node is far from the substation,

We proposed a new controller that integrates the results from the centralized controller into the Steinmetz controller, referred to as the integrated controller. The results show that the voltage violation is reduced when the integrated controller has the total injected reactive power from the centralized controller. No strategy has proven useful to reduce the unbalance at noncritical nodes, which is a topic for future research. When the centralized controller operates infrequently, the integrated controller can further mitigate the unbalance but sometimes might slightly increase the violation of the voltage limits.

Chapter 10

Conclusions and Future Work

This dissertation presented work on using demand response (DR) to improve power system voltage and small-signal stability in transmission systems and controlling solar photovoltaic (PV) systems to mitigate voltage unbalance in distribution systems. In this chapter, we summarize our key findings on these two topics and list several future research topics.

10.1 Key Findings

The work in Chapters 2 - 6 revealed that loads are effective in improving stability margins other than frequency stability. It was shown that DR actions wherein the total demand responsive load is held constant but is shifted between different buses can improve voltage or small-signal stability margins, and in some cases - more effectively than generation actions.

Chapter 2 showed that the smallest singular value (SSV) was improved using our DR strategy. We benchmarked the proposed iterative linear programming with singular value sensitivity against a brute force algorithm, an iterative linear programming with eigenvalue sensitivity, and an iterative nonlinear programming algorithm. Results indicated that our proposed algorithm is able to converge to the global or at least a local optimal solution and is more computationally efficient than other algorithms.

Chapter 3 considered different load models within the SSV maximization problem. We observed changes in the optimal loading patterns when using different load models, revealing the importance of properly modeled loads in the optimization problem. Furthermore, we found it challenging to interpret the stability condition of the system with different structures using the SSV, since structural changes in the power flow Jacobian matrix affect the magnitude of the SSV.

Chapter 4 considered a multiperiod optimization problem. In the first period, we maximized the SSV; in the second period, we minimized the generation cost and paid back energy to each load while maintaining the SSV. We compared the generation cost of the multiperiod DR strategy with that of generation redispatch. We found that the DR strategy led to a lower generation cost in most cases. Even when DR is more expensive than generation redispatch, it may still be desirable to deploy DR because generators may not respond in time.

Chapter 5 considered maximizing the distance to the closest Saddle-Node-Bifurcation (SNB) to improve the voltage stability. We applied the Newton-Raphson method to solve the Karush–Kuhn–Tucker conditions of a nonlinear nonconvex optimization problem in order to obtain the optimal loading pattern. We found that we achieved significantly different loading patterns when maximizing the SSV versus the distance to the closest SNB.

The results from Chapters 2 - 5 revealed the trade-offs between choosing either the SSV or the distance to the closest SNB as the voltage stability margin. The distance to the closest SNB presents the stability margin in the parameter space while SSV only provides implicit information for the distance to instability. Another drawback of using the SSV as the measure of voltage stability is that the value is system-dependent, and it is difficult to compare the SSVs associated with systems that use different load models. On the other hand, the algorithm we proposed for maximizing the distance to the closest SNB relies on good initializations, whereas the iterative linear programming method used to maximize the SSV of the power flow Jacobian matrix does not have this issue, and it scales better to realistically-sized systems. Furthermore, SSV is more straightforward to work with than the distance to the closest SNB because there is only one SSV, whereas there can be a large number of locally closest SNBs. The globally closest SNB is difficult to find, and we observed convergence issues with the algorithm used to maximize the distance to the closest SNB.

Chapter 6 focused on improving the small-signal stability of the system via DR action. In a case study, we found that when we improved the smallest damping ratio, it had adverse effects on the other small-signal stability metrics and voltage stability, indicating the importance of the choice of the stability metric. Case studies were also performed to compare the improvements in the smallest damping ratio achieved by shifting the real power of demand response, shifting the reactive power of demand response, and re-dispatching real power generation. Results showed that only spatially shifting the real power of demand response could significantly increase the smallest damping ratio.

The second part of the dissertation dealt with the question of whether Steinmetz design can be used to control the reactive power of distributed solar PV systems to mitigate volt-

age unbalance. We found that a decentralized controller that applies Steinmetz design in a completely decentralized way can indeed reduce the unbalance in the feeder. With a simple communication network, a distributed controller can further reduce the unbalance.

Chapter 7 presented the reactive power compensation strategies with different load and PV connections and different balancing objectives. Case studies verified the effectiveness of both the decentralized controller and the distributed controller. We also found that the controller did not work well when the critical node was far from the substation. Better performance was achieved by implementing the controller at an upstream node.

Chapter 8 proposed different strategies to overcome the practical challenges in applying the distributed controller to real systems. Results showed that measurement error and noise did not have a significant impact on the performance of the distributed controller, but communication delays could worsen the unbalance. Case studies demonstrated that the proposed compensation strategies effectively reduced the impact of communication delays and improved the unbalance.

Chapter 9 compared the distributed controller with a centralized controller. The pros and cons of each controller were summarized. One drawback of the distributed controller is that it does not consider engineering limits. Results showed that while the distributed controller greatly improved the unbalance at the critical nodes, it also had a negative impact on the voltage profile and/or the unbalance at noncritical nodes. We proposed a new controller that integrated the centralized controller results into the distributed controller. Case studies demonstrated that the integrated controller could be used to further mitigate the unbalance when the centralized controller operated infrequently. We noted the trade-offs between unbalance improvement and violation of engineering limits when using different controllers.

10.2 Future Research Topics

This work has generated a number of potential avenues of future research. We have showed that harnessing demand responsive loads can effectively improve stability margins, the first direction of the future work is to come up with more computationally efficient algorithms to determine the optimal loading pattern. Possible research topics are detailed below:

- *Gaining a better understanding of why the loading patterns change in the way they do:* We would like to conduct an analytical analysis, e.g. sensitivity analysis, of the optimal design to investigate whether a load should be increased or decreased toward achieving

the optimum solution. We believe that the study may provide a starting point toward simple tuning schemes for demand response actions.

- *Considering N-1 security:* We would like to incorporate N-1 security constraints in the optimization formulations such that the optimal loading pattern can ensure adequate stability margin under altered operating conditions.

- *Developing an improved algorithm to maximize the distance to the closest SNB:* The proposed solution algorithm in Chapter 5 has convergence issues and does not scale to realistically-sized system. An improved algorithm is needed to find the optimal loading pattern that has the maximum distance to the globally closest SNB. We would like to develop approaches to deal with the problem caused by the existence of multiple locally closest SNBs.

- *Developing a new voltage stability index:* A possible idea is to find the central of the convex restriction area [76] of the feasibility set. Instead of maximizing any stability margin, we could push the operating point toward the central of an inner approximation of the feasibility set to improve voltage stability.

- *Developing approaches to ensure stability of the transition between different loading patterns:* The multiperiod optimization problem in Chapter 4 neglected the transition between operating points. We would like to improve the solution algorithm to explicitly consider the path between each operating point, ensuring an adequate voltage stability margin along the path. For this, we could leverage ideas from [54, 97, 104].

- *Considering multiple stability margins at the same time:* We would like to combine voltage and small-signal stability into the optimization problem to avoid the circumstance where improving one type of stability will negatively impact on the other. We are also interested in whether we can improve the transient stability using this spatial DR strategy.

The second direction of the future work is to further improve the performance of the Steinmetz controller so that it can be better implemented to real systems to mitigate unbalance. The tasks include:

- *Investigating the proper conditions to implement the Steinmetz controller:* We would like to develop methods to evaluate the source of voltage unbalance. If we could identify

whether the unbalance at a node comes from its upstream or downstream quantitatively, we could figure out the proper conditions to apply the Steinmetz controller. Future work also includes the development of strategies to alleviate the negative impacts on noncritical nodes introduced by the Steinmetz controller.

- *Developing a robust control strategy to deal with communication delays:* A preliminary investigation of strategies for reducing the impact of delays is undertaken in Chapter 8, but we cannot ensure that these strategies would be effective in general cases. Future work will attempt to derive conditions for convergence/divergence of the enhanced Steinmetz controllers and develop a robust control strategy to guarantee the convergence of the Steinmetz controller in the presence of communication delays and missing data.

Bibliography

[1] S. M. Abdelkader and D. J. Morrow. "Online tracking of Thévenin equivalent parameters using PMU measurements". In: *IEEE Transactions on power systems* 27.2 (2012), pp. 975–983.

[2] B. S. Abdulraheem and C. K. Gan. "Power system frequency stability and control: Survey". In: *International Journal of Applied Engineering Research* 11.8 (2016), pp. 5688–5695.

[3] V. Ajjarapu and C. Christy. "The continuation power flow: a tool for steady state voltage stability analysis". In: *IEEE transactions on Power Systems* 7.1 (1992), pp. 416–423.

[4] M. F. Akorede, H. Hizam, and E. Pouresmaeil. "Distributed energy resources and benefits to the environment". In: *Renewable and sustainable energy reviews* 14.2 (2010), pp. 724–734.

[5] R. Al Abri, E. F. El-Saadany, and Y. M. Atwa. "Optimal placement and sizing method to improve the voltage stability margin in a distribution system using distributed generation". In: *IEEE Transactions on Power Systems* 28.1 (2013), pp. 326–334.

[6] M. H. Albadi and E. F. El-Saadany. "A summary of demand response in electricity markets". In: *Electric power systems research* 78.11 (2008), pp. 1989–1996.

[7] M. Aman, G. Jasmon, A. Bakar, and H. Mokhlis. "A new approach for optimum DG placement and sizing based on voltage stability maximization and minimization of power losses". In: *Energy Conversion and Management* 70 (2013), pp. 202–210.

[8] L. R. Araujo, D. Penido, S. Carneiro, and J. L. R. Pereira. "A three-phase optimal power-flow algorithm to mitigate voltage unbalance". In: *IEEE Transactions on Power Delivery* 28.4 (2013), pp. 2394–2402.

[9] C. Arendse and G. Atkinson-Hope. "Design of a Steinmetz symmetrizer and application in unbalanced network". In: *Universities Power Engineering Conference*. 2010.

[10] R. J. Avalos, C. A. Cañizares, and M. F. Anjos. "A practical voltage-stability-constrained optimal power flow". In: *Power and Energy Society General Meeting-Conversion and Delivery of Electrical Energy in the 21st Century, 2008 IEEE*. IEEE. 2008, pp. 1–6.

[11] R. J. Avalos, C. A. Cañizares, F. Milano, and A. J. Conejo. "Equivalency of continuation and optimization methods to determine saddle-node and limit-induced bifurcations in power systems". In: *IEEE Transactions on Circuits and Systems I: Regular Papers* 56.1 (2009), pp. 210–223.

[12] C. G. Bajo, S. Hashemi, S. B. Kjsær, G. Yang, and J. Østergaard. "Voltage unbalance mitigation in LV networks using three-phase PV systems". In: *IEEE International Conference on Industrial Technology (ICIT)*. 2015, pp. 2875–2879.

[13] K. Balamurugan, D. Srinivasan, and T. Reindl. "Impact of distributed generation on power distribution systems". In: *Energy Procedia* 25 (2012), pp. 93–100.

[14] A. K. Basu, S. Chowdhury, S. Chowdhury, and S. Paul. "Microgrids: Energy management by strategic deployment of DERs—A comprehensive survey". In: *Renewable and Sustainable Energy Reviews* 15.9 (2011), pp. 4348–4356.

[15] A. Berizzi, P. Bresesti, P. Marannino, G. Granelli, and M. Montagna. "System-area operating margin assessment and security enhancement against voltage collapse". In: *IEEE Transactions on Power Systems* 11.3 (1996), pp. 1451–1462.

[16] A. Berizzi, P. Finazzi, D. Dosi, P. Marannino, and S. Corsi. "First and second order methods for voltage collapse assessment and security enhancement". In: *IEEE Transactions on Power Systems* 13.2 (1998), pp. 543–551.

[17] A. Berizzi, Y.-G. Zeng, P. Marannino, A. Vaccarini, and P. A. Scarpellini. "A second order method for contingency severity assessment with respect to voltage collapse". In: *IEEE Transactions on Power Systems* 15.1 (2000), pp. 81–87.

[18] A. Bokhari, A. Alkan, R. Dogan, M. Diaz-Aguiló, F. De Leon, D. Czarkowski, Z. Zabar, L. Birenbaum, A. Noel, and R. E. Uosef. "Experimental determination of the ZIP coefficients for modern residential, commercial, and industrial loads". In: *IEEE Transactions on Power Delivery* 29.3 (2014), pp. 1372–1381.

[19] S. Borenstein. "The trouble with electricity markets: understanding California's restructuring disaster". In: *Journal of economic perspectives* 16.1 (2002), pp. 191–211.

[20] S. Borenstein, M. Jaske, and A. Rosenfeld. "Dynamic pricing, advanced metering, and demand response in electricity markets". In: (2002).

[21] R. P. Broadwater, A. H. Khan, H. E. Shaalan, and R. E. Lee. "Time varying load analysis to reduce distribution losses through reconfiguration". In: *IEEE Transactions on Power Delivery* 8.1 (1993), pp. 294–300.

[22] M. Brown, M. Biswal, S. Brahma, S. J. Ranade, and H. Cao. "Characterizing and quantifying noise in PMU data". In: *IEEE Power and Energy Society General Meeting*. 2016.

[23] D. Callaway. "Tapping the energy storage potential in electric loads to deliver load following and regulation, with application to wind energy". In: *Energy Conver. Management* 50 (2009), pp. 1389–1400.

[24] D. S. Callaway and I. A. Hiskens. "Achieving controllability of electric loads". In: *Proceedings of the IEEE* 99.1 (2011), pp. 184–199.

[25] C. A. Cañizares. "Calculating optimal system parameters to maximize the distance to saddle-node bifurcations". In: *IEEE Transactions on Circuits and Systems I: Fundamental Theory and Applications* 45.3 (1998), pp. 225–237.

[26] C. Cañizares, W. Rosehart, A. Berizzi, and C. Bovo. "Comparison of voltage security constrained optimal power flow techniques". In: *Power Engineering Society Summer Meeting, 2001.* Vol. 3. 2001, pp. 1680–1685.

[27] J. Chapman, M. Ilic, C. King, L. Eng, and H. Kaufman. "Stabilizing a multimachine power system via decentralized feedback linearizing excitation control". In: *IEEE Transactions on Power Systems* 8.3 (1993), pp. 830–839.

[28] D. P. Chassin, K. Schneider, and C. Gerkensmeyer. "GridLAB-D: An open-source power systems modeling and simulation environment". In: *IEEE PES Transmission and Distribution Conference*. 2008.

[29] J.-H. Chen, W.-J. Lee, and M.-S. Chen. "Using a static VAR compensator to balance a distribution system". In: *IEEE Industry Applications Conference*. Vol. 4. 1996, pp. 2321–2326.

[30] B. Chew, B. Feldman, D. Ghosh, and M. Surampudy. "2018 Utility Demand Response Market Snapshot". In: *Smart Electric Power Alliance* (2018).

[31] C. Chung, L. Wang, F. Howell, and P. Kundur. "Generation rescheduling methods to improve power transfer capability constrained by small-signal stability". In: *IEEE Transactions on Power Systems* 19.1 (2004), pp. 524–530.

[32] E. Compatibility. "Part 2-2:Environment–compatibility levels for low-frequency conducted disturbances and signalling in public low-voltage power supply systems". In: *International Electrotechnical Commission Stardard* 61 (2002), pp. 000–2.

[33] M. Coppo, A. Raciti, R. Caldon, and R. Turri. "Exploiting inverter-interfaced DG for Voltage unbalance mitigation and ancillary services in distribution systems". In: *IEEE 1st International Forum on Research and Technologies for Society and Industry Leveraging a better tomorrow (RTSI)*. 2015, pp. 371–376.

[34] M. Datta and T. Senjyu. "Fuzzy control of distributed PV invertersenergy storage systems/electric vehicles for frequency regulation in a large power system". In: *IEEE Transactions on Smart Grid* 4.1 (2013), pp. 479–488.

[35] S. Deilami, A. S. Masoum, P. S. Moses, and M. A. Masoum. "Real-time coordination of plug-in electric vehicle charging in smart grids to minimize power losses and improve voltage profile". In: *IEEE Transactions on Smart Grid* 2.3 (2011), pp. 456–467.

[36] I. Dobson. "An iterative method to compute a closest saddle node or Hopf bifurcation instability in multidimensional parameter space". In: *IEEE International Symposium on Circuits and Systems*. Vol. 5. 1992, pp. 2513–2516.

[37] I. Dobson. "Distance to bifurcation in multidimensional parameter space: Margin sensitivity and closest bifurcations". In: *Bifurcation control* (2003), pp. 704–706.

[38] I. Dobson and L. Lu. "Computing an optimum direction in control space to avoid stable node bifurcation and voltage collapse in electric power systems". In: *IEEE Transactions on Automatic Control* 37.10 (1992), pp. 1616–1620.

[39] I. Dobson, L. Lu, and Y. Hu. "A direct method for computing a closest saddle node bifurcation in the load power parameter space of an electric power system". In: *EEE International Symposium on Circuits and Systems*. 1991, pp. 3019–3022.

[40] A. Dysko, W. E. Leithead, and J. O'Reilly. "Enhanced power system stability by coordinated PSS design". In: *IEEE Transactions on Power Systems* 25.1 (2009), pp. 413–422.

[41] S. Eftekharnejad, V. Vittal, G. T. Heydt, B. Keel, and J. Loehr. "Impact of increased penetration of photovoltaic generation on power systems". In: *IEEE Transactions on Power Systems* 28.2 (2013), pp. 893–901.

[42] *Electric Power Systems and Equipment - Voltage Ratings (60 Hertz)*. ANSI Standard Publication no. ANSI C84.1-1995.

[43] J. H. Enslin. "Network impacts of high penetration of photovoltaic solar power systems". In: *IEEE PES General Meeting*. IEEE. 2010, pp. 1–5.

[44] Z. Feng, V. Ajjarapu, and D. J. Maratukulam. "A practical minimum load shedding strategy to mitigate voltage collapse". In: *IEEE Transactions on Power Systems* 13.4 (1998), pp. 1285–1290.

[45] J. Fernandez, S. Bacha, D. Riu, H. Turker, and M. Paupert. "Current unbalance reduction in three-phase systems using single phase PHEV chargers". In: *IEEE Conference on Industrial Technology*. 2013, pp. 1940–1945.

[46] B. Foster, D. Burns, D. Kathan, M. Lee, and S. Peirovi. "2019 Assessment of demand response and advanced metering". In: (2018).

[47] K. Girigoudar and L. A. Roald. "On the impact of different voltage unbalance metrics in distribution system optimization". In: *Power Systems Computation Conference (PSCC)*. 2020.

[48] S. Gomes, N. Martins, and C. Portela. "Computing small-signal stability boundaries for large-scale power systems". In: *IEEE Transactions on Power Systems* 18.2 (2003), pp. 747–752.

[49] S. Greene, I. Dobson, and F. L. Alvarado. "Sensitivity of the loading margin to voltage collapse with respect to arbitrary parameters". In: *IEEE Transactions on Power Systems* 12.1 (1997), pp. 262–272.

[50] L. M. Hajagos and B. Danai. "Laboratory measurements and models of modern loads and their effect on voltage stability studies". In: *IEEE Transactions on Power Systems* 13.2 (1998), pp. 584–592.

[51] E. T. Hale, L. A. Bird, R. Padmanabhan, and C. M. Volpi. *Potential roles for demand response in high-growth electric systems with increasing shares of renewable generation*. Tech. rep. National Renewable Energy Lab.(NREL), Golden, CO (United States), 2018.

[52] I. A. Hiskens and R. J. Davy. "Exploring the power flow solution space boundary". In: *IEEE Transactions on Power Systems* 16.3 (2001), pp. 389–395.

[53] I. A. Hiskens and J. V. Milanovic. "Load modelling in studies of power system damping". In: *IEEE Transactions on Power Systems* 10.4 (1995), pp. 1781–1788.

[54] I. A. Hiskens and M. Pai. "Trajectory sensitivity analysis of hybrid systems". In: *IEEE Transactions on Circuits and Systems I: Fundamental Theory and Applications* 47.2 (2000), pp. 204–220.

[55] T. Hong and F. De Leon. "Controlling non-synchronous microgrids for load balancing of radial distribution systems". In: *IEEE Transactions on Smart Grid* 8.6 (2016), pp. 2608–2616.

[56] R. A. Horn and C. R. Johnson. "Topics in Matrix Analysis". In: *Cambridge University Press, New York* (1991).

[57] Z. Huang, N. Zhou, F. Tuffner, Y. Chen, D. Trudnowski, W. Mittelstadt, J. Hauer, and J. Dagle. "Improving small signal stability through operating point adjustment". In: *Power and Energy Society General Meeting, 2010 IEEE*. IEEE. 2010, pp. 1–8.

[58] IEEE. *PES Test Feeder Cases*. 1992. URL: `https://site.ieee.org/pes-testfeeders/resources/`.

[59] "IEEE recommended practice for electric power distribution for industrial plants". In: *IEEE Standard 141-1993* (Apr. 1994), pp. 1–768.

[60] V. Ilea, A. Berizzi, and M. Eremia. "Damping inter-area oscillations by FACTS devices". In: *Universities Power Engineering Conference (UPEC), 2009 Proceedings of the 44th International*. IEEE. 2009, pp. 1–5.

[61] G. Irisarri, X. Wang, J. Tong, and S. Mokhtari. "Maximum loadability of power systems using interior point nonlinear optimization method". In: *IEEE Transactions on Power Systems* 12.1 (1997), pp. 162–172.

[62] O. Jordi, L. Sainz, and M. Chindris. "Steinmetz system design under unbalanced conditions". In: *European Transactions on Electrical Power* 12.4 (2002), pp. 283–290.

[63] S. Kadam and B. Bletterie. "Balancing the grid with single-phase PV-installations". In: *IEEE 26th International Symposium on Industrial Electronics (ISIE)*. 2017, pp. 63–69.

[64] D. Karlsson and D. J. Hill. "Modelling and identification of nonlinear dynamic loads in power systems". In: *IEEE Transactions on Power Systems* 9.1 (1994), pp. 157–166.

[65] W. Kersting and W. Phillips. "Phase frame analysis of the effects of voltage unbalance on induction machines". In: 33.2 (1997), pp. 415–420.

[66] W. H. Kersting. "Radial distribution test feeders". In: *IEEE Transactions on Power Systems* 6.3 (1991), pp. 975–985.

[67] S. K. Kodsi and C. A. Cañizares. "Application of a stability-constrained optimal power flow to tuning of oscillation controls in competitive electricity markets". In: *IEEE Transactions on Power Systems* 22.4 (2007), pp. 1944–1954.

[68] K. Koorehdavoudi, M. Yao, J. L. Mathieu, and S. Roy. "Using demand response to shape the fast dynamics of the bulk power network". In: *Proceedings of the IREP Symposium on Bulk Power System Dynamics and Control, Espinho, Portugal*. 2017.

[69] D. Kottick, M. Blau, and D. Edelstein. "Battery energy storage for frequency regulation in an island power system". In: *IEEE Transactions on Energy Conversion* 8.3 (1993), pp. 455–459.

[70] P. Kundur, N. J. Balu, and M. G. Lauby. *Power system stability and control*. Vol. 7. McGraw-hill New York, 1994.

[71] P. Kundur, J. Paserba, V. Ajjarapu, G. Andersson, A. Bose, C. Canizares, N. Hatziargyriou, D. Hill, A. Stankovic, C. Taylor, et al. "Definition and classification of power system stability". In: *IEEE Transactions on Power Systems* 19.2 (2004), pp. 1387–1401.

[72] G. G. Lage, G. R. da Costa, and C. A. Cañizares. "Limitations of assigning general critical values to voltage stability indices in voltage-stability-constrained optimal power flows". In: *Power System Technology (POWERCON), 2012 IEEE International Conference on*. IEEE. 2012, pp. 1–6.

[73] J. Lavaei and S. H. Low. "Zero duality gap in optimal power flow problem". In: *IEEE Transactions on Power Systems* 27.1 (2012), pp. 92–107.

[74] G. S. Ledva, S. Peterson, and J. L. Mathieu. "Benchmarking of Aggregate Residential Load Models Used for Demand Response". In: *IEEE Power and Energy Society General Meeting*. 2018.

[75] C.-Y. Lee. "Effects of unbalanced voltage on the operation performance of a three-phase induction motor". In: *IEEE Transactions on Energy Conversion* 14.2 (1999), pp. 202–208.

[76] D. Lee, H. D. Nguyen, K. Dvijotham, and K. Turitsyn. "Convex restriction of power flow feasibility sets". In: *IEEE Transactions on Control of Network Systems* 6.3 (2019), pp. 1235–1245.

[77] S.-Y. Lee and C.-J. Wu. "On-line reactive power compensation schemes for unbalanced three phase four wire distribution feeders". In: *IEEE Transactions on Power Delivery* 8.4 (1993), pp. 1958–1965.

[78] X. Liang. "Emerging power quality challenges due to integration of renewable energy sources". In: *IEEE Transactions on Industry Applications* 53.2 (2017), pp. 855–866.

[79] P.-A. Lof, T. Smed, G. Andersson, and D. Hill. "Fast calculation of a voltage stability index". In: *IEEE Transactions on Power Systems* 7.1 (1992), pp. 54–64.

[80] R. Londero, C. Affonso, and M. Nunes. "Impact of distributed generation in steady state, voltage and transient stability-Real case". In: *2009 IEEE Bucharest PowerTech*. IEEE. 2009, pp. 1–6.

[81] Y. V. Makarov, V. A. Maslennikov, and D. J. Hill. "Calculation of oscillatory stability margins in the space of power system controlled parameters". In: *Proceedings Stockholm Power Tech, Stockholm* (1995), pp. 416–421.

[82] E. Mallada and A. Tang. "Dynamics-aware optimal power flow". In: *52nd IEEE Conference on Decision and Control*. IEEE. 2013, pp. 1646–1652.

[83] E. Mallada and A. Tang. "Improving damping of power networks: Power scheduling and impedance adaptation". In: *Decision and Control and European Control Conference (CDC-ECC), 2011 50th IEEE Conference on*. IEEE. 2011, pp. 7729–7734.

[84] J. F. Marley, D. K. Molzahn, and I. A. Hiskens. "Solving Multiperiod OPF Problems using an AC-QP Algorithm Initialized with an SOCP Relaxation". In: *IEEE Transactions on Power Systems* (2016).

[85] S. Mendoza-Armenta and I. Dobson. "A formula for damping interarea oscillations with generator redispatch". In: *Bulk Power System Dynamics and Control-IX Optimization, Security and Control of the Emerging Power Grid (IREP), 2013 IREP Symposium*. IEEE. 2013, pp. 1–18.

[86] S. Mendoza-Armenta and I. Dobson. "Applying a formula for generator redispatch to damp interarea oscillations using synchrophasors". In: *IEEE Transactions on Power Systems* 31.4 (2016), pp. 3119–3128.

[87] P. Mercier, R. Cherkaoui, and A. Oudalov. "Optimizing a battery energy storage system for frequency control application in an isolated power system". In: *IEEE Transactions on Power Systems* 24.3 (2009), pp. 1469–1477.

[88] F. Milano. *Power system modelling and scripting*. Springer Science & Business Media, 2010.

[89] N. Mithulananthan, C. A. Cañizares, and J. Reeve. "Hopf bifurcation control in power system using power system stabilizers and static var compensators". In: *Proceedings of IEEE North American Power Symposium*. 1999, pp. 155–163.

[90] M. Moghavvemi and M. Faruque. "Effects of FACTS devices on static voltage stability". In: *2000 TENCON Proceedings. Intelligent Systems and Technologies for the New Millennium (Cat. No. 00CH37119)*. Vol. 2. IEEE. 2000, pp. 357–362.

[91] A. K. Mohanty and A. K. Barik. "Power system stability improvement using FACTS devices". In: *International Journal of Modern Engineering Research (IJMER)* 1.2 (2011), pp. 666–672.

[92] D. K. Molzahn. "Incorporating Squirrel-Cage Induction Machine Models in Convex Relaxations of OPF Problems". In: *IEEE Transactions on Power Systems, to be published.[Online]. Available: https://doi. org/10.1109/TPWRS* (2017).

[93] D. K. Molzahn and I. A. Hiskens. "Convex Relaxations of Optimal Power Flow Problems: An Illustrative Example". In: *IEEE Transactions on Circuits and Systems I: Regular Papers* 63.5 (2016), pp. 650–660.

[94] L. Monjo, L. Sainz, S. Riera, and J. Bergas. "Theoretical study of the Steinmetz circuit design". In: *Electric Power Components and Systems* 41.3 (2013), pp. 304–323.

[95] F. Nejabatkhah and Y. W. Li. "Flexible Unbalanced Compensation of Three-Phase Distribution System Using Single-Phase Distributed Generation Inverters". In: *IEEE Transactions on Smart Grid* 10.2 (2019), pp. 1845–1857.

[96] NEMA, MG. "MG 1-2006". In: *Motors and Generators* 8 (2006).

[97] T. B. Nguyen and M. Pai. "Dynamic security-constrained rescheduling of power systems using trajectory sensitivities". In: *IEEE Transactions on Power Systems* 18.2 (2003), pp. 848–854.

[98] NICTA/Monash University. *Steady-State AC Network Visualization in the Browser*. URL: `http://immersive.erc.monash.edu.au/stac/`.

[99] NRECA. *Open Modeling Framework*. 2020. URL: `https://github.com/dpinney/omf`.

[100] *NREL Measurement and Instrumentation Data Center*. URL: `https://midcdmz.nrel.gov/`.

[101] R. Otto, T. Putman, and L. Gyugyi. "Principles and applications of static, thyristor-controlled shunt compensators". In: *IEEE Transactions on Power apparatus and Systems* 5 (1978), pp. 1935–1945.

[102] T. Overbye. "Effects of load modelling on analysis of power system voltage stability". In: *International Journal of Electrical Power & Energy Systems* 16.5 (1994), pp. 329–338.

[103] M. Pai. *Energy function analysis for power system stability*. Springer Science & Business Media, 2012.

[104] R. Pedersen, C. Sloth, and R. Wisniewski. "Verification of power grid voltage constraint satisfaction—A barrier certificate approach". In: *Control Conference (ECC), 2016 European*. IEEE. 2016, pp. 447–452.

[105] P. Pillay and M. Manyage. "Definitions of voltage unbalance". In: *IEEE Power Engineering Review* 21.5 (2001), pp. 50–51.

[106] PNNL. *GridLAB-D software*. URL: `https://www.gridlabd.org/`.

[107] PNNL. *GridLAB-D Taxonomy Feeder*. 2020. URL: `https://github.com/gridlab-d/Taxonomy_Feeders`.

[108] G. Putrus, P. Suwanapingkarl, D. Johnston, E. Bentley, and M. Narayana. "Impact of electric vehicles on power distribution networks". In: *IEEE Vehicle Power and Propulsion Conference*. 2009, pp. 827–831.

[109] K. Qian, C. Zhou, Y. Yuan, X. Shi, and M. Allan. "Analysis of the environmental benefits of distributed generation". In: *2008 IEEE Power and Energy Society General Meeting-Conversion and Delivery of Electrical Energy in the 21st Century*. IEEE. 2008, pp. 1–5.

[110] W. D. Rosehart, C. A. Cañizares, and V. H. Quintana. "Effect of detailed power system models in traditional and voltage-stability-constrained optimal power-flow problems". In: *IEEE Transactions on Power Systems* 18.1 (2003), pp. 27–35.

[111] W. Rosehart, C. Cañizares, and V. Quintana. "Optimal power flow incorporating voltage collapse constraints". In: *Power Engineering Society Summer Meeting, 1999. IEEE*. Vol. 2. 1999, pp. 820–825.

[112] T. Sadamoto, A. Chakrabortty, T. Ishizaki, and J.-i. Imura. "Dynamic modeling, stability, and control of power systems with distributed energy resources: Handling faults using two control methods in tandem". In: *IEEE Control Systems Magazine* 39.2 (2019), pp. 34–65.

[113] M. El-Sadek, M. Dessouky, G. Mahmoud, and W. Rashed. "Enhancement of steady-state voltage stability by static VAR compensators". In: *Electric Power Systems Research* 43.3 (1997), pp. 179–185.

[114] P. W. Sauer and M. Pai. *Power system dynamics and stability*. Stipes, 1997.

[115] F. Shahnia, P. J. Wolfs, and A. Ghosh. "Voltage unbalance reduction in low voltage feeders by dynamic switching of residential customers among three phases". In: *IEEE Transactions on Smart Grid* 5.3 (2014), pp. 1318–1327.

[116] J. Short, D. Infield, and L. Freris. "Stabilization of grid frequency through dynamic demand control". In: *IEEE Transactions on Power Systems* 22.3 (2007), pp. 1284–1293.

[117] T. Smed. "Feasible eigenvalue sensitivity for large power systems". In: *IEEE Transactions on Power Systems* 8.2 (1993), pp. 555–563.

[118] O. Solomon and E. Fridman. "Systems with gamma-distributed delays: a Lyapunov-based analysis". In: *IEEE Conference on Decision and Control*. 2013, pp. 318–323.

[119] P. Street. "Dataport: the world's largest energy data resource". In: *Pecan Street Inc* (2015).

[120] X. Su, M. A. Masoum, and P. J. Wolfs. "Optimal PV inverter reactive power control and real power curtailment to improve performance of unbalanced four-wire LV distribution networks". In: *IEEE Transactions on Sustainable Energy* 5.3 (2014), pp. 967–977.

[121] S. Sun, B. Liang, M. Dong, and J. A. Taylor. "Phase balancing using energy storage in power grids under uncertainty". In: *IEEE Transactions on Power Systems* 31.5 (2016), pp. 3891–3903.

[122] M. Surampudy, B. Chew, M. Keller, and T. Gibson. "2019 Utility Demand Response Market Snapshot". In: *Smart Electric Power Alliance* (2019).

[123] R. J. Thomas and A. Tiranuchit. "Voltage instabilities in electric power networks". In: *Proceedings of 18th Southeast Symposium System Theory*. 1986, pp. 359–363.

[124] W. F. Tinney and C. E. Hart. "Power flow solution by Newton's method". In: *IEEE Transactions on Power Apparatus and systems* 11 (1967), pp. 1449–1460.

[125] A. Tiranuchit, L. Ewerbring, R. Duryea, R. Thomas, and F. Luk. "Towards a computationally feasible on-line voltage instability index". In: *IEEE Transactions on Power Systems* 3.2 (1988), pp. 669–675.

[126] A. Tiranuchit and R. Thomas. "A posturing strategy against voltage instabilities in electric power systems". In: *IEEE Transactions on Power Systems* 3.1 (1988), pp. 87–93.

[127] K. Tran and M. Vaziri. "Effects of dispersed generation (DG) on distribution systems". In: *IEEE Power Engineering Society General Meeting, 2005*. IEEE. 2005, pp. 2173–2178.

[128] A. P. Transmission. "Multiple SVC installations for traction load balancing in Central Queensland". In: *Pamphlet A02* 134.26 (2011), p. 02.

[129] U.S. Department of Energy. *Benefits of demand response in electricity markets and recommendations for achieving them*. Tech. rep. `http://www.oe.energy.gov/DocumentsandMedia/congress_1252d.pdf`. 2006.

[130] U.S. Department of Energy. *Stopping a costly leak: The effects of unbalanced voltage on the life and efficiency of three-phase electric motors*. Tech. rep. 2005.

[131] A. Ulbig, T. S. Borsche, and G. Andersson. "Impact of low rotational inertia on power system stability and operation". In: *Proceedings of IFAC* 47.3 (2014), pp. 7290–7297.

[132] O. A. Urquidez and L. Xie. "Singular value sensitivity based optimal control of embedded VSC-HVDC for steady-state voltage stability enhancement". In: *IEEE Transactions on Power Systems* 31.1 (2016), pp. 216–225.

[133] P. Varaiya, F. F. Wu, and R.-L. Chen. "Direct methods for transient stability analysis of power systems: Recent results". In: *Proceedings of the IEEE* 73.12 (1985), pp. 1703–1715.

[134] H. Vardhan, C. A. Barreto, and W. Emfinger. *GridLAB-D Design Studio*. URL: `https://cps-vo.org/group/gridlabd`.

[135] V. Vignesh, S. Chakrabarti, and S. Srivastava. "An experimental study on the load modelling using PMU measurements". In: *T&D Conference and Exposition, 2014 IEEE PES*. 2014.

[136] V. Vittal, J. McCalley, V. Ajjarapu, and U. V. Shanbhag. *Impact of Increased DFIG Wind Penetration on Power Systems and Markets*. Tech. rep. 09-10. Power Systems Engineering Research Center (PSERC), 2009.

[137] A. Von Jouanne and B. Banerjee. "Assessment of voltage unbalance". In: *IEEE Transactions on Power Delivery* 16.4 (2001), pp. 782–790.

[138] L. Wang and C. Chung. "Increasing power transfer limits at interfaces constrained by small-signal stability". In: *Power Engineering Society Winter Meeting, 2002. IEEE.* Vol. 2. IEEE. 2002, pp. 1184–1187.

[139] L. Wang, F. Howell, P. Kundur, C. Chung, and W. Xu. "A tool for small-signal security assessment of power systems". In: *PICA 2001. Innovative Computing for Power-Electric Energy Meets the Market. 22nd IEEE Power Engineering Society. International Conference on Power Industry Computer Applications*. IEEE. 2001, pp. 246–252.

[140] R. Wang and R. H. Lasseter. "Re-dispatching generation to increase power system security margin and support low voltage bus". In: *IEEE Transactions on Power Systems* 15.2 (2000), pp. 496–501.

[141] S. Weckx, C. Gonzalez, and J. Driesen. "Reducing grid losses and voltage unbalance with PV inverters". In: *IEEE PES General Meeting*. 2014.

[142] A. J. Wood and B. F. Wollenberg. *Power Generation, Operation, and Control*. John Wiley & Sons, 2012.

[143] D. Wu, D. K. Molzahn, B. C. Lesieutre, and K. Dvijotham. "A deterministic method to identify multiple local extrema for the AC optimal power flow problem". In: *IEEE Transactions on Power Systems* 33.1 (2018), pp. 654–668.

[144] M. Yao. *Modified GridLAB-D R1-12.47-1 Feeder*. 2020. URL: `https://github.com/MengqiYao/Modified-GridLabD-feeder.git`.

[145] L. Yazdani and M. R. Aghamohammadi. "Damping inter-area oscillation by generation rescheduling based on wide-area measurement information". In: *International Journal of Electrical Power & Energy Systems* 67 (2015), pp. 138–151.

[146] Y. Yu, L. Liu, K. Pei, H. Li, Y. Shen, and W. Sun. "An under voltage load shedding optimization method based on the online voltage stability analysis". In: *Power System Technology (POWERCON), 2016 IEEE International Conference on*. 2016.

[147] W. Zhang, J. Lian, C.-Y. Chang, and K. Kalsi. "Aggregated modeling and control of air conditioning loads for demand response". In: *IEEE Transactions on Power Systems* 28.4 (2013), pp. 4655–4664.

[148] Y. Zhang, L. Wehenkel, P. Rousseaux, and M. Pavella. "SIME: A hybrid approach to fast transient stability assessment and contingency selection". In: *International Journal of Electrical Power & Energy Systems* 19.3 (1997), pp. 195–208.

[149] R. Zimmerman, C. Murillo-Sanchez, and R. Thomas. "MATPOWER: Steady-State Operations, Planning, and Analysis Tools for Power Systems Research and Education". In: *IEEE Transactions on Power Systems* 26.1 (Feb. 2011), pp. 12–19. ISSN: 0885-8950. DOI: 10.1109/TPWRS.2010.2051168.